

Electronic Properties of Molecular Silicon

Haixing Li

Submitted in partial fulfillment of the  
requirements for the degree of  
Doctor of Philosophy  
in the Graduate School of Arts and Sciences

COLUMBIA UNIVERSITY

2017

© 2017  
Haixing Li  
All rights reserved

## ABSTRACT

### Electronic Properties of Molecular Silicon

Haixing Li

This dissertation explores the electronic characteristics of silicon at the single molecule level. This idea is born as we enter the post-Moore's law era when the exponential shrinking of conventional silicon microelectronics has begun to stall and an investigation of molecular materials is timely. Single-molecule electronic components have shown promising functionalities such as conductors, switches, and diodes, and single molecule junctions have become a widely used test-bed for probing electron transport properties at the molecular level. In this thesis, we use scanning tunneling microscope break junction method to create single molecule junctions with a variety of silicon molecular wires. Our results demonstrate electronic properties of silicon beyond it being a semiconductor in its bulk form.

We begin this work in pursuit of an expanded understanding of low- $\kappa$  dielectric components with an experimental goal on determining the cause of its breakdown. Low- $\kappa$  dielectrics are beneficial as they enable faster switching speeds and lower heat dissipation, however, they tend to breakdown after prolonged usage under an applied voltage. At the atomic level, low- $\kappa$  dielectric breakdown involves bond rupture. To determine which bond breaks easily, we conduct experimental studies on the robustness of individual chemical bonds that are commonly found in low- $\kappa$  dielectrics. We subject the single molecule junctions to a high bias and investigate the breakdown phenomenon of individual Si-Si, Ge-Ge, Si-O, and Si-C bonds. Among these, Si-C proved to be significantly

more durable than the others. To further prove our hypothesis that the Si-Si bond ruptures under the applied high bias, we design a two-path molecular structure consisting of a Si-Si bond in parallel with a naphthyl group. The broken junction shows conduction through the naphthyl pathway, strongly indicating that the Si-Si bond is breaking. This demonstrates a method for probing the bond cleavage under an electric field and provides insights to the weak links in low- $\kappa$  dielectrics.

Next, we study the fundamental charge transport characteristics of single molecule junctions comprised of Si and Ge-based molecular wires, starting with the simplest form - linear atomic chains. We observe a slower decay of conductance with increasing length in the silanes and germanes than in alkanes, indicating that the electronic delocalization in the Si-Si and Ge-Ge  $\sigma$ -bonds is stronger than that of the well-studied C-C bonds. Furthermore, we demonstrate that this electronic delocalization in the Si-Si and Ge-Ge bonded backbones enables single-molecule conductance switching. This conductance switch, induced by a mechanical modulation, relies on the nature of the terminal groups and constitutes the first example of a stereoelectronic switch. We also study the molecular conductance of these silanes with metal contacts other than Au, which can potentially open up interesting avenues as metal varies in its electronic states and catalytic activities. We find that Ag electrodes enable higher conductance for thiol-terminated silanes than Au or Pt electrodes.

The electrical properties of more complex silicon structures - silicon rings - were probed. We choose a five-membered silicon ring as a target system to investigate the effect of isomerism on single molecule conductance. We find that due to the flexibility of the ring, multiple conformations contribute to the spread in the measured conductance for

each isomer. This provides us with a starting point to further compare the conductance of a variety of silicon rings. We find that most of the silicon rings are less conductive than their linear counterparts due to the suboptimal backbone conformation for electronic coupling. In particular, destructive quantum interference appears in one of the bicyclic structures and leads to an exceptionally low conductance. This is the first example of a destructive quantum interference feature ever observed experimentally in a  $\sigma$ -bonded rather than a  $\pi$ -bonded system.

Finally, we investigate the impact of strain on molecular conductance of silanes. In one case, we introduce the strain using a silacyclobutane ring in the backbone. Unexpectedly, we find that ring strain enables a new Au-silacycle binding mode, resulting in a much higher conductance state. In another molecular design, we choose disilaacenaphthene in the backbone. This strained disilane is found to constitute an example of a direct Si-to-Au contact in single molecule circuits, thereby demonstrating a new binding motif that is valuable for designing high conducting molecular components.

Taken together, this body of work provides important knowledge about the transport properties of silicon at the nano-scale, as well as insights on the design of silicon components for nanoelectronics. This work represents one step forward to create functional silicon molecular components.

---

## Contents

<b>List of Figures</b>	<b>iii</b>
<b>List of Tables</b>	<b>ix</b>
<b>Acknowledgements</b>	<b>x</b>
<b>Introduction</b>	<b>1</b>
0.1 Silicon: From Bulk to a Molecule . . . . .	3
0.2 Experimental Method . . . . .	5
0.3 Electron Transport through Molecular Junctions . . . . .	8
0.4 Outline . . . . .	11
<b>1 Probing Si—Si Bond Rupture in Single Molecule Junctions</b>	<b>13</b>
1.1 Electric Field Breakdown in Single Molecule Junctions . . . . .	13
1.2 Mechanism for Si-Si Bond Rupture . . . . .	32
<b>2 Single Molecule Conductance of Linear Silanes and Germanes</b>	<b>48</b>
2.1 Stereoelectronic Switching . . . . .	48
2.2 Conductance Trend From Alkanes to Silanes to Germanes . . . . .	68
2.3 Gold, Silver and Platinum as Electrical Contacts for Silanes . . . . .	88

<b>3</b>	<b>Single Molecule Conductance of Cyclic Silanes</b>	<b>98</b>
3.1	Cyclopentasilane: Conformations Control Conductance . . . . .	98
3.2	Understanding Electron Transport through Cyclic and Bicyclic Silanes . .	113
<b>4</b>	<b>Straining Silanes to Create High Conductance Pathways</b>	<b>128</b>
4.1	Strained Silacyclobutane Ring Creates High Conductance Pathways by Forming Au-silacycle Contact . . . . .	128
4.2	Ring-Strained Disilanes Creates High Conductance Pathways by Way of Direct $\sigma$ Si-Si to Au Coordination . . . . .	143
	<b>Conclusion</b>	<b>154</b>
	<b>Bibliography</b>	<b>158</b>

---

*List of Figures*

0.1	Examples of nanoscale silicon . . . . .	4
0.2	Gold atomic contact created by STM-BJ method . . . . .	6
0.3	Conductance data of a gold atomic contact . . . . .	6
0.4	A single molecule junction created by STM-BJ method . . . . .	7
0.5	Conductance data of a single molecule junction . . . . .	7
0.6	Energy level diagram for transport through a single molecule junction . . . .	9
0.7	Calculated transmissions of two example cyclic silanes . . . . .	10

1.1	Experimental method for high bias measurement . . . . .	17
1.2	Junction breaking data for molecules with varied linkers . . . . .	18
1.3	Junction breaking probability for hexane-dimethylsulfide . . . . .	19
1.4	Control experiment with piezo modulation . . . . .	20
1.5	Synthetic scheme for silanes and germanes. . . . .	22
1.6	Conductance data for <b>Si4-Si6</b> dithiols . . . . .	22
1.7	Junction breaking probability for CH <sub>2</sub> SH terminated molecules . . . . .	24
1.8	Method to determine the conductance at different voltages . . . . .	26
1.9	Junction rupture probability plotted against the conductance . . . . .	27
1.10	Junction rupture probability plotted against the joule heat . . . . .	27
1.11	Junction breaking probability for SMe terminated molecules . . . . .	28
1.12	Time dependence analysis algorithm . . . . .	31
1.13	Synthesis of <b>Si2Naph</b> . . . . .	34
1.14	Conductance measurement for <b>Si2Naph</b> and <b>Si2</b> . . . . .	36
1.15	Method for high bias measurement for <b>Si2Naph</b> and <b>Si2</b> . . . . .	38
1.16	2D histograms for high bias measurement for <b>Si2Naph</b> and <b>Si2</b> . . . . .	39
1.17	Conductance data for control molecules . . . . .	40
1.18	Calculated voltage drop across the <b>Si2</b> junction . . . . .	42
1.19	Calculated vibrational modes for <b>Si2</b> and <b>Si2Naph</b> . . . . .	43
1.20	Calculated vibrational modes for <b>Si2</b> as a function of applied voltage . . . . .	44
1.21	Calculated vibrational modes for <b>Si2Naph</b> as a function of applied voltage . . . . .	44
1.22	Calculated vibrational modes for <b>Si2</b> as a function of charge. . . . .	45
1.23	Calculated vibrational modes for <b>Si2Naph</b> as a function of charge . . . . .	45

1.24	Molecular dynamics simulations for <b>Si2</b> . . . . .	46
2.1	Structures of oligosilanes <b>Si1–Si10</b> . . . . .	51
2.2	Synthesis of oligosilanes . . . . .	52
2.3	Conductance histograms of the oligosilanes . . . . .	53
2.4	$\beta$ plot for oligosilanes with thioanisole and methylthiomethyl linkers . . . . .	54
2.5	Conductance data of <b>Si4</b> . . . . .	55
2.6	2D histograms of <b>Si1–Si3; Si5–Si10</b> . . . . .	57
2.7	$\beta$ values of the low G and high G peaks for oligosilanes . . . . .	58
2.8	2D histograms of compression-elongation experiment for <b>Si6</b> . . . . .	58
2.9	2D histogram of compression-elongation experiment for <b>Si6</b> and <b>C8</b> . . . . .	60
2.10	Si-Si-Si-Si dihedral angles for the lowest energy structures . . . . .	61
2.11	Algorithm for 2D conductance analysis . . . . .	61
2.12	A sample trace showing the analysis of <b>Si4</b> . . . . .	62
2.13	Energy plot for $\text{H}_3\text{C-S-CH}_2\text{-SiMe}_3$ . . . . .	63
2.14	DFT calculations of terminal dihedrals of Au-Si4-Au junction . . . . .	65
2.15	Tunnel coupling as a function of Au-Au distance for <b>C6</b> . . . . .	67
2.16	Structures of <b>Ge1–Ge10</b> . . . . .	71
2.17	Synthesis of germanes <b>Ge1–Ge10</b> . . . . .	72
2.18	1D conductance histograms and $\beta$ plot of <b>Ge1–Ge10</b> . . . . .	74
2.19	$\beta$ plot of alkanes, silanes and germanes . . . . .	75
2.20	Cyclic voltammetry-derived HOMO levels for $\text{Si}_n, \text{Ge}_n$ series . . . . .	78
2.21	1D histograms of <b>Ge1–10</b> for odd even comparison . . . . .	79

2.22	2D histograms of conductance measurements for <b>Ge1-Ge10</b> . . . . .	80
2.23	2D histograms with displacement aligned to the switching event for <b>Ge1-10</b> .	81
2.24	DFT calculations for Au- <b>Ge4</b> -Au junction . . . . .	82
2.25	Representation of an AND logic gate . . . . .	83
2.26	Compression-elongation experiment analysis for <b>Ge5</b> . . . . .	84
2.27	$\beta$ plot for low G (pre-switching) and high G (post switching) of germanes . .	85
2.28	A comparison of junction training in <b>Ge5</b> vs. <b>Si6</b> . . . . .	85
2.29	Example traces for metal- <b>Si6</b> -metal junctions (Metal = Ag, Au and Pt) . . . .	91
2.30	1D conductance histograms and $\beta$ plot for metal-Si <sub>n</sub> -metal junctions (Metal = Ag, Au and Pt) . . . . .	92
2.31	2D conductance histograms for <b>Si6-Si9</b> measured with Au, Ag, and Pt electrodes	95
2.32	Junction elongation length for metal-Si <sub>n</sub> -metal junctions (Metal = Ag, Au and Pt) . . . . .	95
3.1	Synthesis of trans and cis cyclopentasilane terminated with methylthiomethyl	101
3.2	Six generic conformer types of a di-substituted five membered ring . . . . .	103
3.3	1D and 2D conductance histograms of <b>cis-Si5</b> and <b>trans-Si5</b> . . . . .	104
3.4	Conductance data of <b>cis-Si5</b> and <b>trans-Si5</b> in comparison with <b>Si3</b> and <b>Si4</b> .	105
3.5	Geometries and transmissions of two example conformers of <b>cis-Si5</b> and <b>trans-Si5</b> . . . . .	106
3.6	DFT calculations for <b>trans-Si5</b> and <b>cis-Si5</b> with terminal dihedrals in or- tho/ortho conformation . . . . .	108

3.7	DFT calculations for <b>trans-Si5</b> and <b>cis-Si5</b> with terminal dihedrals in anti/ortho conformation . . . . .	110
3.8	DFT calculations for <b>trans-Si5</b> and <b>cis-Si5</b> with terminal dihedrals in anti/anti conformation . . . . .	111
3.9	Chemical structures of four cyclic silanes . . . . .	117
3.10	1D conductance histograms for four cyclic silane series . . . . .	119
3.11	Measured and calculated conductance of four cyclic silane series . . . . .	120
3.12	2D conductance histograms for <b>4-ring</b> series. . . . .	120
3.13	2D conductance histograms for <b>5-ring</b> series. . . . .	120
3.14	2D conductance histograms for <b>221</b> series. . . . .	121
3.15	2D conductance histograms for <b>222</b> series. . . . .	122
3.16	1D conductance histograms of TMS and isobutyl substituted <b>4-ring</b> series . . . . .	122
3.17	$\beta$ plot of TMS and isobutyl substituted <b>4-ring</b> series . . . . .	123
3.18	Measured and calculated junction length for four cyclic silane series . . . . .	125
3.19	Calculated transmissions for <b>222</b> series . . . . .	126
4.1	Chemical Structure of <b>1</b> (silacyclobutane with thioanisole linkers) . . . . .	130
4.2	Conductance data for <b>1</b> . . . . .	131
4.3	Time dependence in conductance measurement of <b>1</b> . . . . .	132
4.4	Concentration effect in conductance measurement of <b>1</b> . . . . .	133
4.5	Solvent effect in conductance measurement of <b>1</b> . . . . .	134
4.6	Conductance histograms of control <b>2, 3</b> . . . . .	135
4.7	Schematic of binding geometries . . . . .	135

4.8	Conductance histograms of control <b>4, 5, 6, 7, 8</b> and <b>14</b> . . . . .	137
4.9	Conductance histograms of control <b>9, 10, 11</b> and <b>12</b> . . . . .	139
4.10	Conductance histograms of control <b>20</b> . . . . .	140
4.11	2D histograms of elongation and compression measurement of <b>1</b> . . . . .	142
4.12	Structures of 1,2-Disilaacenaphthenes <b>1</b> and <b>2</b> . . . . .	145
4.13	1D and 2D conductance histograms for <b>1</b> and <b>2</b> . . . . .	145
4.14	Schematic of binding geometries for <b>2</b> . . . . .	146
4.15	1D and 2D conductance histograms for <b>3</b> and <b>4</b> . . . . .	147
4.16	Schematic of binding geometries for <b>3</b> and <b>4</b> . . . . .	149
4.17	Piezo displacement plotted versus time for the push-pull experiment . . . . .	150
4.18	2D histograms for <b>2</b> with 0.1nm stretch/compress distance . . . . .	150
4.19	2D histograms for <b>2</b> with 0.2nm stretch/compress distance . . . . .	151
4.20	2D histograms for <b>3</b> with 0.2nm stretch/compress distance . . . . .	151
4.21	2D histograms for <b>4</b> with 0.2nm stretch/compress distance . . . . .	152

---

*List of Tables*

3.1	Conductance values of four cyclic silane series . . . . .	118
4.1	Switching percentages for <b>2-4</b> in the push-pull experiments . . . . .	149

---

## *Acknowledgements*

I am forever grateful to my advisor Professor Latha Venkataraman and my mentor Professor Colin Nuckolls. I am also incredibly thankful to Professor Gemma Solomon, Professor James Leighton, Dr. Michael Steigerwald, Dr. Pierre Darancet, Professor Ferdinand Evers, Timothy Su, Marc Garner and Nathaniel Kim, and many others who taught me a lot of things throughout the years.

To my parents

致我的母亲刘效英和父亲李荣

---

## *Introduction*

On December 29th 1959, physicist Richard P. Feynman delivered a talk “There’s Plenty of Room at the Bottom” at the annual meeting of the American Physical Society.<sup>1</sup> This is now regarded as one of the earliest proposals of making, manipulating and controlling things on a small scale. “Small scale” can be very small, down to single atoms, as in Feynman’s example in his proposal of miniaturizing the computer:

“For instance, the wires should be 10 or 100 atoms in diameter, and the circuits should be a few thousand angstroms across. ”

Feynman considers this speech as an invitation for others to enter a new field of physics, as well as an opportunity to have an enormous number of technical applications.

“The problems of chemistry and biology can be greatly helped if our ability to see what we are doing, and to do things on an atomic level, is ultimately developed - a development which I think cannot be avoided.”

Decades later, the research field “Molecular Electronics” embodies this idea by using molecules, nature’s smallest building blocks, to create functional electronic circuits. Research in this area currently focuses on developing a fundamental understanding of transport phenomenon at the single molecule level, while exploring the potential for technological applications in the future. The molecules are attractive due to their sizes

in contrast to the micro-fabricated components, for example, the typical commercial fabrication node is in tens of nanometers<sup>2</sup> and the diameter of a benzene ring is 0.28 nm.<sup>3</sup> More importantly, this small size leads to quantum mechanical behaviors that are not observed in classic systems. These unique properties of molecules provide a fascinating framework for the theorists to resolve these intricate molecular-scale properties into clear physical language. Investigations of atomic-scale transport also relies on tools that allow us to observe and measure the fundamental properties of systems at the molecular scale.

A vast number of tools have been widely used in studies of single molecule phenomenon, such as single-molecule fluorescence resonance energy transfer<sup>4</sup>, single-molecule-based super-resolution light microscopy,<sup>5-7</sup> and scanning tunneling microscope break junction technique (STM-BJ). Invented and developed by scientists in the last decade,<sup>8,9</sup> STM-BJ has been used to uncover the electronic properties of single molecules bound to metal electrodes. This technique is a modified form of scanning tunneling microscopy where the STM tip is controlled to repeatedly form and break single molecule junctions. In my doctoral work, I used this technique to create single molecule circuits and studied a variety of silicon-based molecules.<sup>10-18</sup> With a continuing scaling down of the silicon devices, our findings provide important insight as they help us understand the electronic characteristics of silicon at the molecular scale and provide a starting point towards the realization of silicon-based molecular electronic devices.

## 0.1 Silicon: From Bulk to a Molecule

Silicon has been used as the major material for microelectronic devices and has revolutionized our world in the past five decades. The first breakthrough was the invention of the point-contact transistor in 1947 at Bell labs, then the first metal-oxide semiconductor field-effect transistor (MOSFET) was demonstrated in 1960;<sup>19</sup> numerous innovations in silicon technology happened in a short period of time. These pioneering works paved the way for the invention and continual development of integrated circuits,<sup>20</sup> which eventually became an integral part of our modern technology.

Now we are still living in the silicon age and technological progress continues. While the industry keeps on manufacturing smaller silicon transistor nodes with lithographic technique, researchers are exploring forms of silicon that can realize functionalities useful at the nanometer scale. One-dimensional (1D) silicon nanowires, assembled with boron or phosphor-doped versions, have exhibited rectifying transport similar to planar p-n junctions (Figure 0.1a).<sup>21</sup> The coaxial silicon nanowires of p-type/intrinsic/n-type structure have been shown to function as a solar cell with the energy conversion efficiency of up to 3.4 percent.<sup>22</sup> Two-dimensional (2D) silicene, a silicon analogue of graphene, has been predicted to have quantum spin hall effect<sup>23</sup> and chiral superconductivity<sup>24</sup> and has been reported to work as a field effect transistor at room temperature (Figure 0.1b).<sup>25</sup> Three-dimensional (3D) silicon nanoparticles with controlled size and morphology have played a significant role in working as the anodes in lithium-ion batteries (Figure 0.1c).<sup>26,27</sup> With the continuing demand for miniaturization, the understanding of the electronic properties of an even smaller silicon system, a single molecule, becomes relevant and critical.

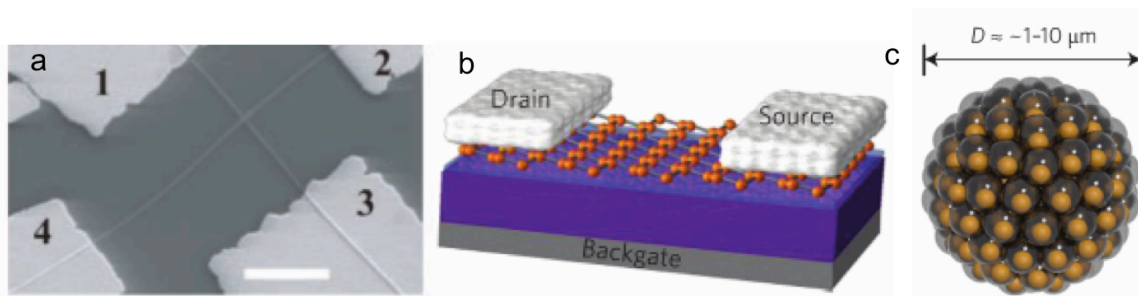


Figure 0.1: (a) Field emission scanning electron microscopy image of a crossed silicon nanowire junction. Scale bar is  $2 \mu\text{m}$ . (b) Schematic of a back-gated silicene transistor. (c) Three-dimensional view of a silicon pomogranate structure. (orange: silicon) The figures are adapted from references [21, 25, 26].

Apart from the perspective of fabricating silicon nanoelectronics using molecules, studies on molecular silicon can also shed light on the problems we encounter in the usage of bulk silicon materials. For example, materials with dielectric constant smaller than silicon dioxide have been used in semiconductor manufacturing because a low- $\kappa$  dielectric of the same thickness reduces parasitic capacitance, allowing more transistors packed onto a single chip. However, the low- $\kappa$  dielectrics are not perfect as they tend to breakdown after period of use. Researchers have been looking for the underlying cause of the fragility of these materials and trying to find solutions to eliminate this breakdown phenomenon. We decided to use a single molecule approach to shed light on this problem, hence the breakdown behavior of individual bonds commonly found in low- $\kappa$  dielectrics can be studied systematically, allowing us to identify the weak bonds that could cause the breakdown in bulk dielectrics.

Owing to the progress in silicon synthesis and the development in single molecule electronics, we are now able to create single molecule circuits containing silicon atoms. A number of observations from the single molecule studies on silanes have shown they ex-

hibit behaviors distinct from the commonly studied carbon-based analogs, from the electron transport properties, junction formation geometries to bond stabilities under high bias. Examples of such are discussed in this thesis.

## 0.2 Experimental Method

In order to determine the conductance of a molecule experimentally, we need a method that can incorporate a molecule into a molecular-size gap and then wire this unit into a circuit. In recent decades, a number of techniques that measure the conductance of single molecules have been developed including mechanically controlled break junctions,<sup>28</sup> conductive atomic force microscopes,<sup>29</sup> electromigration,<sup>30,31</sup> nanoparticle arrays,<sup>32</sup> and functionalized carbon nanotube and graphene electrodes.<sup>33-36</sup> The technique this thesis focuses on is the scanning tunneling microscope break junction (STM-BJ),<sup>8,9</sup> and we provide a brief overview here in this section.

In the STM-BJ method, we measure the conductance of single molecules bound to gold electrodes using a modified Scanning Tunneling Microscope (STM). We bring the Au tip in contact with the substrate first, then withdraw the tip while simultaneously measuring the current and the applied voltage. A schematic representation of the break junction process is shown in Figure 0.2. Briefly, the Au tip is first brought in contact with the substrate. Then as the tip is retracted, the Au-Au contact ultimately thins down to an atomic point contact. As the tip is further withdrawn from the substrate, this point contact ruptures. We observe that as we withdraw the tip, conductance decreases in a step-wise fashion with plateaus close to integer multiples of quantum conductance, defined as  $2e^2/h$

(Figure 0.3a). The last plateau at one quantum conductance indicates the formation of a single Au-Au atom contact. We repeatedly bring the Au tip in and out of contact with the substrate and collect thousands of such traces. We then use all traces to construct a histogram of conductance as shown in Figure 0.3b. We can see conductance peaks close to integer multiples of quantum conductance.

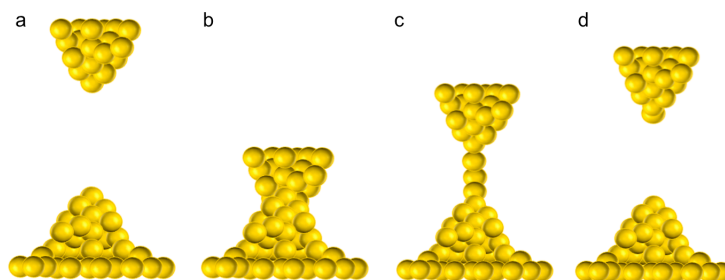


Figure 0.2: Schematic shows the STM-BJ method for clean Au measurement (a) Au tip and Au substrate, (b) Au tip is brought into contact with the substrate, (c) Tip is withdrawn until the contact thins down to a single Au atom contact, (d) Au-Au contact ruptures.

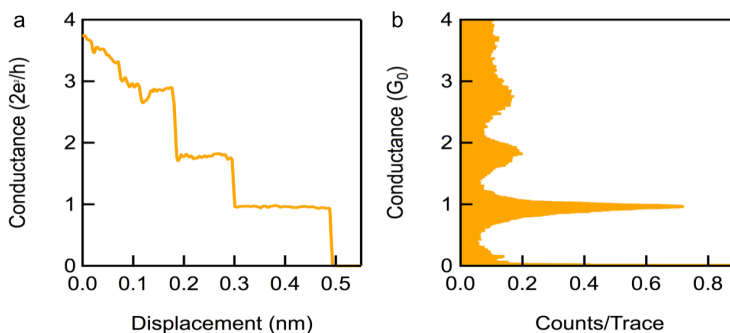


Figure 0.3: Conductance data of clean Au (a) A sample trace shows the conductance decreases in multiple integers of quantum conductance indicating the formation of atomic point contact, (b) 1D histogram constructed from 1000 traces measured on clean Au.

Solutions of the target molecule at 0.1 - 1 mM concentration in 1,2,4-trichlorobenzene are added to the substrate for molecular conductance measurements. In this case, when the Au-Au point contact breaks, a molecule with two aurophilic binding groups can bridge the gap between the tip and substrate (Figure 0.4a), forming a Au-molecule-Au junction.

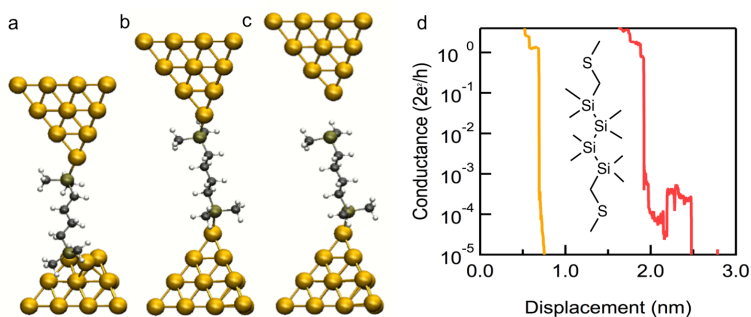


Figure 0.4: Schematic of STM-BJ method and example trace for single molecule conductance measurement (a) A molecule bridges the gap once the tip-substrate contact breaks, (b) The molecular junction extends to its full elongation, (c) The tip continues to be retracted until the molecular junction ruptures, (d) Left (yellow): Example trace of clean Au measurement shows that conductance sharply drops to noise floor after the  $1G_0$  plateau. Right (red): Example trace of molecular measurement displays an additional plateau below  $1G_0$ . Figure (a) is adapted from [37].

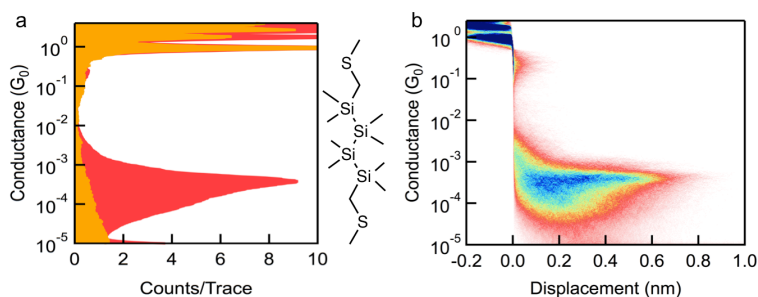


Figure 0.5: Conductance data of an example molecule (a) Logarithmically-binned 1D histogram compiled from traces before (yellow) and after (red) a solution of target molecule is added. The molecular structure is shown on the right. (b) Logarithmically-binned 2D histogram created by aligning the traces at the point when conductance crosses  $0.5 G_0$  and overlaying them.

The molecular junction is then elongated as we withdraw the tip and will reach its fully elongated geometry (Figure 0.4b) before its final rupture (Figure 0.4c). This junction formation contributes to additional plateaus in the recorded conductance versus displacement trace, as can be seen in the example trace (red) in Figure 0.4d, in contrast to the clean Au measurement (yellow) where the conductance drops sharply to instrument noise after  $1 G_0$  plateau.

For each molecule, we collect over 10,000 traces so that we can sample across all junction geometries and obtain statistically significant results. We compile all traces to generate logarithmically-binned one dimensional (1D) histograms, as shown in Figure 0.5a. We also create two dimensional (2D) conductance histograms (Figure 0.5b) by first aligning all the traces at the point where the conductance crosses  $0.5 G_0$  and then overlaying them. From this 2D analysis, we can learn the molecular junction conductance as well as the molecular junction elongation length.

### 0.3 Electron Transport through Molecular Junctions

The conductance of an atomic gold wire between two gold surfaces (Figure 0.2c) is equal to conductance quantum  $2e^2/h \approx 77.5mS \approx 12.9k\Omega^{-1}$ , irrespective of temperature or the length of the wire. This phenomenon, which had not been observed before 1988,<sup>38,39</sup> is clearly inconsistent with Ohm's law as one would expect the conductance to scale with the length of the wire as  $G \sim 1/L$ . The reason for this deviation from Ohm's law is that transport at the nanoscale is no longer diffusive but rather ballistic.

How does this physical picture change when we replace the gold wire with an Au-molecule-Au junction? Transport is still going to be ballistic but the details will depend on the available energetic states. The metal has continuous energy eigenstates filled up to the Fermi level ( $E_f$ ); a molecule has discrete energy eigenstates. Among all the energy levels of a neutral molecule, the highest occupied molecular orbital (HOMO) and the lowest unoccupied molecular orbital (LUMO) are the frontier orbitals. A transmission function is to describe the probability of an incident electron, of a given energy E, tunneling across

the junction. If the Fermi level of the metal is in resonance with one of the molecular orbitals, the transmission at  $E_f$  is 1 and we would observe a conductance close to single conductance channel  $2e^2/h$ . Typically the Fermi level of the metal lies in between the HOMO and LUMO,<sup>40-42</sup> therefore in most air stable molecules, we do not expect to see significant charge transfer between the metal states and the frontier orbitals. When the molecule attaches to the electrodes and forms a Au-molecule-Au junction, the discrete molecular orbitals hybridize with the electrode bands and broaden upon interacting with the leads (Figure 0.6a). When a bias is applied on the molecular junction, the chemical potential of the left electrode shifts up and that of the right electrode shifts down, resulting in molecular density of states in between. The electrons can transfer from the left to the right electrode with a charge current described by the integration of the transmission in this bias window (shaded area in Figure 0.6b). Therefore an accurate calculation of the transmission function is critical for understanding the charge transfer characteristics in molecular junctions.

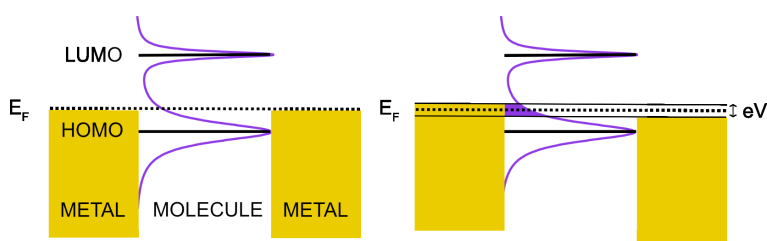


Figure 0.6: Transport through a single molecule junction. Schematic of a Au-molecule-Au junction with its energy level diagram when (a) in equilibrium and (b) under an applied bias. The purple toy transmission curves indicate the broadened HOMO and LUMO.

In most simple cases, transmission is well described by the broadening of a single molecular orbital (LUMO-dominated transport in Figure 0.6). However, in more complex

systems, the transmission can be dramatically altered. For example, one such case is the electron transport through molecular junctions dominated by the quantum interference effect.<sup>43-45</sup> The first study that explored the interference effect in a metal-molecule-metal junction was a theoretical work performed by Sautet and Joachim in 1988 on the electronic tunneling probability of a benzene ring embedded in a polyacetylene.<sup>46</sup> This work showed the calculated transmissions of para-, meta- and ortho-connected benzene rings using a simple method, concluding that the interference significantly alters the electronic transmission through the benzene in the meta- and ortho-cases. Since then, many theoretical works have predicted interference features in other molecular systems.<sup>47,48</sup>

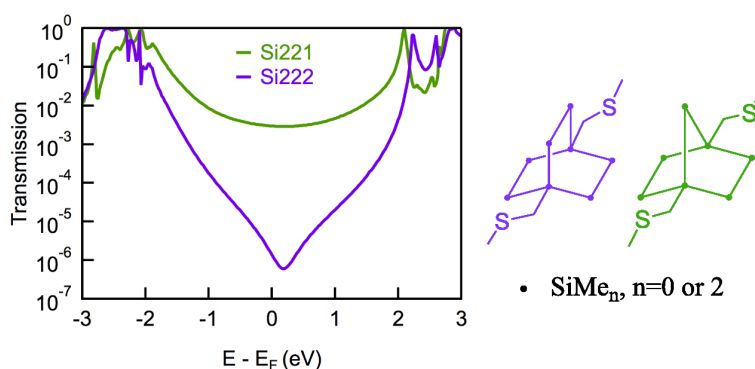


Figure 0.7: Calculated transmissions of two example cyclic silanes. Corresponding chemical structures are shown on the right.

In the literature, many examples of destructive quantum interference exist for  $\pi$ -conjugated molecules where quantum interference results in a much weakened  $\pi$ -bond coupling with the transmission dominated by the  $\sigma$ -bond coupling or through-space transport.<sup>49-53</sup> Much less discussed is quantum interference in  $\sigma$ -coupled systems. Except theoretical predictions,<sup>54</sup> destructive quantum interference in  $\sigma$ -coupled systems has not been observed experimentally. The silane rings studied in this thesis serve as the first example of such a case. A sharp dip in the transmission curve is commonly interpreted

as theoretical evidence for destructive quantum interference.<sup>43</sup> In Figure 0.7, we show the calculated transmissions for two  $\sigma$ -bonded bicyclic silicon structures. One (Si222) shows a quantum interference feature close to the Fermi energy, indicating a much lower conductance than the other bicyclic structure (Si221). We will continue the discussion on this topic in later sections.

## 0.4 Outline

This thesis focuses on probing the electronic characteristics of molecular silicon. We accomplish this by experimentally creating single-molecule junctions with silicon-based molecular components and measuring their single molecule conductance. This thesis is comprised of four chapters as follows:

**Chapter 1** presents work assessing the stability of molecular junctions under an applied electric field, in particular, the ones with molecular backbones consisting of chemical bonds that are commonly found in the low- $\kappa$  dielectrics. We show that C-C and Si-C bonds are much more durable under a voltage above 1V than Si-Si or Ge-Ge bonds. We further design a two-path molecular backbone where we observe considerable current in the broken species, demonstrating that the Si-Si bond ruptures under an applied bias and the junction conducts current through the other path.

**Chapter 2** details studies on the single-molecule conductance of linear silanes and germanes. Silane and germane wires demonstrate a slower conductance decay with increasing molecular length compared with alkanes; this  $\sigma$  electron interaction in Si-Si and Ge-Ge bonds is comparable to the electronic conjugation in the  $\pi$ -bonds such as oligo-

p-phenylenes. Combining the strong electronic coupling in the silicon and germanium backbone and the stereoelectronic nature of the sulfur-methylene  $\sigma$ -bonds that terminate the molecule, we realize a single-molecule conductance switch. We then explore the single-molecule conductance of silanes with Ag and Pt electrodes and find that the Ag electrodes enable a higher molecular junction conductance compared to Au and Pt electrodes.

**Chapter 3** continues to investigate the electronic property of cyclic silanes. We use the cyclopentasilane as an example system to investigate how the ring conformation affects the molecular conductance. We find the two isomers of the cyclopentasilane show distinct conductance; the distribution of the conductance measured from thousands of junctions for each isomer result from multiple conformers. We then compare the single-molecule conductance of four different cyclic structures and find that most of the cyclic silanes are worse conductors compared with their linear counterparts.

**Chapter 4** describes two examples of high-conducting molecular junctions created by incorporating strains in the silicon backbone. In the first example, a ring strain constitutes a silacycle-to-Au binding geometry; in the second example, the strained disilane enables a Si-to-Au contact. In both cases, the novel binding mode reaches a shortened junction length and a high-conducting pathway.

*Probing Si—Si Bond Rupture in Single Molecule Junctions*

## 1.1 Electric Field Breakdown in Single Molecule Junctions

### Preface

This section is based on the manuscript entitled *Electric Field Breakdown in Single Molecule Junctions* by Haixing Li, Timothy A. Su, Vivian Zhang, Michael L. Steigerwald, Colin Nuckolls, and Latha Venkataraman published in JACS.<sup>13</sup> Timothy Su and Vivian Zhang of Prof. Nuckolls' group synthesized and characterized all the compounds. I performed the conductance measurements and data analysis.

### Abstract

Here we study the stability and rupture of molecular junctions under high voltage bias at the single-molecule/single-bond level using the scanning tunneling microscope-based break-junction technique. We synthesize carbon, silicon and germanium-based molecular wires terminated by aurophilic linker groups and study how the molecular backbone and linker group affect the probability of voltage-induced junction rupture. First,

we find that junctions formed with covalent S—Au bonds are robust under high voltage and their rupture does not demonstrate bias dependence within our bias range. In contrast, junctions formed through donor-acceptor bonds rupture more frequently and their rupture probability demonstrates a strong bias dependence. Moreover, we find that the junction rupture probability increases significantly above  $\sim 1$  V in junctions formed from methylthiol-terminated disilanes and digermanes, indicating a voltage-induced rupture of individual Si—Si and Ge—Ge bonds. Finally, we compare the rupture probabilities of the thiol-terminated silane derivatives containing Si—Si, Si—C and Si—O bonds and find that Si—C backbones have higher probabilities to sustain the highest voltage. These results establish a new method for studying electric field breakdown phenomena at the single molecule level.

## Introduction

A challenge in the semiconductor industry is to lower the dielectric constant ( $\kappa$ ) of the dielectric material without diminishing its ability to withstand breakdown in strong electric fields. Low- $\kappa$  materials have a lower dielectric constant than traditional SiO<sub>2</sub> dielectric materials and therefore improve device speed as well as power efficiency. However, low- $\kappa$  materials are less robust than traditional dielectric materials and degrade through a mechanism referred to as time dependent dielectric breakdown.<sup>55,56</sup> While many theoretical models<sup>57-59</sup> have been developed to rationalize electric field breakdown in silicon-based networks<sup>60,61</sup> of three-dimensional low- $\kappa$  materials, an experimental study of voltage-induced breakdown at the single bond level is lacking.<sup>62-64</sup>

Here we investigate the voltage-induced breakdown characteristics of single bonds

commonly found in semiconductor materials. We study the behavior of these bonds in the context of a single molecule junction with the scanning tunneling microscope-based break junction technique (STM-BJ). We alter the structure of the molecular backbone to include either Si—Si, Ge—Ge, C—C, Si—C or Si—O bonds and study the effect of a high electric field on each of these individual bonds. This enables us to determine how each atomic component contributes to the probability of field-induced bond rupture. We show that: (1) junction rupture probability increases with applied voltage for Au-linker donor-acceptor bonds but remains constant with increasing voltage for covalent Au—S bonds, (2) molecular junctions containing a single Si—Si or Ge—Ge bond have an abrupt increase in rupture probability above 1 V, indicating Si—Si/Ge—Ge bond rupture, (3) molecular junctions with Si—Si and Si—O bonds demonstrate a higher rupture probability relative to those with only Si—C bond at voltages exceeding 1 V and (4) the rupture probability for junctions formed with covalent Au—S bonds is positively correlated with the molecular junction conductance; such a correlation is not seen for donor-acceptor bonded junctions. Our results from this study of electric field breakdown at the single molecule level provide guidance for designing low- $\kappa$  dielectric materials as well as molecular devices that require stability under high voltage bias.

## Results and Discussion

We use the scanning tunneling microscope-based break-junction (STM-BJ) technique<sup>8,9</sup> to determine the stability and rupture probability of single molecule junctions under an applied voltage (Figure 1.1a). Unlike the standard STM-BJ measurements where Au point-contacts are pulled apart in a solution of molecules while measuring conductance, here we

develop a new technique to evaluate the breakdown voltage of single-molecule junctions that contain different chemical bonds. We modify the ramp applied to the STM piezoelectric transducer to hold the junction in place for 150 ms during each measurement and apply a voltage pulse ranging in amplitude from 0.2 V to 1.4 V (gray-colored areas in Figure 1.1b) during this “hold” section.<sup>65</sup> In Figure 1.1b we show example traces measured for 1,6-hexanedithiol junction that either sustains the voltage pulse for the entire hold period (green) or breaks during the hold (red).

We analyze all data using an automated algorithm to statistically determine the percentage of junctions that break during their measurement. We determine the conductance of the trace prior to the voltage pulse to ensure that we are selecting a trace where a molecule is bridging the electrodes. We then use the conductance after the pulse to sort the junctions into two types: those that persist and those that break under the bias. We create two-dimensional overlays of all traces that either sustain or break and align them to the start of the “hold”. Figure 1.1c and d show such 2D histograms from data obtained while applying a 1.4V bias to Au-1,6-hexanedithiol-Au junctions. In Figure 1.1c, the histogram of traces that do not break shows that the conductance remains roughly constant throughout the hold section, indicating that we are indeed maintaining a molecular junction. We also see the slight increase in conductance when we apply the 1.4 V voltage pulse, which is seen in most of the molecules we tested here.<sup>13</sup> This shows that the bias window used here goes beyond the linear current-voltage regime for most molecules.<sup>66</sup> The histogram in Figure 1.1d demonstrates that junctions tend to break shortly after the high bias is applied. As we will show later in the manuscript, the break time distribution follows an exponential decay. We note that molecular backbones that are terminated by

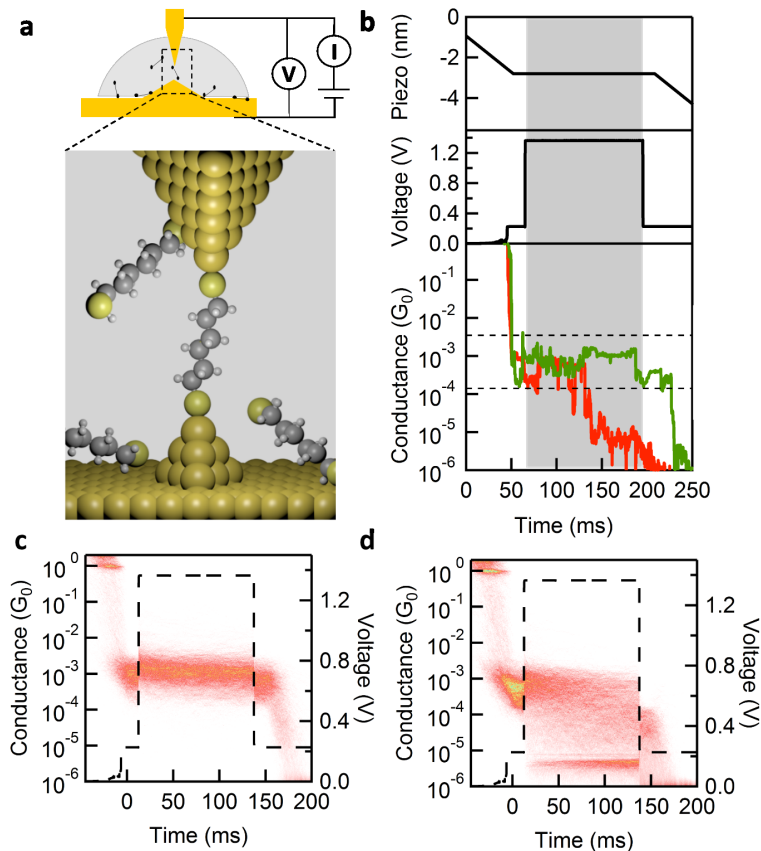


Figure 1.1: (a) Schematic of experimental setup and cartoon of a single molecule junction formed with 1,6-hexanedithiol. (b) Upper panel: piezo displacement versus time. Middle panel: applied voltage versus time. Lower panel: two sample traces measured with the molecule 1,6-hexanedithiol. The green (red) curve represents a molecular junction that sustains (ruptures) under the bias. Note the bias across the junction is very low before  $1G_0$  rupture due to a  $100\text{ k}\Omega$  resistor placed in series with the junction. Two-dimensional histograms made from traces with 1,6-hexanedithiol that sustain (c) and rupture (d) while applying a bias voltage as shown by the dashed line. The flat feature below  $10^{-5} G_0$  in (d) is from measurements of broken junctions at  $1.4\text{ V}$ .

thiols at each end (“dithiol junctions”) have a broader distribution of conductance values compared to molecular backbones terminated with the dative linkers in this study.<sup>9</sup> However, for the measurements discussed here, we do not distinguish different types of dithiol-junctions based on conductance values. We simply analyze all junction and contact conformations together.

We first apply our measurement technique to investigate the impact of different elec-

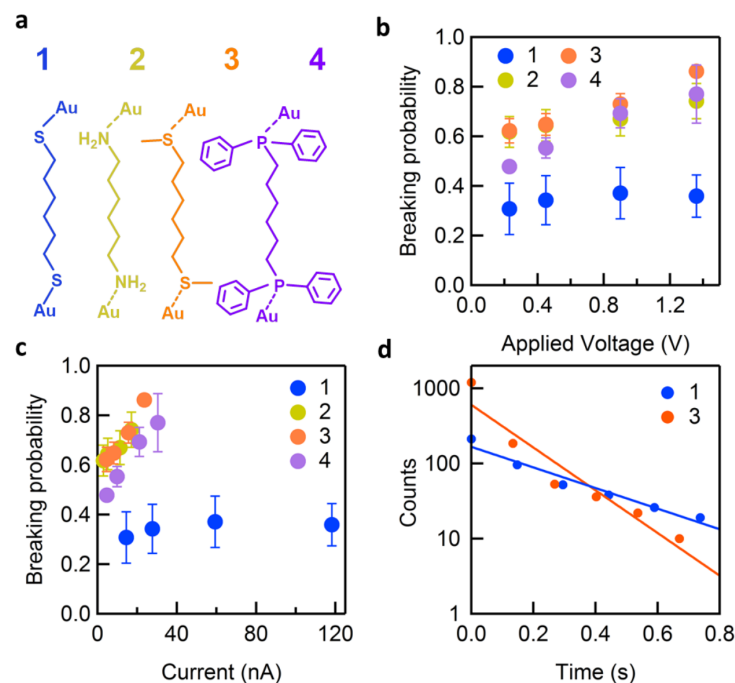


Figure 1.2: (a) Structures of molecules **1-4**. Junction breaking probability plotted against (b) applied bias voltage and (c) current through the junction for **1-4**. The error bars show the standard deviation determined from variations in sets of thousand measurements. (d) Histograms of junction rupture time made from 500 measurements of **1** (blue dots) and 1500 measurements of **3** (orange dots). The linear fits on a semilog scale (blue and orange lines) indicate an exponential decay with decay time  $\tau = 0.32$  s for **1** and  $\tau = 0.15$  s for **3**.

trode linker groups on the stability of the molecular junction under applied electric field. For this study, we measure a series of  $\alpha,\omega$ -difunctionalized hexane backbones with thiol, amine,<sup>9</sup> methylsulfide<sup>67</sup> and diphenylphosphine<sup>68</sup> terminations. Specifically, we compare rupture probabilities in junctions formed with 1,6-hexanedithiol (**1**), 1,6-hexanediamine (**2**), 2,9-dithiadecane (**3**), and 1,6-bis(diphenylphosphino)-hexane (**4**) as illustrated in Figure 1.2a. We employ the method outlined above to determine the rupture probability for each molecule at different bias voltages. In Figure 1.2b, we plot the junction rupture probability as a function of applied voltage. Junctions formed with **1** have the lowest rupture probability and the probability of rupture is independent of the magnitude the applied

voltage (up to  $V=1.4V$ ). The rupture probability is much higher for **2-4** compared to **1**; the rupture probability for **2-4** also increases with increasing bias voltage. Figure 1.2c shows the rupture probability as a function of the current flowing through the junction and depicts a similar trend: **2-4** show a linear increase in rupture probability as the current through the junction increases while the rupture probability of **1** remains constant as current increases. We attribute this difference to the nature of bonding between the molecule and gold electrode. Molecules **2-4** form donor-acceptor bonds<sup>67,68</sup> between the N (2), S (3), and P (4) lone pairs and the undercoordinated gold atoms on the electrode surface. These bonds are inherently weak with a binding energy ranging from 0.5 eV - 1.2 eV.<sup>67,68</sup> In contrast, **1** forms a covalent Au—S<sup>69</sup> bond with a binding energy around 2 eV<sup>70</sup> that enables thiols to form robust junctions that withstand a high applied voltage.

Our measurements show that the covalently linked systems have a voltage-independent rupture probability across the whole bias range that we apply while the donor-acceptor linked systems have a voltage-independent rupture probability below  $\sim 0.2$  V (Figure 1.3) and a strong voltage dependence above  $\sim 0.2$  V.

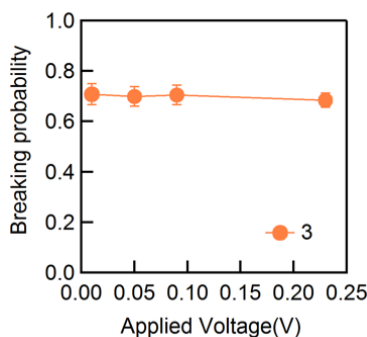


Figure 1.3: Junction breaking probability at low bias for molecule **3**.

We can explain the results of both systems as follows. The voltage independent rup-

ture that is seen most clearly for **1** at all voltages and for **2-4** at low voltages is attributed to thermally activated processes due to room temperature measurement or mechanically induced rupture due to vibrations inherent to our STM setup. Indeed, if we add a white noise modulation with a 1 Å amplitude to the piezo (Figure 1.4a), we see an increase in junction rupture probability irrespective of the voltage applied (Figure 1.4b).

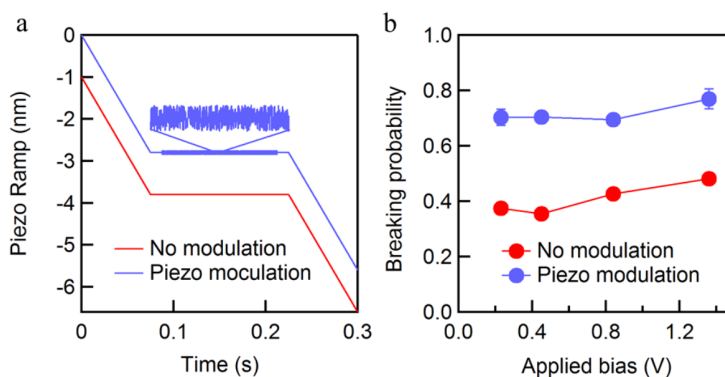


Figure 1.4: Control experiment with piezo modulation. (a) Two piezo ramps with (blue) and without (red) an additional mechanical modulation. The modulation is added by applying white noise within 1 Å to the piezo. (b) Junction breaking probability plotted against the applied bias voltage with (blue) and without (red) piezo modulation for molecule Si4.

In contrast, the junction rupture that occurs in donor-acceptor linked junctions with increasing voltage arises from a voltage-activated process. We hypothesize that this voltage-induced rupture results from electrons exciting vibrational modes of the linker-gold bonds. Previous inelastic electron tunneling spectroscopy (IETS) studies have shown that the voltage required to excite a Au—S stretching mode in a mechanically controlled break-junction (MCBJ) measurement of 1,8-octanedithiol between Au electrodes is 35 mV while that to excite the Au—N stretching mode for the donor-acceptor linked junction with 1,8-octanediamine is 29 mV.<sup>71</sup> When the applied voltage exceeds the IETS threshold, the incoming electrons are able to excite the vibrational mode, which can in turn lead to

bond rupture, though the probability for rupture will also depend on the bond energy. The higher the applied voltage, the higher the current through the junction and hence a higher probability of exciting a vibrational mode. The fact that a voltage-dependent rupture is not seen in **1** is likely due to its higher binding energy, and rupture of the Au—S bond would require multiple excitations to occur, requiring a higher current, and thus a higher voltage range than we apply in these experiments.

Additionally, the presence of an electric field can polarize and weaken a bond. Calculations show that the voltage drop across a Au—S<sup>72</sup> covalent bond is much smaller than that across a Au—SMe donor-acceptor bond,<sup>73</sup> suggesting that the donor-acceptor interactions experience strong voltage-induced bond weakening. Additionally, we note that the voltage drop across the Au electrode and the Au—Au bonds within the junction is considerably smaller than that across the Au-linker bond or the molecular backbone.<sup>72</sup> Taken together, we can conclude that the voltage applied across the molecular junction can polarize and weaken the Au-linker bond; if it is larger than the threshold voltage for exciting bond vibrational modes, it can control bond rupture by determining the junction current.

Next, we compare the length of time that each junction can sustain an applied voltage 1.4 V before it ruptures. For these measurements, we modify the ramp applied to the piezoelectric transducer to hold the junction at a fixed displacement for 1.5 s. We only consider traces with a molecular junction at the start of the hold and determine the time that the junction ruptures within the hold section. We generate a histogram of the break times, as shown in Figure 1.2d for **1** and **3**. We fit each distribution with an exponential function  $P = P_0 e^{-t/\tau}$  (lines in Figure 1.2d) and find that molecule **1** has decay

time constant  $\tau = 0.32$  s, twice that of molecule **3** ( $\tau = 0.15$  s). This result confirms that single molecule junctions formed with Au—S covalent bonds are less likely to rupture under an applied voltage and can sustain the bias for longer time when compared with the molecular junctions formed with donor-acceptor bonds.

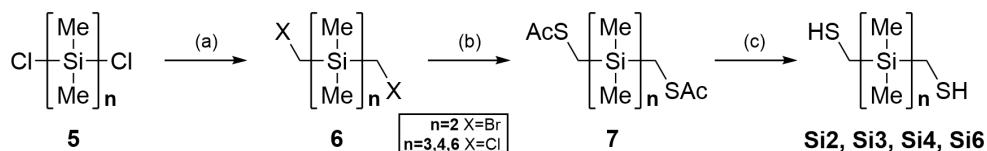


Figure 1.5: General approach for installing methylthiol linkers on the silanes and germanes. (a) For  $n = 2$ : LiBr,  $\text{CH}_2\text{Br}_2$ ,  $n\text{-BuLi}$ , THF,  $-78^\circ\text{C}$ . For  $n = 3,4,6$ :  $\text{CH}_2\text{BrCl}$ ,  $n\text{-BuLi}$ , THF,  $-78^\circ\text{C}$ . 69% to 93% yield. (b) KSac, THF, reflux. 37% to 75% yield. (c)  $\text{LiAlH}_4$ ,  $\text{Et}_2\text{O}$ ,  $0^\circ\text{C}$ . 51% to 84% yield.

Our study of the rupture behavior of different linker groups under applied voltage suggests that methylthiol ( $-\text{CH}_2\text{SH}$ ) linkers provide a promising test bed to study how different molecular analogs of low- $\kappa$  dielectric materials influence junction breakdown under an applied voltage. We synthesized all silanes and germanes following the method showing in Figure 1.5.

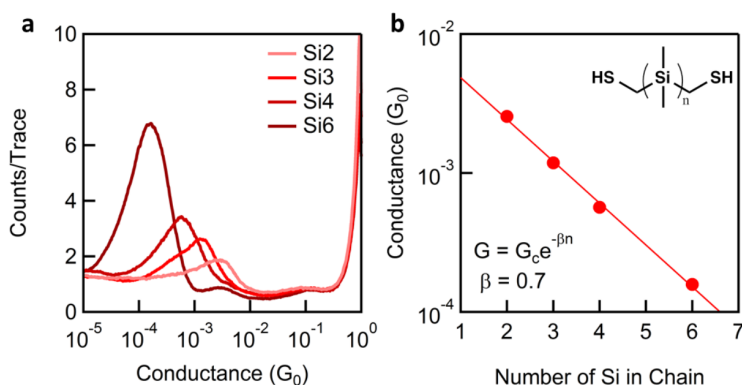


Figure 1.6: (a) Logarithm-binned 1D conductance histograms of molecules **Si2-4** and **Si6** (100 bins/decade). (b) Conductance peak values are plotted against the number of silicon atoms in the backbone of molecules **Si2-4** and **Si6**. The decay constant ( $\beta$ ) for the permethyloligosilanes with  $\text{CH}_2\text{SH}$  linkers is  $0.70 \pm 0.02$  per Si atom.

We measured the conductance of the oligosilanes using our standard STM-BJ method. Figure 1.6a shows the normalized log-binned conductance histograms constructed from approximately 30,000 measured traces for each molecule without any data selection. We obtained an average conductance for these junctions by fitting the conductance peak with a Gaussian function. In Figure 1.6b, we plot the conductance peak value as a function of the number of silicon atoms in the backbone on a semi-log scale. We find that the conductance decays exponentially with  $n$ , the number of Si atoms in the chain, as  $G \sim e^{-\beta n}$ . The tunneling decay constant  $\beta$  is  $0.70 \pm 0.02$  per Si atom, determined by fitting a line using the least-squares method. Here we will use this CH<sub>2</sub>-SH terminated series for the bias-dependent rupture measurements.

We carry out junction rupture measurements at voltages ranging from 0.2 V to 1.4 V for the oligosilanes and compare these results with alkanes, germanes, and other silane derivatives. We use the same general technique outlined in Figure 1.5 to synthesize **Ge2**, **SiOSi**, and **SiCSi** (Figure 1.7). In Figure 1.7, we plot the fraction of junctions that rupture as a function of the applied bias voltage. **Si2** and **Ge2** show a roughly constant rupture probability below 1 V and a roughly linear increase in rupture probability with voltage above 1V. This constant rupture probability below 1 V is attributed to the thermally or mechanically activated rupture mechanisms described above. The increase in rupture probability observed for the **Si2** and **Ge2** above 1V is distinct from the constant rupture probability we observe for the **C6** (Figure 1.2b) and **C8** (Figure 1.7) alkane analogs: this suggests that a bond other than the Au—S or Au—Au<sup>74,75</sup> bond is breaking. Our experimental data suggests that we are breaking the Si—Si and Ge—Ge bonds in these systems. This interpretation is supported by the well-established trends in bond strength

and atomic polarizability in Group 14 elements as they descend the periodic table. The bond strengths for C—C, Si—Si and Ge—Ge bonds are 3.7 eV, 2.3 eV, and 1.9 eV respectively, which implies that C—C bonds are significantly harder to break.<sup>76</sup> Polarizability describes the ease with which an electron cloud can be distorted in response to an external electric field. This suggests that large, “soft” bonds can be influenced to break more easily under a high voltage bias than small, “hard” bonds.

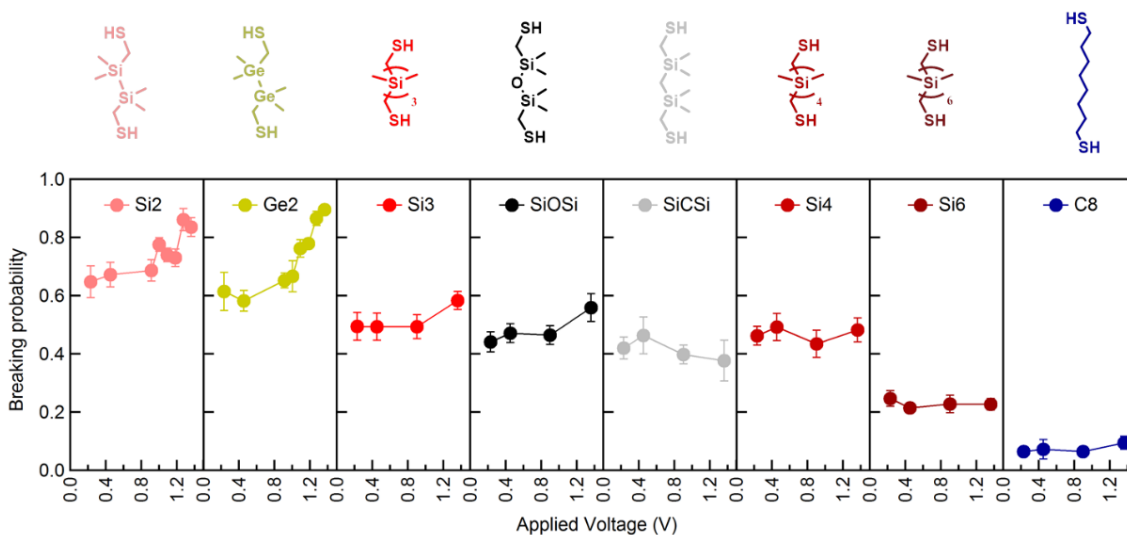


Figure 1.7: Junction rupture probability plotted against the applied voltage for CH<sub>2</sub>SH terminated molecules. The molecular structures are shown above their respective measurement data. Error bars show the standard deviation determined from variations in sets of thousand measurements.

The polarizability calculated for C atoms is 1.67 a.u. while Si and Ge atomic polarizabilities are 5.53 a.u. and 5.84 a.u. respectively.<sup>77</sup> These trends are consistent with our measurement results that indicate that junctions formed with the germanes and silanes are more likely to rupture under a high bias than those formed with the alkanes. Figure 1.7 also depicts a comparison of rupture probabilities in -SiMe<sub>2</sub>-X-SiMe<sub>2</sub>- molecular backbones where X = SiMe<sub>2</sub>, CH<sub>2</sub>, or O. We find that junctions formed with **Si3** and **SiOSi**

show a slight increased rupture probability above 1 V, but **SiCSi** does not. This suggests that the Si—C—Si bond array has a higher capacity for sustaining large applied voltages compared to Si—O—Si and Si—Si—Si arrays. The latter two differ from the former in two distinct ways: the Si—O bonds are more polar than the Si—C bonds, and the Si—Si bonds are more polarizable than the Si—C bonds. These features could explain our results, although detailed calculations would be required to understand the impact of an applied bias on these systems. The more polar Si(+)—O(-)—Si(+) molecule should couple more strongly to the applied field, perhaps even leading to the heterolytic cleavage of one of the Si—O bonds. In a similar way, although the Si—Si—Si structure itself is nonpolar, in the presence of the applied field the Si—Si bonds, being more polarizable, should also couple more strongly to the applied field.

Results shown in Figure 1.7 indicate that we do not see voltage-dependent rupture in the longer silanes (**Si4** and **Si6**). This can be explained by considering the mechanism for voltage-induced bond rupture detailed above. In these longer silanes, the field across each bond is smaller, and thus the bonds are less polarized. Additionally, the current through these junctions is smaller and results in a reduced probability for exciting vibrational modes. Since there are more vibrational modes that can be excited in these longer systems, the probability of a single bond rupturing is lower.

We now look at the junction rupture probability as a function of molecular junction conductance. We use the 2D conductance-time histograms and integrate all counts while the voltage pulse is applied to determine the average conductance value at the applied voltage (details shown in Figure 1.8). In Figure 1.9a, we plot the rupture probabilities against these conductance values for all molecules shown in the Figure 1.7 and for mea-

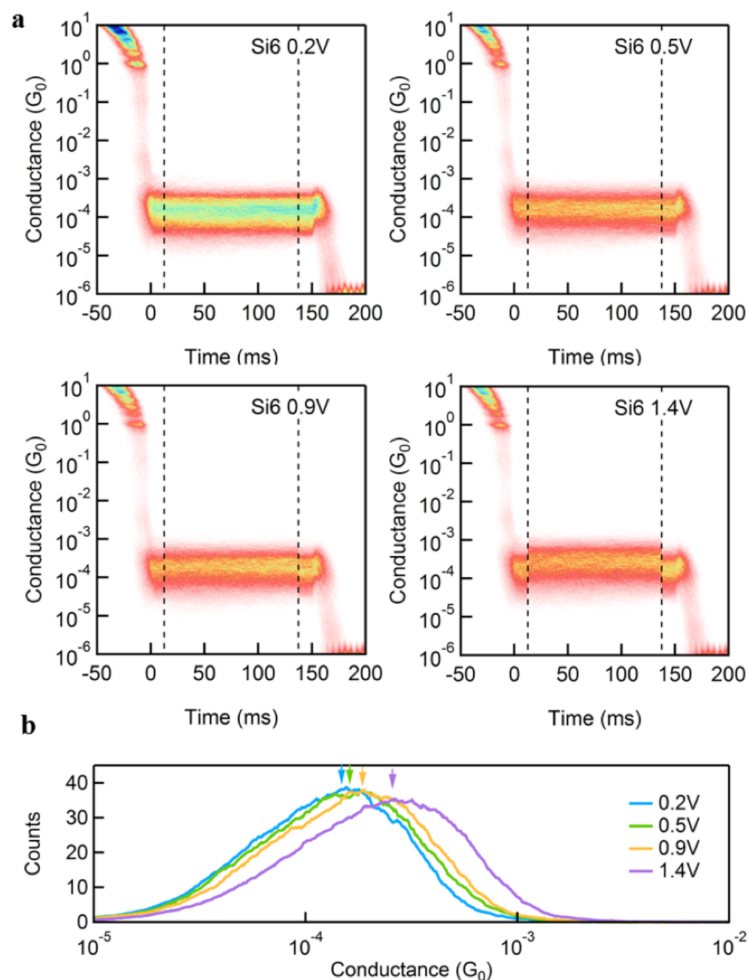


Figure 1.8: Determination of the conductance of molecule Si6 with CH<sub>2</sub>—SH linkers at different voltages. (a) Two-dimensional conductance histograms of sustaining traces under an applied voltage of 0.2V, 0.5V, 0.9V and 1.4V. (b) Respective conductance profiles generated from the 125 ms windows delineated by the black dashed lines in (a) where a voltage pulse is applied. Arrows indicate the conductance peak values at different applied bias voltages.

measurements of molecule **1** on a semi-logarithm scale.

For each molecule, the junction conductance depends slightly on the applied bias voltage. However, the most striking result is that the rupture probability increases linearly with the logarithm of the conductance. In contrast, we do not see a dependence of the breaking probability on the heat produced (calculated as (current) x (voltage)) for each

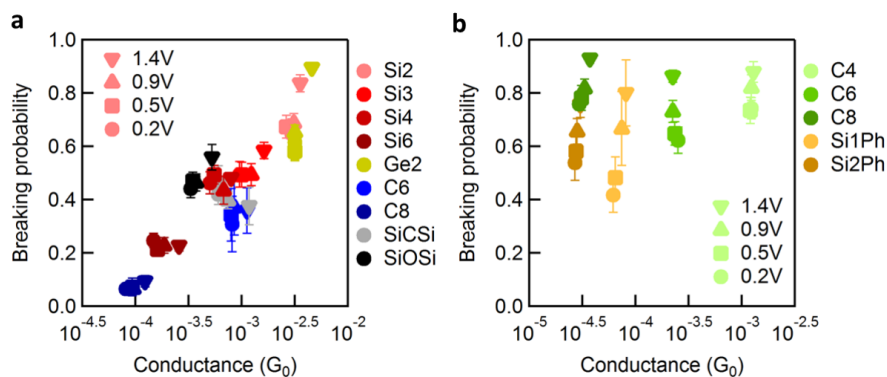


Figure 1.9: Junction rupture probability plotted against the conductance for (a) all thiol-terminated molecules from Figure 1.7 and C6 (Molecule 1 in Figure 1.2) and (b) for SME terminated molecules on a semi-logarithm scale. The shape of the marker indicates the applied voltage: circle is 0.2V, square is 0.5V, up triangle is 0.9V and down triangle is 1.4V. Error bars show the standard deviation determined from variations in sets of thousand measurements.

junction (as shown in Figure 1.10), which indicates that a local heating mechanism cannot explain the breaking process measured here.

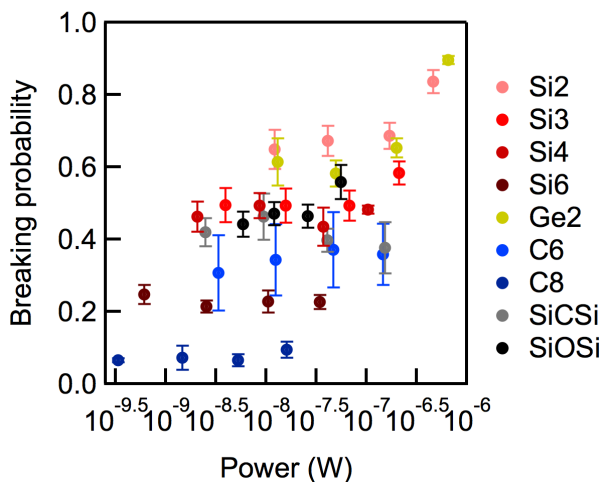


Figure 1.10: Junction rupture probability plotted against the heat produced (calculated as (current) $\times$  (voltage)) for each junction on a semi-logarithm scale. Error bars show the standard deviation determined from variations in sets of thousand measurements.

Finally, to compare this with results from junctions formed through donor-acceptor links, we show in Figure 1.9b analogous results from measurements of methylsulfide-

terminated alkanes and silanes (structures shown in Figure 1.11). We see a clear increase in the rupture probability as increasing the voltage. However, we find that there is no correlation between the rupture probability and molecular junction conductance for these methylsulfide-terminated junctions. These results provide a new perspective with which to distinguish donor-acceptor linked and covalent linked molecular junctions.

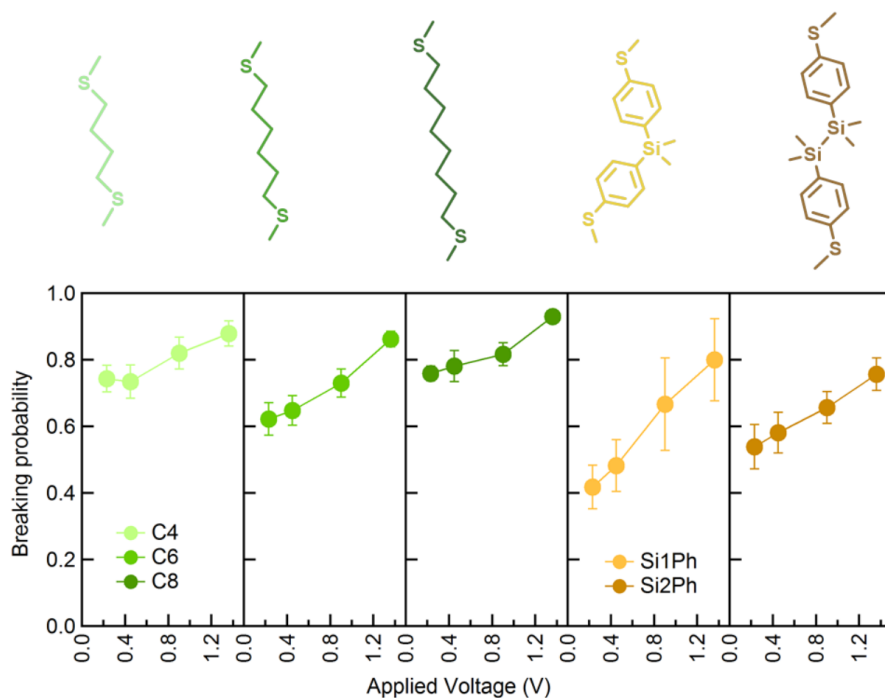


Figure 1.11: Junction breaking probability plotted against the applied voltage for molecules **C4**, **C6**, **C8**, **Si1Ph**, **Si2Ph** terminated with methylsulfide (SMe) linker group; structures are shown above. Error bars show the standard deviation determined from variations in sets of thousand measurements.

## Conclusion

In this work, we have used a modified scanning tunneling microscope-based break-junction technique to probe the rupture probability of single molecule junctions under applied voltage. We find that the junctions formed through donor-acceptor linkers have

a lower threshold voltage for rupture than those formed with covalent linkers. Moreover, our results provide evidence that Si—Si and Ge—Ge bonds rupture above 1 V. Finally, we show that the Si—C bond is more robust under applied voltage than either the Si—Si or the Si—O bond. This study demonstrates that we can detect voltage-induced bond rupture in single molecule junctions. This provides a new approach to investigate the problem of time dependent dielectric breakdown in low- $\kappa$  materials and also sheds light on the reliability of molecular electronic devices under applied voltage.

## Methods

**Synthetic Details** Molecules 1,6-hexanedithiol (1), 1,6-hexanediamine (2), 2,9-dithiadecane (3), and 1,6-bis(diphenylphosphino)-hexane (4) as illustrated in Figure 1.2 are obtained from Fluka (97%), Sigma-Aldrich (98%), Alfa Aesar (97%), and Sigma-Aldrich (97%) respectively and used without further purification. We synthesized all silanes and germanes with methylthiol linkers by the same general method. We previously reported the synthesis of  $\alpha,\omega$ -dichlorooligosilanes.<sup>78</sup> Here, we react the  $\alpha,\omega$ -dichlorooligosilane 5 with a halomethyl lithium species to furnish the  $\alpha,\omega$ -bis(halomethyl)oligosilane 6 (Figure 1.5).<sup>79,80</sup> We obtain the  $\alpha,\omega$ -bis(acetylthiomethyl)oligosilane 7 by nucleophilic substitution of the primary halide with potassium thioacetate; we convert the resulting compounds to the final  $\alpha,\omega$ -bis(methylthiol)oligosilane  $\text{Si}_n$  ( $n=2, 3, 4, 6$ ) via lithium aluminum hydride reduction.<sup>81,82</sup> See Li et al.<sup>13</sup> for characterization and methods for synthesis of the molecules used here.

**Experimental Details** STM-BJ experiments are carried out in a custom instrument designed to have a high mechanical stability under ambient conditions. The STM tip is

a gold wire (0.25 mm diameter, Alfa Aesar, 99.999% purity) and the substrate is a thermally evaporated gold-on-mica substrate. Measurements are carried out at room temperature under ambient conditions in a 1 mM solution of the target molecule in 1,2,4-trichlorobenzene (Alfa Aesar, 99%). For the standard STM-BJ experiment, we start by making a gold-gold contact with a conductance greater than  $5G_0$  ( $G_0=2e^2/h$ , quantum of conductance) and then withdraw the tip at a rate of 37 nm/s to break the junctions. We collect 30,000 traces and create logarithmically binned 1D histograms of these traces to determine the molecular junction conductance. For the rupture probability measurements, we modify this by first pulling a distance of 2.8 nm, holding the tip at a constant distance from the substrate for 150 ms (or 1.5 s), then pulling an additional 2.8 nm to break the junction. During the “hold”, we apply a bias of 0.2 V, 0.5 V, 0.9 V or 1.4 V for 125 ms to the junction. For molecules **Si2** and **Ge2**, we additionally collected data at 1 V, 1.1 V, 1.2 V and 1.3 V. For each bias voltage, we collect 5000 traces.

**Data Analysis Details** We first fit a Gaussian to the 1D conductance histogram peaks to obtain a conductance range for each molecule based on the peak position and width. We analyze the conductance during first and last 12.5 ms of the hold measurements to determine if the trace has a molecule bridging the gap between the electrodes. We require the average conductance of the 12.5 ms period before the voltage peak to be within the full-width of the conductance histogram peak. Among these selected traces, we determine the fraction that rupture under the bias by determining the conductance at the 12.5 ms period after the voltage peak. If this is within the full-width of the conductance histogram peak, then the junction did not rupture.

In order to know the break time for junctions that break within the hold, we apply an

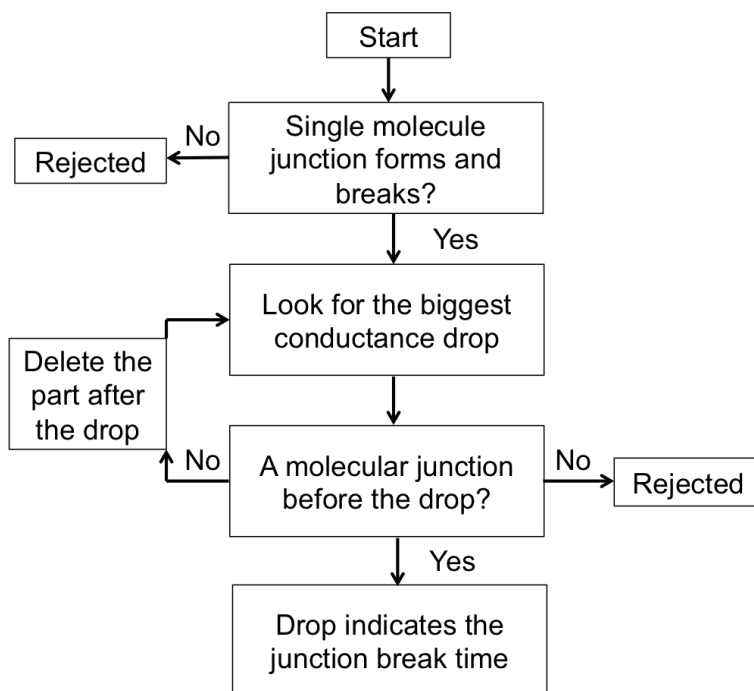


Figure 1.12: Time dependence analysis algorithm flow chart. An automated algorithm looks for the first large conductance drop during the hold using a previously detailed method.<sup>83</sup>

automated algorithm as illustrated in Figure 1.12 that looks for the first large conductance drop during the hold. We require the average conductance before this drop to be within the full-width of the conductance histogram peak to ensure a molecular junction. The time at which this drop is observed is the junction breaking time. We compile these times determined from 500-1000 junctions to generate a histogram and perform a statistical study.

## 1.2 Mechanism for Si-Si Bond Rupture

### Preface

This section is based on the manuscript entitled *Mechanism for Si—Si Bond Rupture in Single Molecule Junctions* by Haixing Li, Nathaniel Kim, Timothy Su, Michael Steigerwald, Colin Nuckolls, Pierre Darancet, James Leighton, and Latha Venkataraman published in JACS.<sup>15</sup> Nathaniel Kim of Prof. Leighton's group and Timothy Su of Prof. Nuckolls' group synthesized and characterized all the compounds. Dr. Pierre Darancet carried out theoretical calculations. I performed the bond rupture measurements and data analysis.

### Abstract

The stability of chemical bonds can be studied experimentally by rupturing single molecule junctions under applied voltage. Here we compare voltage-induced bond rupture in two Si—Si backbones: one has no alternate conductive pathway while the other contains an additional naphthyl pathway in parallel to the Si—Si bond. We show that in contrast to the first system, the second can conduct through the naphthyl group when the Si—Si bond is ruptured using an applied voltage. We investigate this voltage induced Si—Si bond rupture by *ab initio* density functional theory calculations and molecular dynamics simulations that ultimately demonstrate that the excitation of molecular vibrational modes by tunneling electrons leads to homolytic Si—Si bond rupture.

## Introduction

Silicon is a vital component of modern information technology where it serves as the active material in transistors, integrated circuits, and fiber optics. With an increasing demand for miniaturized electronics, new forms of silicon devices are being investigated including two-dimensional silicene transistors,<sup>25</sup> silicon nanowire transistor<sup>84</sup> and photovoltaic devices,<sup>22,85,86</sup> nanoscale silicon photonic devices,<sup>87,88</sup> and silicon-based single molecule devices.<sup>12,89</sup> A thorough understanding of the mechanical and electrical characteristics of Si—Si bonds is thus of essential importance as silicon based materials are fast approaching the molecular scale. Here, we focus on the failure mechanism of silicon and investigate voltage-induced rupture of the Si—Si bond in the context of single molecule junctions.

Though individual Si—Si bond strength is only 2.3 eV (for example, C—C bond strength is 3.7 eV with the same valence configuration),<sup>76</sup> networks of Si—Si bonds are ubiquitous in electronic devices. It is therefore crucial to investigate the stability of Si—Si bonds under an applied electric field. Previously, we had measured the electric field breakdown properties of Si—Si bonds – however, we could not rule out bond breakage at other locations along the backbone. In this study, we conclusively demonstrate that bond breakage can occur at the Si—Si bond by devising a double-backbone system. We find that in the double-backbone molecule, conductance occurs through the alternate pathway after the Si—Si bond is broken. We also support our experimental results with computations that suggest strongly that the Si—Si bond ruptures under an applied bias. We synthesize and study two molecules (**Si2** and **Si2Naph**). **Si2** has a single backbone

comprising a Si—Si bond; **Si2Naph** has a double backbone that features a mechanically robust carbon linkage in parallel with the Si—Si bond. We apply a large voltage across the molecular junctions formed with these two molecules and compare their rupture behaviors. We observe different conductance values of the junctions formed with these two molecular backbones when the junctions break, signifying Si—Si bond ruptures in both cases. We attribute this voltage-dependent bond rupture to a current-induced mechanism involving heating of the molecule through electron-vibrational mode coupling. We calculate the molecular vibrational modes using density functional theory and find that a number of modes involving Si—Si bond stretching can be excited since they are within the applied voltage for both junctions studied. We further carry out molecular dynamics simulations to show that the Si—Si bond is more likely to break upon current-induced heating than the Si—C or Au—S bond which are also present in the junctions.

## Synthesis

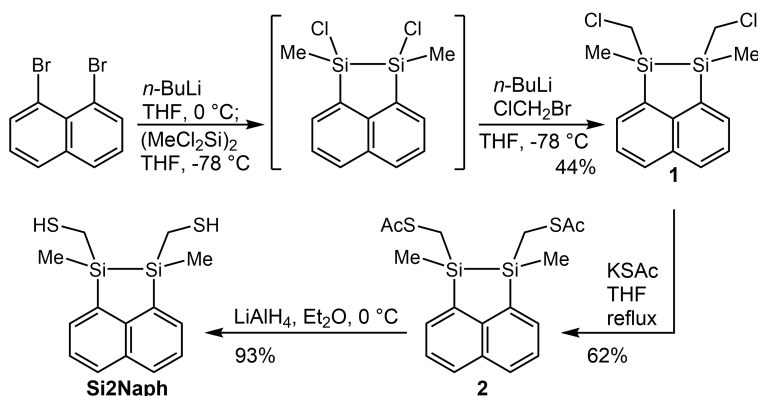


Figure 1.13: Synthesis of **Si2Naph**.

We prepare **Si2** using previously published methods<sup>13</sup> and naphthyldisilane **Si2Naph** by the sequence shown in Figure 1.13.<sup>13,16,90–92</sup> The synthesis begins with bismetallation

of 1,8-dibromonaphthalene by lithium halogen exchange and treatment of the resulting dianion with 1,1,2,2-tetrachloro-1,2-dimethyldisilane followed by *in situ* treatment with the anion formed from bromochloromethane and n-BuLi to give **1** in 44% overall yield (Figure 1.13). Displacement of the chlorides with KSAc delivered **2** in 62% yield, and reductive cleavage of the acetates provides **Si2Naph** in 93% yield. Compounds **1**, **2**, and **Si2Naph** were all isolated and employed as 1.2:1 mixtures of diastereomers. The trans and cis isomers of both **2** and **Si2Naph** were also separated and characterized (see the SI of Li et al.<sup>15</sup> for details).

## Conductance Measurement

We first measure the conductance of **Si2Naph** and **Si2** (structures are shown in Figure 1.14a) with the scanning tunneling microscope (STM) based break junction technique (schematic in Figure 1.14b).<sup>8,9</sup> In this technique, we repeatedly bring the Au STM tip into and out of contact with the substrate and record the conductance (current/voltage) of the junction as we withdraw the tip. We see plateaus at integer multiples of the conductance quantum ( $G_0 = 2e^2/h$ ) corresponding to atomic Au contact in each conductance-displacement trace. We then see additional features below  $1 G_0$  once we add a solution of the target molecule in 1,2,4-trichlorobenzene. These features below  $1 G_0$  signify that an Au-molecule-Au junction is formed after the Au contact breaks. Here we use thiols as the terminal groups to attach the silicon backbone to the Au electrodes by forming Au—S covalent bonds.<sup>13</sup> We collect thousands of traces and compile them into logarithmically binned one-dimensional histograms shown in Figure 1.14c.

We see that **Si2Naph** shows a conductance peak at  $2.4 \times 10^{-4} G_0$ , about one-tenth

of the conductance for **Si2**. We note here that the cis and trans isomers of **Si2Naph** show similar results in conductance measurements,<sup>15</sup> unlike the analogous molecules terminated with thioanisole linkers,<sup>16</sup> the cis isomer of which, uniquely, forms a high-conducting junction with one of the Au electrodes coupling directly to the Si—Si bond.

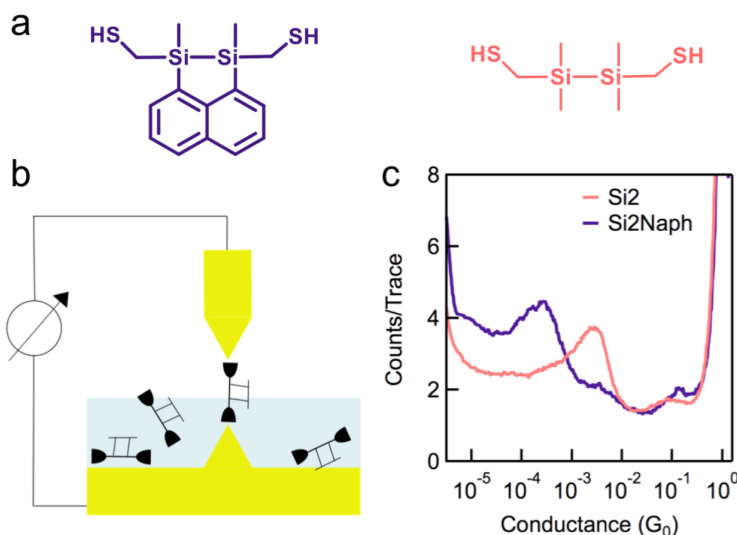


Figure 1.14: (a) Chemical structures of **Si2Naph** (purple) and **Si2** (pink). (b) Schematic of STM-BJ setup. (c) Logarithmically binned conductance histograms for **Si2Naph** and **Si2** generated without data selection using 100 bins/decade from 17000 and 27000 traces respectively.

## Bond Rupture Measurement

Next, we investigate the rupture behaviors of the junctions formed with these two molecules under an applied voltage. We use a modified experimental technique that we have described in detail previously.<sup>13</sup> Briefly, we start with an Au—Au contact and withdraw the tip to a fixed distance to form a single molecule junction. We then hold the junction for 150 ms and withdraw the tip again until the junction breaks by applying a modified ramp to the piezo as shown by the blue trace in Figure 1.15a. We apply a voltage

pulse ranging in amplitude from 0.2 to 1.4 V when the junction is held (green trace in Figure 1.15a) and record the junction conductance during the entire trace. We first select traces with a conductance within the range of the conductance histogram peak (range indicated by dashed lines in Figure 1.15b and 1.15c) at the start of the hold segment. Of these traces, we observe that some show a roughly constant conductance during the high-bias pulse while others show a sudden drop below the molecular conductance range. The former traces (light shades of red/purple for **Si2/Si2Naph**) correspond to those with a molecular junction that sustains the high-voltage, while the latter (dark shades of red/purple for **Si2/Si2Naph**) are molecular junctions that rupture under the high voltage.

Our primary finding here is that **Si2** junctions break to a conductance that is at our instrument noise floor, while the **Si2Naph** junctions break to a conductance that is slightly smaller than that of the **Si2Naph** junction. We analyze all traces that start with a molecular junction and determine the fraction that break under the applied bias using an automated algorithm. Through this analysis, we determine the breaking probabilities for **Si2** and **Si2Naph** molecular junctions based on the measurement of 6000 traces at each applied voltage and plot them in the insets of Figure 1.15b and Figure 1.15c. **Si2** shows a sharp increase at 0.9 V and **Si2Naph** shows a rather linear increase across the whole bias range from 0.2 V to 1.4 V.

To further investigate whether the difference in the broken junction conductance between **Si2** and **Si2Naph** is statistically significant, we create separate two-dimensional conductance histograms of all the traces that either sustain or break at an applied bias of 0.9 V. We see in Figure 1.16a and 1.16b that both **Si2** and **Si2Naph** junctions that sustain the high bias display a conductance around their conductance peak values (as seen

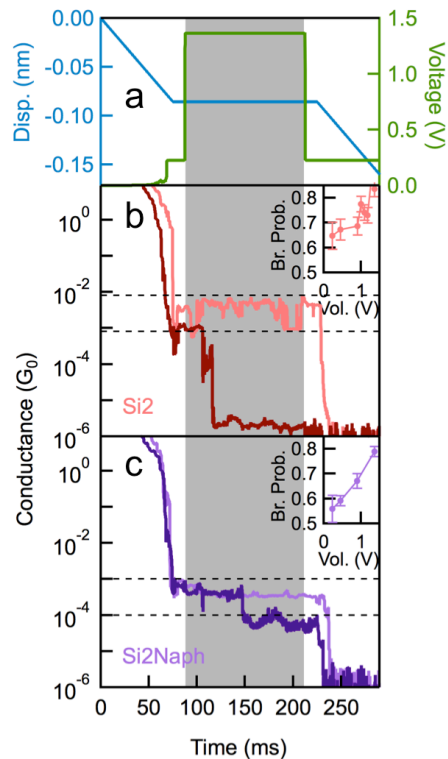


Figure 1.15: (a) Piezo displacement (blue; left) and applied voltage (green; right) plotted against time in each pull-hold-pull measurement. (b) (and (c)) Two sample traces measured with **Si2** (**Si2Naph**) showing a molecular junction sustain (light color) or rupture (dark color) under a 0.9 V applied bias. Dashed vertical lines show the range of the molecular junction's conductance as determined from the conductance histograms in Figure 1.14. Inset shows the breaking probability as a function of the applied peak voltage for **Si2** (**Si2Naph**) and the error bars show the standard deviation determined from variations in sets of thousand measurements.

from Figure 1.14c). For the junctions that rupture, we find that the distribution of the conductance for **Si2** is across a wide range  $10^{-2} \sim 10^{-6}G_0$ , whereas the conductance for **Si2Naph** shows a distribution that is sharply peaked at  $10^{-4}G_0$ .

We hypothesize that the Si—Si bond can rupture under an applied bias of 0.9 V in both cases: **Si2Naph** can still conduct through the 1,8-substituted naphthalene system but **Si2** has no conduction pathway when Si—Si bond is broken. This explains the clear conductance observed for junctions with **Si2Naph** when the Si—Si bond is bro-

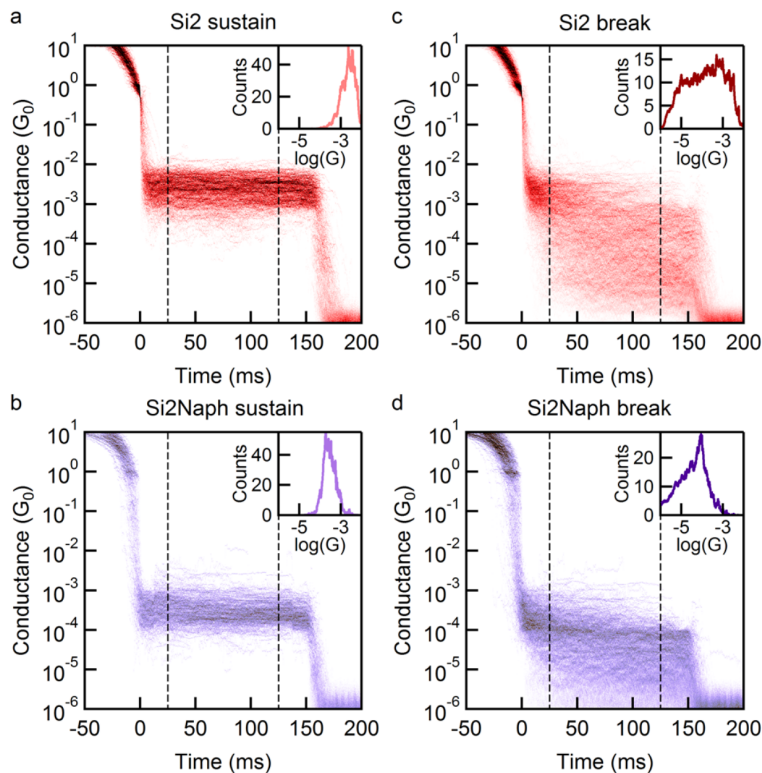


Figure 1.16: Two-dimensional conductance histograms of all traces showing sustaining junctions of (a) **Si2** and (b) **Si2Naph** and breaking junctions of (c) **Si2** and (d) **Si2Naph** while a voltage of 0.9V is applied during the time indicated by the region in between the two dashed lines. Each inset shows a conductance distribution of its corresponding 2D histogram while the high bias is applied.

ken, which is not observed in the broken **Si2** junction. To show that the **Si2Naph** can conduct through the 1,8-connection across the naphthyl bridge, we synthesize 1,8-bis(2-(methylthio)ethyl)-naphthalene, measure its conductance and find a clear conductance signature (structure and conductance histogram in Figure 1.17a). This result shows that 1,8 substituted naphthalene bridging the Au electrodes can provide electron transport pathways, likely through the  $\sigma$ -system as the  $\pi$ -system should evidence a destructive quantum interference effect.<sup>43</sup>

One possible mechanism for the Si—Si bond rupture in the **Si2Naph** system could involve an oxidative addition of the Au to the bond, and we note that oxidative addition

of Au nanoparticles to Si—Si bonds has been demonstrated.<sup>93,94</sup> However, and in contrast to our recent study,<sup>16</sup> we do not see any evidence for a contact between the Au electrodes and the Si—Si bond in the conductance histograms. Further, we have observed no evidence for the formation of an alternative molecular junction upon rupture of the Si—Si bond, or the reformation of the junction. We suggest that rotation about one or both of the naphthyl—Si bonds subsequent to Si—Si cleavage could prevent bond reformation. Another possibility we considered is high-bias induced oxidation of the disilane to the siloxane since these experiments are performed under ambient conditions.<sup>94</sup> To test this hypothesis, we independently synthesize the siloxane<sup>78</sup> corresponding to **5** (structure in Figure 1.17b). We find that its conductance is 1.5 times the conductance of the broken **Si2Naph** junction (conductance histogram in Figure 1.17b). We conclude that it is unlikely that the conductance we observe upon Si—Si bond rupture may be attributed to the formation of the siloxane.

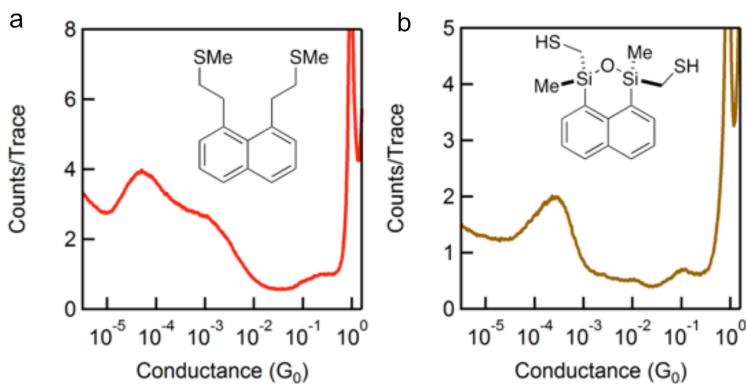


Figure 1.17: Chemical structures and the corresponding conductance histograms of (a) 1,8-bis(2-(methylthio)ethyl)-naphthalene and (b) siloxane **5**.

## Density Functional Theory Calculations

We now turn to *ab initio* computations carried out using density functional theory and molecular dynamics to understand the mechanism of the voltage-induced bond rupture processes observed here. We first consider impact of an applied voltage on the junction to see if any Stark effect<sup>95</sup> could polarize the Si—Si bond, thus destabilizing it. We construct a molecular junction using electrodes that consist of seven layers of 16 gold atoms on both sides terminated by a trimer that serves as a tip structure on which the molecule is bound. This junction is relaxed using DFT within the GGA of Perdew, Burke, and Ernzenhof (PBE)<sup>96,97</sup> and a double- $\zeta$ -basis set as implemented in SIESTA.<sup>98,99</sup> Details of our DFT calculations are provided in a previous work.<sup>66</sup> The DFT optimized junction geometry is first determined and then a bias-dependent steady-state density matrix is calculated self-consistently following a standard first principles approach.<sup>100,101</sup> A bias voltage of 1.0 V is applied to the junction by fixing the chemical potential of the two electrodes symmetrically around the junction Fermi level and the potential profile across the molecule is obtained. From this profile, we find that about 15% of the voltage drops across the Si—Si bond in the Au-Si2Naph-Au junction (Figure 1.18). This indicates that with a bias of 1.0 V applied on the junction, the Si—Si bond is under a 0.09 V/ electric field, which is unlikely to have any significant impact on the bond.<sup>102–104</sup> We add further that transmission calculations for similar junctions have shown that there are no molecular resonances accessible within the bias window and thus transport is through an off-resonance tunneling mechanism.<sup>17</sup>

We therefore conclude that bond rupture is through a current-induced mechanism

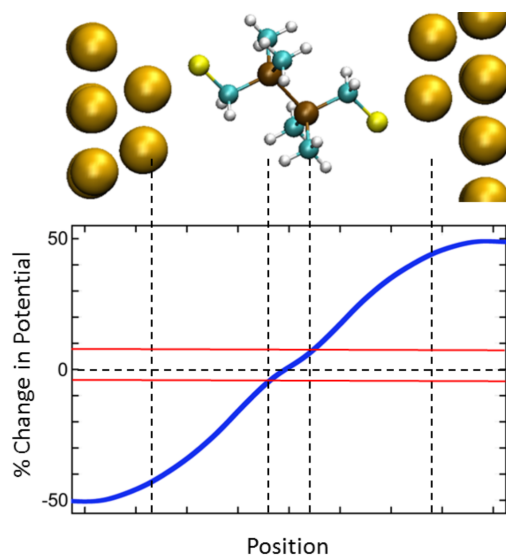


Figure 1.18: 3D structure of **Si2** molecular junction with electrodes and calculated voltage drop across the **Si2** junction.

where the incoming electrons excite molecular vibrational modes of the junction. We calculate the vibrational modes of **Si2** and **Si2Naph** both in the isolated case and as a junction using DFT with a finite difference procedure. The dynamical matrix is generated using displacements of  $0.025\text{\AA}$  for each atom, along each Cartesian direction. In the case of the junction, forces are computed using four layers of gold on each side, with only the top-most layer and the binding motif included in the dynamical matrix, corresponding to 384 and 432 displacements for the **Si2** and **Si2Naph** junctions, respectively.

In Figure 1.19, we plot the calculated vibrational spectra for **Si2** (red) and **Si2Naph** (purple) with the tick marks showing the decomposition of the Si—Si stretch modes with significant displacement. For **Si2**, the Si—Si stretch is maximal for the modes at 28.9 and 50.8 meV, with non-negligible displacements for up to 103 meV. For **Si2Naph**, there is significant hybridization of the Si—Si stretch and the Si—Naphthalene stretch, leading to a denser spectrum of modes with significant Si—Si stretch in the 28-60 meV energy

range. We first note that there are many Si—Si vibrational modes at low energies that can be relatively easily excited as long as the voltage across the junction is greater than  $\sim 200$  mV. We note further that, due to their heavy mass, the Au-related modes are all at energies below 20 meV, i.e. spectrally decoupled from the Si—Si stretch modes. Finally, we find that a mode around 320 meV, which corresponds to an S—H stretching mode is shifted to low energies upon the formation of an S—Au bond and H desorption.

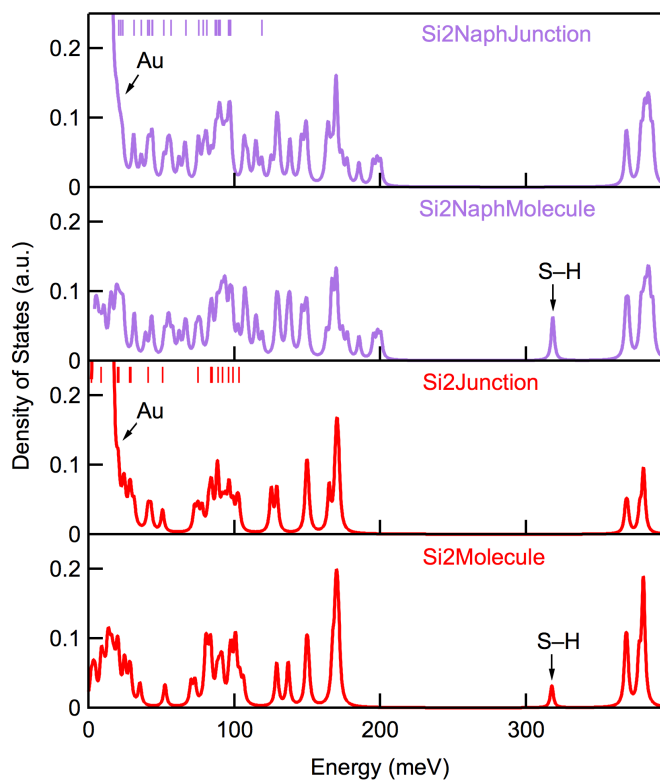


Figure 1.19: Calculated vibrational modes for **Si2** (red) and **Si2Naph** (purple) for the molecule and molecular junction (including the electrodes) configurations. The vertical tick marks indicate the decomposition of the most significant Si—Si stretch modes.

We have also calculated the vibrational spectra of **Si2** and **Si2Naph** at finite electric fields ( $-1$  V  $\sim$  1V) and do not see any strong field-dependence (Figure 1.20, 1.21) or any charging dependence (Figure 1.22, 1.23) in agreement with the weak voltage drop found

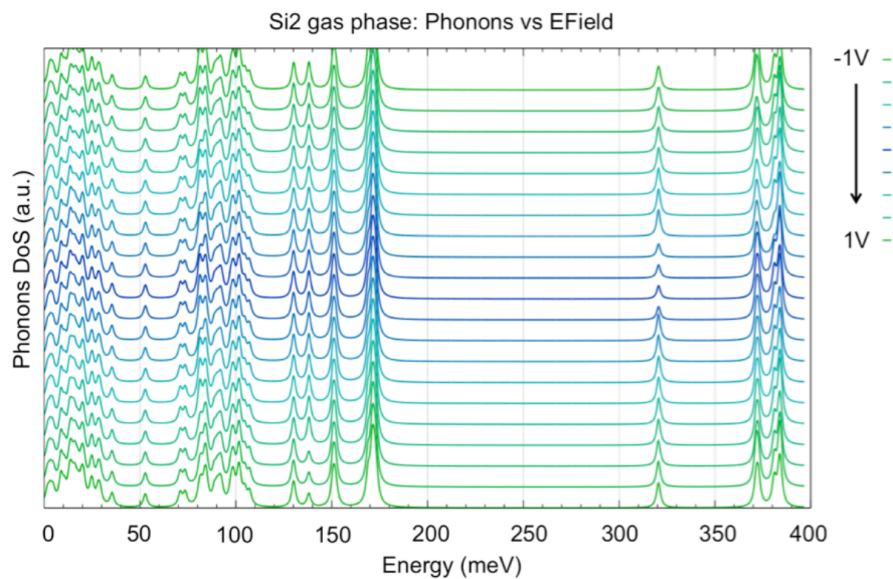


Figure 1.20: Calculated vibrational modes for gas phase **Si2** as a function of applied voltage.

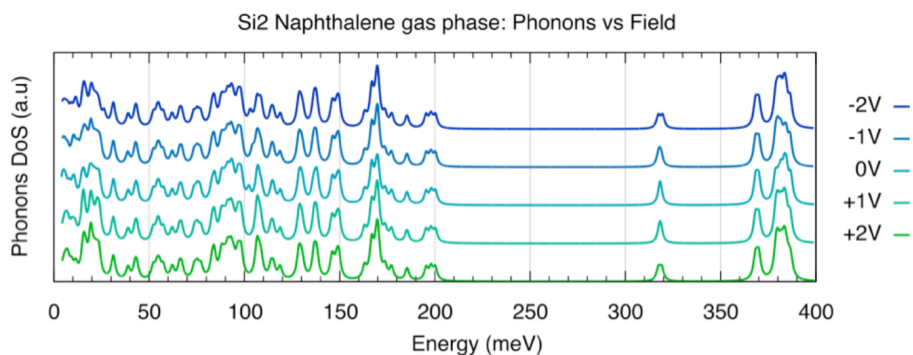


Figure 1.21: Calculated vibrational modes for gas phase **Si2Naph** as a function of applied voltage.

at the Si—Si bond (Figure 1.18).<sup>105</sup> We conclude that we can excite the Si—Si modes at all biases where we observe bond rupture. As the voltage is increased, the probability that these vibrational modes are excited increases as the composition of the scattering states around the Fermi energy has a weak energy dependence, and wider bias windows enable multiple excitations to the vibrational modes. This proposed mechanism indicates that the Si—Si bond rupture is a simple, direct homolytic cleavage as opposed to heterolysis

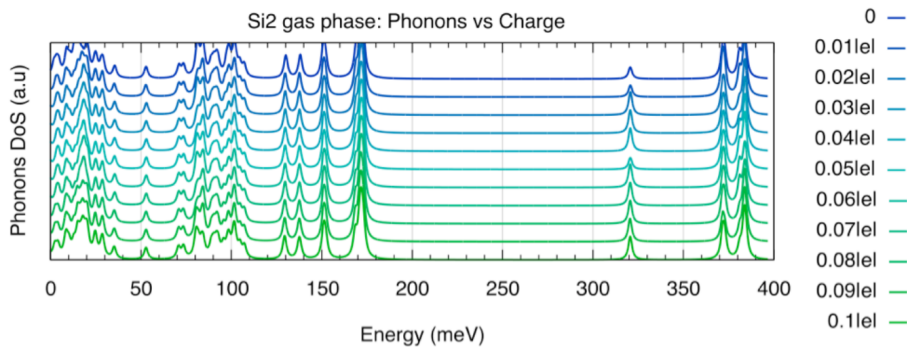


Figure 1.22: Calculated vibrational modes for gas phase **Si2** as a function of charge.

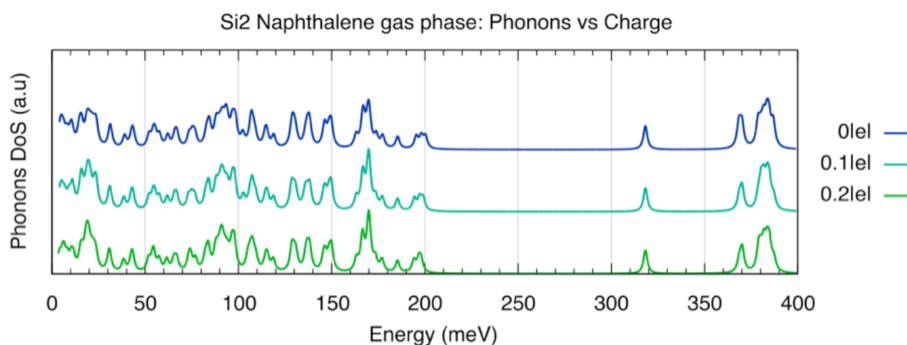


Figure 1.23: Calculated vibrational modes for gas phase **Si2Naph** as a function of charge.

or disintegration.

## Molecular Dynamics Simulations

Next, we carry out *ab initio* molecular dynamics (MD) simulations of bond stability at different finite temperatures using an NVT ensemble and the SIESTA code.<sup>100</sup> We model the junctions with one fixed layer of gold on each side and an ad-atom binding motif. We compute 5 ps-long MD trajectories using a 1 fs time step at constant volume and temperature. We compute the pair-distribution function for temperatures ranging from 300K to 1600K and determine the length of the Si—Si, Si—C and Au—S bonds at each temperature. In Figure 1.24, we plot the length distributions for these bonds in a **Si2** molecular

junction at different temperatures. We see that at temperature above 1000 K, the Si—Si bond length varies by as much as 20% from the energy minimum bond length while the Au—S bond length distributions show only a modest increase, and the C—Si bond length distributions do not show any significant increase. While these temperatures are in excess of the local temperature in molecular devices,<sup>106</sup> they are compatible with non-equilibrium mode occupations induced by large current densities in a slowly-thermalizing environment.<sup>107</sup> This indicates that if the molecular vibrational modes are indeed excited by the current, the Si—Si bond is most likely to rupture.

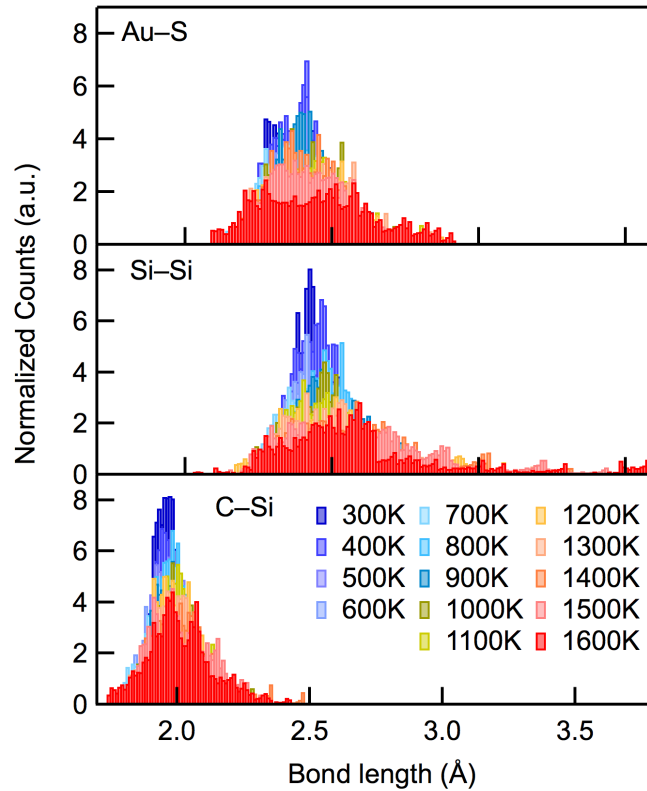


Figure 1.24: Molecular dynamics simulations showing distributions of bond lengths for Si—Si (top), Si—C (middle) and Au—S (bottom) bonds as a function of temperature in a **Si<sub>2</sub>** molecular junction. Color scale indicates temperature range of 300 - 1600 K or 25.8 - 137.9 meV.

## Conclusions

To conclude, we demonstrate an experimental method to investigate the bond stability under an electric field using single molecule circuits. In this study, we apply this method to **Si<sub>2</sub>** and **Si<sub>2</sub>Naph** single molecule junctions and find different transport properties between them when the junctions rupture under an electric field. This provides strong evidence that a Si—Si bond ruptures in both cases. We further investigate the bond rupture mechanism through density functional theory and molecular dynamics calculations and conclude that excitation of the vibrational modes in the molecular junction is the cause of bond rupture in our measurements. The studies described here help deepen our understanding of the nature of the chemical bond in extreme environments.

### *Single Molecule Conductance of Linear Silanes and Germanes*

## 2.1 Stereoelectronic Switching

### Preface

This section is based on the manuscript entitled *Stereoelectronic switching in single-molecule junctions* by Timothy Su, Haixing Li, Michael Steigerwald, Latha Venkataraman, and Colin Nuckolls published in *Nature Chemistry*.<sup>12</sup> Timothy Su of Prof. Nuckolls' group synthesized and characterized all the compounds. Timothy Su and Dr. Michael Steigerwald carried out calculations. I performed the conductance measurements and data analysis.

### Abstract

A new intersection between reaction chemistry and electronic circuitry is emerging from the ultraminiaturization of electronic devices. Over decades chemists have developed a nuanced understanding of stereoelectronics to establish how the electronic properties of molecules relate to their conformation; the recent advent of single-molecule break-junction techniques provides the means to alter this conformation with a level of control previously unimagined. Here we unite these ideas by demonstrating the first single-

molecule switch that operates through a stereoelectronic effect. We demonstrate this behaviour in permethyloligosilanes with methylthiomethyl electrode linkers. The strong  $\sigma$  conjugation in the oligosilane backbone couples the stereoelectronic properties of the sulfur-methylene  $\sigma$  bonds that terminate the molecule. Theoretical calculations support the existence of three distinct dihedral conformations that differ drastically in their electronic character. We can shift between these three species by simply lengthening or compressing the molecular junction, and, in doing so, we can switch conductance digitally between two states.

## Introduction

The development of single-molecule conductance switches is crucial to the realization of nanoscale electronic devices in which molecules will serve as components in electrical circuitry.<sup>108,109</sup> Controlling the electronic properties of single molecules in the context of electronic devices is a relatively new field of interest; however, chemists have studied the electronic properties of molecules in the context of chemical reactivity over many decades. Incorporating the paradigms of reaction chemistry into the design of molecular electronic components can provide a tremendous impetus to advance the field of molecular electronics. For example, chemical principles such as photocyclization,<sup>110</sup> tautomerization<sup>111</sup> and cross-conjugation<sup>112</sup> have inspired the genesis of many new types of molecular electronic components.<sup>113-115</sup>

Here we introduce the first example of a molecular electronic switch that operates through a stereoelectronic effect. Stereoelectronic effects are fundamental to reaction chemistry because they determine how the properties and reactivities of molecules de-

pend on the relative spatial orientations of their electron orbitals.<sup>116</sup> The vast stereoelectronics knowledge base can therefore serve as a tremendous resource in controlling electronics at the single-molecule level by directing molecular conformation. Although conformational effects have been reported in other single-molecule devices, none of these reported components have demonstrated digital switching between conductance states by controlling bond rotation, as is shown here.<sup>117-122</sup>

We utilize the sub-ångström level of control in a scanning tunnelling microscope-based break-junction (STM-BJ) technique to manipulate specific dihedral angles in permethyloligosilanes with aurophilic methylthiomethyl electrode contacts (Figure 2.1). We can increase the conductance by elongating the molecular junction and decrease the conductance by compressing the electrodes; each terminal (C—S—C—Si) dihedral angle that couples the electrode-linker orbital into the  $\sigma$  framework acts as a gate to control conductance. We find an analogy in the computational studies of Franco et al., who predicted the same principle in a cyclophane in which junction elongation opens a more conductive channel for transport.<sup>123</sup> The switching that we see is binary in the sense that there are only two discrete conductances. We see no evidence of intermediate conductance values, and therefore the switching is faster than the microsecond time resolution of the STM.

## Results and Discussion

**Synthetic Design** Figure 2.2 shows the iterative synthesis we devised for the  $[\text{SiMe}_2]_n$  oligosilanes ( $n=1-10$ ) terminated by methylthiomethyl linkers (**Si1-Si10**). We grow  $\alpha,\omega$ -diphenyloligosilane **2** outwards, two silicon subunits at a time, by treating  $\alpha,\omega$ -dichlorooligosilane **3** with two equivalents of dimethylphenylsilyl magnesium **1**.<sup>124</sup>

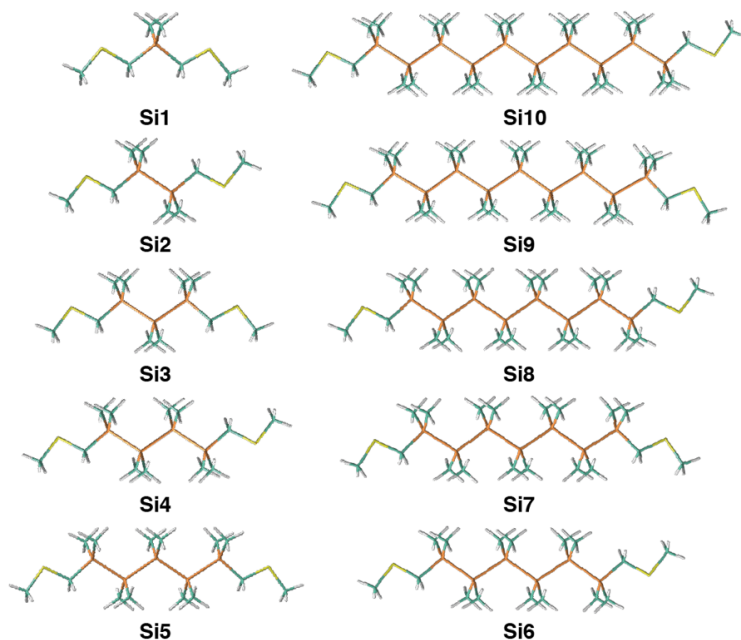


Figure 2.1: Structures of oligosilanes **Si1–Si10** (Si (orange), C (teal), S (yellow), H (gray)) calculated at the B3LYP/6-31G\*\* level of theory. The backbone (Si—Si—Si—Si) dihedral angles are held to 180° to emphasize the length difference across the oligosilane series. Si, orange; C, teal; S, yellow; H, grey.

Protodesilylation of  $\alpha,\omega$ -diphenyloligo-silane **2** under acidic conditions furnished the chain-extended  $\alpha,\omega$ -dichlorooligosilane **3**.<sup>125</sup> The odd and even series were built from the commercially available mono- and disilanes, respectively. We functionalized  $\alpha,\omega$ -dichlorooligosilane **3** with electrode linkers ( $\text{CH}_2\text{SMe}$ ) in two steps. We installed the halomethyl groups in  $\alpha,\omega$ -bis(halomethyl)oligosilane **4** by generating the halomethyl lithium in the presence of **3**.<sup>79,80</sup> We obtained the final  $\alpha,\omega$ -bis(methylthiomethyl)oligosilanes **Si1–Si10** from nucleophilic substitution of the primary halide with sodium thiomethoxide.<sup>126</sup>

**STM-BJ** We measured the single-molecule conductance of **Si1–Si10** using the STM-BJ technique.<sup>8</sup> The STM-BJ measurement proceeds as follows: point contacts between the Au STM tip and the substrate electrodes are repeatedly broken and formed in a so-

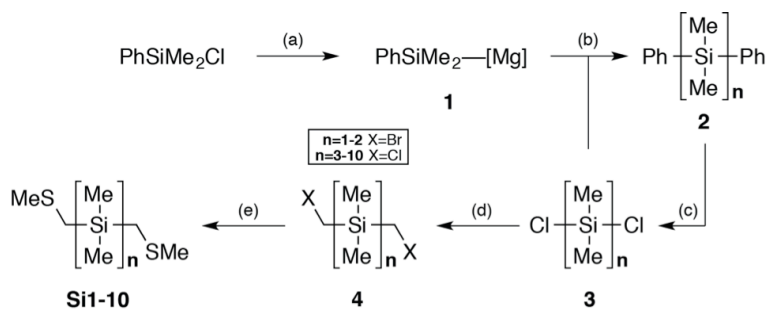


Figure 2.2: Iterative synthesis of oligosilanes terminated with methylthiomethyl end-groups. (a) Li (0), THF, 0 °C; iPrMgCl, 0 °C. (b) THF, 0 °C. n = 3-10 were synthesized in 60% to 84% yield. (c) For n = 3-4: HCl, AlCl<sub>3</sub>, toluene, r.t. For n=5-10: TfOH, DCM, 0 °C; NEt<sub>3</sub>•HCl, Et<sub>2</sub>O, 0 °C. 64% to 77% yield. (d) For n = 1-2: LiBr, CH<sub>2</sub>Br<sub>2</sub>, n-BuLi, THF, -78 °C. For n = 3-10: CH<sub>2</sub>BrCl, n-BuLi, THF, -78 °C. 48% to 93% yield. (e) NaSMe, EtOH, 0 °C. 11-86% yield.

lution of the target molecule (1mM for **Si1-6**, 0.1mM for **Si7-9**, 0.05mM for **Si10** in 1,2,4-trichlorobenzene) at room temperature and under ambient conditions. After the Au—Au point contact is broken, aurophilic thiomethyl groups<sup>67</sup> on the molecule bridge the electrodes to form an Au-molecule-Au junction. Conductance is measured across the gap as a function of the tip-substrate displacement, and the resulting traces reveal molecule-dependent plateaus that signify junction formations with conductance values below  $G_0$  ( $2e^2/h$ ), the quantum of conductance, where  $e$  is charge of an electron and  $h$  is Planck's constant.<sup>127</sup> The molecular junction breaks once the tip-substrate electrode gap becomes too wide for the molecule to coordinate to both electrodes. Thousands of molecular junctions are analyzed using logarithm-binned one-dimensional (1D) and two-dimensional (2D) histograms. 1D histograms provide a distribution of all measured conductance values from all traces; 2D histograms sum all the conductance values and retain the relative displacement information.<sup>128</sup>

The 1D conductance histograms for **Si1-Si10** are compiled in Figure 2.3a. All the

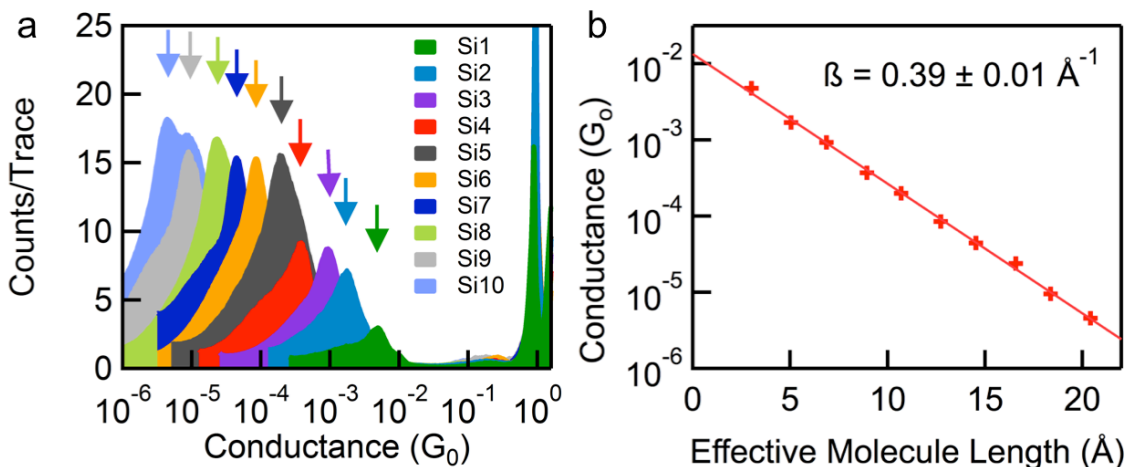


Figure 2.3: Conductance histograms of the oligosilane series. (a) Logarithm-binned 1D histograms for **Si1-Si10**. The arrows denote the peak maxima used in **b**. All histograms are normalized by the number of traces used to construct the histograms. (b) Conductance peak values for **Si1-Si10** plotted against the effective molecule length give the decay constant  $\beta$ .

oligosilanes ( $n = 1-10$ ) gave the same general peak shape: a sharp maximum at higher conductance followed by a broad tail at lower conductance. There is an exponential decrease in conductance as  $n$  increases; we quantified this decrease by deriving the length-dependent conductance decay value ( $\beta$ ).<sup>42,78</sup> Figure 2.3b shows a plot of the conductance maxima from the 1D histograms against each oligomer's effective molecular length ( $L$ ).  $L$  is defined as the distance between the two distal methylenes in each density functional theory (DFT)-optimized structure. We obtain  $\beta$  by fitting a line through these points on a semi-log scale. Figure 2.3b shows that the conductances of **Si1-Si10** fit to a line with  $\beta = 0.39 \pm 0.01 \text{ \AA}^{-1}$ . As a comparison, linear alkanes terminated with thiomethyl linkers have a  $\beta$  value of  $0.70 \pm 0.03 \text{ \AA}^{-1}$ .<sup>67</sup> This difference arises from the increased  $\sigma$  delocalization that occurs in Si compared with C, as bonding orbitals increase in size and energy down the periodic table.<sup>129,130</sup> As we show below, this additional delocalization in the silanes enables us to observe different conductance values for two distinct sets of rotational isomers

in a single molecule.

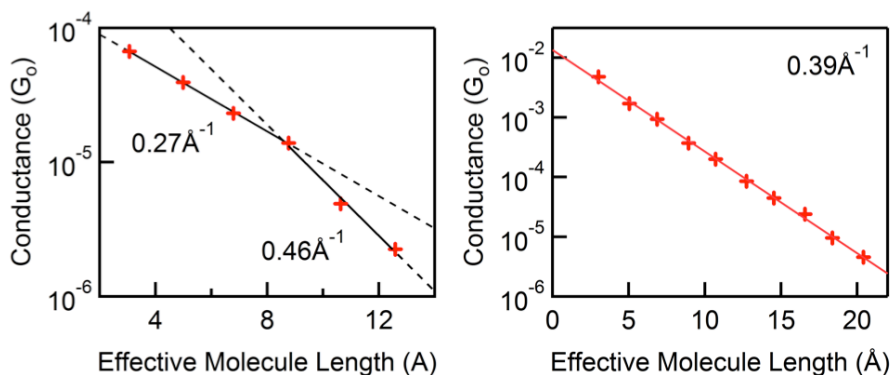


Figure 2.4:  $\beta$  plot for oligosilanes with thioanisole linkers (left) and methylthiomethyl linkers (right).

We note that in our previous study of the length-dependent properties in oligosilanes with thioanisole linkers,<sup>78</sup> we found  $\beta = 0.27 \text{ \AA}^{-1}$  for  $n=1-4$ . The longer oligomers with thioanisole contacts do not fall on the same fit and instead we find that  $n=4-6$  fit to  $\beta = 0.46 \text{ \AA}^{-1}$  (Figure 2.4). The high “contact resistance” of the thioanisole linker prevented us from measuring oligomers longer than  $n=7$ . A rigorous study comparing the shorter and longer thioanisole-terminated oligosilanes is outside the scope of this study; however, we offer here a simple qualitative reason for why they are different. For the short oligosilanes, the tunneling orbital is predominately comprised of the S  $p\pi$  lone pair and aryl C  $\pi$ -orbitals so the tunneling orbital has much more  $\pi$ -character rather than  $\sigma$ -character. In the methylthiomethyl-terminated oligosilanes here, there are only  $\sigma$ -bonds between the two S atoms, so we never see a sudden change in our  $\beta$  plot where the  $\sigma$ -orbitals start to play a more dominant role as we do with the thioanisole-terminated silanes.

We defined  $L$  in this study as the distance between the distal methylenes in **Si1-Si10** to compare the results with our previous study of oligosilanes that have thioanisole link-

ers, in which  $L$  was defined as the distance between the two aryl carbons that terminated the silane chain.<sup>78</sup> By extrapolating our fit to  $L = 0$ , we found that the contact resistance of the methylthiomethyl linker ( $0.95 \text{ M}\Omega$ ) was two orders of magnitude smaller than that of our previous thioanisole linker ( $83 \text{ M}\Omega$ ). The low contact resistance of the methylthiomethyl linkers enabled us to measure the longer oligosilanes in this study and, more importantly, to show that the conductance mechanism in these longer silane chains occurs through non-resonant transport, as evidenced by the clear exponential dependence of conductance with length.<sup>131</sup>

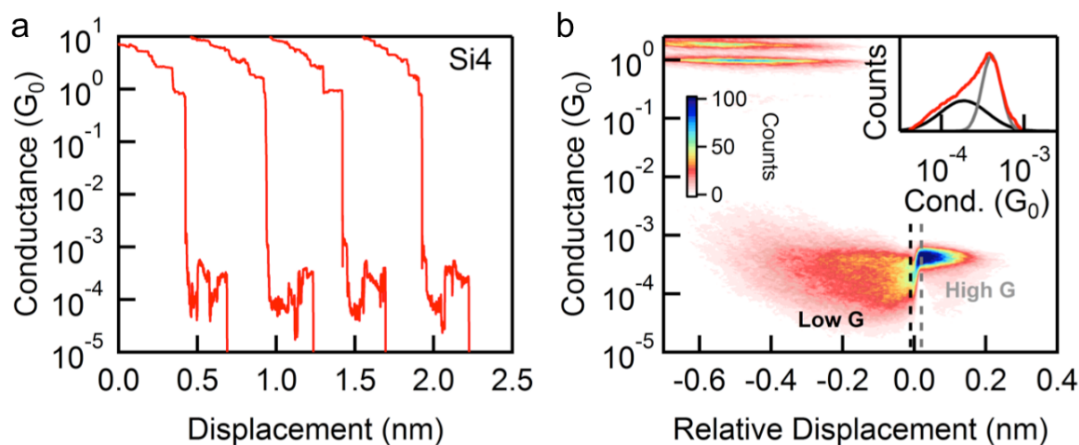


Figure 2.5: Conductance data of **Si4**. (a) Individual traces from the measurement of **Si4** as electrode displacement increases. Sample traces are offset along the displacement axis for clarity. (b) 2D conductance-displacement histogram for **Si4** compiled from traces that demonstrate switching. The inset is a compilation of the pre-switching (black line) and post-switching (grey line) regions into 1D histogram plots; the total 1D histogram for **Si4** (red line) is superimposed for comparison.

**Analysis of switching behaviour** For each silane (**Si1-Si10**) a large fraction of traces showed an abrupt jump from a lower to a higher value of conductance as the tip-substrate electrode gap widened. Although a similar effect has been observed before in other systems,<sup>132–134</sup> it is uncommon; molecular junctions do not typically demonstrate

this inverted conductance behaviour. Figure 2.5a demonstrates this effect in individual traces. 2D histograms allow us to interpret conductance as a function of electrode displacement. We compiled our 2D histograms from traces that exhibited a switch from low to high conductance. Figure 2.5b depicts such a histogram for **Si4**, in which switching from low to high conductance occurs on elongation in 50% of 6,000 total traces in which we observe a clear molecular conductance plateau (Figure 2.6 gives the 2D histograms for the other oligosilanes). We defined the point of zero relative displacement as the point along the elongation trajectory at which switching occurs (Figure 2.5b). Aligning the traces to the switching event enabled us to sort the histogram into two regimes: the lower-conducting (low G) pre-switch state (where  $x < 0$ ) and the higher-conducting (high G) post-switch state (where  $x > 0$ ). The insets of Figure 2.5b and 2.6 show the 1D histograms that resulted from this separation of the low and high G states (grey and black lines, respectively). The high G peak is sharp and the low G peak is broad. The inset reveals that the sharp peak and broad tail characteristic of each oligosilane arises from the superposition of these two distinct conductance states: in each case a broad low-conductance peak and a sharp high-conductance peak combine to give the asymmetric peak seen in Figure 2.3a. The conductances of the low and high G peaks for each oligosilane are plotted against molecular length in Figure 2.7. Both states decay across the series with the same  $\beta$  value, but in each member of the series the two conductance values differ by about a factor of two.

These molecular switches are robust; we can exercise them in real time. We performed five consecutive compression-elongation cycles in **Si6** in which we compressed and retracted the Au-**Si6**-Au junction near the point of full extension (Figure 2.8). In each

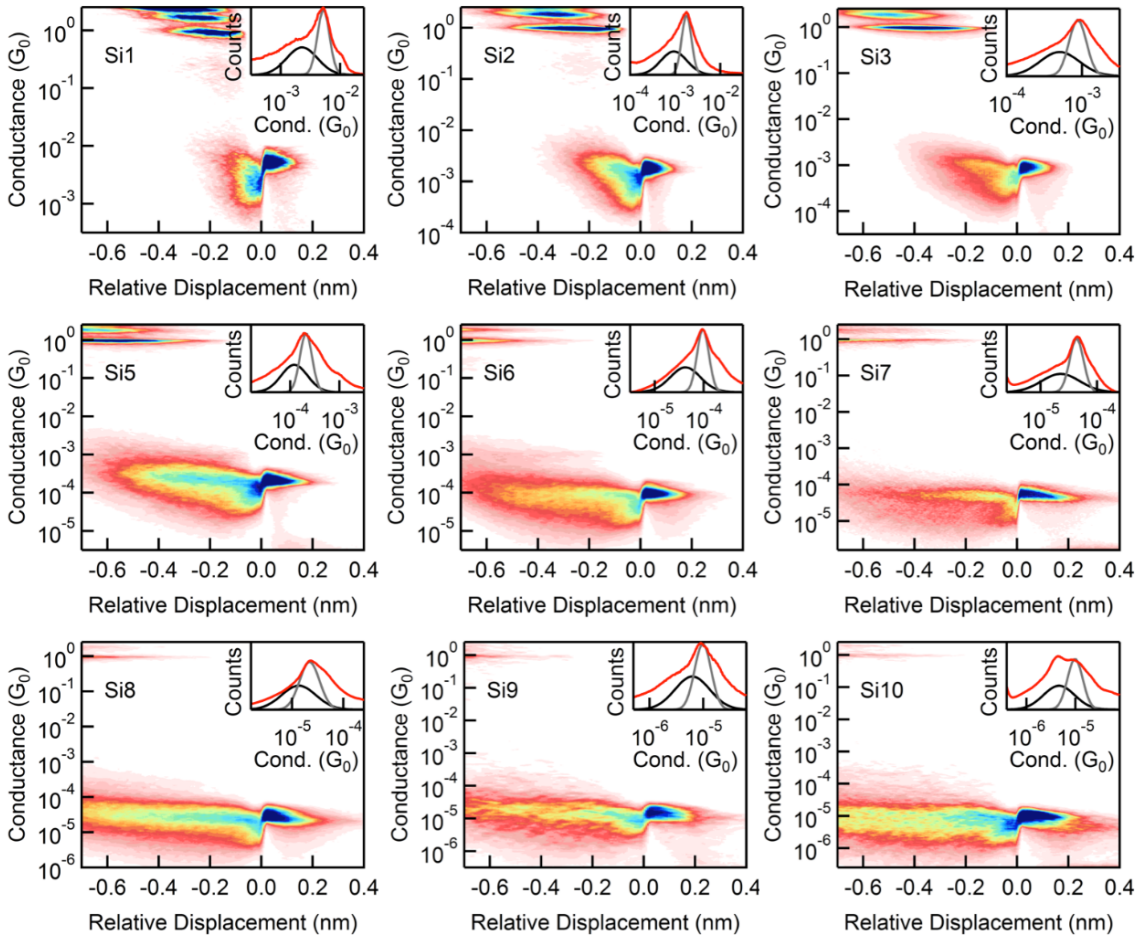


Figure 2.6: 2D histograms of **Si1-Si3**; **Si5-Si10**. For measurements with **Si10**, we observe two high  $G$  peaks (apparent in Figure 2.3a) that are most probably due to the frequent formation of junctions with two molecules in parallel. The switching data presented in the 2D histogram for **Si10** below should then also describe switching events where two molecules in the low  $G$  state switch to two molecules in the high  $G$  state. This can be rationalized from the corresponding inset where the conductance profiles of the pre- and post-switching states are overlaid with the 1D conductance histogram of Figure 2.3a.

cycle we elongated the molecular junction fully, held the junction in place for 50 ms, compressed the electrodes by  $1.9 \text{ \AA}$  and then held the junction at this new displacement for another 50 ms (we chose the  $1.9 \text{ \AA}$  distance by which we compressed and elongated these junctions from the 2D histogram shown in Figure 2.6, which shows the extent of the high  $G$  state). Figure 2.8a shows a compilation of our results over 10,600 traces that started

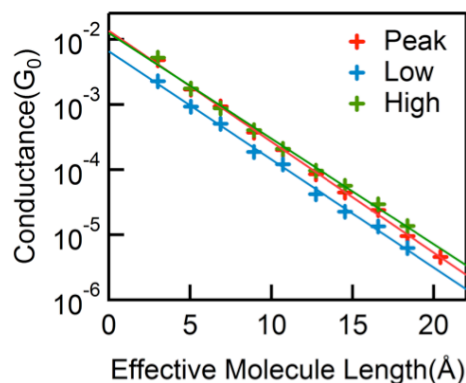


Figure 2.7:  $\beta$  values of the low G and high G peaks from the 1D histograms in the inset of Figure 2.5b and 2.6. “Peak” describes the conductance value determined from the 1D histograms in Figure 2.5b, 2.6 without selection. The  $\beta$  values are as follows: Peak =  $0.39 \pm 0.01$ ; High =  $0.37 \pm 0.01$ ; Low =  $0.38 \pm 0.01$ . As described in the caption of Figure 2.6, the same analysis does not apply for **Si10**. The “contact resistance” of the high G and Low G states are  $1.036 \text{ M}\Omega$  and  $1.972 \text{ M}\Omega$  respectively.

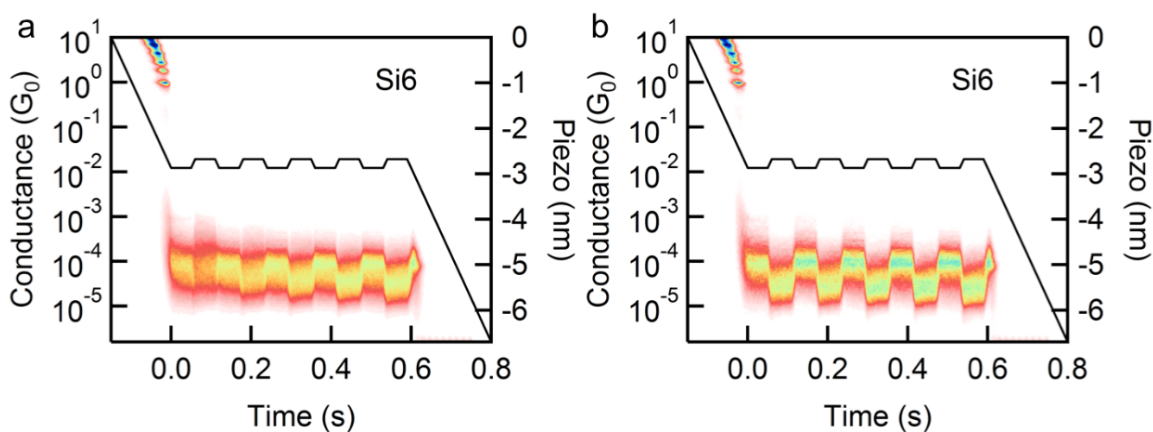


Figure 2.8: 2D histograms of compression-elongation cycles for the Au-**Si6**-Au junction. (a) A modified piezo ramp (black line) is applied to induce switching. Traces are aligned to the beginning of the first hold period. 2D histogram constructed from all traces for which a molecule remains in the junction during all the hold periods. No other selection was applied. Switching sharpens with each oscillation. (b) Clean switching from the first to last oscillation occurs in 33% of traces.

at a conductance that corresponded to the peak shown in the histogram in Figure 2.3a.

The majority of these traces switched between a high and low state, as is clearly visible in the 2D histogram. Further, we observed a “burn in” effect in which switching between the states became sharper with each additional compression-elongation cycle. This be-

behaviour suggests that the oscillation cycles are training<sup>135</sup> our device by reorganizing the junction into a new environment in which it behaves more effectively as a switch. Clean switching from the first to last elongation-compression cycle occurs in about one-third of traces (Figure 2.8b).

We performed a single compression-elongation cycle on **Si6** and compared our results with those for 1,8 bis(thiomethyl)octane(**C8**), which has the same -CH<sub>2</sub>SMe linker as **Si6** but an aliphatic carbon backbone between the linkers (Figure 2.9). Although the Au-**Si6**-Au junction demonstrates two-state conductance switching with the conductance increasing on elongation, the Au-**C8**-Au junction maintains a relatively constant conductance over the course of the cycle and shows only a small decrease in conductance on elongation, probably because of a decrease in the through-space conductance component.<sup>29,136-139</sup>

We can begin to understand why switching occurs as the junction elongates by comparing the 2D histogram characteristics of the low and high G states across the oligosilane series (Figure 2.6). First, conductance changes by a factor of two for all oligosilanes regardless of the length of the Si chain. Second, the length of the conductance-plateau characteristic of the low G state increases from **Si1** to **Si10** (1 Å for **Si1** to 10 Å for **Si10**), whereas that of the high G state stays relatively constant (1.5-2.0 Å). The consistency in the switching ratio and high G length across the entire oligosilane series suggests that the high G state arises from a molecular feature that is common to all oligomers and invariant among them. We therefore do not believe that the switching we observed here arose from sudden rotations of the internal Si—Si—Si—Si dihedral geometries (Figure 2.10).<sup>140-142</sup> Given these details and the stereoelectronics of bonding around sulfur,<sup>143</sup> we

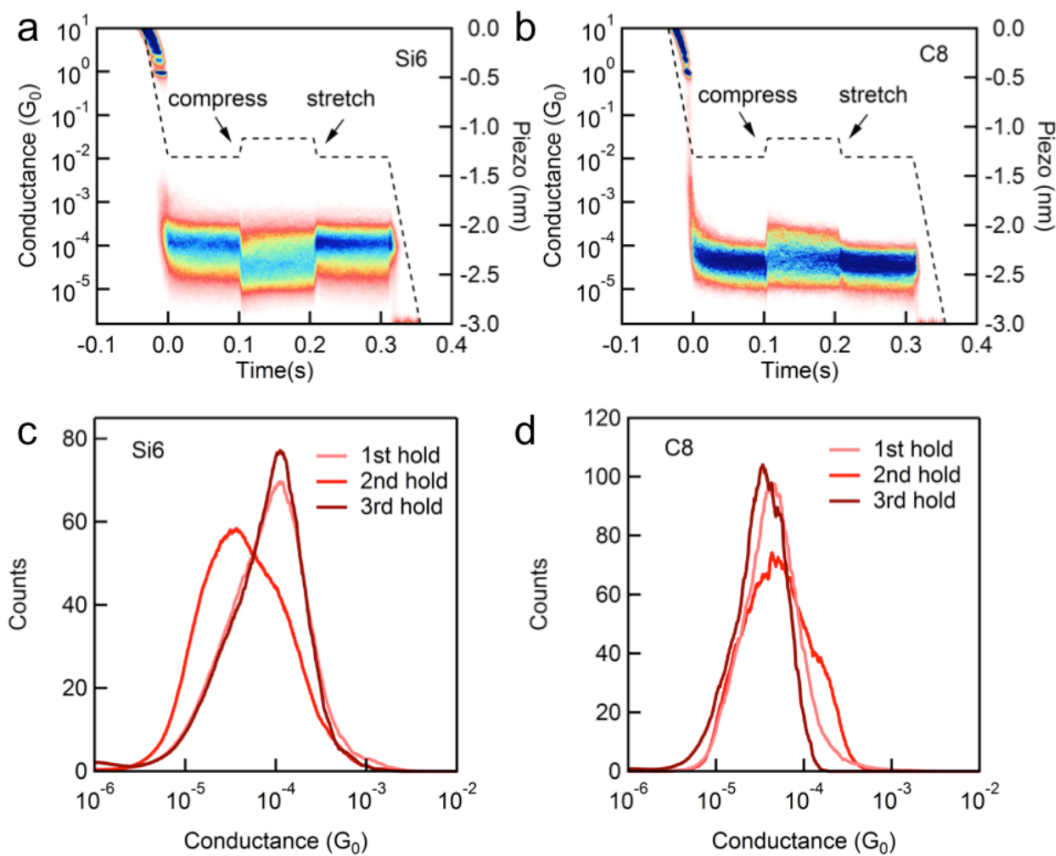


Figure 2.9: 2D histogram of compression-elongation experiment for **Si6** and **C8**. The histograms are constructed from all traces where a molecule remains in the junction during all three hold periods. No other selection is applied. We elongate the molecular junction, hold the junction in place for 0.1 s, compress the electrodes by 1.9 Å, hold the junction at this new displacement for another 0.1 s, then retract the electrodes until the junction breaks. (a) 2D histogram for **Si6** demonstrates switching between states over three hold periods. (b) 2D histogram for **C8** does not demonstrate switching between discrete states. (c) 1D histograms of the three hold periods for **Si6**. We observe some residual high  $G$  character in the 2nd hold period possibly from junctions that do not switch. (d) 1D histograms of the three hold periods for **C8**. We see that the peak maximum stays at approximately the same conductance during each hold period. The higher conducting shoulder in the 2nd hold period originates from the distance-dependent nature of tunneling.

hypothesize that the stereoelectronic effects of the two terminal dihedral angles ( $\text{H}_3\text{C}-\text{S}-\text{CH}_2-\text{SiMe}_2$ ) that terminate each oligosilane are fundamentally responsible for the switching we observed here. These dihedral angles should be particularly susceptible to changes in the tip-substrate distance because they involve gold atoms from the electrodes

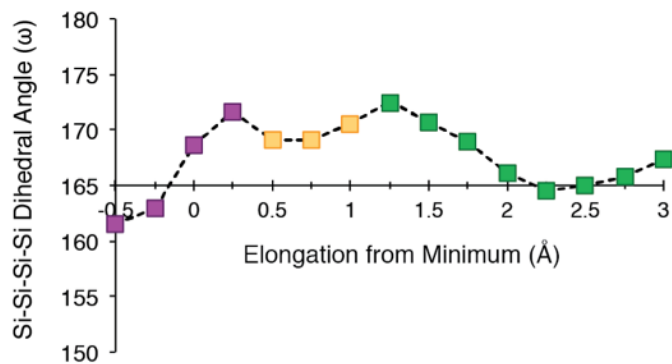


Figure 2.10: Si-Si-Si-Si dihedral angles for the lowest energy structures from Figure 2.14c (purple = A-A; yellow = O-A; green = O-O). Each lowest energy geometry at every Au-Au distance calculated has a transoid Si—Si—Si—Si geometry.

exerting torque on the molecule via the sulfur lone pair.

**Experimental Details** 2D conductance histograms (Figure 2.5b,2.6) were generated using the selection algorithm flow chart shown in Figure 2.11. First, we select the traces

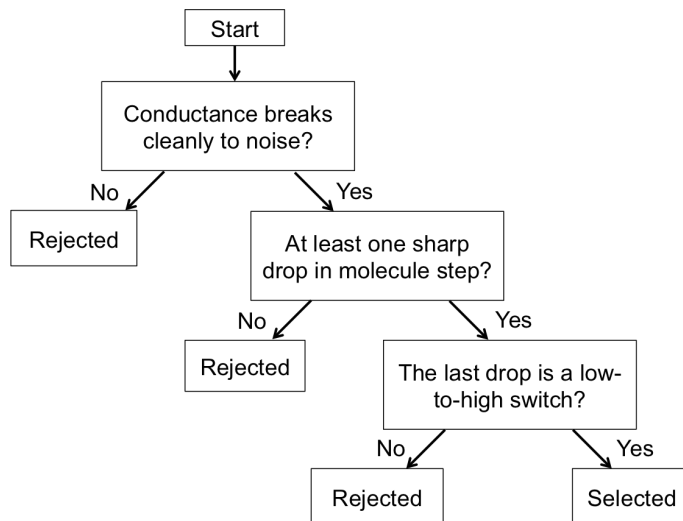


Figure 2.11: Algorithm for 2D conductance analysis

that demonstrate a clean break in conductance from the molecular plateau to the noise level of the instrument ( $3 \times 10^{-6} G_0$ ). This ensures that we are selecting traces where a junction rupture event occurs. Second, we select traces that demonstrate at least one

abrupt conductance change from within the plateau, which we define as a switching event. We use an algorithm that includes looking at the conductance derivative to identify such events following a procedure detailed in Aradhya et al.<sup>83</sup> We scan this derivative plot from right to left and select the first maximum above an oligosilane-specific threshold (we determine this threshold from trace-by-trace analysis). This allows us to align the traces to the final switching event. Finally, we select traces that demonstrate a switch from low to high conductance. We use 100 data points on both sides of the drop to compare the two conductance states. All traces are aligned to zero-displacement at their switch position to construct the 2D histogram. These three criteria ensure that selection is not based on conductance plateau value, plateau shape or plateau length.

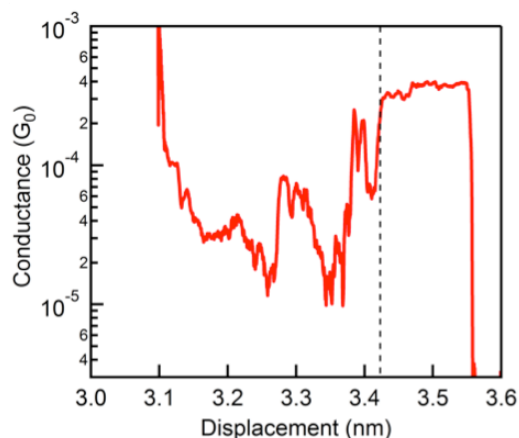


Figure 2.12: A sample trace of **Si4** showing the location of the switch as determined following our algorithm. The black dashed line denotes the switch position where we align the trace to zero-displacement in the 2D histogram.

**DFT analysis** We examined the effect of electrode displacement on molecular geometry in a DFT model system using Jaguar. In this model we attached single Au atoms to both sulfur atoms in **Si4** to simulate the bonding to Au electrodes and varied the Au-to-Au distance. In the STM-BJ experiment the two Au electrodes perform two distinct, albeit

closely related functions: (1) they provide the electrical environment through which the current passes, and (2) they dictate the geometry of the included molecule. Our computational model describes both features. We first performed geometry optimizations to determine how the lowest energy conformation of the molecule changes on increasing the Au-Au distance. To model the influence that the Au electrodes have on the geometry of the molecule, we considered the  $[\text{Au-Si4-Au}]^{2+}$  model system (removing two electrons from the complex) to increase the Au—S bond strength and mimic binding to a slightly positive undercoordinated Au atom on an Au electrode.<sup>67</sup> Model calculations on the free trimethyl(methylsulfanylmethyl)silane ( $\text{Me-S-CH}_2\text{-SiMe}_3$ ) molecule demonstrated two isoenergetic local minima at  $90^\circ$  and  $270^\circ$  (ortho) and a global minimum at  $180^\circ$  (anti), as expected from simple stereoelectronic considerations (Figure 2.13). We therefore

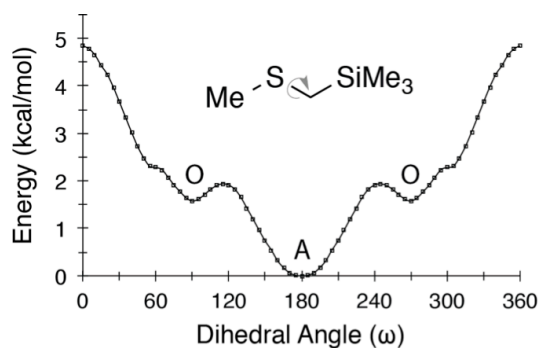


Figure 2.13: Energy plot for tetramethylsilylmethylsulfide  $\text{H}_3\text{C-S-CH}_2\text{-SiMe}_3$ . We find a global minimum (A) at  $\omega=180^\circ$  and two local minima (O) at  $\omega=90^\circ$  and  $270^\circ$ . These geometries were calculated in  $5^\circ$  increments at the B3LYP/6-31G\*\* level.

set both dihedral angles to anti in our starting geometry, optimized the  $[\text{Au-Si4-Au}]^{2+}$  complex without constraint and defined the resulting Au-Au distance as the elongation = 0 point (Figure 2.14b,c). We then performed a series of calculations to understand the response of the **Si4** bridge to changes in the Au-Au gap. To obtain the lowest energy

structure at each Au-Au distance, we varied the (fixed) Au-Au distance in 0.25 Å increments while allowing the rest of the molecule to optimize its geometry without additional constraints. These geometry optimizations confirm that the terminal dihedral orientation depends strongly on the distance between the Au atoms (that is, the size of the inter-electrode gap). Just as in the free Me—S—CH<sub>2</sub>—SiMe<sub>3</sub> molecule, there are two distinct anti and ortho Me—S—CH<sub>2</sub>—SiMe<sub>2</sub>- dihedral geometries in our Au-**Si4**-Au model. The anti (A) geometry places the Me-S bond antiperiplanar (Au-S bond is perpendicular) to the CH<sub>2</sub>—SiMe<sub>2</sub> bond; the ortho (O) geometry places the Me-S bond perpendicular (Au-S bond is antiperiplanar) to the CH<sub>2</sub>—SiMe<sub>2</sub> bond (Figure 2.14a). The results of our geometry optimizations suggest that there are two competing sources of strain: steric strain from the S—CH<sub>2</sub> σ-bond stereochemistry and mechanical strain from electrode separation. Steric strain favors the anti geometry because it minimizes steric repulsion between the bulky S-methyl and SiMe<sub>2</sub> groups. Mechanical strain pulls the S—Au bond into an antiperiplanar position to adopt the longest possible molecular geometry, and thereby forces the S-methyl group into an ortho relationship with the SiMe<sub>2</sub> group. As the mechanical strain starts to eclipse the steric strain, the two terminal Me—S—CH<sub>2</sub>—SiMe<sub>2</sub> dihedral angles in the lowest-energy Au-**Si4**-Au geometries change, as shown in Figure 2.14a, from A-A (purple) to O-A (yellow) to O-O (green).

The competing effect of steric versus mechanical strain on the molecular geometry is evident in Figure 2.14b. We fixed the terminal dihedrals to A-A, O-A and O-O to demonstrate how the relative energies of these three configurations change as a function of Au-Au distance. At short distances the steric strain has a stronger influence on molecular geometry: the A-A configuration is the lowest in energy and the energy difference

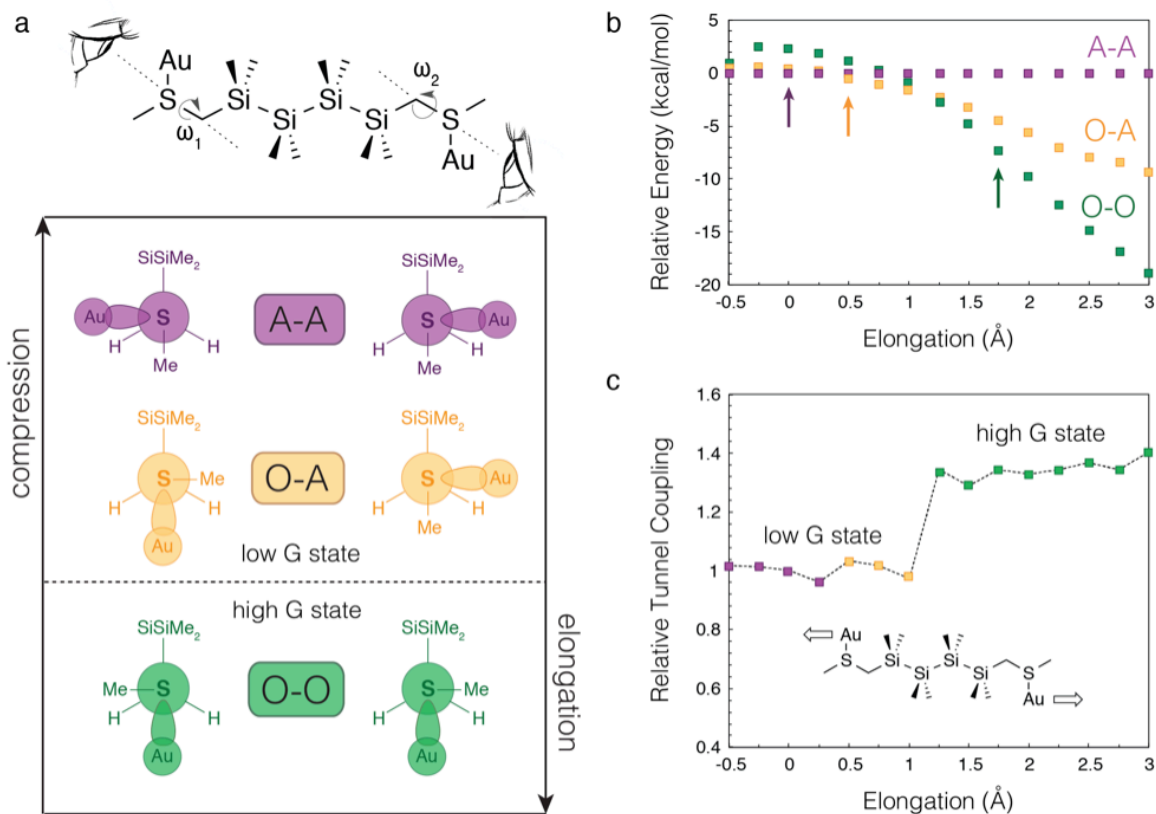


Figure 2.14: (a) Newman projections for the A-A (purple), O-A (yellow), and O-O (green) dihedral configurations from the perspective of the sulfur-methylene  $\sigma$ -bond in the Au-Si<sub>4</sub>-Au system. Junction elongation strains the molecule into the higher conducting O-O conformer. (b) The relative energies of the A-A, O-A, and O-O conformers in the  $[\text{Au-Si}_4\text{-Au}]^{2+}$  model system (B3LYP/LACVP\*\*) are obtained by subtracting the total energy of the A-A conformer at each particular Au-Au distance. The colored arrows denote the specific Au-Au distance where each configuration experiences its lowest total energy. (c) Tunnel coupling as a function of Au-Au distance plotted relative to tunnel coupling at the elongation = 0 point for the Au-Si<sub>4</sub>-Au model system (B3LYP/LACVP\*\*). Tunnel coupling calculations were performed on the lowest energy geometries that were optimized without dihedral constraint.

between each conformational state is relatively small. As the distance between the Au atoms increases and more mechanical strain is imposed on the molecule, the O-O configuration becomes the most energetically stable state and the energy differences between the three conformers become relatively large. To determine the trends in conductance for the lowest-energy structures that occur at each Au-Au distance, we calculated the energy

splitting between the frontier molecular orbitals of the neutral Au-molecule-Au complex. The frontier orbitals are predominantly of Au 6s and S lone-pair antibonding character and are tunnel-coupled through the molecular backbone, which results in a symmetric and antisymmetric pair with a splitting of  $2t$ , where  $t$  is defined as the tunnel coupling parameter.<sup>42</sup> The square of the tunnel coupling has been shown to be proportional to molecular conductance for many different systems.<sup>42,68,144–146</sup> We plot in Figure 2.14c the square of the tunnel coupling ( $4t^2$ ) for the Au-Si4-Au geometries relative to the elongation = 0 point. Conductance reflects the strength of coupling between the two gold electrodes through the molecule. We have shown previously that the Si—Si  $\sigma$ -bond framework provides the orbital through which the electron tunnels in an oligosilane.<sup>78</sup> Considering these two factors, one would predict a lower conductivity for the A-A and O-A configurations because the anti dihedral describes a S-Au bond that is perpendicular to the plane of the Si-Si bonds and therefore poorly coupled to the rest of the molecule. Conversely, one would predict higher conductivity for the O-O configuration because both S-Au bonds are aligned with the neighbouring C-Si bonds, and therefore the entire set of Si-Si bonds in the molecule.

This intuition rationalizes why the tunnel coupling remains constant as the minimum geometry transitions from A-A to O-A, but increases significantly as the molecule transitions from O-A to O-O (Figure 2.14c). In the O-O state, both Au atoms are finally aligned for coupling through the strong  $\sigma$  conjugation in the silane backbone. This interpretation implies that, even though there are three conformational states (A-A, O-A and O-O), we only observe a two-state conductance system because the A-A and O-A conformers have a similar tunnel coupling and are therefore indistinguishable in the junc-

tion. We applied the same DFT treatment to 1,6-bis(thiomethyl)hexane (**C6**) and found that the same conformational shift from A-A to O-A to O-O states occurred as we increased the Au-Au distance; however, the tunnel coupling remained constant because the poorly conjugated C-C  $\sigma$  bonds did not improve the coupling between the Au atoms in the O-O dihedral configuration (Figure 2.15). The experimental implication is that,

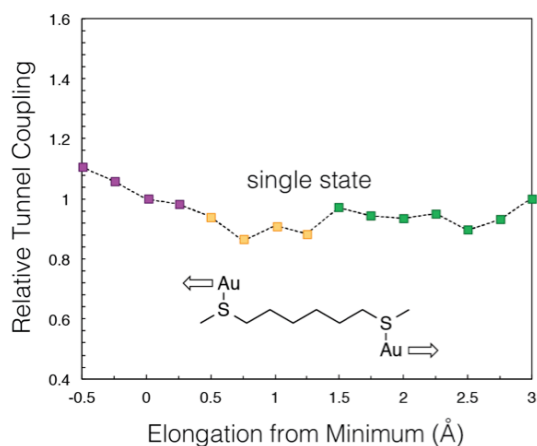


Figure 2.15: Tunnel coupling as a function of Au-Au distance plotted relative to the D=0 point for the Au-C6-Au model system. The dihedral configurations are labeled in A-A=purple, O-A=yellow, O-O=green.

even though this three-state conformational system exists in alkanes, we only observe a one-state electronic system because all three dihedral conformers are indistinguishable in conductance. The strong  $\sigma$  conjugation in the oligosilane backbone electronically couples the linker dihedrals that terminate each end of the molecule - we can therefore resolve the conductances of two different sets of rotational isomers that arise from the stereo-electronics of the sulfur-methylene  $\sigma$  bond and switch between them by stretching and compressing our molecular junction.

## Conclusion

The canons of  $\sigma$  stereoelectronics were developed to understand the relationship between conformation and electronics in aliphatic systems. However, the weak conjugation in C-C  $\sigma$  bonds diminishes the utility of stereoelectronics in controlling charge transport through aliphatic wires. In this study, we demonstrate that the strong conjugation in Si—Si  $\sigma$  bonds enables us to observe and exploit stereoelectronic effects in single-molecule junctions. The oligosilane switches developed here are the first in a new class of stereoelectronic device components; these switches function from the stereoelectronic properties of the sulfur—methylene  $\sigma$  bond. We can transpose the  $\sigma$ -stereoelectronic models originally devised for alkanes to silanes because they share a similar tetrahedral bonding geometry. We therefore envision that many more silicon-based electronic components inspired from the expansive  $\sigma$ -stereoelectronics literature will soon be realized.

## 2.2 Conductance Trend From Alkanes to Silanes to Germanes

### Preface

This section is based on the manuscript entitled *Single-Molecule Conductance in Atomically Precise Germanium Wires* by Timothy Su,<sup>†</sup> Haixing Li,<sup>†</sup> Vivian Zhang, Madhav Neupane, Arunabh Batra, Rebekka Klausen, Bharat Kumar, Michael Steigerwald, Latha Venkataraman, and Colin Nuckolls published in JACS (<sup>†</sup> indicates equal contribution).<sup>14</sup> Timothy Su, Vivian Zhang, and Madhav Neupane of Prof. Nuckolls' group synthesized and char-

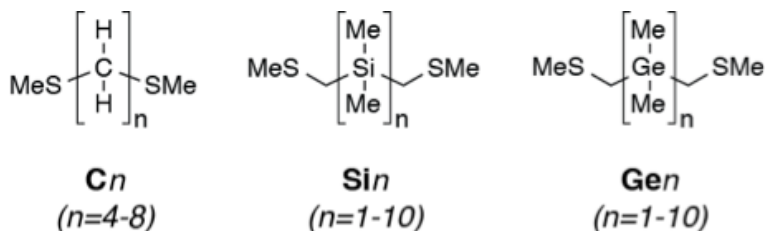
acterized all compounds. Timothy Su carried out theoretical calculations. I performed the conductance measurements and data analysis.

## **Abstract**

While the electrical conductivity of bulk-scale group 14 materials such as diamond carbon, silicon, and germanium is well understood, there is a gap in knowledge regarding the conductivity of these materials at the nano- and molecular-scale. Filling this gap is important because integrated circuits have shrunk so far that their active regions, which rely so heavily on silicon and germanium, begin to resemble ornate molecules rather than extended solids. Here we unveil a new approach for synthesizing atomically discrete wires of germanium and present the first conductance measurements of molecular germanium using a scanning tunneling microscope-based break-junction (STM-BJ) technique. Our findings show that germanium and silicon wires are nearly identical in conductivity at the molecular scale, and that both are much more conductive than aliphatic carbon. We demonstrate that the strong donor ability of C-Ge  $\sigma$ -bonds can be used to raise the energy of the anchor lone pair and increase conductance. Furthermore the oligogermane wires behave as conductance switches that function through stereoelectronic logic. These devices can be trained to operate with a higher switching factor by repeatedly compressing and elongating the molecular junction.

## Introduction

Here we describe both the first deterministic synthesis of long, linear permethyloligogermanes and the first conductance measurements on these atomically precise, single-molecule strands of germanium (Figure 2.16). An understanding of charge transport in atomically precise, molecular scale germanium will inform the transport issues and opportunities in ever-smaller silicon-germanium integrated circuits.<sup>147</sup> Moreover, nanoscale forms of germanium such as germanene,<sup>148,149</sup> germanium quantum dots,<sup>150</sup> and germanium nanowires,<sup>151-155</sup> are emerging as new materials with interesting electronic properties.



The synthesis that is developed here allows us to easily functionalize these germanium wires with aurophilic methylthiomethyl groups on their termini to allow connection to gold electrodes. Using the scanning tunneling microscope-based break-junction (STM-BJ) method, we find that each  $\text{Ge}_n$  oligomer is more conductive than its  $\text{Si}_n$  isostructure due to the enhanced interaction in the contact group between the sulfur lone pair and the more strongly donating C-Ge  $\sigma$ -bond. However, adding an additional Ge-Ge  $\sigma$ -bond in the germanium wires has essentially the same effect on the magnitude of conductance as adding an additional Si-Si  $\sigma$ -bond in silicon wires. The Au- $\text{Ge}_n$ -Au junction switches to a high conductance (G) state only when both terminal Me-S-CH<sub>2</sub>-GeMe<sub>2</sub>- dihedral angles are twisted into ortho configurations, suggesting a possible route to an “AND” logic gate

that operates by means of a stereoelectronic effect. Furthermore, we find that the repeated compression and elongation of the Au-Ge<sub>n</sub>-Au junction causes the device to switch with a higher conductive magnitude with each successive cycle; these cycles effectively mold the electrodes into an optimal morphology for mechanically manipulating the geometry of the molecule in the junction.

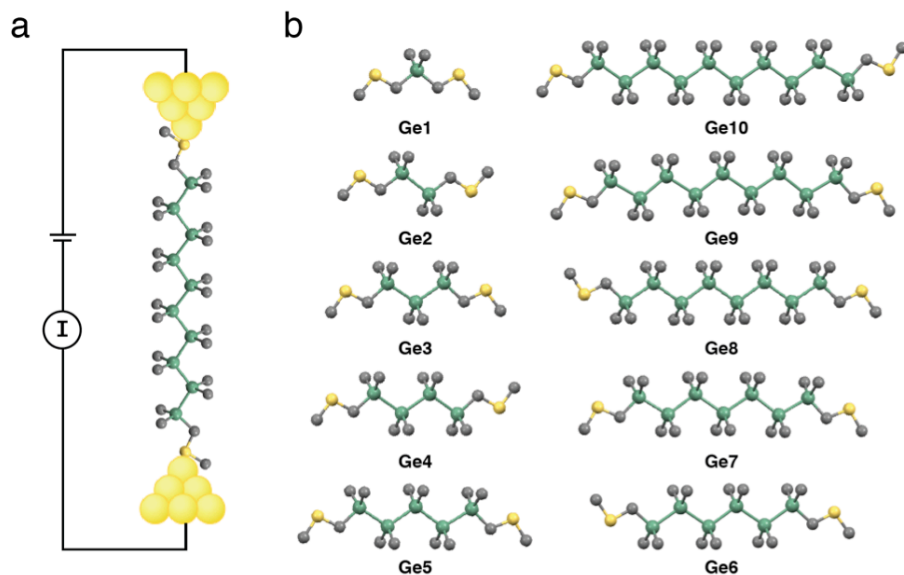


Figure 2.16: (a) STM-BJ experimental diagram of Au-Ge<sub>10</sub>-Au junction. (b) DFT-optimized structures for the Ge<sub>1</sub>-Ge<sub>10</sub> series with backbone dihedrals held at 180°. Ge, green; C, gray; S, yellow; H omitted to clarify the view.

## Results and Discussion

**Synthesis** In order to study the conductance properties of molecular germanium, we needed to develop a new synthesis that was robust and produced linear-chain oligogermane wires in a stepwise fashion. Though germanium oligomers have been known since 1925,<sup>156</sup> methods for the facile synthesis and isolation of long ( $n > 6$ ) linear oligogermanes have not been reported.<sup>157-159</sup> Wurtz coupling between Me<sub>3</sub>GeCl and Me<sub>2</sub>GeCl<sub>2</sub> has been

used to synthesize long oligogermanes ( $\leq \text{Ge}_{10}\text{Me}_{22}$ ), but these reactions give low yielding mixtures that are difficult to separate and products that are not functionalized.<sup>160</sup>

Here we introduce a new method for synthesizing an entire series of permethyloligogermanes (from  $n = 1-10$ ) that are terminated with methylthiomethyl contacts in high yields with easy purification. Our approach was inspired by the iterative synthesis of  $\alpha,\omega$ -diphenylpermethyloligogermanes ( $\text{Ph}-[\text{GeMe}_2]_n-\text{Ph}$ ) for  $n=1-5$  pioneered by Kumada and coworkers.<sup>161</sup> They observed low yields for this reaction due to the tendency of Ge-Ge bonds to disproportionate in the presence of strong nucleophiles such as dimethylphenylgermyl lithium. We were able to prevent oligogermane disproportionation by attenuating the strength of the nucleophile via transmetalation with  $\text{MgBr}_2$ , thereby accessing high yields (62-87%) of the longer oligomers. This simple adaptation has enabled us to achieve the first deterministic synthesis of germanium oligomers with  $n > 6$ . Using this new approach we have synthesized the longest linear oligogermane ( $\text{Ge}_{11}\text{Me}_{22}\text{Ph}_2$ ) reported to date.

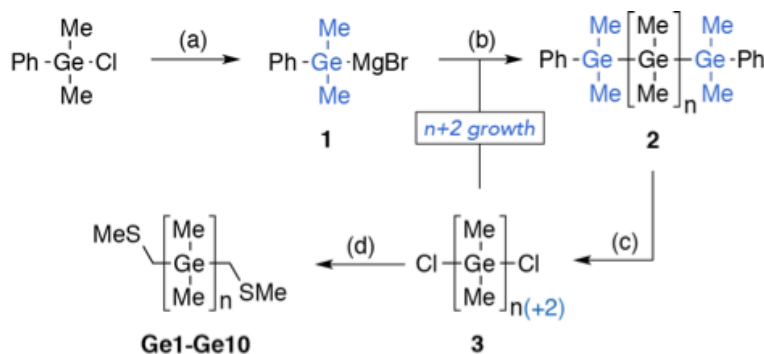


Figure 2.17: Iterative synthesis of permethyloligogermanes terminated with methylthiomethyl end groups. The  $n+2$  oligomer growth cycle is depicted in blue. (a) i. Li, THF. ii.  $\text{MgBr}_2$ , THF. (b) THF, 0 °C. For  $n = 3-10$  yields are 62-87%. (c) i.  $\text{CF}_3\text{SO}_3\text{H}$ ,  $\text{CH}_2\text{Cl}_2$ . ii.  $\text{Et}_3\text{N}\cdot\text{HCl}$ ,  $\text{Et}_2\text{O}$ . For  $n = 3-10$  yields are 65 - 94%. (d)  $n\text{-BuLi}$ , TMEDA,  $\text{CH}_3\text{SCH}_3$ , THF. For  $n = 1-10$  yields are 40 - 84%.

Figure 2.17 illustrates our iterative approach to synthesizing the  $[\text{GeMe}_2]_n$  oligogermanes ( $n = 1-10$ ) terminated by electrode-binding methylthiomethyl endgroups (**Ge1-Ge10**, Figure 2.16). We reduce chlorodimethylphenylgermane with lithium metal<sup>161</sup> and then transmetalate with  $\text{MgBr}_2$  to access dimethylphenylgermylmagnesium bromide **1**. We grow  $\alpha,\omega$ -diphenyloligogermane **2** outwards, two germanium subunits at a time, by treating  $\alpha,\omega$ -dichlorooligogermane **3** with two equivalents of **1**. After purification of **2**, protiodegermylation of  $\alpha,\omega$ -diphenyloligogermane **2** under acidic conditions furnishes the chain-extended  $\alpha,\omega$ -dichlorooligogermane **3**.<sup>125</sup> We functionalize  $\alpha,\omega$ -dichlorooligogermane **3** with electrode contacts ( $\text{CH}_2\text{SMe}$ ) by reacting **3** with methylthiomethyl lithium<sup>162</sup> to furnish the final  $\alpha,\omega$ -bis(methylthiomethyl)oligogermanes **Ge1-Ge10**.

**Conductance Measurements** We measured the single molecule conductance of oligogermanes **Ge1-10** with a scanning tunneling microscope-based break-junction (STM-BJ) technique.<sup>8</sup> In brief,  $\text{Au-Ge}_n\text{-Au}$  junctions are formed by repeatedly breaking and forming point contacts between Au tip and substrate electrodes in a dilute (0.10-1.00 mM) solution of the oligogermane in 1,2,4-trichlorobenzene under ambient conditions. After the Au-Au point contact is broken, the aurophilic thiomethyl groups<sup>67</sup> on the oligogermane bind the electrodes to form a  $\text{Au-Ge}_n\text{-Au}$  junction. Conductance is measured across the gap as a function of tip-substrate displacement, and the resulting traces reveal molecule-dependent plateaus signifying junction formation with conductance values below  $G_0$  ( $2e^2/h$ ), the quantum of conductance describing a single Au-Au atomic contact.<sup>127</sup> The junction breaks once the distance between the electrodes becomes too large for the molecule to bridge this gap. We form and break thousands of molecular junc-

tions and analyze all measured traces using logarithm-binned one-dimensional (1D) and two-dimensional (2D) histograms. 1D histograms provide a distribution of all measured conductance values from all traces; 2D histograms sum all conductance values while retaining relative displacement information.<sup>163</sup>

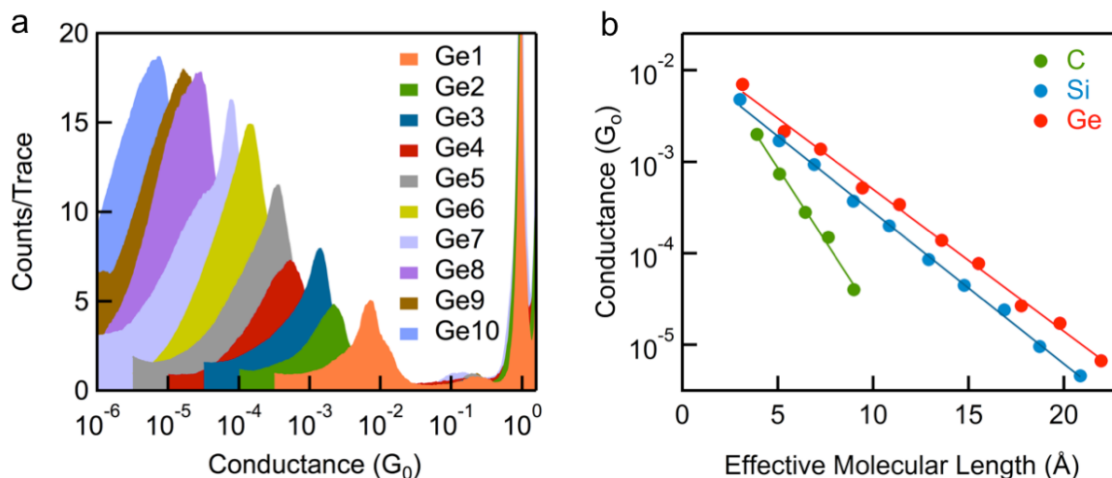


Figure 2.18: (a) Logarithm-binned 1D conductance histograms of **Ge1-Ge10**, each comprising thousands of measurement traces. (b) Conductance peak positions from the simple elongation measurements of **C4-C8**; **Si1-Si10**; **Ge1-10** (Figure a) plotted against effective molecular length ( $L$ , in Å) give the decay constant  $\beta$ .  $\beta_C = 0.74 \pm 0.03 \text{ \AA}^{-1}$ ,  $\beta_{Si} = 0.39 \pm 0.01 \text{ \AA}^{-1}$ ,  $\beta_{Ge} = 0.36 \pm 0.01 \text{ \AA}^{-1}$ .

The 1D histograms for the conductance measurements of **Ge1-Ge10** are shown in Figure 2.18a. The peak positions demonstrate a clear exponential decrease in conductance as the molecular length increases from  $n = 1$ -10. We obtain  $\beta$  for the  $Ge_n$  series in Figure 2.18b by plotting the conductance peaks from Figure 2.18a against the effective molecular length ( $L$ ) on a semi-log plot and fitting a line through these points, with  $G = R^{-1}e^{-\beta L}$ . For every molecule described here,  $L$  is defined as the distance between the two distal methylene carbons in the density functional theory (DFT) optimized structures,  $R$  is an effective contact resistance, and  $\beta$  is the conductance decay parameter.  $\beta$  describes the extent to

which conductance in a given oligomeric material decreases as the number of repeat units increases, and depends strongly on the extent of electronic delocalization (conjugation) in the backbone. We find that conductances from **Ge1-Ge10** follow an exponential in  $L$  with  $\beta_{Ge} = 0.36 \pm 0.01 \text{ \AA}^{-1}$  ( $0.74 \pm 0.02 n^{-1}$ ). This signifies that charge transport in molecular germanium (up to **Ge10**) occurs through a coherent tunneling mechanism.<sup>131</sup> Figure 2.19 plots the conductances of all molecules against  $n$ .

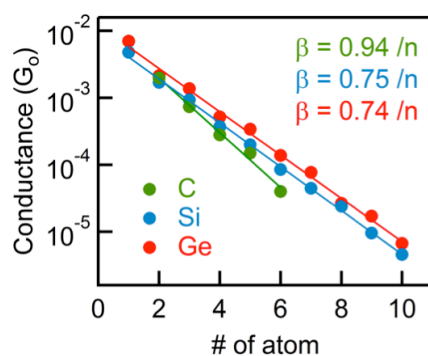


Figure 2.19: Conductance peak positions for measurements with **C4-C8**; **Si1-Si10**; **Ge1-10** plotted against the number ( $n$ ) of atoms in the backbone chain between the distal methylene units. Based on how we defined the nomenclature of **C4-C8**,  $n=2$  for **C4** and  $n=6$  for **C8**.  $\beta_C = 0.94 \pm 0.05 n^{-1}$ ,  $\beta_{Si} = 0.75 \pm 0.01 n^{-1}$ ,  $\beta_{Ge} = 0.74 \pm 0.02 n^{-1}$ .

We find that the decay constant of oligogermanes is very similar to that of oligosilanes ( $\beta_{Si} = 0.39 \pm 0.01 \text{ \AA}^{-1}$ ,  $0.75 \pm 0.01 n^{-1}$ ) and oligoparaphenylenes<sup>146</sup> while much shallower than that of alkanes ( $\beta_C = 0.74 \pm 0.03 \text{ \AA}^{-1}$ ,  $0.94 \pm 0.05 n^{-1}$ ). Our experimental findings are consistent with calculations of Matsuura on permethylated  $n=2-6$  oligomers of carbon, silicon, and germanium with  $-\text{CH}_2\text{SH}$  linker endgroups.<sup>164</sup> Matsuura calculated  $\beta_C=0.71 \text{ \AA}^{-1}$  for alkanes,  $\beta_{Si}=0.31 \text{ \AA}^{-1}$  for oligosilanes, and  $\beta_{Ge}=0.34 \text{ \AA}^{-1}$  for oligogermanes. The  $\beta$  values determined from these computations are remarkably close to what we observe experimentally.

Because the repeat units in the alkane, silane, and germane oligomers are single atomic units,  $\beta$  can serve as an index for comparing the intrinsic electrical  $\sigma$ -conductivity of the group 14 elements at the single-bond level. The near-identical  $\beta$  values for silanes and germanes suggest that Si-Si and Ge-Ge  $\sigma$ -bonds are similar in charge transport ability at the molecular scale, and that both are much more conductive than C-C  $\sigma$ -bonds. This is perhaps not surprising based on the relationship between conductance and conjugation or electronic delocalization through the molecule.<sup>146</sup> Alkanes demonstrate a high  $\beta$  value because of the weak delocalization in the C-C  $\sigma$ -backbone.<sup>129</sup> We previously established that the shallow  $\beta$  value<sup>12,78</sup> observed for oligosilanes is related to the strong conjugation in the Si-Si bonds, which are much larger and more strongly interacting compared to C-C  $\sigma$ -bond orbitals.<sup>165-169</sup> Since oligosilanes and oligogermanes are known to display similar degrees of  $\sigma$ -conjugation based on the spectroscopic and electrochemical studies of group 14 oligomers from the past several decades, it is not surprising that they also show near-identical  $\beta$  values here. Drenth and co-workers characterized the ultraviolet absorption in a series of peralkylated silicon and germanium oligomers ( $n = 2-6$ ).<sup>170</sup> By measuring the transition energy as a function of  $n$ , they elucidated the resonance stabilization energy between adjacent atoms and ultimately demonstrated that silane and germane oligomers share the same strength of conjugation between their  $\sigma$ -bonding orbitals. Boberski et al. and Okano et al. studied  $\sigma$ -conjugation by probing the electrochemical oxidation potentials of permethylated silicon and germanium oligomers.<sup>171,172</sup> The data from these two studies demonstrated that the first oxidation potential decreased by roughly the same extent in silanes and germanes with increasing  $n$ . We find the same to be true for the molecules studied here (Figure 2.19). Importantly, these single molecule measurements

demonstrate that the numerous studies devoted to understanding the nature of orbital interactions can serve as a predictive tool for designing molecular electronic components.

Though the  $\text{Ge}_n$  and  $\text{Si}_n$  series are near-identical in  $\beta$  value, the conductance of each germanium oligomer is  $\sim 1.5$  times higher than that of its silicon counterpart; this difference in conductance arises from subtle differences in the way  $\text{H}_2\text{C-GeMe}_2$  and  $\text{H}_2\text{C-SiMe}_2$   $\sigma$ -bonds interact with the S  $p\pi$  lone pair at each termini. C-Ge  $\sigma$ -bonds are more electron donating than C-Si  $\sigma$ -bonds because they are higher in energy and more diffuse.<sup>173-177</sup> The molecular orbital most relevant to conductance in these systems is the HOMO, which features strong S lone pair orbital character.<sup>10,12,178-180</sup> The destabilizing interaction between the filled S lone pair and the more strongly donating C-Ge  $\sigma$ -bond raises the HOMO energy closer toward the Au Fermi level, thereby increasing conductance.<sup>178,180,181</sup>

This line of reasoning is consistent with our DFT calculations of **Si1** and **Ge1**. **Ge1** (-5.49 eV) possesses a higher HOMO energy than **Si1** (-5.56 eV) in conformations where the S lone pair and C-Si(Ge)  $\sigma$ -bond are coplanar. Our calculations are supported by Glass et al., who demonstrated that the ionization energy of organosulfides is inversely proportional to the donor ability of the  $\sigma$ -bond in the  $\beta$ -position relative to the S atom.<sup>182</sup> We also find evidence for these destabilizing effects in our estimations of the HOMO energy from cyclic voltammetry studies on the  $\text{Si}_n$  and  $\text{Ge}_n$  series (Figure 2.20). As  $n$  increases, the HOMO energies in both  $\text{Ge}_n$  and  $\text{Si}_n$  rise with a similar slope but are offset by a roughly constant energy value. These results demonstrate that we can utilize the differential donor ability of  $\sigma$ -bonds to tune the energetics of the linker lone pair, and therefore, conductance. We also note that there is an appreciable odd-even effect on conductance that exists for the  $\text{Ge}_n$  series in Figure 2.18b, where the even-numbered oligomers fall below the decay line

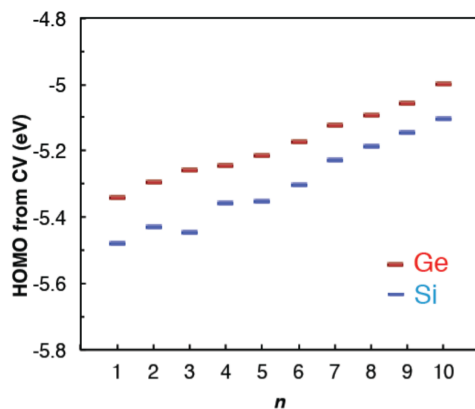


Figure 2.20: Cyclic voltammetry-derived HOMO levels (eV) for  $\text{Si}_n$ ,  $\text{Ge}_n$  series plotted against  $n$ . The HOMO energies are determined from the onset of the first oxidation by CV vs.  $\text{Fc}^+/\text{Fc}$  and the equation  $E_{HOMO} = -(4.80 \text{ V} + E_{onset}^{ox})$ .<sup>183</sup>

(error is within the size of the marker). The odd-even effect is also manifested in the peak shapes of the odd and even oligomers - the odd oligomers are much sharper in conductance width than the even ones (Figure 2.21). This alternate trend seems to occur in the  $\text{Si}_n$  series as well, although with a smaller magnitude. These odd-even effects may stem from the strong vicinal hyperconjugation in germanes, and are the subject of further study.<sup>184</sup>

**Stereoelectronic Switching** 2D histogram analysis (Figure 2.22, 2.23) and tunnel coupling calculations (Figure 2.24) suggest that each  $\text{Ge}_n$  oligomer acts as a mechanically-triggered switch that operates with a stereoelectronic mechanism analogous to what was previously described for **Si1-Si10** in chapter 2.1. In brief, elongating the  $\text{Au-Ge}_n\text{-Au}$  junction changes the lowest energy configuration of the two terminal  $\text{Me-S-CH}_2\text{-GeMe}_2$  dihedrals from the sterically favored anti (A) conformation to the mechanically favored ortho (O) conformation (Figure 2.25). The conductance-switching event likely embodies a shift in molecular geometry from the low conducting A-A and O-A configurations to

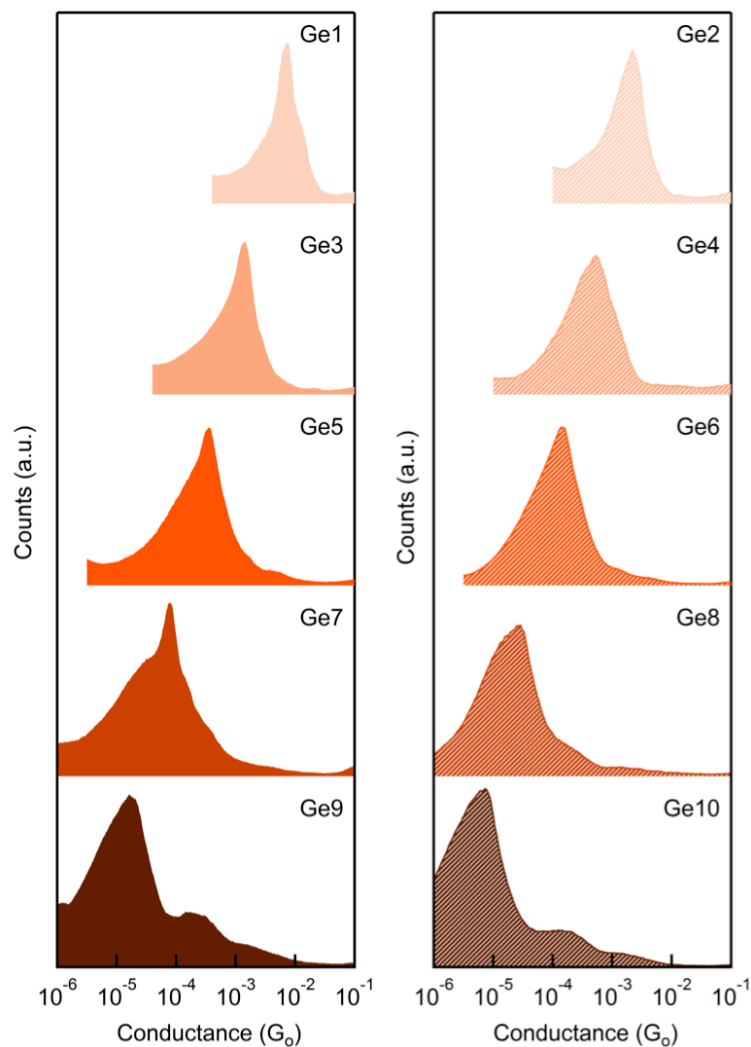


Figure 2.21: Log-binned 1D histograms of **Ge1-10** shown as comparison between odd (left) and even (right) series.

the high conducting O-O configuration. The conjugation in the  $Ge_n$   $\sigma$ -backbone should enable this mechanism of switching because it electronically couples the two terminal Me-S-CH<sub>2</sub>-GeMe<sub>2</sub>- dihedrals.

George et al. modeled the relationship between conformation and conductance in hydrogenated oligosilanes and found that conductance (and  $\sigma$ -conjugation) is maximized when the Si-Si-Si-Si dihedrals have an anti ( $\omega=180^\circ$ ) geometry.<sup>141</sup> Michl and coworkers<sup>140,185</sup> have demonstrated that permethyloligosilanes settle into transoid ( $\omega=160-$

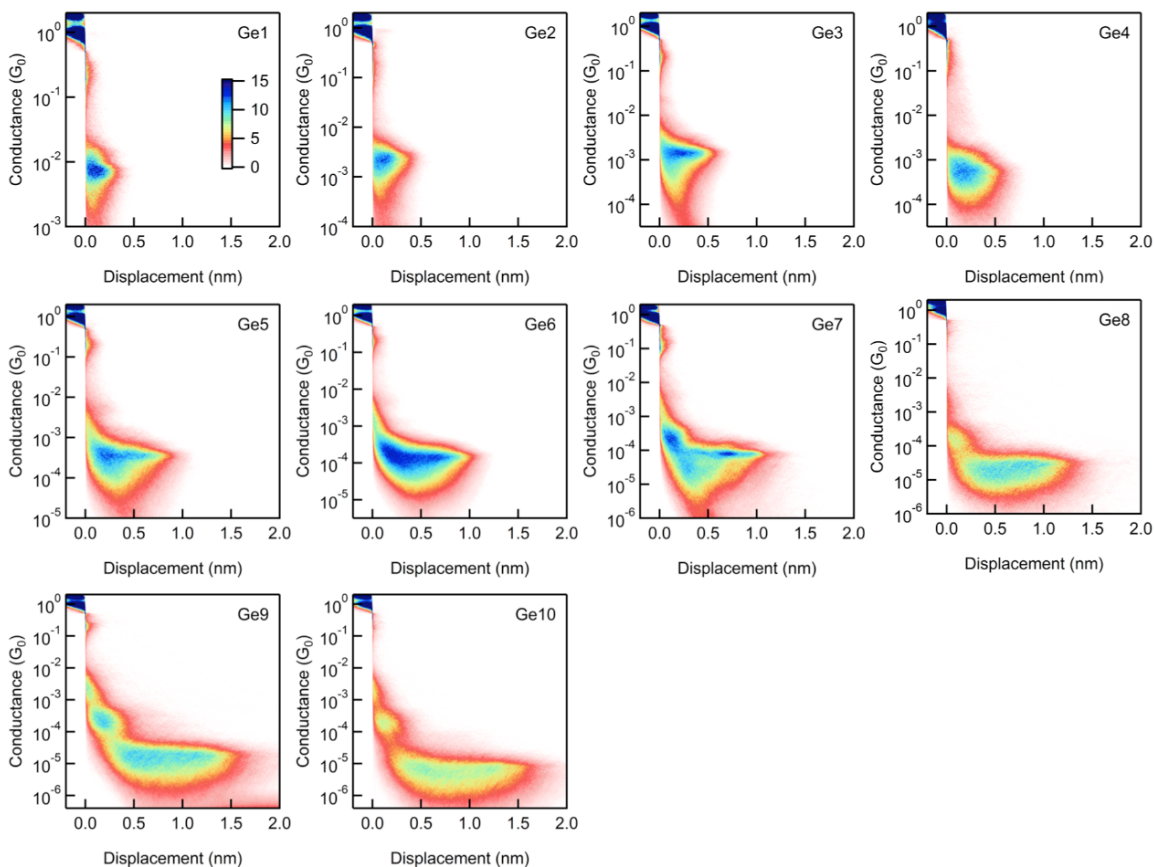


Figure 2.22: 2D histograms of conductance measurements for **Ge1-Ge10**. Histograms are created by aligning all traces to the displacement point where conductance crosses  $0.5G_0$ . The color bar indicates the number of counts per 1000 traces.

$175^\circ$ )<sup>142</sup> rather than anti minimum energy geometries due to steric effects from the methyl groups. We study permethylated oligosilanes and -germanes because they are much more stable than their hydrogenated structural analogues. In our previous calculations on the Au-**Si4**-Au system, we found that the internal Si-Si-Si-Si backbone geometry maintains a relatively constant dihedral angle that averages around  $\omega=168^\circ$ . Here we find that the Ge-Ge-Ge-Ge dihedral in the Au-**Ge4**-Au system remains relatively constant with an average of  $\omega=172^\circ$ . We hypothesize that the tetragermane dihedral is closer to anti than the tetrasilane because the Ge-Ge bonds (2.51 Å) are longer than the Si-Si bonds (2.38 Å), which would reduce the steric repulsion from the methyl groups. These results sug-

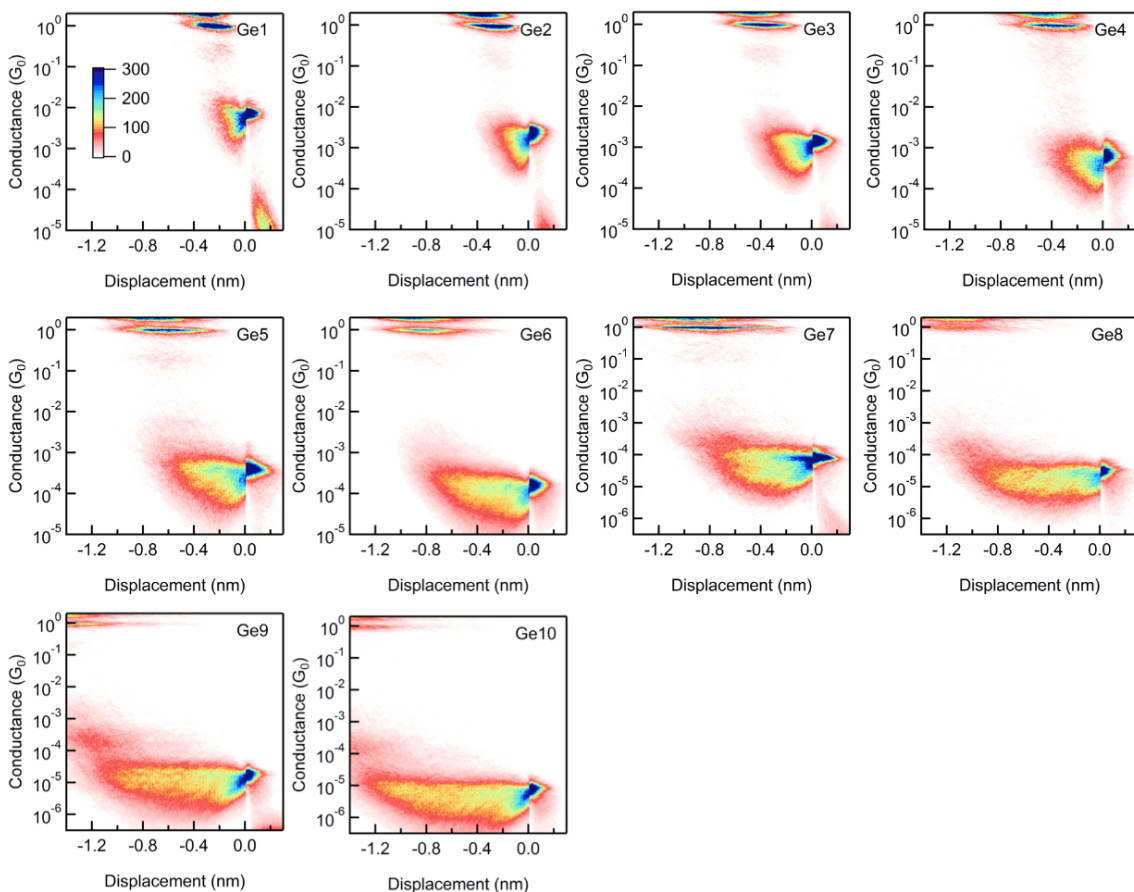


Figure 2.23: 2D histograms with displacement aligned to the switching event for **Ge1-10**. Histograms are made from the traces showing a low to high  $G$  switching event during the molecular junction elongation. The color bar indicates the number of counts per 1000 traces. The method for 2D histogram switching analysis is detailed in chapter 2.1. The consistent factor of 1.6 switching ratio (see Figure 2.27) and  $\sim 2$  Å high  $G$  displacement length indicate that the source of switching comes from a structural feature common to all germanes studied here. These results evidence that it is the terminal dihedral angles that account for switching, and not rotations to the internal Ge-Ge-Ge-Ge angles.

gest that the  $\sigma$ -conjugation in the oligogermane backbone is slightly stronger than in the oligosilane backbone, since the dihedral angles are closer to anti. This would account for the lower  $\beta$  value that we observe experimentally for the  $\text{Ge}_n$  series and the higher tunnel coupling ratio that we calculate for the high and low  $G$  states in oligogermanes versus oligosilanes (Figure 2.24). Following this line of reasoning, we predict that structurally constraining the  $\sigma$ -backbone to  $\omega=180^\circ$  in group 14 wires may enable even lower  $\beta$  values

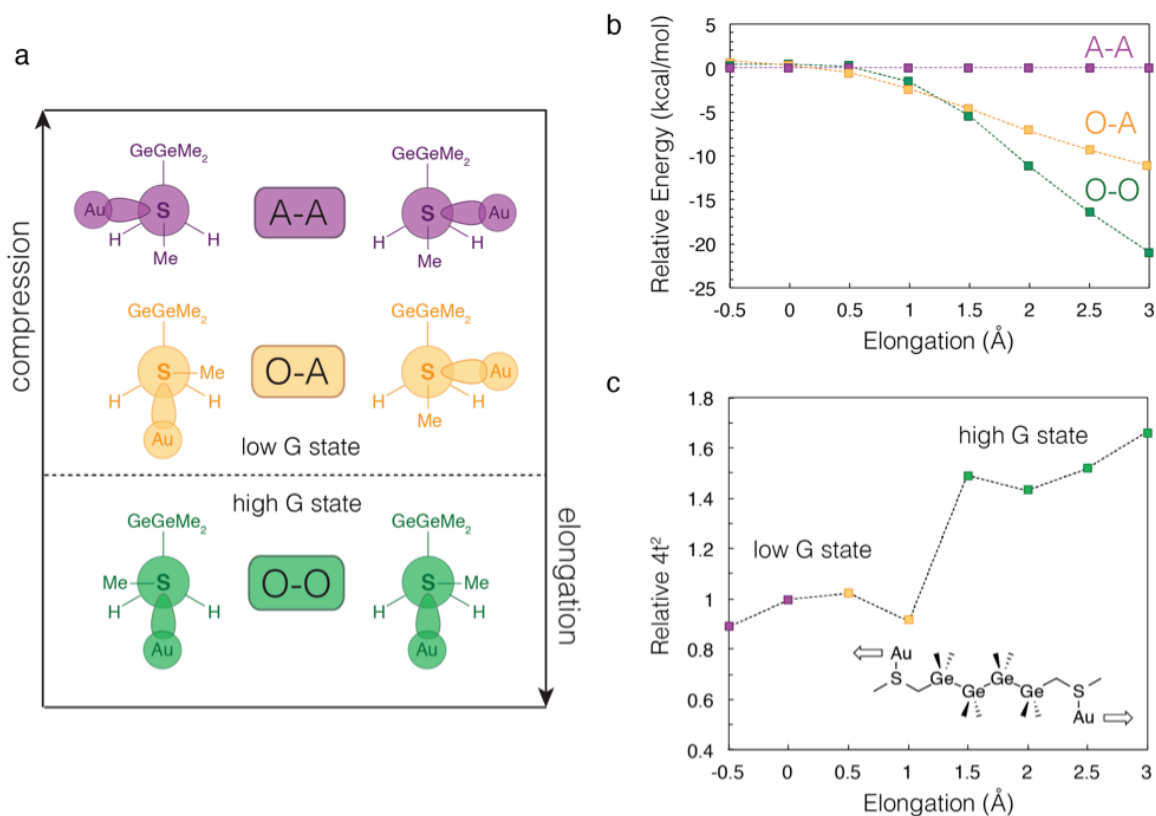


Figure 2.24: (a) Newman projections for the A-A (purple), O-A (yellow), and O-O (green) dihedral configurations from the perspective of the sulfur-methylene  $\sigma$ -bond in the Au-Ge<sub>4</sub>-Au system. (b) The relative energies of the A-A, O-A, and O-O conformers in the [Au-Ge<sub>4</sub>-Au]<sup>2+</sup> model system (B3LYP/LACVP\*\*) are obtained by subtracting the total energy of the A-A conformer at each particular Au-Au distance. (c) Tunnel coupling squared as a function of Au-Au distance plotted relative to  $4t^2$  at the elongation = 0 point for the Au-Ge<sub>4</sub>-Au model system (B3LYP/LACVP\*\*). Tunnel coupling calculations were performed on the lowest energy geometries optimized without Me-S-CH<sub>2</sub>-GeMe<sub>2</sub>- dihedral constraint.

and higher switching factors to be observed. Tamao and coworkers have synthesized such conformationally locked oligosilanes and have demonstrated increased  $\sigma$ -conjugation in the context of charge transfer<sup>124</sup> and absorption<sup>186</sup> studies.

Our tunnel coupling calculations also demonstrate that, in principle, the Ge<sub>n</sub> switches are capable of behaving as AND logic gates that follow the truth table in Figure 2.25 where the high G state is only observed under the condition that both terminal di-

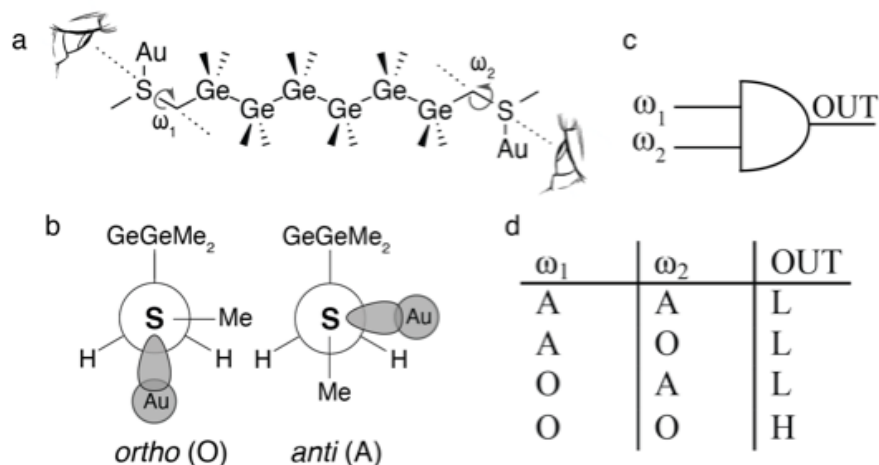


Figure 2.25: (a) Molecular structure of **Ge6** with two terminal Me-S-CH<sub>2</sub>-GeMe<sub>2</sub>- dihedrals  $\omega_1$  and  $\omega_2$ . (b) Newman projections of the mechanically favored ortho (left) and sterically favored anti (right) dihedral configurations. (c) Standard representation of an AND logic gate with  $\omega_1$  and  $\omega_2$  as inputs for stereoelectronic switching. (d) Truth table for observing either the low conducting (L) or high conducting (H) state based on tunnel coupling calculations.

hedral angles are in the ortho state. We have not yet experimentally realized such a logic device because we can only indirectly set the dihedral configuration by regulating the inter-electrode distance; developing a precise method for controlling each dihedral input independently will enable the creation of a true stereoelectronic logic device.

**Junction Training** In the simple elongation experiments described above, we continually widen the electrode gap until the molecular junction breaks. For all  $Ge_n$  oligomers, conductance switches from a low to high G state (Figure 2.26a) in the final 2 Å of elongation with a factor that varies slightly from molecule to molecule (Figure 2.23, 2.27). For instance, Au-**Ge5**-Au junctions demonstrate a switching factor (defined as the ratio of the conductance of the high G state to that of the low G state) of 1.6 upon the initial elongation (Figure 2.27). Here we demonstrate that we can increase the switching factor beyond this initial ratio by repeatedly compressing and elongating the molecular

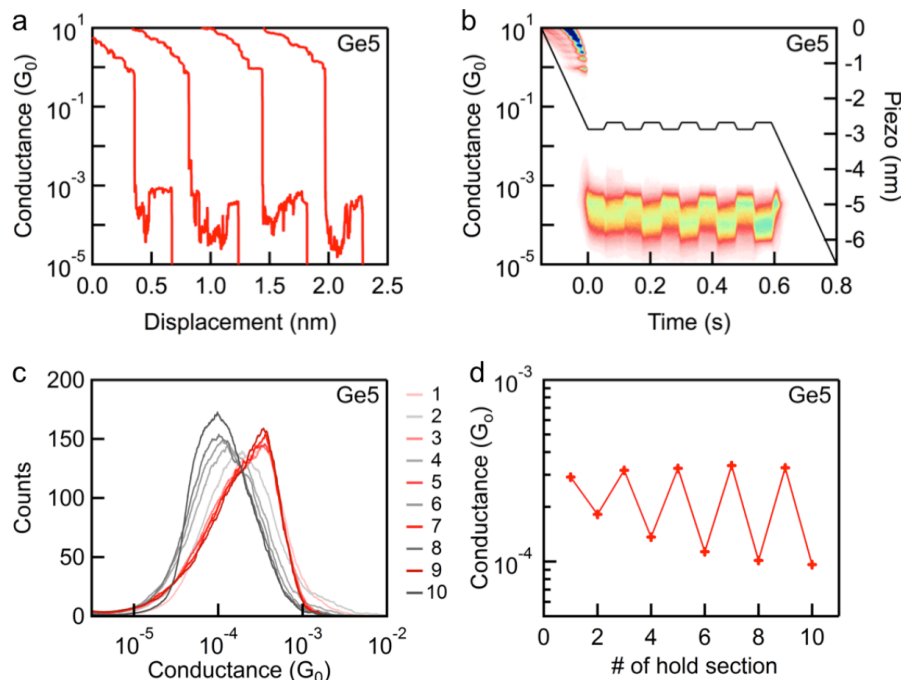


Figure 2.26: (a) Individual traces of **Ge5** demonstrate switching from low to high conductance as the molecular junction is elongated. (b) 2D histogram of five successive 2 Å compression-elongation cycles for the Au-**Ge5**-Au junction measured using a modified piezo ramp (black line). Switching is induced between low and high  $G$  states when the junction is pushed and pulled consecutively. The 2D histogram is constructed from all traces sustaining a junction over all ten hold sections. (c) 1D histograms compiled from each hold period after compressions (gray lines) and hold periods after elongations (red lines) from (b). (d) The conductance peak positions from the 1D histograms in (c) plotted against the hold section. The ratio of conductance between the compression (low  $G$ ) and elongation (high  $G$ ) peaks gives the switching factor for a single cycle. The switching factors upon compression from cycles 1-5 are 1.6, 2.3, 2.9, 3.3, and 3.4 respectively.

junction with a modified piezo ramp (Figure 2.26b). Instead of elongating the junction to rupture after we fully extend the Au- $\text{Ge}_n$ -Au junction, we perform push-pull cycles by first compressing the electrode gap by 2 Å, holding the electrodes fixed for 50 ms, widening the electrode gap by 2 Å, then holding for 50 ms. Figure 2.26b shows a 2D histogram describing five consecutive push-pull cycles for the Au-**Ge5**-Au junction. Figure 2.26c compiles the conductance measured during each hold section into 1D histograms; the resulting conductance peak values are plotted in Figure 2.26d. Figure 2.26d shows

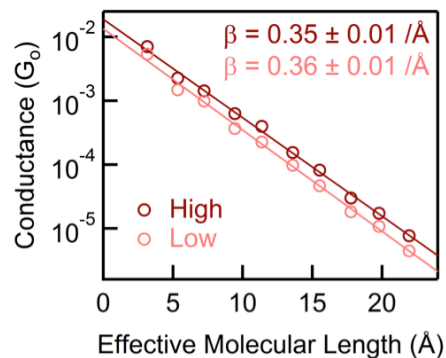


Figure 2.27: Conductance peak positions plotted from the low G (pre-switching) and high G (post switching) regions in Figure 2.23 against the DFT-optimized effective molecular lengths of **Ge1-Ge10**. Fitting a line through each set of peak values demonstrates that the low G and high G states decay with nearly the same  $\beta$  value, and are offset in conductance by a factor of 1.6.

that the first compression gives a switching factor of 1.6 and the final compression gives a switching factor of 3.4. Each successive push-pull cycle increases the switching factor and sharpness of switching, training the junction to perform increasingly better as a switch. We also find that the final switching factor for **Ge5** (3.4) is larger than for **Si6** (2.5) (Figure 2.28); this difference is likely related to the slightly stronger  $\sigma$ -conjugation in the germane backbone that we discussed in the subsection above.

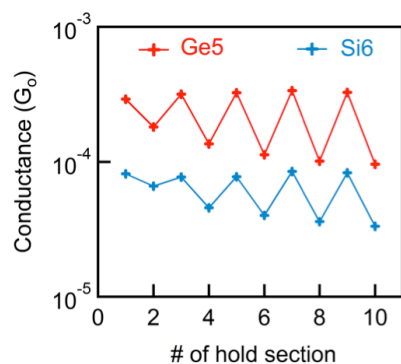


Figure 2.28: A comparison of junction training in **Ge5** vs. **Si6**. The conductance peak positions of **Si6** were determined with the same method described for **Ge5**. For **Ge5**, the switching factors upon compression from cycles 1-5 are 1.6, 2.3, 2.9, 3.3, and 3.4 respectively. For **Si6**, the switching factors upon compression from cycles 1-5 are 1.2, 1.7, 1.9, 2.4, and 2.5 respectively.

The conductance trends in Figure 2.26 demonstrate that this junction training effect arises from the decreasing conductance of the low G state. In each successive cycle, the elongation (high G) conductance peak value remains constant whereas the compression (low G) peak value decreases steadily (Figure 2.26d). Figure 2.26c reveals that in the first cycle, the compressed low G state is broad in conductance and features a significant amount of high G character. Every subsequent cycle narrows the conductance distribution by decreasing the amount of high G character in the compressed low G state; this in turn decreases the conductance of the low G peak and maximizes the switching factor with each additional cycle.

As we described in chapter 2.1, fully stretching the molecular junction imposes mechanical strain on the system. The data here suggests that for initial compression events, the system frequently relaxes by reorganizing the atomic electrode environment while sustaining the high conducting O-O junction geometry. Repeatedly stretching and compressing the junction likely shapes the malleable electrodes into a structure where electrode surface reorganization is no longer the dominant relaxation pathway; instead, the system compensates for the changing interelectrode distance by twisting the junction's terminal dihedrals into a shorter, less conductive geometry. These cycles mechanically anneal<sup>187</sup> the electrodes into an optimal morphology for stereoelectronic switching and enable the junction to distinguish molecular conformations with more clarity.

Trouwborst et al. previously reported a similar junction training technique to create reproducible Au-Au point contacts from disordered electrode environments.<sup>135</sup> In that study, the authors organized the tip atoms by performing consecutive 1-2 Å compression-elongation cycles near the point of contact between two Au atoms at cryogenic tempera-

tures, and in this way allowed the electrode atoms to probe different geometries and find the most stable configuration. It seems likely that we are organizing the electrodes here in much of the same way at room temperature, but are doing so with a molecular tether; this method might then serve as a valuable approach to organizing the atomic arrangement of the electrode surface in situations where direct contact between the electrodes is undesirable.

## Conclusion

In this study we developed a new method for synthesizing long (>2 nm) molecular germanium wires with atomic precision that utilizes the attenuated nucleophilicity of germylmagnesium species. To demonstrate the utility of this system, we performed the first single molecule conductance measurements on atomically defined molecular germanium wires. As in the silicon series, the germanium series behave as stereoelectronic switches activated by stretching or compressing our junction. Consecutive compression-elongation cycles train the molecular junction to both exhibit a higher switching factor and distinguish molecular geometries of disparate electronic character with more accuracy. Each  $\text{Ge}_n$  oligomer demonstrates a heightened conductance relative to its  $\text{Si}_n$  congener due to the stronger destabilizing interaction between the S lone pair and methylene-Ge  $\sigma$ -bond in the contact group. And yet, adding an extra Ge-Ge  $\sigma$ -bond to the  $\text{Ge}_n$  series has essentially the same effect on conductance magnitude as adding an extra Si-Si  $\sigma$ -bond to the  $\text{Si}_n$  series. More broadly, these results show that Si and Ge molecular wires possess essentially the same length-dependent conductivity due to the similar extent of  $\sigma$ -conjugation in these systems. The intrinsic electrical conductivity of bulk silicon is the

same order of magnitude as bulk germanium at room temperature, and both are many orders of magnitude more conductive than bulk diamond.<sup>188</sup> The periodic trends in molecular conductivity that we observe here therefore mirror group 14 conductivity trends in solid-state materials; this is not the case for stochastically-grown Si and Ge nanowires where reported conductivities vary by many orders of magnitude due to a number of extrinsic factors.<sup>152–155</sup> We envision that the atomic precision in the molecular wires here will enable their use as reliable platforms for studying effects such as strain and doping in electronic materials, to not only probe the fundamental nature of these effects in bulk systems but also to inform the design of next-generation electronic circuit materials.

## **2.3 Gold, Silver and Platinum as Electrical Contacts for Silanes**

### **Preface**

Timothy Su synthesized and characterized all compounds. Simon Henn conducted the measurements with Pt electrical contacts. I carried out the measurements with Ag and Au electrical contacts.

### **Abstract**

We study the conductance of thiol-terminated oligosilane single molecule junctions formed with Ag, Au and Pt metal electrodes. We measure the molecular junction conductance using the scanning tunneling microscope break junction technique and demonstrate

that thiol binds to all three metal contacts and enables the metal-Si<sub>n</sub>-metal junction formation. From measurements with a series of oligosilanes (Si<sub>n</sub>, n=6~9), we find that decay of the conductance with increasing molecular length is essentially the same for measurements with Ag and Au electrodes, and slightly larger for measurements with Pt electrodes. Moreover, the measured molecular conductance follows a trend  $G_{Ag} > G_{Au} > G_{Pt}$  at all junction lengths. Specifically the conductance of junctions formed with Ag electrodes are about 3~5 times that of junctions formed with Au and Pt electrodes, while conductance of the junctions formed with Au and Pt electrodes are similar. These results are in contrast to the trends in the metal work function  $\Phi(\text{Pt}) > \Phi(\text{Ag}) > \Phi(\text{Au})$  as we would expect a closer alignment of Fermi level of Pt to the highest occupied molecular orbital. These findings add to our understanding of the impact of metal contacts on the electron transport through metal-molecule-metal junctions.

## Introduction

Single molecule junctions have been most commonly formed with Au electrodes due to the malleability and chemical inertness of Au under ambient condition. Use of other metals as the electrical contacts in molecular electronics can offer new platforms for investigating the electrical characteristics of single molecule junctions. For instance, the high catalytic property of Ag and Pt can potentially enable in situ chemical reaction at the presence of organic molecules.<sup>189-192</sup> The density of states and optical properties of Ag and Pt, differing from Au, can open up new approaches in understanding the electron transport through molecular junctions under light illumination.<sup>193-196</sup> Although recent studies have shown that Ag,<sup>197-200</sup> Pt,<sup>201-203</sup> Cu,<sup>199,200</sup> and Pd<sup>201,204,205</sup> can be used as contacts to form

single molecule junctions, very few molecules have been shown to form stable junctions with these metals compared to Au, especially under ambient condition.

In this section, we present conductance measurements of a series of methylthiol-terminated permethyloligosilanes (**Si6-Si9**) attached to Ag, Au and Pt electrodes using the scanning tunneling microscope-based break junction (STM-BJ) technique. Thiols are known to form covalent links with Au electrodes,<sup>69</sup> and we demonstrate that thiol group is also able to bind to Ag and Pt electrodes likely by forming Ag—S and Pt—S covalent bonds.<sup>206</sup> We find that Pt-Si<sub>n</sub>-Pt junctions show the lowest conductance compared with Ag-Si<sub>n</sub>-Ag and Au-Si<sub>n</sub>-Au junctions. This result stands in contrast with previous theoretical studies<sup>206,207</sup> on benzene-dithiol and experimental studies<sup>201</sup> on alkane-dithiol, both of which show that the conductance of single molecule junctions formed with Pt electrodes is higher than that of the molecular junctions formed with other metal contacts such as Au or Ag. We further show that Ag-Si<sub>n</sub>-Ag junctions display higher conductance than Au-Si<sub>n</sub>-Au junctions. Again, this demonstrates a trend opposite to what has been previously observed in amine-linked alkanes and oligophenylenes.<sup>198</sup> We also note that the charge transport measurements on alkane-,<sup>180</sup> oligophenylene-,<sup>208</sup> and oligoacene-dithiol<sup>209</sup> monolayers formed with Au, Pt and Ag electrodes show the opposite trend as what we have observed here. Finally, we show that the molecular junctions formed with Pt electrodes show a slightly faster conductance decrease with increasing molecular length when compared with those formed with Au and Ag electrodes.

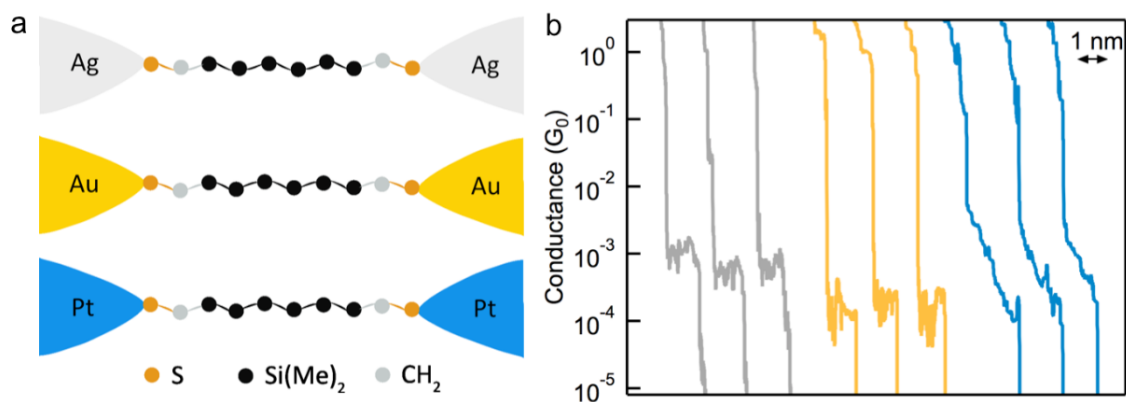


Figure 2.29: (a) Schematic of metal-**Si6**-metal junctions. (Metal = Ag, Au and Pt) (b) Sample conductance traces of **Si6** measured with Ag (grey), Au (yellow) and Pt (blue) electrical contacts.

## Results and Discussion

Molecules **Si2** - **Si4** and **Si6** - **Si9** are synthesized following the synthetic procedure described previously.<sup>13</sup> Conductance measurements were carried out by repeatedly breaking and forming Ag, Au and Pt point contacts in the presence of a solution of target molecules with STM-BJ technique.<sup>8,9</sup> The STM was operated under ambient condition at room temperature for Ag and Au measurements. For measurements with Pt, we additionally flushed the setup chamber with Argon for 10 minutes prior to the measurement. We use mechanically polished Ag and Pt slug (Alfa-Aesar, Ag: 99.99% purity, Pt: 99.9% purity) and Au-coated mica surface as the substrate, and the corresponding 0.25mm diameter metal wire as the tip (Alfa-Aesa, Ag: 99.9985% purity, Pt: 99.95% purity, Au: 99.998% purity).

Prior to adding the solution of molecules, we collect 1000 traces to make sure the metal is clean in the measurement with Au and Ag metal contacts. We polish and sonicate the Pt slug in acetone immediately before the measurement of molecules. In each

measurement, we start by bringing the tip into the substrate to create a metal point contact with a conductance higher than  $5G_0$  ( $G_0 = 2e^2/h = 77.6 \mu\text{S}$ ), then we retract the tip at a rate of  $19\text{nm/s}$  (except measurement with Pt is at  $38\text{nm/s}$ ) while measuring the current and the voltage of the junction. A molecule in the vicinity can bridge the gap between the tip and substrate once the metal point-contact breaks (Figure 2.29a), displaying a plateau in the conductance versus displacement trace. (Figure 2.29b) We repeat this measurement for thousands of junctions for each molecule studied in order to sample across a wide range of junction conformations and determine the statistically significant molecular conductance.

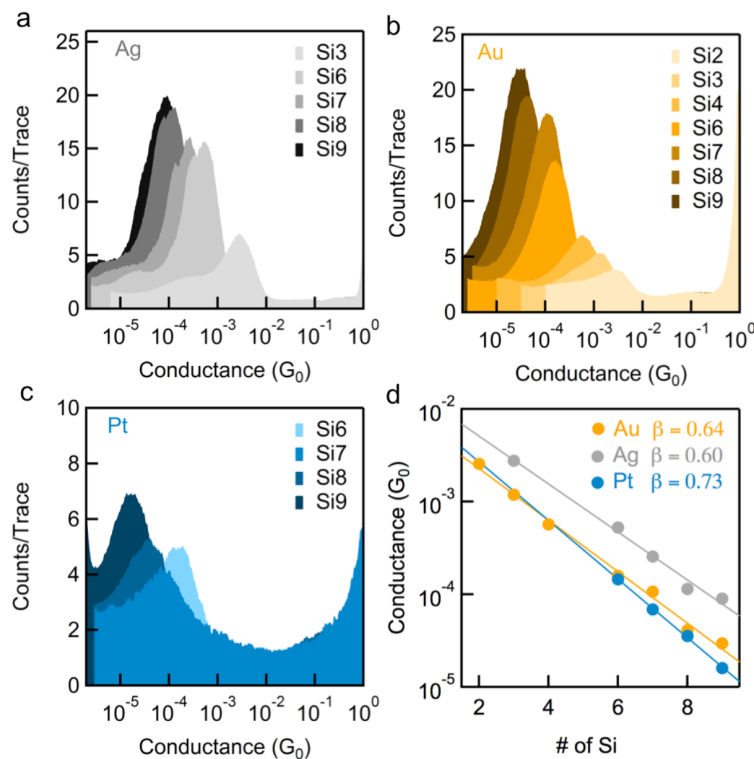


Figure 2.30: One-dimensional logarithmically-binned conductance histograms for junctions of silanes of varying length with (a) Ag, (b) Au, and (c) Pt electrodes. (d) Conductance peak values plotted against the number of silicon atoms in the backbone on a semi-log scale. Error is within the size of the marker. An exponential decrease in conductance with increasing silicon chain length is observed. Lines show linear fits to the data following  $G = G_c e^{-\beta n}$  and corresponding decay constants  $\beta$  are shown in the legend.

We collect 4000 - 20000 conductance traces for each molecular junction and compile them into normalized log-binned conductance histograms shown in Figure 2.30a - 2.30c. We generate conductance histograms for molecular junctions formed with Au and Pt electrodes without any data selection, and apply an automated algorithm to exclude the traces which show long oxygen contamination plateaus<sup>198,210</sup> between  $1 G_0$  and  $0.1 G_0$  before creating the histograms for junctions formed with Ag electrodes. We note that we do not observe conductance peak at  $1 G_0$  for the platinum metal-point contact in agreement with previous reports.<sup>203,211</sup> This has been explained by calculations which show that transport in Pt atomic contact, unlike the single fully open channel 6s for Au, has contributions from d bands.<sup>203,211</sup> Details about electron transport through Ag atomic contacts have been discussed previously.<sup>198,210</sup>

We have previously shown that thiol-terminated silanes bind to Au electrodes and show clear conductance peaks in log-binned histograms.<sup>13</sup> Here we observe similar conductance signatures for silanes using Ag and Pt electrodes (Figure 2.30a, 2.30c). This indicates that thiol anchoring groups enable junction formation of silicon backbone with Ag and Pt metal leads. By comparing the peak intensities in Figure 2.30a-2.30c, we find that Ag-Si<sub>n</sub>-Ag and Au-Si<sub>n</sub>-Au junctions show higher junction formation probability than Pt-Si<sub>n</sub>-Pt junctions.

We fit Gaussian functions to the conductance peaks in the histograms in Figure 2.30a-2.30c to determine the most probable conductance value for each silane bound to Ag/Au/Pt metal contacts. We plot the conductance value as a function of the number of silicon atoms in the backbone in Figure 2.30d. We first find that the junction conductance decreases exponentially as the molecular length increases, and the decay constant for Pt-Si<sub>n</sub>-Pt is about

20% higher than that for Au-Si<sub>n</sub>-Au and Ag-Si<sub>n</sub>-Ag. Comparing the conductance for each silane bound to three different metal contacts, we find that the conductance of molecular junctions formed with Ag electrodes is about three times that of junctions formed with Au electrodes. We also see that molecular junctions formed with Pt electrodes have the lowest conductance.

We note an odd-even effect in the conductance of Au-Si<sub>n</sub>-Au (n=6~9) junction (Figure 2.30d). The conductance of **Si7** and **Si9** junctions lie above the exponential decay line while that of **Si6** and **Si8** junctions lie below. We have observed this effect in the methylsulfide-terminated linear silanes and germanes single molecule junctions formed with Au electrodes.<sup>14</sup> However, we do not observe this odd-even effect in Ag-Si<sub>n</sub>-Ag or Pt-Si<sub>n</sub>-Pt junctions (Figure 2.30d). Therefore we propose that metal contact plays a role in this odd-even alternation, however, the underlying reason why this odd-even effect only appears in junctions formed with Au electrodes not Ag and Pt electrodes remains a topic for further investigation.

To further understand the origin of the different peak shapes in 1D conductance histograms between measurements with three metal contacts, we create 2D conductance-displacement histograms. These histograms, shown in Figure 2.31, are created by overlaying all measured conductance traces after aligning them along the displacement axis at a conductance of 0.5 G<sub>0</sub> (Au and Ag) or 0.01G<sub>0</sub> (Pt). The histogram is constructed using logarithmic bins along the conductance axis and linear bins along the displacement axis.

We first find that the Au-Si<sub>n</sub>-Au junctions show a sharp conductance drop from the 1G<sub>0</sub> plateau to the molecular junction plateau; the same is observed for selected Ag-Si<sub>n</sub>-Ag junctions that do not display oxygen plateaus above 0.1G<sub>0</sub> (zero displacement region in

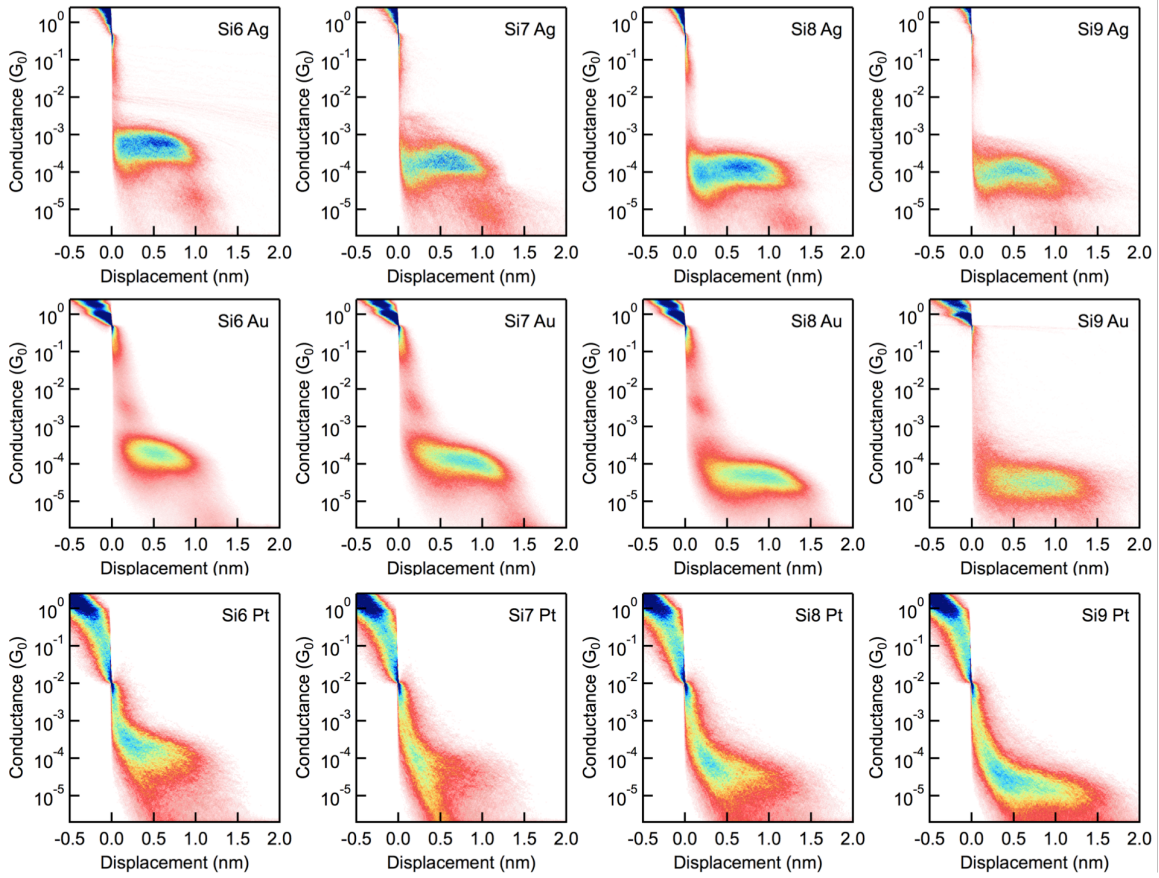


Figure 2.31: Two-dimensional (2D) conductance histograms for **Si6-Si9** measured with Au, Ag, and Pt electrical contacts.

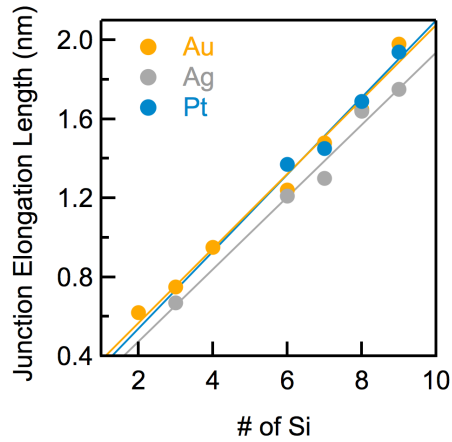


Figure 2.32: Junction elongation length plotted against the number of silicon atoms in the backbone for measurements with Ag (grey), Au (yellow) and Pt (blue) electrodes.

Figure 2.31). In contrast, majority of the Pt-Si<sub>n</sub>-Pt junctions show sloped conductance decrease from above 1G<sub>0</sub> to the molecular junction formation. Next we compare the molecular junction plateau lengths and shapes between measurements with the three metal contacts. We find that Au-Si<sub>n</sub>-Au and Ag-Si<sub>n</sub>-Ag junctions show similar conductance distribution at given displacement and both show a systematic increase in the junction elongation length with increasing molecular length. We determine the junction elongation length from the 2D histogram<sup>163</sup> and plot them as a function of the backbone length for measurements with Au, Ag, and Pt electrodes in Figure 2.32. Here a linear increase in the measured junction elongation length with the increasing backbone length is observed in measurements with all three metal contacts. For Pt-Si<sub>n</sub>-Pt junctions, the start of the conductance plateau is not well defined due to the lack of a sharp conductance drop following the metal contact rupture. Specifically, a very sloped feature at the beginning of the conductance plateaus for Pt-Si<sub>n</sub>-Pt junctions is observed for all molecular lengths. Nonetheless, we still observe a clear increase in junction elongation length with molecular backbone length indicating that we are indeed forming junctions that are terminally bound through a Pt—S bond (Figure fig:chapter2-3-4).

## Conclusion

We demonstrate that atomically precise silicon molecular wires terminated with methylthiol linkage groups can form single molecule junctions with Ag, Au and Pt electrodes. For each silane, the junction conductance is the highest when the molecule attaches to Ag electrodes and the lowest when the molecule attaches to Pt electrodes. This result is the opposite to what we would expect if we simply consider the work function of

the three metals (Ag(100): 4.64 eV; Au (100): 5.47 eV; Pt (100): 5.84 eV),<sup>212</sup> as we assume the coupling through the highest occupied molecular orbital (HOMO) of the molecule dominates the charge transport. Further theoretical investigation is needed to fully understand these experimental results.

*Single Molecule Conductance of Ring Silanes*

### **3.1 Cyclopentasilane: Conformations Control Conductance**

#### **Preface**

This section is based on the manuscript entitled *Conformations of Cyclopentasilane Stereoisomers Control Molecular Junction Conductance* by Haixing Li,<sup>†</sup> Marc Garner,<sup>†</sup> Zhichun Shangguan,<sup>†</sup> Qianwen Zheng, Timothy Su, Madhav Neupane, Panpan Li, Alexandra Velian, Michael Steigerwald, Shengxiong Xiao, Colin Nuckolls, Gemma Solomon and Latha Venkataraman published in *chemical science* (<sup>†</sup> indicates equal contribution).<sup>17</sup> Zhichun Shangguan and Qianwen Zheng of Prof. Xiao's group synthesized and characterized all compounds. Timothy Su, Madhav Neupane, and Alexandra Velian of Prof. Nuckolls' group and Panpan Li of Prof. Xiao's group assisted in compound characterization. Marc Garner of Prof. Solomon's group carried out theoretical calculations. I performed the conductance measurements and data analysis.

## Abstract

Here we examine the impact of ring conformation on the charge transport characteristics of cyclic pentasilane structures bound to gold electrodes in single molecule junctions. We investigate the conductance properties of alkylated cyclopentasilane cis and trans stereoisomers substituted in the 1,3-position with methylthiomethyl electrode binding groups using both the scanning tunneling microscope-based break junction technique and density functional theory based *ab initio* calculations. In contrast with the linear ones, these cyclic silanes yield lower conductance values; calculations reveal that the constrained dihedral geometries occurring within the ring are suboptimal for  $\sigma$ -orbital delocalization, and therefore, conductance. Theoretical calculations reproduce the measured conductance trends for both cis and trans isomers and find several distinct conformations that are likely to form stable molecular junctions at room temperature. Due to the weakened  $\sigma$ -conjugation in the molecule, through-space interactions are found to contribute significantly to the conductance. This manuscript details the vast conformational flexibility in cyclopentasilanes and the tremendous impact it has on controlling conductance.

## Introduction

Though silicon is the most prevalent semiconductor material in integrated circuits, its conductance has been scarcely studied at the molecular scale. With the dramatic scaling of silicon devices to the sub-20 nm length scale, it is becoming critical to probe transport properties of complex silicon-based nanoscale structures, such as silicon clusters, nanowires and silicene 2D layers.<sup>21,25,213,214</sup> Efforts in molecular electronics have demon-

strated the use of silicon surfaces as electrodes<sup>215–218</sup> and amino-silanes or the cleavage of trimethylsilyl as binding schemes to the electrodes.<sup>219–221</sup> Moreover, investigations on cyclohexasilane<sup>222</sup> and [2,2,2]bicyclic carbosilane systems<sup>223</sup> have shown that conformations affect the molecule's electronic structures and that different disilanylene bridges in the cage compounds do not act as parallel resistors. Recently we synthesized linear chains of molecular silicon that demonstrated conductance decay properties comparable to those of  $\pi$ -conjugated hydrocarbons.<sup>12,78</sup> While Si—Si  $\sigma$ -bonds are strongly conjugated, similar to C—C  $\pi$ -bonds, a fundamental difference between them is that the Si—Si  $\sigma$ -bond network is tetrahedral and not planar. This tetrahedrality enables oligosilane-based wires to access many more conformations, which opens up the possibility to harness  $\sigma$ -bond stereoelectronics to design functional molecular electronic components.<sup>12</sup>

Cyclic  $sp^3$   $\sigma$ -based structures can adopt many possible ring conformations as demonstrated by many years of synthetic<sup>224–226</sup> and theoretical studies,<sup>227–229</sup> however, charge transport measurements at a single molecule level on such systems are heretofore unexplored. Here we synthesize the cis and trans isomers of a cyclic pentasilane difunctionalized with aurophilic methyl sulfide groups (chemical structures shown in Figure 3.1) and measure their single-molecule junction conductance using scanning tunneling microscope-based break junction technique (STM-BJ).<sup>8,9</sup> We find that the cis and trans isomers are distinctly different in their conductance behavior. The cis isomer shows a double-peaked conductance histogram indicative of the formation of two structures. In contrast, the trans isomer shows a single-peaked conductance histogram at a conductance value lower than that of the cis. Through density functional theory (DFT) based *ab initio* calculations, we model junctions for a large number of conformers of both the

cis and trans isomers. Our calculations indicate that the constraint imposed on the internal ring dihedrals hinders  $\sigma$ -conjugation across the molecule, which contributes to the lower conductance value that we observe in these cyclic structures compared with linear oligosilanes of similar oligomer order. We find that the unique conductance profile of each isomer we observe experimentally relates to the different junction conformations accessible to each isomer and the structural differences between the two isomers.

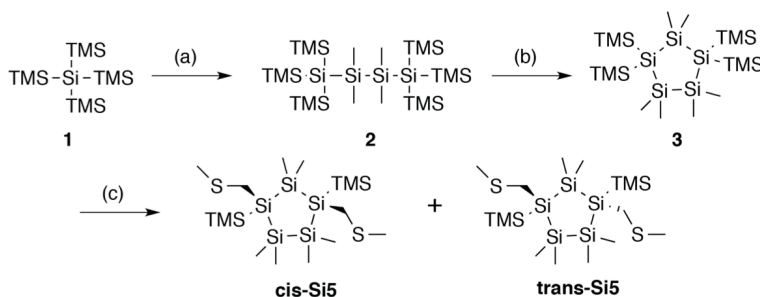


Figure 3.1: Synthesis of trans and cis cyclopentasilane terminated with methylthiomethyl end groups. (a) i.  $\text{KO}^t\text{Bu}$ , THF, r.t. ii.  $\text{ClSiMe}_2\text{-SiMe}_2\text{Cl}$ , toluene,  $-70^\circ\text{C}$  to r.t., 85% yield. (b) i.  $\text{KO}^t\text{Bu}$ , 18-crown-6, toluene, r.t. ii.  $\text{SiMe}_2\text{Cl}_2$ , toluene, r.t., 81% yield. (c) i.  $\text{KO}^t\text{Bu}$ , 18-crown-6, toluene, r.t. ii.  $\text{ClCH}_2\text{SMe}$ , toluene,  $-78^\circ\text{C}$  to r.t. 15% yield for **cis-Si5**, 10% yield for **trans-Si5**.

## Results and Discussion

We prepare the cis and trans isomers following the synthetic procedure shown in Figure 3.1. We quench the combination of tetrakis(trimethylsilyl)silane 1 and potassium tert-butoxide ( $\text{KO}^t\text{Bu}$ ),<sup>226</sup> with 1, 2-dichlorotetrahydrodisilane to yield oligosilane 2. Next, we cleave two TMS groups from 2 with  $\text{KO}^t\text{Bu}$  and 18-crown-6 and quench the dianion with dichlorodimethylsilane to produce cyclopentasilane 3.<sup>224,225</sup> We then functionalize cyclopentasilane 3 with electrode linking methylthiomethyl ( $\text{CH}_2\text{SMe}$ ) groups at the 1,3-positions by cleaving the terminal TMS groups with  $\text{KO}^t\text{Bu}$ /18-C-6 and adding the

chloromethyl methyl sulfide electrophile. We separate the two isomers by silica gel chromatography to yield the **cis-Si5** and **trans-Si5** molecules for this study. We were able to grow single crystals suitable for single crystal x-ray diffraction for **cis-Si5** from diethyl ether at -30°C.

The five-membered rings have two predominant conformations, envelope (C<sub>s</sub>) and twist (C<sub>2</sub>), with the nomenclature defined by the number of Si-atoms that lie in and out of the plane of the ring. The envelope conformer has four Si-atoms in plane and one above or below the plane of the ring. The twist conformer has three Si-atoms in plane, one above the plane, and one below the plane. As the cyclopentasilane is di-substituted, six unique conformations appear by rotating the position of the substituents relative to the ring conformation as illustrated in Figure 3.2. Five of these conformations are further divided in two classes as the linkers can be on either side of the plane of the ring, the exceptions being cis 2-twist and trans 2-envelope as the linker positions are symmetric.

We measure the single molecule junction conductance (current/voltage) of **cis-Si5** and **trans-Si5** using STM-BJ technique (schematic shown in Figure 3.2b) under ambient conditions.<sup>8,9</sup> We repeatedly form and break Au point contacts between an Au tip and an Au-on-mica substrate and measure conductance as a function of displacement. A single molecule junction is formed when the atomic contact is broken in a 1 mM solution of the target molecule in 1,2,4-trichlorobenzene. Each conductance-displacement measurement shows plateaus at a conductance close to integer multiples of the conductance quantum,  $G_0 = 2e^2/h$  and additional molecular plateaus below  $1 G_0$ . These plateaus below  $1 G_0$  signify that an Au-molecule-Au junction is formed after the metal contact breaks.

We repeat the measurements and collect thousands of traces to determine the most

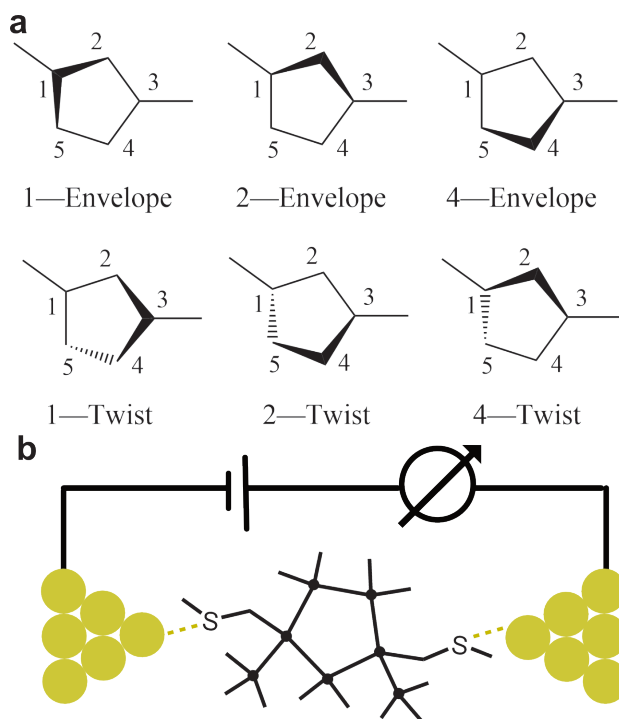


Figure 3.2: (a) Six generic conformer types of a di-substituted five membered ring. (b) A schematic of the scanning tunneling microscope break-junction (STM-BJ).

frequently measured conductance value for each molecule. We compile all measured conductance traces into logarithmically binned one-dimensional histograms<sup>128</sup> in Figure 3.3a. We find that the **trans-Si5** histogram shows a single conductance peak at  $\sim 1.6 \times 10^{-4} G_0$  while that of **cis-Si5** shows a higher conducting peak at  $6 \times 10^{-4} G_0$  and a lower conducting peak at  $2 \times 10^{-4} G_0$ . In Figure 3.3b and 3.3c, we overlay all measured conductance traces, aligning them along the displacement axis at  $0.5 G_0$  and generate two-dimensional conductance-displacement histograms to show the evolution of conductance as we elongate the junction.<sup>163</sup> We see that both **cis-Si5** and **trans-Si5** can form junctions that extend to roughly 6 Å beyond the rupture of the Au point-contact, although a majority of the junctions rupture after a  $\sim 2$ -3 Å elongation.

Our past work has shown that the displacement extent of the molecular plateau in a

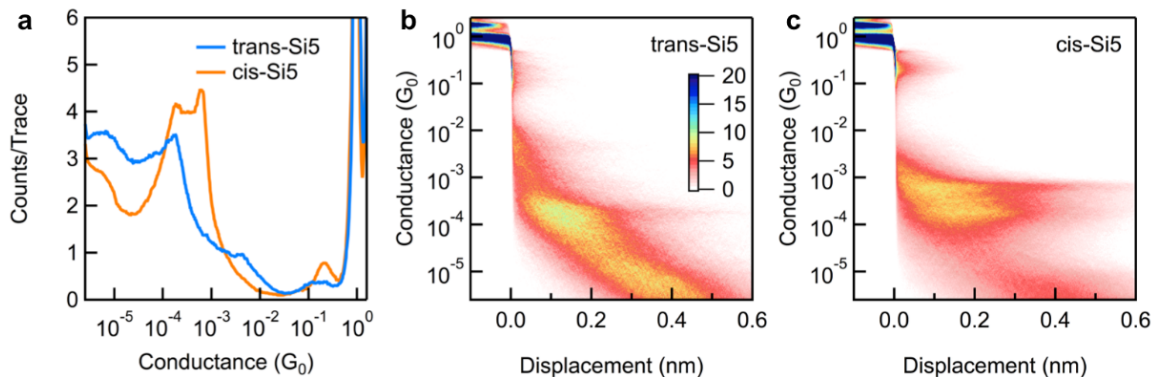


Figure 3.3: (a) Logarithmically binned one-dimensional conductance histogram of **cis-Si5** (orange) and **trans-Si5** (blue). Histograms are made without data selection and normalized by the total number of traces. (b) and (c) Two-dimensional conductance histograms of **trans-Si5** and **cis-Si5** respectively, made from the same data as in (a).

2D histogram is related to the molecular backbone length.<sup>163</sup> Since both the **cis-Si5** and **trans-Si5** show similar plateau lengths in their 2D histograms, we can conclude that the lower intensity observed for **trans-Si5** in the 1D histogram is a result of fewer junctions formed with this isomer. It has been shown computationally<sup>141,230,231</sup> and experimentally<sup>12</sup> that linear oligosilanes attain maximum elongation and conductance as they are near all-anti conformations where all backbone dihedral angles are 180°. Such anti conformations are not accessible in the cyclopentasilane molecules here because of the intrinsic dihedral constraints of tetrahedral bonds in the rings. We would therefore expect that conductance is lower in cyclic oligosilane pathways in contrast to their equivalent linear counterparts considering one of the two pathways can be completely suppressed due to unfavorable dihedrals. Two possible through-bond conduction pathways occur in the cyclopentasilane from one anchor group to the other: a trisilane and tetrasilane pathway. We compare the conductance properties of the cyclopentasilane molecules with the linear Si3 and Si4 oligosilane (Figure 3.4).<sup>12</sup> In contrast, we find that the higher conductance peak

value of **cis-Si5** is between that of **Si3** and **Si4** while the lower conductance peak value is lower than that of the **Si4**. This distinct double-peak conductance feature we observed for **cis-Si5** indicates that cyclopentasilanes are significantly different from linear silanes. To understand these phenomena further, we turn to *ab initio* calculations carried out using DFT to investigate both the conformers of each isomer that are likely to form junctions at room temperature and their computed conductance values.

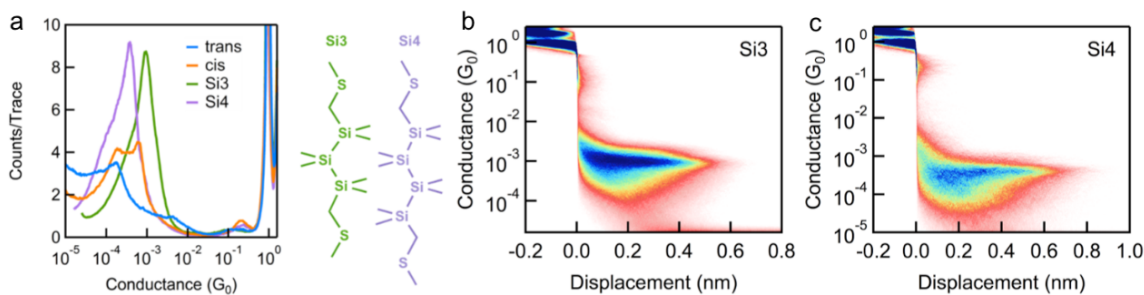


Figure 3.4: (a) Logarithmically binned 1D conductance histogram of **cis-Si5** (orange), **trans-Si5** (blue), **Si3** (green) and **Si4** (purple). Histograms are made without data selection and normalized by the total number of traces. (b) 2D conductance histograms of **Si3** and **Si4**. 2D histograms are created by overlaying all conductance traces after aligning them to zero-displacement at the point when the conductance crosses  $0.5G_0$ .

We examine the conductance behavior of a large number of conformers of **cis-Si5** and **trans-Si5** by calculating the transmission with a combined DFT and non-equilibrium Green's functions approach.<sup>232</sup> Our aim is to understand the impact of the molecular conformation on conductance; we do not intend to quantitatively compare DFT results with experiment due to errors inherent to DFT.<sup>233,234</sup> We create the full set of conformers for both **cis-Si5** and **trans-Si5** by varying the  $\text{Si}(\text{CH}_3)_2\text{—Si—CH}_2\text{—S}$  dihedrals around their threefold torsional axis while keeping the terminal  $\text{Si—CH}_2\text{—S—CH}_3$  dihedrals in anti-configuration ( $180^\circ$ ). This procedure yields 93 conformers each. We optimize the structures to a force threshold of  $0.02 \text{ eV/\AA}$  using DFT with the PBE exchange-correlation

functional<sup>96</sup> and double-zeta plus polarization basis sets as implemented in ASE<sup>235</sup> and GPAW.<sup>236,237</sup> After this process, we are left with 84 **cis-Si5** and 86 **trans-Si5** conformers in their local energy minima. We have not calculated the energy barriers between these conformers, but a previous report shows the energy barriers are quite low for a simpler unsubstituted cyclopentasilane.<sup>228</sup>

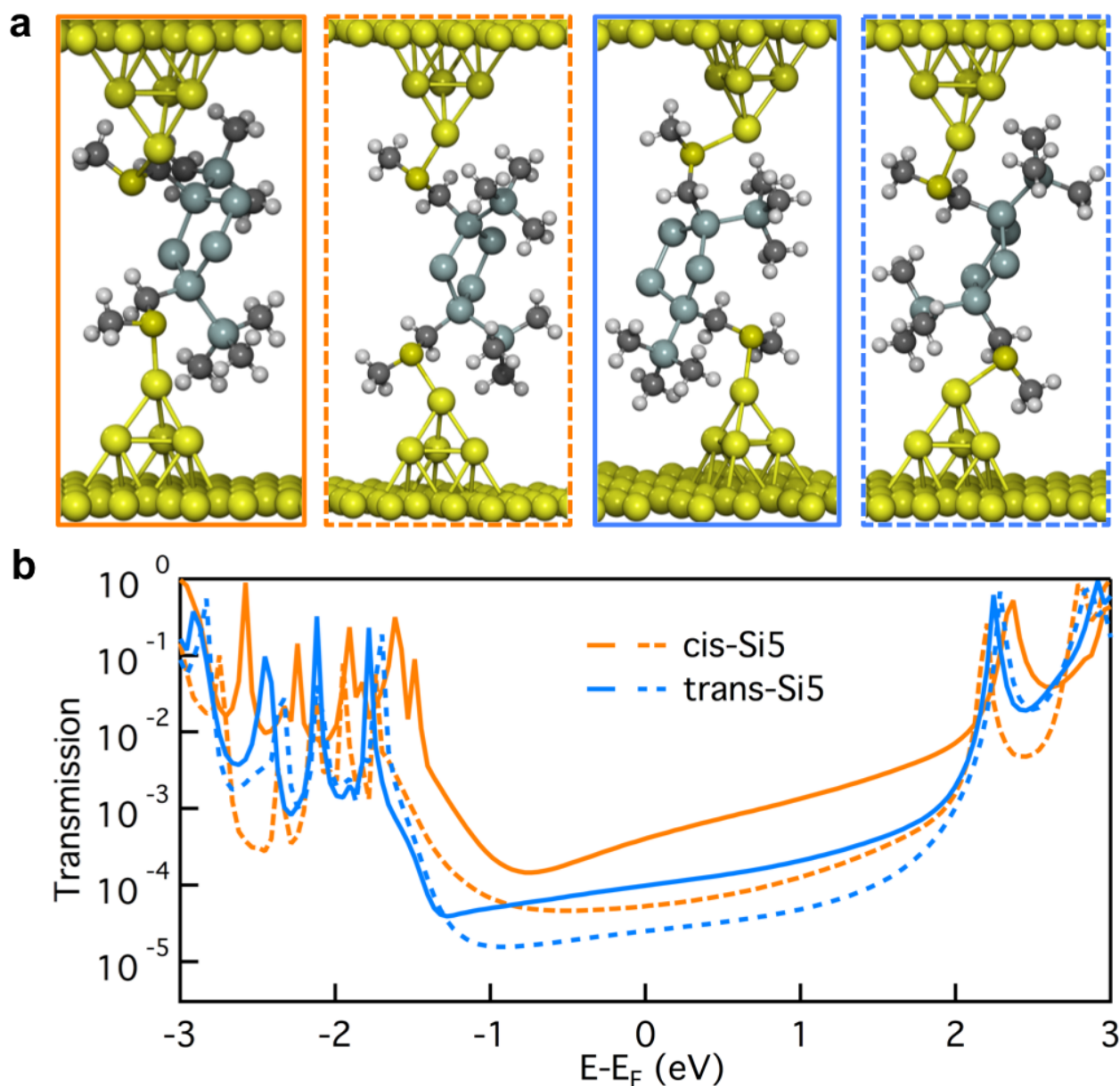


Figure 3.5: (a) Geometries and (b) transmission curves of two example conformers of **cis-Si5** and **trans-Si5** (solid orange: cis-4-envelope-f2; dashed orange: cis-1-twist-e2; solid blue: trans-1-envelope-b4; dashed blue: trans-1-envelope-b3). Methyl groups on the ring have been removed for clarity.

Next, we attach gold electrodes onto the calculated vacuum conformers. In principle, each conformer can bind to the electrodes in 16 different idealized configurations, as the Si—CH<sub>2</sub>—S—Au dihedral of each linker can be in either the ortho ( $\pm 90^\circ$ ) or transoid ( $\pm 170^\circ$ ) conformation. However, the majority of these structures are unrealistic, as parts of the molecule will block the electrodes from binding to the linker group. After applying an algorithm to exclude the sterically unfeasible junction structures, we generate a complete set of junction geometries for all vacuum conformers. We place the molecule between two 4-atom Au-pyramids on 4x4 fcc Au(111) surfaces and relax the molecule to 0.05 eV with the Au-atoms fixed using DFT with the PBE exchange-correlation functional. A single-zeta basis set is used for the Au-surface and double-zeta plus polarization basis sets are used for the Au-pyramids and molecule. Finally the transmission is calculated using double-zeta plus polarization basis sets for all atoms.

We optimize and calculate the transmissions for a total of 279 **trans-Si5** junctions and 211 **cis-Si5** junctions. Previous studies for linear systems indicate that the geometry with the terminal methyl group in ortho-configuration (equivalent to Au—S—CH<sub>2</sub>—Si dihedrals in anti) is dominant as the junction is fully elongated. However, the cyclic pentasilane is structurally very different from the equivalent linear systems. In vacuum the most stable configuration for cyclic pentasilane is CH<sub>3</sub>—S—CH<sub>2</sub>—Si dihedrals in the anti-configuration. Therefore, we hypothesize that the initial junction structure binds to the electrodes with Au—S—CH<sub>2</sub>—Si dihedrals in ortho-configuration and proceed to analyze the results for junctions with this geometry alone here.

We illustrate the optimized junction structures for sample **cis-Si5** and **trans-Si5** conformers in Figure 3.5a and plot their transmissions in Figure 3.5b. Due to the structural

variation in these junction geometries, the transmission close to the Fermi energy varies considerably. Considering the vast conformational flexibility of the molecule, we do not think that each of the experimental conductance peaks in Figure 3.3 can originate from a single dominant conformer. Instead we hypothesize that a number of conformations can be accessed at different junction lengths during the junction elongation. To test this hypothesis we analyze the structural information for 74 **cis-Si5** and 91 **trans-Si5** junction conformations optimized with Au—S—CH<sub>2</sub>—Si dihedrals in ortho-configuration (the full set of junctions with ortho/ortho contact geometry).

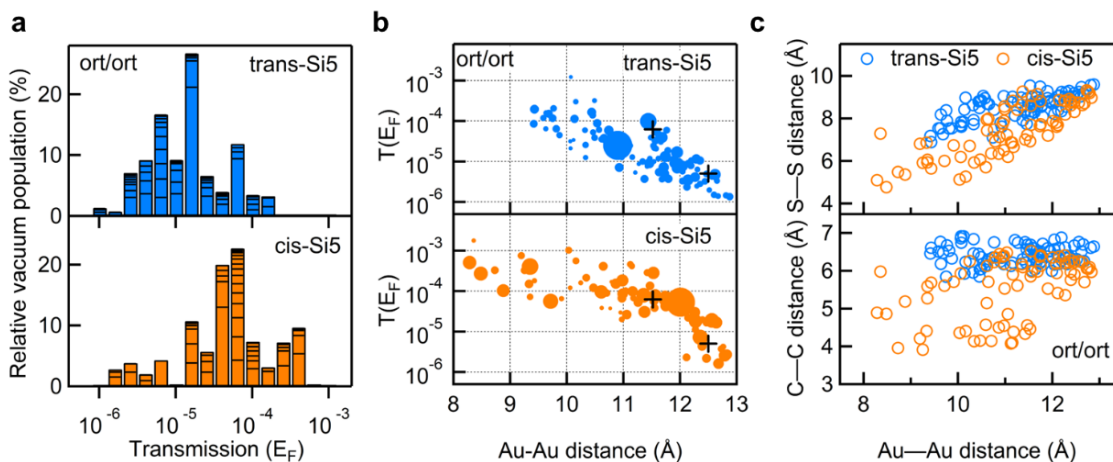


Figure 3.6: (a) Logarithmically binned histogram of transmission at Fermi energy of the 91 **trans-Si5** and 74 **cis-Si5** conformers. The horizontal stack lines in the bars indicate the vacuum population of each conformer. The histogram is normalized to sum up to 100%. (b) Transmission at Fermi energy plotted against the Au—Au junction distance for each **trans-Si5** and **cis-Si5** conformer bridged between four-atom Au pyramids. For easier visualization, the size of each dot has been scaled by  $1/(1+E)$ , where  $E$  is the relative vacuum energy of each conformer in units of  $kT$  at 300K. Black + are the calculated transmissions for the two configurations of the linear **Si3** with both terminal Au—S—CH<sub>2</sub>—Si dihedrals in ortho conformations. Black circles and lines highlight the difference between the two isomers. (c) S—S (upper panel) and C—C junction distance (lower panel) plotted against the Au—Au junction distance for each **trans-Si5** and **cis-Si5** conformer. S refers to sulfur; C refers to the CH<sub>2</sub>-group that bridges the silicon ring and the methyl-sulfide group. All three plots share the same color scheme: orange for **cis-Si5** and blue for **trans-Si5**.

In Figure 3.6a we compare the calculated conductance for **cis-Si5** and **trans-Si5** by generating the histogram of the transmissions at the Fermi energy with the contribution from each conformer weighted by its vacuum population at 300K. The calculated histograms do not fully represent the experimental data as we do not pull the system or allow it to switch from one conformation to another. The shapes of these calculated histograms are sensitive to the bin-size and the method used to calculate the vacuum energies therefore should not be over-interpreted. We see that in agreement with the experiment, the transmissions for **cis-Si5** are distributed at higher values than the transmissions for **trans-Si5**. Although the exact values are underestimated, we note that this is the analysis for ortho/ortho contact geometry only. Same analysis for anti/ortho and anti/anti are shown in Figure 3.7 and 3.8.

To compare the experimental data of conductance as a function of junction elongation, we plot the transmission of each conformer at the Fermi energy against the Au—Au distance of the junction in Figure 3.6b. The size of each dot scales with the energy of the conformer (in units of  $kT$ ) in vacuum by  $1/(1+E)$ . Therefore a larger dot corresponds to a conformer with higher vacuum population. First, we note that more **cis-Si5** conformers are populated at short Au—Au lengths (highlighted in black circles) and obtain higher transmission compared with **trans-Si5**, which agrees with what we observe in the experiment (Figure 3.3). Both plots indicate that the junction length can reach an Au—Au separation of 8-13 Å, which would yield a step length of around 1-6 Å in the 2-dimensional histograms considering the distance that the Au electrodes snap back (6-8 Å) after the Au point contact ruptures.<sup>163,238–240</sup> We note that the snap back of the Au electrodes is not considered in other cases, such as the STM current-distance technique where the Au

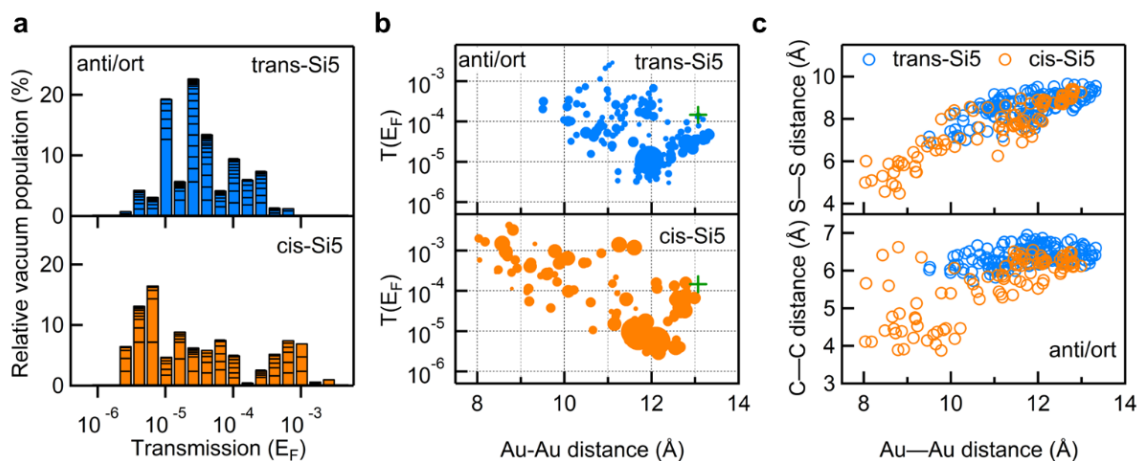


Figure 3.7: Transmission data of 140 **trans-Si5** and 98 **cis-Si5** with terminal Au—S—CH<sub>2</sub>—Si dihedrals in anti/ortho contact geometry. (a) Logarithmically binned histogram of transmission at Fermi energy. The horizontal stack lines in the bars indicate the vacuum population of each conformer. The histogram is normalized to sum up to 100%. (b) Transmission at Fermi energy plotted against the Au—Au junction distance for each **trans-Si5** and **cis-Si5** conformer bridged between four-atom Au pyramids. The size of each dot scales with  $1/(1+E)$ , where  $E$  is the relative vacuum energy of each conformer in units of  $kT$ . Green + is the calculated transmission for linear **Si3** with one electrode in ortho and the other in anti conformation. (c) S—S (upper panel) and C—C junction distance (lower panel) plotted against the Au—Au junction distance for each **trans-Si5** and **cis-Si5** conformer. S refers to sulfur; C refers to the CH<sub>2</sub>-group that bridges between the silicon ring and the methylsulfide group. All three plots share the same color scale: orange for **cis-Si5** and blue for **trans-Si5**.

tip is positioned above the Au substrate (no Au—Au contact) before forming a molecular junction.<sup>241</sup> The transmissions for both **cis-Si5** and **trans-Si5** conformers decay with an increasing Au—Au distance, however, **cis-Si5** conformers have higher transmissions than **trans-Si5** conformers at the same junction length. The transmission data suggests that the different conductivity for **cis-Si5** and **trans-Si5** may be due to intrinsic structural differences beyond the junction length.

The transmission of the silanes is very sensitive to the dihedrals of the backbone,<sup>54,141</sup> however, we do not find any significant difference in backbone dihedrals between **cis-Si5** and **trans-Si5**. Next, apart from the backbone  $\sigma$ -conjugation, we also consider the trans-

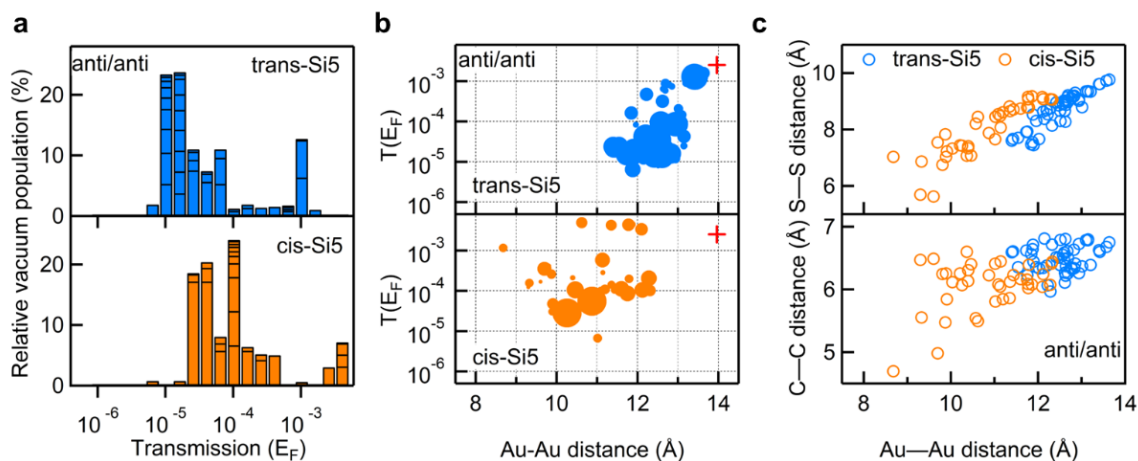


Figure 3.8: Transmission data of 48 **trans-Si5** and 39 **cis-Si5** with terminal Au—S—CH<sub>2</sub>—Si dihedrals in anti/anti contact geometry. (a) Logarithmically binned histogram of transmission at Fermi energy. The horizontal stack lines in the bars indicate the vacuum population of each conformer. The histogram is normalized to sum up to 100%. (b) Transmission at Fermi energy plotted against the Au—Au junction distance for each **trans-Si5** and **cis-Si5** conformer bridged between four-atom Au pyramids. The size of each dot scales with  $1/(1+E)$ , where  $E$  is the relative vacuum energy of each conformer in units of  $kT$ . Red + is the calculated transmission for linear **Si3** with both electrodes in anti conformation. (c) S—S (upper panel) and C—C junction distance (lower panel) plotted against the Au—Au junction distance for each **trans-Si5** and **cis-Si5** conformer. S refers to sulfur; C refers to the CH<sub>2</sub>-group that bridges between the silicon ring and the methyl-sulfide group. All three plots share the same color scale: orange for **cis-Si5** and blue for **trans-Si5**.

mission originating from through-space interactions in the molecule, i.e., non-nearest neighbor interactions that might contribute to the different conductance in **cis-Si5** and **trans-Si5**. As the molecule is spatially crowded, intramolecular distances between atoms are relatively small, so that through-space interactions may give rise to a significant contribution to the total transmission. This contribution to the transmission has recently been thoroughly studied in  $\pi$ -conjugated helicenes,<sup>242–244</sup> and have also been demonstrated to be significant in cyclic and linear silanes systems.<sup>54,222,223</sup> We note the distinction between through-bond and through-space interactions is a bit arbitrary and no difference was found between the physical mechanisms of these two processes.<sup>54,245</sup> In Figure 3.6c we plot

two decisive through-space distances of the molecule, the S—S and CH<sub>2</sub>—CH<sub>2</sub> linker-to-linker distances, against the Au—Au distance of the junction. For junctions of the same Au—Au length, the S—S and CH<sub>2</sub>—CH<sub>2</sub> distances are consistently shorter for **cis-Si5** than for **trans-Si5**. This is a geometrical consequence of cis-trans isomerism: while the absolute values of backbone dihedrals are similar, the intramolecular distances in the trans-isomer are longer. The systematically higher transmission for **cis-Si5** in junction with the same Au—Au length is a direct consequence of this structural difference of the two isomers.

Finally, we re-examine the conductance measurements with the theoretical conformational analysis. As discussed above, when considering the experimental conductance peak obtained for **cis-Si5**, **trans-Si5** and linear **Si3**, we see that the cyclic isomers exhibit lower conductance. However, for the linear **Si3**, junctions with one or both terminal Au—S—CH<sub>2</sub>—Si dihedrals in ortho conformation have a lower conductance than the peak conductance measured for junctions with both dihedrals in the anti conformation. Thus, the low conductance measured for the cyclic systems could result from some of their dihedrals never achieving a 180° anti-configuration, which maximizes the conductance.<sup>12,141</sup> The Si—SiMe<sub>2</sub>—Si—CH<sub>2</sub> dihedrals range from gauche (60°) to deviant orientation (~140°)<sup>142</sup>. In contrast, a linear silane achieves an anti conformation with dihedral angles close to 180° along its entire backbone in its energetically favorable conformation, giving the linear **Si3** and **Si4** the best orbital delocalization and a higher conductance than is achievable for the cyclic structures. Calculations also support the finding that the tetrasilane path within the cyclic pentasilane has a Si—SiMe<sub>2</sub>—SiMe<sub>2</sub>—Si dihedral smaller than 50° and therefore does not contribute significantly to the **cis-Si5** or **trans-Si5**

conductance when compared with the trisilane path.

## Conclusion

To conclude, in this study, we synthesize cis and trans isomers of cyclic pentasilane with aurophilic methylsulfide anchor groups, measure their conductance using the STM-BJ technique and compare these results with DFT calculations. We show that the large conformational freedom in these systems controls both the probability of junction formation and the measured conductance. We attribute the reduced conductance of the studied cyclic structures compared with linear chains to the diminished conjugation in Si—Si  $\sigma$ -bond together with through-space coupling effect when an all-anti conformation cannot be achieved. Our results illustrate the importance of bond orientation in  $\sigma$ -coupled silicon systems that is comparable to the impact of dihedral angles in  $\pi$ -conjugated carbon structures.<sup>146</sup>

## 3.2 Understanding Electron Transport through Cyclic and Bicyclic Silanes

### Preface

This section is based on the manuscript entitled *Understanding Electron Transport through Cyclic and Bicyclic Silanes* by Haixing Li,<sup>†</sup> Marc Garner,<sup>†</sup> Yan Chen,<sup>†</sup> Zhichun Shang-guan, Qianwen Zheng, Timothy Su, Madhav Neupane, Yaping Zang, Michael Steigerwald, Fay Ng, Shengxiong Xiao, Colin Nuckolls, Gemma Solomon, and Latha Venkataraman in

preparation. Yan Chen, Zhichun Shangguan, and Qianwen Zheng of Prof. Xiao's group synthesized and characterized all compounds. Marc Garner carried out theoretical calculations. I performed the conductance measurements and data analysis.

## **Abstract**

Linear silanes demonstrate strong  $\sigma$ -conjugation in a transoid conformation, however, little is known about the electron transport through silicon rings. We report a synthesis, electronic and theoretical characterization of functionalized cyclic and bicyclic silanes, aiming to test (1) whether the constrained silicon backbone decreases the molecular conductance and (2) whether the electron transport is a sum of all pathways. The cyclic systems that we have created include a cyclotetrasilane, a cyclopentasilane, a bicyclo[2,2,1]heptasilane, and a bicyclo[2,2,2]octasilane. These are connected to two silane "arms" of varying length that are terminated with methylthiomethyl linkers that bind to gold electrodes. We determine the impact of ring structure on conductance by comparing our results to those of linear silanes, demonstrating that silanes constrained with dihedrals less than  $165^\circ$  (transoid) show lower conductance than the transoid linear silanes. Density Functional Theory calculations reproduce the conductance trend for the four silicon rings and reveal that if a single pathway with less constrained dihedrals is available, it alone will dominate the transport. These results add to our understanding of silicon electronics at the single molecule level.

## Introduction

With a continuing scaling down of the silicon devices,<sup>246</sup> molecules consisting of several silicon atoms become perfect systems to investigate to understand nanoscale transport in silicon. However, despite the progress in silicon synthesis<sup>225,227,247–251</sup> and molecular electronics,<sup>252–254</sup> to date there have been very few experimental reports of silicon-based single-molecule devices, especially with silanes of structures that are more complex than simple one-dimensional chains. Theory has predicted that  $\sigma$ -conjugation in silanes and alkanes is dihedral dependent,<sup>54,141,255</sup> another theoretical work on the highly constrained silane system with multiple pathways show that all pathways contribute to the transmission.<sup>223</sup> However, the experimental studies exploring the relationship between backbone dihedrals and charge carrier mobility have been limited to conducting silane polymers.<sup>256–258</sup> An experimental single-molecule conductance study on the silane rings is lacking.

Indeed, the complexity that the silicon rings and cages bring to the molecular junction tremendously affects their fundamental electron-transport properties.<sup>17</sup> For example, silicon rings represent a class of molecules of which transport contains through-space components and quantum interference features,<sup>17,54,222,223,245</sup> rather than a sum of through-bond pathways. In addition, as the silicon rings and cages mimic the bulk materials, studies on these silanes can potentially provide knowledge for silicon materials in other forms.

Here we design cyclotetrasilane (**4-ring**), cyclopentasilane (**5-ring**), bicyclo[2,2,1]heptasilane (**221**), and bicyclo[2,2,2]octasilane (**222**) with varied extending

backbone length and investigate their single-molecule conductance properties using scanning tunneling microscope break junction (STM-BJ) technique. We demonstrate a reliable method of determining the silicon ring conductance by fitting the conductance values of the molecules at all lengths and extrapolating the fit to zero length. This method relies on the fact that linear silanes show a clear exponential attenuation of conductance with increasing length.<sup>12</sup> These trends are expected to be general when contact geometries and conformations of the linear wire do not vary significantly. Through this approach, we demonstrate a conductance trend of  $G_{221} > G_{4\text{-ring}} > G_{5\text{-ring}} > G_{222}$ . We emphasize that to compare the conductance of these cyclic and bicyclic structures we cannot simply compare one set of molecules at one particular molecular length, because the relative conductance ratios can differ significantly depending on the length of the extending silane arm. Combined with density functional theory (DFT) calculations, our important findings are that the conductance of these rings are not simply determined by the number of atoms in the shortest path but by the entire junction geometry. Despite that **221**, **4-ring**, and **5-ring** all have three silicon atoms in the shortest path, their conductance are a factor of 1.12, 0.52, 0.37 of their linear counterparts. The low conductance of **222** (a factor of 0.2 of its linear counterpart) is attributed to the appearance of quantum interference in the transmission close to the Fermi energy.

## Single Molecule Conductance Measurement

We design and synthesize cyclic **4-ring** and **5-ring** and bicyclic **221** and **222** structures shown in Figure 3.9a. The **4-ring** and **5-ring** have cis and trans isomers; here we focus on the trans isomers only and results comparing cis and trans isomers have been detailed

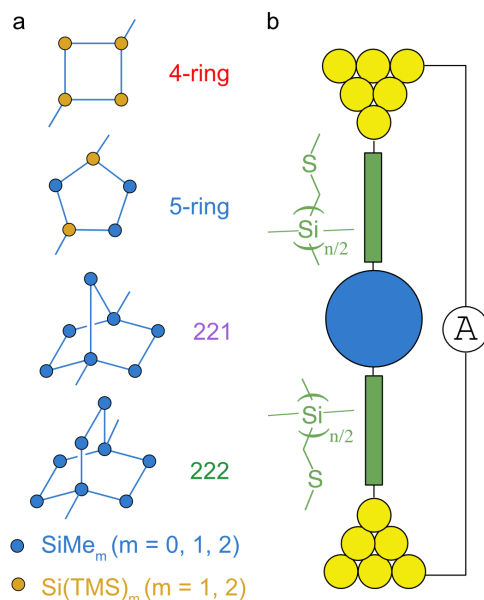


Figure 3.9: (a) Chemical structures of the central units. The two dangling bonds on each structure indicate the positions for attaching the linear silicon wires. For the extending silicon chain length,  $n = 2, 4, 6$  for **4-ring** and **5-ring** and  $n = 0, 2, 4, 6$  for **221** and **222**. TMS represents trimethylsilyl. (b) Schematic of a single molecule junction formed with a silicon molecular wire containing a ring (blue dot) and extending arm (green rectangles).

previously.<sup>17</sup> To compare the single-molecule junction conductance of these silicon ring structures, we synthetically attach silicon molecular wires to these rings and create a series of molecules at different chain lengths with  $n = 2, 4, 6$  for **4-ring** and **5-ring**;  $n = 0, 2, 4, 6$  for **221** and **222**.<sup>12,78,259–262</sup> Each silicon arm is functionalized with terminal methylthiolmethyl groups to enable the formation of molecular junctions with Au electrodes.<sup>78</sup> We measure the conductance of single-molecule junctions using a scanning tunneling microscope-based break junction (STM-BJ) method (schematic shown in Figure 3.9b).<sup>8,9</sup> For each molecule studied, we repeatedly form and break Au point contacts in a 1,2,4-trichlorobenzene solution of the target molecule. The conductance versus displacement traces reveal plateaus near integer multiples of the conductance quantum ( $G_0, 2e^2/h$ ) with one or sometimes two additional plateaus below  $G_0$ ; these additional steps indicate the

formation of Au-molecule-Au junctions.

We compile 10,000 – 30,000 traces into a logarithmically-binned conductance histogram for each molecule studied without any data selection. Figure 3.10a-d displays the conductance histograms for **221**, **4-ring**, **5-ring**, and **222** series at varied chain length. We see clear conductance peaks for all systems, indicating that the silicon ring structures provide an electronic pathway and are well-coupled to the rest of the junction. Here we focus on the most significant peak for each molecule; cause for the multiple-peak feature has been discussed previously.<sup>17</sup> We obtain the most probable conductance value for each molecule by fitting a Gaussian function to the conductance peak that corresponds to a fully elongated junction as determined from 2-dimensional histograms (Figure 3.12 - 3.15). In figure 3.11, we plot the single-molecule junction conductance as a function of the number of silicon atoms in the silane arms. These data reveal that the conductance decreases exponentially with increasing length  $G = G_c e^{-\beta n}$  except the shortest one of the **222** series which falls off the line. We find that these four series share a very similar tunneling decay constant  $\beta$  (Table 3.1) determined from the fit to the conductance data.

Molecule	Measured <sup>a</sup>					Calculated	Measured	Calculated
	$G_{\text{Ring-Si0}}/G_L^b$	$G_{\text{Ring-Si2}}/G_L$	$G_{\text{Ring-Si4}}/G_L$	$G_{\text{Ring-Si6}}/G_L$	$G_{n=0}/G_L^c$	$G_{n=0}/G_L^c$	Decay $\beta$	Decay $\beta$
<b>221</b>	1.10	0.97	1.01	0.74	1.12	1.19	0.82	0.72
<b>4-ring</b>	NA	0.71	0.36	0.79	0.52	0.31	0.73	0.76
<b>5-ring</b>	NA	0.42	0.36	0.47	0.37	0.05	0.73	0.73
<b>222</b>	0.09	0.21	0.15	0.18	0.22	NA	0.76	NA

Table 3.1: <sup>a</sup> Conductance peak values are obtained from fitting a Gaussian function to the corresponding 1D conductance histogram. <sup>b</sup> To calculate each conductance ratio, we divide the conductance of the indicated silicon-ring wire to its corresponding linear counterpart. The linear counterparts are Si3, Si5, Si7 and Si9 for **221**, **4-ring** and **5-ring**; are Si4, Si6, Si8, and Si10 for **222**. <sup>c</sup> Ring conductance determined from the intersect of the fit at  $n = 0$ .

We now compare the measured conductance of these ring systems with linear silanes.

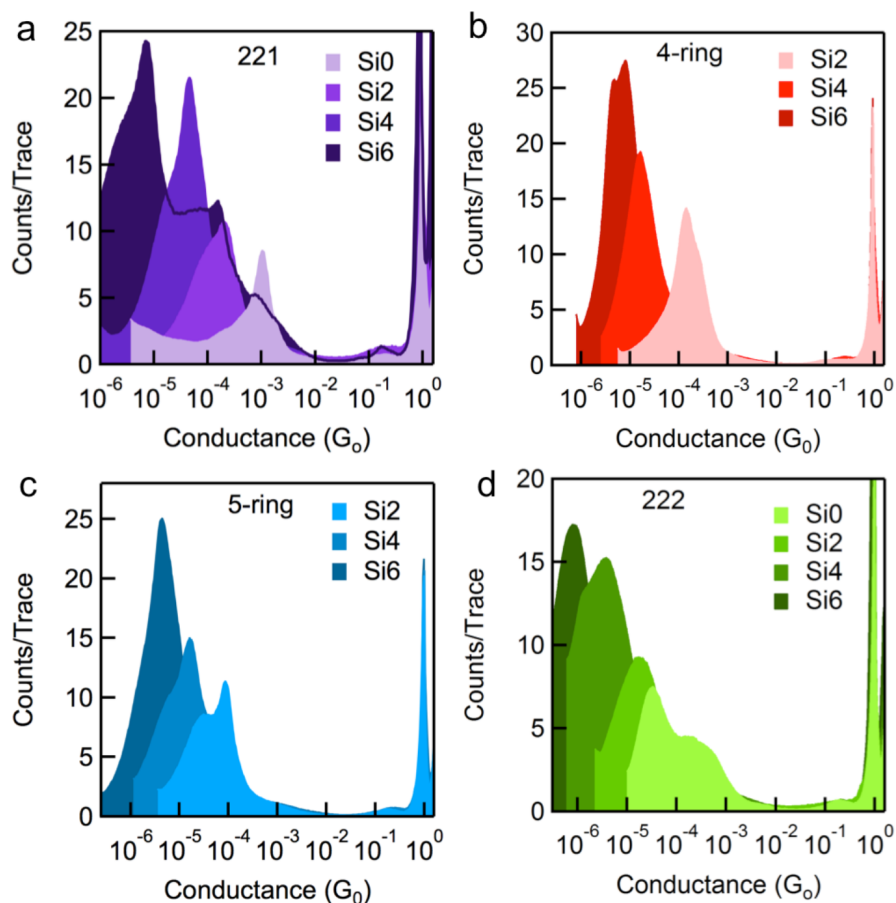


Figure 3.10: Conductance histograms for silicon molecular wires containing (a)**221**, (b)**4-ring**, (c)**5-ring**, and (d)**222**. The counts/trace intensity of the Si6 data for **222** series is multiplied by a factor of 3. The number of silicon atoms in the oligosilane wire  $[\text{SiMe}_2]_n$  ( $n = 0, 2, 4, 6$ ) is indicated by a light to dark color scheme.

In order to do this, we first consider the shortest path in each ring. **4-ring**, **5-ring** and **221** all have three silicon atoms in the shortest path while **222** has four. Since we have measured these cyclic systems with silicon arms that have 0, 2, 4 and 6 atoms, we can consider the ratio of the conductance of the wires with an embedded cycle to that of their linear counterparts. Specifically, we take the measured conductance of the **4-ring**, **5-ring** and **221** wires and divide these by the conductance of linear silanes with 3, 5, 7 or 9 atoms. For the **222** wires, we divide the conductance by that of linear silanes with 4, 6, 8 or 10

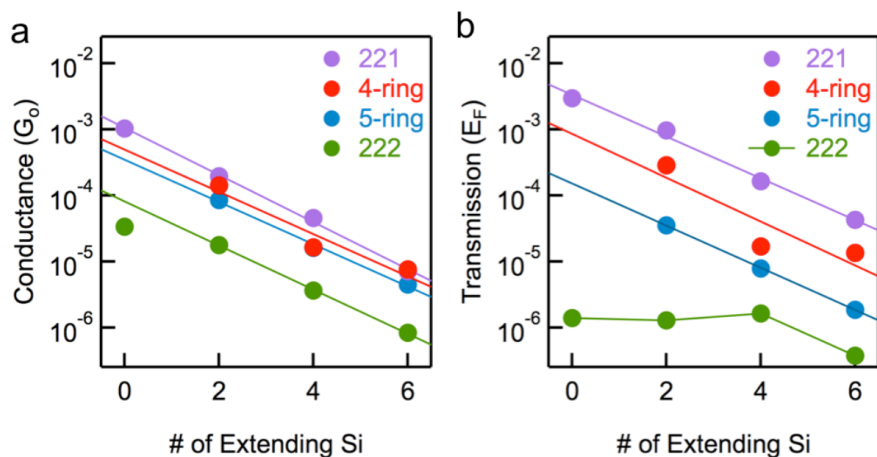


Figure 3.11: (a) Measured single-molecule junction conductance and (c) calculated transmissions at the Fermi energy plotted against silane arm length for 221 (purple), 4-ring (red), 5-ring (blue), 222 (green) based oligosilanes.

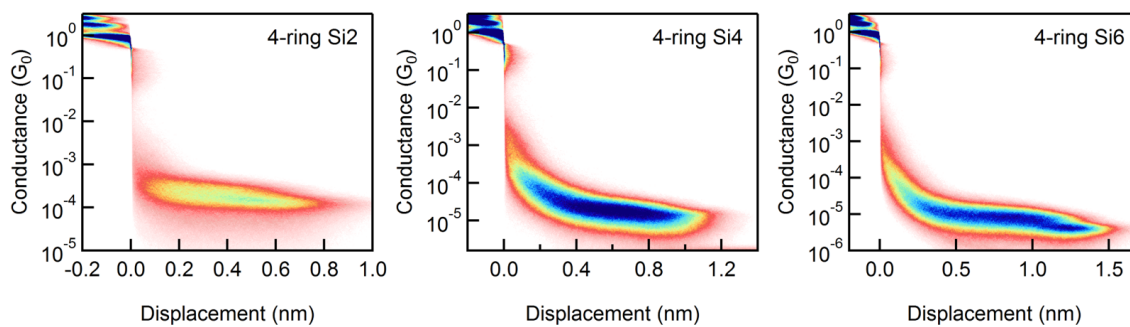


Figure 3.12: 2D conductance histograms for 4-ring series.

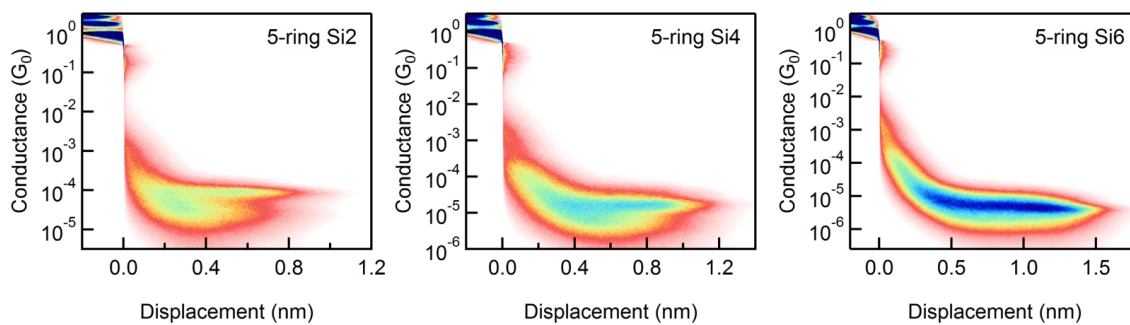


Figure 3.13: 2D conductance histograms for 5-ring series.

silicon atoms. We list the results in Table 3.1.

We find that for each ring structure, this relative conductance can vary significantly

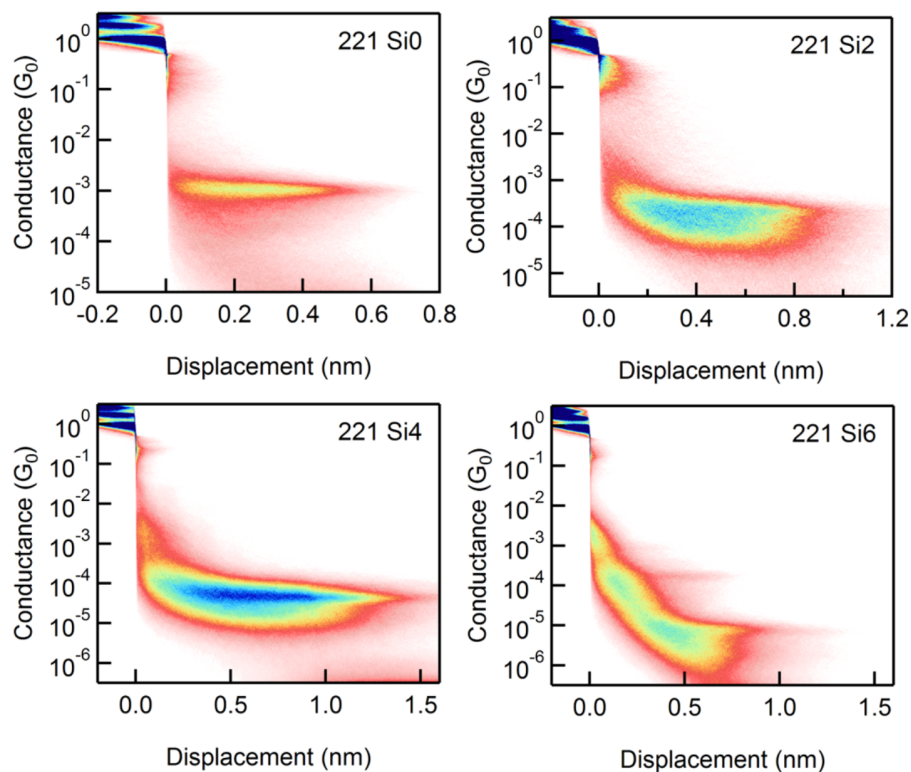


Figure 3.14: 2D conductance histograms for **221** series.

depending on the molecular length. This result strongly suggests that we cannot simply compare the four ring structures at one length but need to consider a series of lengths and extrapolate the effective conductance  $G_c$  at  $n = 0$ , as listed in Table 3.1. Applying this method, we find that **5-ring** is a worse conductor than **4-ring**. In addition, we observe an odd-even effect in the conductance of the **4-ring** series as can be seen in Figure 3.11. This phenomenon is intrinsic to **4-ring** systems as we also observe the odd-even effect in three other series containing **4-ring**. (Figure 3.16, 3.17)

## Density Functional Theory Calculations

To investigate the nature of the transport through these silicon ring structures and explain these observations, we perform *ab initio* calculations based on density functional theory

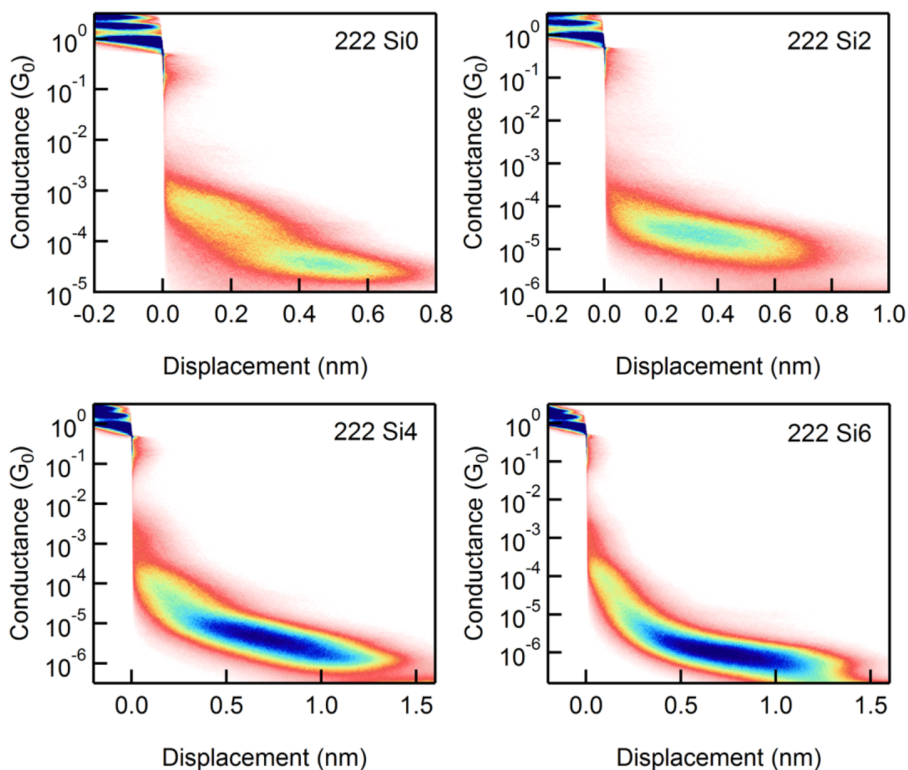


Figure 3.15: 2D conductance histograms for **222** series.

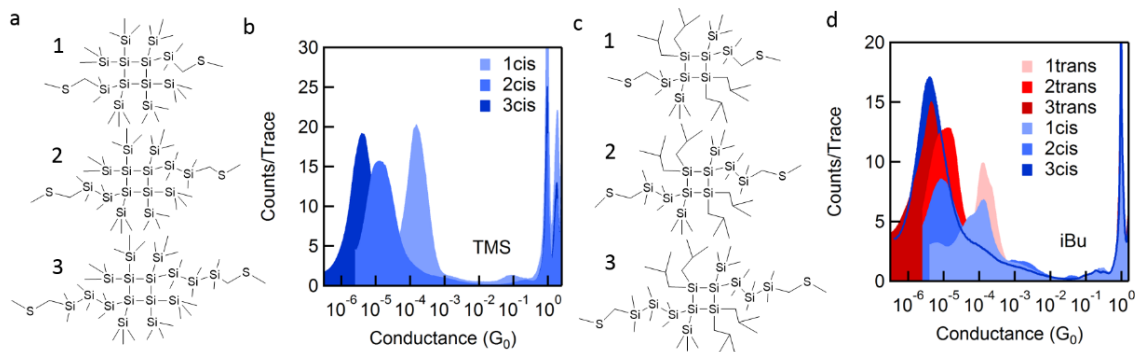


Figure 3.16: (a) Chemical structures and (b) 1D conductance histograms of TMS substituted **4-ring** series. (c) Chemical structures and (d) 1D conductance histograms of isobutyl substituted **4-ring** series. The counts/trace intensity of the data of 1trans-iBu is multiplied by a factor of 0.3.

(DFT). The molecular structures are optimized in vacuum and placed between two 4-atom Au-pyramids on  $5 \times 5$  fcc Au(111) surfaces to form a junction. The molecule is relaxed to a threshold of  $0.05 \text{ eV/\AA}$  with the Au-atoms kept fixed. DFT with the PBE exchange–

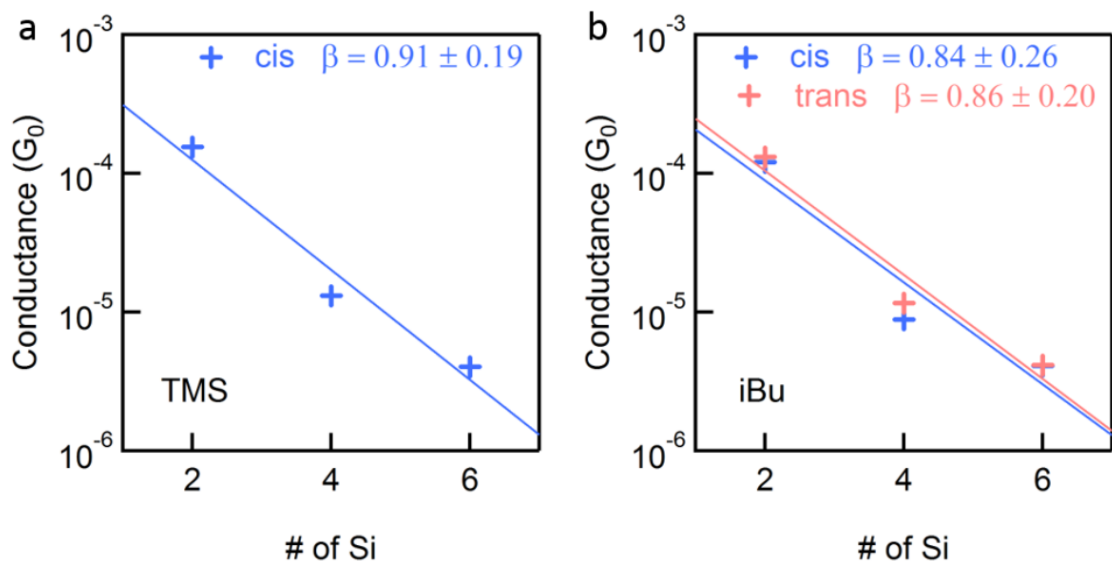


Figure 3.17: Measured single-molecule junction conductance plotted against extending silicon chain length for cis TMS substituted **4-ring**. (b) Measured single-molecule junction conductance plotted against extending silicon chain length for cis (blue) and trans (pink) isobutyl substituted **4-ring**.

correlation functional and double- $\zeta$  plus polarization basis set is used as implemented in ASE and GPAW.<sup>96,232,235–237</sup> The transmission is calculated with the non-equilibrium Green's functions approach. The transmission at the Fermi energy is plotted against the chain length for each series in Figure 3.11b. We find the calculated decay constant for the four series agree with the experimental data, except for the **222** series that shows a non-exponential trend. We also find that the calculated transmission fully reproduces the experimental odd-even observation for the **4-ring** systems. However, we note the exact transmission values lack quantitative accuracy due to errors inherent to DFT.<sup>17,263–265</sup>

Our calculations show that **221** has higher conductance than **4-ring** and **5-ring** because the dihedral angles involving the three-Si path of the ring are rigidly locked in the anti-configuration ( $\text{Si-Si-Si-Si} = 180^\circ \pm 2^\circ$ ) making it favorable for transport.<sup>141,230</sup> For **4-ring** and **5-ring**, we present the transmissions in Figure 3.11b where **5-ring** has con-

formations with dihedrals more favorable for transport than **4-ring** (both around 130°). We note that **5-ring** also has conformations show lower transmission than **4-ring**. Finally, we find that for **222** there is a clear suppression of  $\sigma$ -conjugation as the Si-Si-Si-Si dihedral across the ring of **222** is 18° - this explains its low conductance determined both from theory and experiment.<sup>141,166,230,249</sup>

## Odd-Even Effect and Quantum Interference

To further investigate the conductance fluctuation in the **4-ring** and **222** series, we compare the calculated and the measured junction lengths. In individual conductance traces, the length of the plateaus at the molecule-dependent conductance value corresponds to the distance a junction can be elongated before it is broken. We determine the average distance a single-molecule junction can be elongated before the junction breaks by analyzing the distance at which the distribution in the 2D histogram drops to 20% of its peak value for each molecule measured (Figure 3.12 - 3.15). Considering that the Au electrodes snap back after the Au point contact is ruptured by about 6-8 Å, these elongation lengths yield the junction length and can be compared to the calculated Au-Au distance for each system.<sup>163,238</sup>

In Figure 3.18b and c we show these experimentally and theoretically determined lengths. We did not include the **221(Si6)** because the molecular junction seems to break before it reaches the fully elongated junction therefore is not comparable with others. We see that in both experiments and calculations, the **221** and **5-ring** series show a rather linear correlation between the junction length and the number of Si in the silicon arm, in agreement with past findings.<sup>163</sup> However, the **4-ring** and **222** series do not show such a

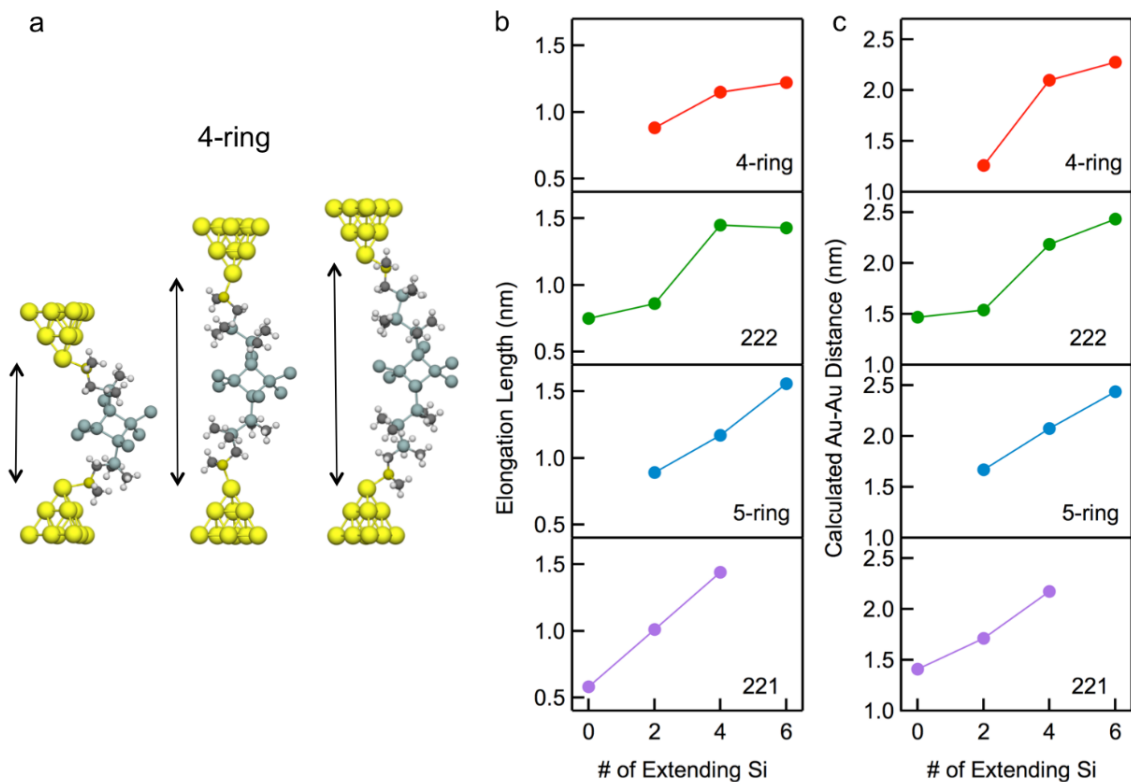


Figure 3.18: (a) Calculated geometries for junctions of Si<sub>2</sub>, Si<sub>4</sub> and Si<sub>6</sub> extended **4-ring**. Methyl groups on TMS substituents are omitted for clarity. (b) Experimental junction elongation length and (c) Calculated Au-Au distance plotted against the molecule length for **4-ring** (red), **222** (green), **5-ring** (blue), and **221** (purple) based oligosilanes.

linear trend. The origin of the odd-even effect in the conductance of **4-ring** series thus likely comes from an alternation of the junction length. As illustrated in Figure 3.18a from the calculated junction structures, the ones with an odd-number (even-number) chain on each side of 4-ring form junctions with shorter (longer) Au-Au distance, which consequently leads to higher (lower) tunneling current. We suggest that this mechanism might also explain the previously observed much weaker odd-even effect in linear oligogermanes.<sup>14</sup> This finding bears resemblance to the odd-even alternation effect in the conductance of self-assembled monolayers of alkanethiolates, where the results were attributed to the restricted contact angles of the molecules.<sup>266–269</sup>

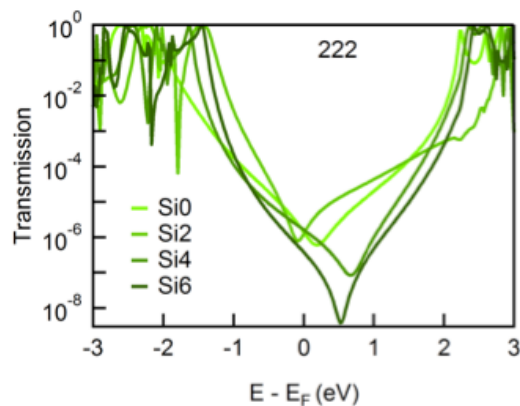


Figure 3.19: Calculated transmissions plotted on a semi logarithmic scale against energy for the **222** series in one conformation.

Similar to **4-ring**, **222** series also show alternation in the junction elongation lengths, yet systematic alternation is not observed in their measured conductance. The calculated junction lengths reproduce the trend from experiment, however, the transmissions at the Fermi energy do not. In particular, the transmissions of **222-Si0** and **222-Si2** are underestimated in the calculations. We see in Figure 3.19 that the transmissions are low due to the appearance of an anti-resonance close to the Fermi energy for all **222** molecules. The alignment of the anti-resonance relative to the Fermi energy changes through the series. However, this alignment cannot be predicted accurately due to the well-described quantitative limitations of DFT.<sup>264,265,270</sup> The large discrepancy between experiment and theory may result from the appearance of destructive quantum interference in the **222** series, which can alter conductance values and trends. Furthermore, expected trends such as exponential decay and odd-even alternation of the conductance may be distorted when an anti-resonance in transmission is close to or within the measured bias window.

## Conclusion

The observed conductance trends and DFT calculations reveal a reliable method of determining the conductance of silicon ring structures by considering a set of molecules with varying extending chain-lengths. Using this method we find that the conductance of **221**, **4-ring**, **5-ring** and **222** are a factor of 1.12, 0.52, 0.37, and 0.2 of the conductance of their linear counterparts. These results confirm that constraining the dihedrals in non-transoid/anti conformation in silane backbone decreases the conductance; **221** is an example of an all-anti pathway dominating the total transport. The exponential decay constants of the series do not differ significantly, confirming that the Si—Si  $\sigma$ -conjugation in the extending linear backbones is not affected by the ring. We envision this approach can be applied to single-molecule studies of other complex molecular structures and this result can provide insightful design-principles for silicon nanoelectronics.

*Straining Silanes to Create High Conductance Pathways*

**4.1 Strained Silacyclobutane Ring Creates High  
Conductance Pathways by Forming Au-silacycle  
Contact**

**Preface**

This section is based on the manuscript entitled *Silicon Ring Strain Creates High-Conductance Pathways in Single-Molecule Circuits* by Timothy Su, Jonathan Widawsky, Haixing Li, Rebekka Klausen, James Leighton, Michael Steigerwald, Latha Venkataraman, and Colin Nuckolls published in JACS.<sup>10</sup> Timothy Su and Rebekka Klausen of Prof. Nuckolls' group synthesized and characterized all compounds. Jonathan Widawsky and I performed the conductance measurements and data analysis.

**Abstract**

Here we demonstrate for the first time that strained silanes couple directly to gold electrodes in break-junction conductance measurements. We find that strained silicon molecular wires terminated by alkyl sulfide aurophiles behave effectively as single-molecule

parallel circuits with competing sulfur-to-sulfur (low G) and sulfur-to-silacycle (high G) pathways. We can switch off the high conducting sulfur-to-silacycle pathway by altering the environment of the electrode surface to disable the Au-silacycle coupling. Additionally, we can switch between conductive pathways in a single molecular junction by modulating the tip-substrate electrode distance. This study provides a new molecular design to control electronics in silicon-based single molecule wires.

## Introduction

This section unveils the characteristics of strained silicon in single molecule electrical devices. Current state-of-the-art integrated circuits incorporate strain in the silicon crystal lattice to improve charge mobility and channel conductance. As electronic devices continue their ultra-miniaturization,<sup>40,271-274</sup> understanding the effects of strain in molecular versions of silicon will be crucial. In this study, we incorporate the strained silacyclobutane ring into a molecular wire to investigate how silicon ring strain manifests in molecular conductance. Previously, we found that permethylated oligosilanes with alkyl sulfide contacts at both ends of the molecule conduct through a single pathway from sulfur to sulfur.<sup>78</sup> Here, we demonstrate that silane **1** conducts not only from sulfur to sulfur (red, low G pathway) but also from sulfur to silacycle (blue, high G pathway). The latter pathway arises as a consequence of the significant strain of the silacycle. Additionally, we find that we can control the pathway through which conductance occurs and thereby switch between two distinct conductance states.

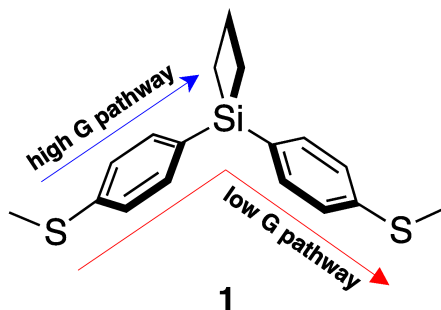


Figure 4.1: Chemical Structure of **1**.

## Results and Discussion

We synthesize **1** from 1,1-dichlorosilacyclobutane and 4-(methylthio)phenylmagnesium bromide. We grew single crystals suitable for X-ray diffraction from methanol vapor diffusion into a solution of **1** in 1,2,4-trichlorobenzene (TCB). The bond angle about the aryl carbons and silicon atom describes a standard tetrahedron ( $109^\circ$ ) while the silacyclobutane ring is significantly distorted ( $\text{CH}_2\text{-Si-CH}_2$ ,  $79^\circ$ ). We measure single-molecule conductance using a scanning tunneling microscope-based break-junction (STM-BJ) technique.<sup>8</sup> Point contacts between the Au tip and substrate electrodes are repeatedly broken and formed in a solution of the target molecule at room temperature and low voltage (225 mV). After the Au–Au point contact is broken, aurophilic thiomethyl groups<sup>67</sup> on the molecule bind to undercoordinated gold atoms to form Au–molecule–Au junctions. Conductance (current/voltage) is measured across the gap as a function of tip–substrate displacement ( $\Delta x$ ), and the resulting traces reveal molecule-dependent plateaus signifying junction formation with conductance values below  $G_0$  ( $2e^2/h$ ), the quantum of conductance describing a single Au–Au contact.<sup>127</sup> Junctions form and break thousands of times, and we analyze the measured traces using one- and two-dimensional histograms<sup>275</sup> as

detailed below.

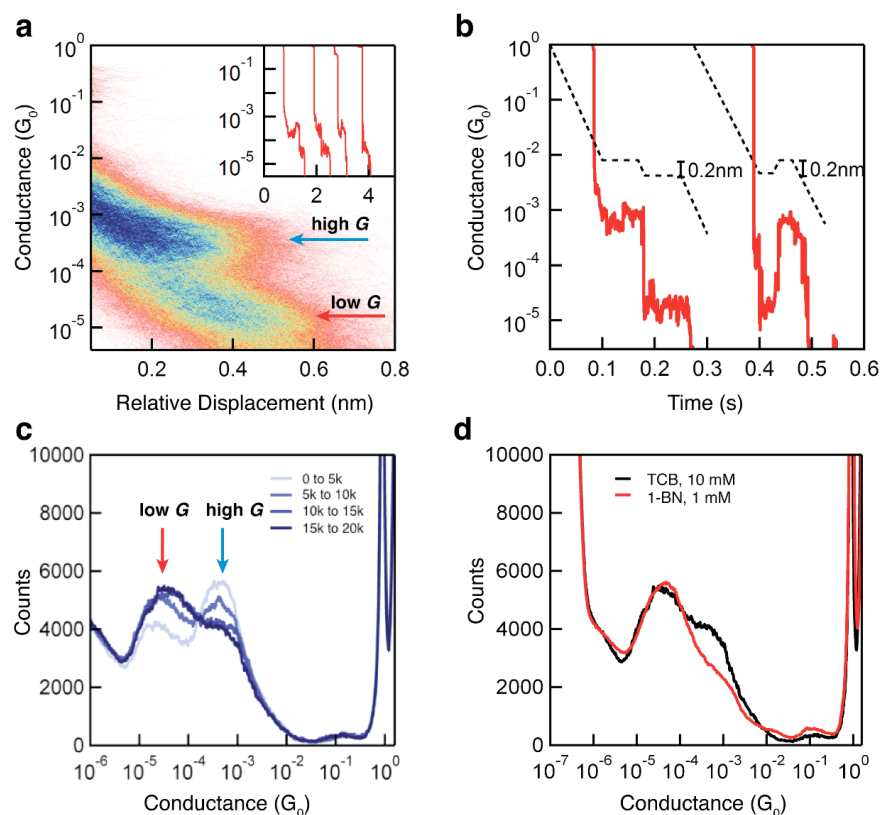


Figure 4.2: (a) 2D histogram of the first 5000 traces of **1** (1 mM TCB) with selected sample traces (inset). (b) Single-junction elongation (left) and compression traces (right) showing switching events. The black dotted line denotes the piezoelectric motion while the red solid line shows the conductive response. (c) 1D histogram tracking sequential sets of 5000 traces (20000 total) to show peak evolution with increasing concentration. (d) 1D histogram of **1** in 1-BN solvent (1 mM), compared with TCB (10 mM).

The results from STM-BJ measurement of **1** in 1,2,4-trichlorobenzene demonstrate four unique characteristics that are unlike any molecule we have ever measured. First, as we see from a two-dimensional conductance-displacement histogram shown in Figure 4.2a, we have two distinct conductance states that differ by an order of magnitude. This difference is significantly greater than we previously observed for 4,4'-bipyridine.<sup>276</sup> We define the region around  $4.2 \times 10^{-4} G_0$  as the high G state and the region around  $4.0 \times 10^{-5} G_0$  as the low G state. Sample conductance traces have plateaus at these conduc-

tance values, as shown in the inset. Second, we note that both high and low G states occur directly after the Au–Au contact rupture ( $\Delta x = 0$ ); yet, a high G junction can only sustain a 0.4 nm elongation while a low G junction can sustain a 0.6 nm elongation. Since junction elongation length correlates with the conduction path length,<sup>277</sup> we hypothesize the conduction path in the high G state is shorter than in the low G state.

Third, we find that we can induce switching from the high to low G state reliably; however, the reverse occurs infrequently. To switch from a high to low G state (elongation), we first form a high G junction and then pull the junction an additional 0.2 nm as shown in Figure 4.2b. We find that, with this modified ramp, 65% of the traces switch from high to low G, 12% stay in high G, and 23% break. To switch from low to high G, we form a low G junction, then compress the electrodes by 0.2 nm. The fraction of traces that switch from low to high G is small (13%). Under compression, the majority of measured traces remain in the low G state, indicating that the high G state is not easily accessible once the low G state is formed.

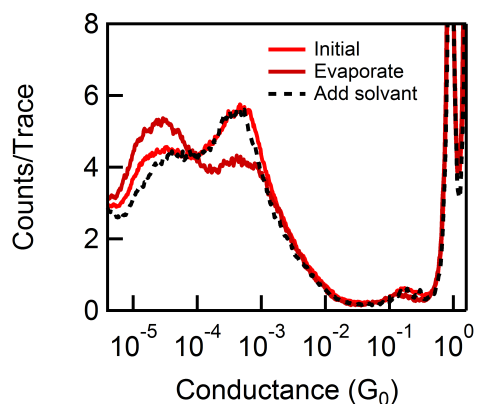


Figure 4.3: Conductance histograms of **1**. “Initial” is constructed from the data of 1 - 5,000 traces. “Evaporate” is constructed from the data of 15,000 - 20,000. “Add solvent” is constructed from data of 5000 traces collected immediately after 2 drops of solvent was added.

The fourth and most surprising distinction between **1** and other molecular wires demonstrating multiple conductance states<sup>255,276,277</sup> is that the ratio between the high and low G states is concentration-dependent. The one-dimensional conductance histogram in Figure 4.2c shows that as solvent evaporates over time, the high G peak diminishes as the low G peak grows in. This effect is reversible: replenishing the solvent subsequent to evaporation restores the initial peak distribution (Figure 4.3). We find the high G peak is more intense in dilute solutions (1 mM) whereas the low G peak is more intense in concentrated solutions (10 mM) in both trichlorobenzene and trimethoxybenzene solvents (Figures 4.4 and 4.5). At 1 mM in 1-bromonaphthalene (1-BN), however, the high G peak is conspicuously absent (Figure 4.2d, red).

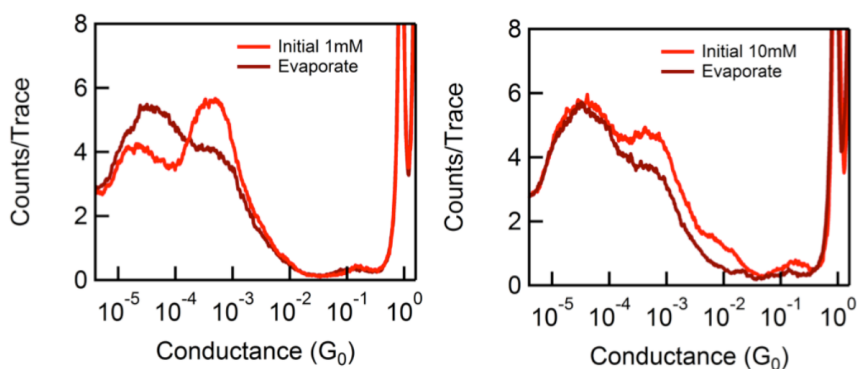


Figure 4.4: Conductance histograms of **1** in solvent 1,2,4-trichlorobenzene (TCB) with initial concentration 1 mM (left) and 10 mM (right). “Add solvent” is constructed from data of last 5000 traces collected. We see that at 10 mM, the measurement nears the upper limit of the shifting peak distribution towards the low G state.

We attribute the low G state in **1** to sulfur-to-sulfur conductance because its conductance-displacement profile is nearly identical to that of dimethylsilane **2** (Figure 4.6a).<sup>78</sup> We hypothesize that the high G state represents a junction where current flows between one of the sulfides and the silacycle (Figure 4.7a). This junction geometry is

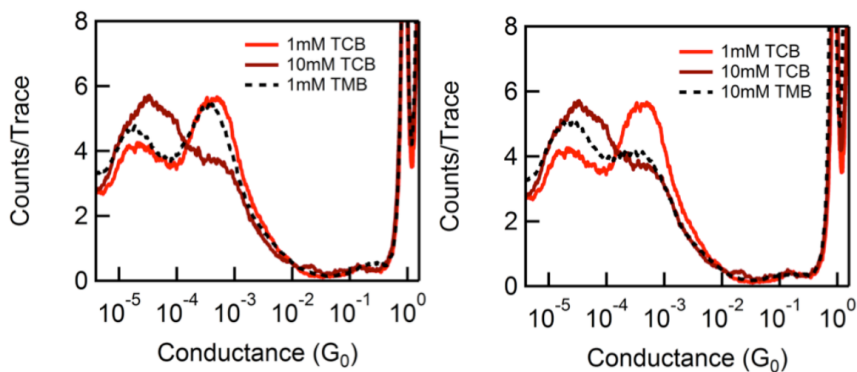


Figure 4.5: Conductance histograms of **1** in solvent 1,2,4-trimethoxybenzene (TMB) with initial concentration 1 mM (left) and 10 mM (right) compared with TCB.

consistent with the shorter elongation length of the high G state. Furthermore, it explains the lack of the high G peak in 1-bromonaphthalene. We have previously shown that 1-bromonaphthalene binds much more strongly to undercoordinated Au sites relative to chlorinated and ethereal solvents.<sup>278</sup> Accordingly, the absence of the high G state suggests that bromonaphthalene molecules are preventing the formation of the weak Au–silacycle contact in the high G geometry. This Au–silacycle interaction must also be weaker than the Au-SMe linkage because the low G state is unaffected in the 1-BN experiment. Indeed, we find that the Au–silacycle conduit is too fragile to form on its own, as monosulfide **3** has no measurable conductance (Figure 4.6b). The secondary Au–SMe linkage is therefore necessary to organize the silacycle onto a nearby Au atom. Because the Au–silacycle interaction is easily disrupted, the high G state only occurs if the Au atoms that span the auxiliary sulfide and silacyclobutane linkages are uncoordinated, thus explaining the concentration dependence in trichlorobenzene: at high concentrations, there are significantly more Au atoms coordinated by stronger sulfide linkages and, therefore, a lower probability that the high G junction geometry can be accessed (Figure 4.7b).

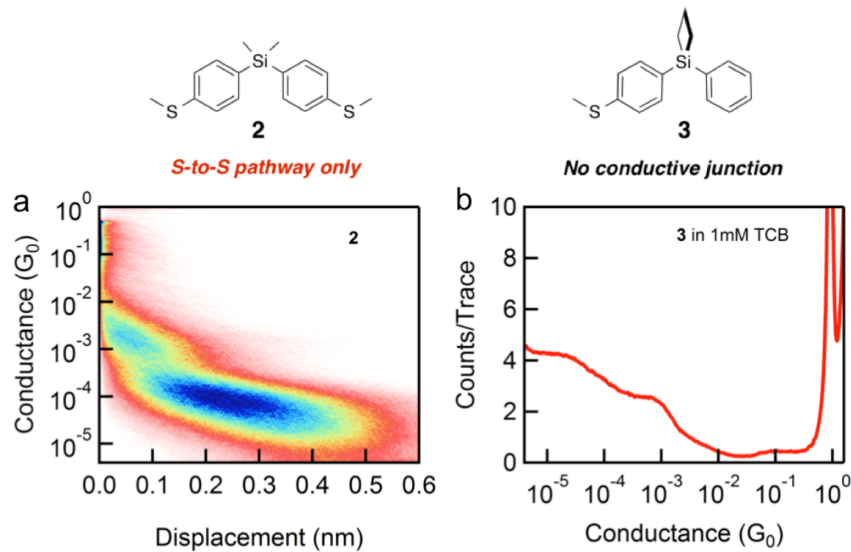


Figure 4.6: (a) Conductance histograms of **2** in TCB. (b) Conductance histogram of **3**. No conductive junction is observed for **3** in TCB at 1 mM concentration.

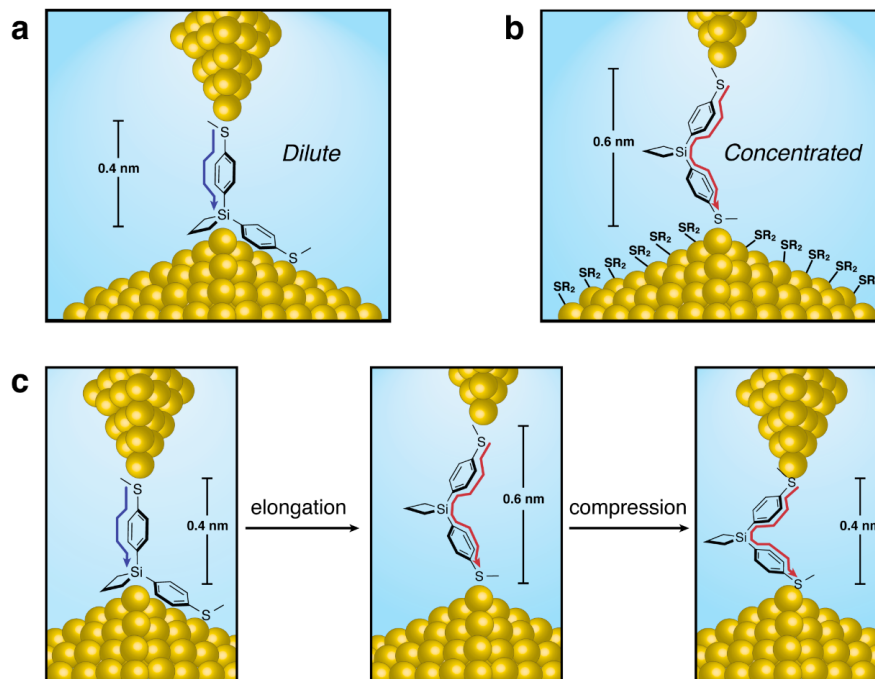


Figure 4.7: (a) In dilute conditions, an auxiliary sulfur group organizes the Au–silacycle conduit. (b) At higher concentrations, more molecules assemble on the electrode surface and the weak Au–silacycle conduit is more easily displaced. (c) A schematic explaining the non-adiabatic nature of single-junction switching.

The switching statistics from the elongation and compression experiments are also consistent with this explanation. Switching from high to low G is frequent (65%) because the molecule is easily pulled out of the Au–silacycle interaction to the more stable low G conformer at  $\Delta x = 0.6$  nm. Switching from low to high G is less frequent (13%) because there is poor incentive to form the Au–silacycle complex, as there are other geometries the low G state can adopt at  $\Delta x = 0.4$  nm (Figure 4.7c). This model for our high G state is also supported by the bondings of others<sup>279,280</sup> who have shown that ethynyltrimethylsilanes form self-assembled monolayers on gold surfaces through Au–silane interactions.

The Au–silane conduit observed here is specific to highly strained silicon rings. The STM-BJ measurement of less strained silacyclopentane **4** ( $\text{CH}_2\text{-Si-CH}_2$ ,  $96^\circ$ ) gives a single conductance peak at  $5.1 \times 10^{-5} G_0$  corresponding to the low G state and analogous to dimethylsilane **2** (Figure 4.8a). We also find this high G state is not a generality of strained four-membered rings. All-carbon cyclobutane analog **5** gives a single conductance peak ( $1.7 \times 10^{-4} G_0$ ) close in magnitude to that for bis((4-methylthio)-phenyl)methane **14** ( $1.2 \times 10^{-4} G_0$  (Figure 4.8b)). Cyclobutane **5** is significantly strained, with a ring angle of  $87^\circ$  in the crystal structure. The fact that cyclobutane **5** does not yield a secondary conductance state highlights a fundamental difference between carbon and silicon: though **1** and **5** are structurally analogous, the electronics of strained silicon enables coupling between the gold electrode and silacycle.

Conductance in these molecular systems typically occurs through tunneling, which is strongly distance dependent.<sup>274</sup> The Au–silacycle interaction provides a shorter conduit relative to the distal methyl sulfide, thereby enabling high conductance even in structures that do not typically conduct. Previously we demonstrated that tetramethyldisilox-

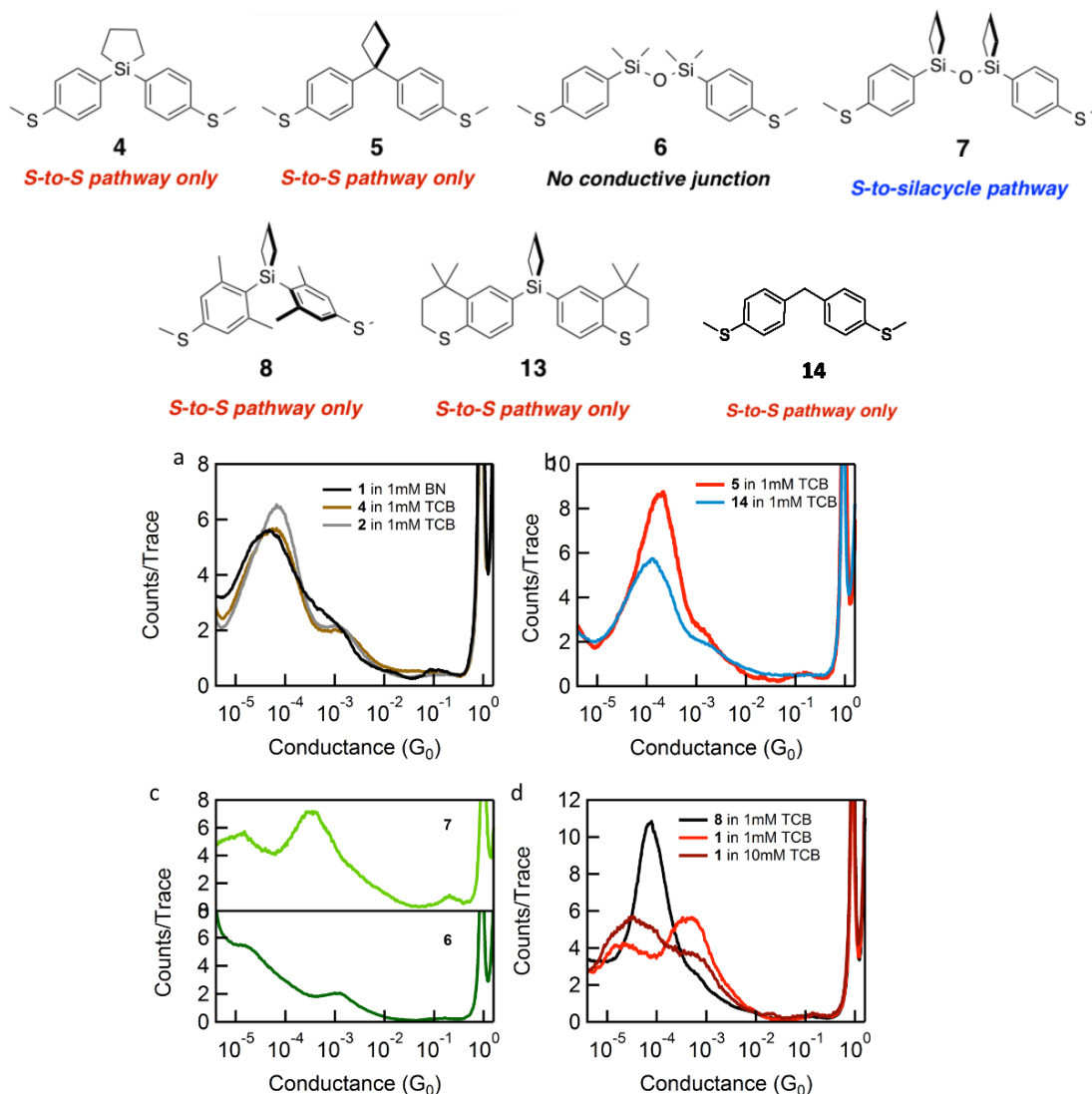


Figure 4.8: Conductance histogram of (a) **1** in 1 mM BN, **2** and **4** in 1 mM TCB, (b) **5** and **14** in 1 mM TCB, (c) **6** and **7** in 1 mM TCB, (d) **8** in 1 mM TCB, **1** in 1 mM and 10 mM TCB.

ane **6** does not form conductive junctions because the oxygen atom disrupts delocalization across the molecule in the orbital most commonly ascribed to S-to-S conductance (HOMO).<sup>78</sup> DFT calculations show that the HOMO of bis(cyclobutyl)disiloxane **7** is similarly localized on one end of the molecule. We find that disiloxane **7** gives a high  $G$  peak ( $2.5 \times 10^{-4} G_0$ ) that strongly diminishes with increasing concentration (Figure 4.7c). These results can be rationalized if the silacycle is an electronic contact that opens an alternative

conductance pathway.

We find that steric encumbrance near the silacyclobutane disables the Au–silacycle interaction and suppresses the high G state. We install ortho-methyl groups in silacyclobutane **8** to simultaneously frustrate arene rotation<sup>146,281</sup> and restrict the Au–silane interaction. Accordingly, the STM-BJ measurement of **8** yields a single, sharp, low G peak ( $7.6 \times 10^{-5} G_0$ , Figure 4.7d). We can also tune the high G state’s sensitivity to concentration by modifying the structure of the gold-molecule chelate. Butyl-linked **9** gives both high ( $3.1 \times 10^{-4} G_0$ ) and low G ( $1.8 \times 10^{-5} G_0$ ) peaks at 1 mM (Figure 4.9a). As solvent evaporates, the high G peak in **9** disappears entirely (darkest blue line) and resembles the analogous dimethylsilane **10** ( $2.6 \times 10^{-5} G_0$ ). This is in contrast with **1**, where the high G state is still accessible at higher concentrations. Like **1**, we find the high G peak in **9** re-emerges when solvent is replenished. These molecules demonstrate that the behavior of the high G state - whether it diminishes completely or does not appear at all, can be tuned by changing the linker structure.

To elucidate the conductance mechanism in these monosilane systems (and particularly the strained silanes), we synthesized **11** and **12** with meta-thioanisole linkers. Previous studies have shown that molecular wires with meta-substituted linkers are poor  $\pi$ -conductors due to quantum interference effects,<sup>45,47,282,283</sup> in which the nodes at the meta-position prevent the distal sulfur  $p\pi$  orbitals from coupling through the molecule. Our own investigations of oligoenes,<sup>283</sup> inorganic clusters,<sup>284</sup> fluorenes,<sup>178</sup> and longer silanes (Figure 4.10) have shown that while molecules with para-substituted thioanisole linkers strongly conduct, meta-substituted linkers yield little to no conductance. In the monosilanes studied here, we find that the magnitude of conductance is not significantly affected

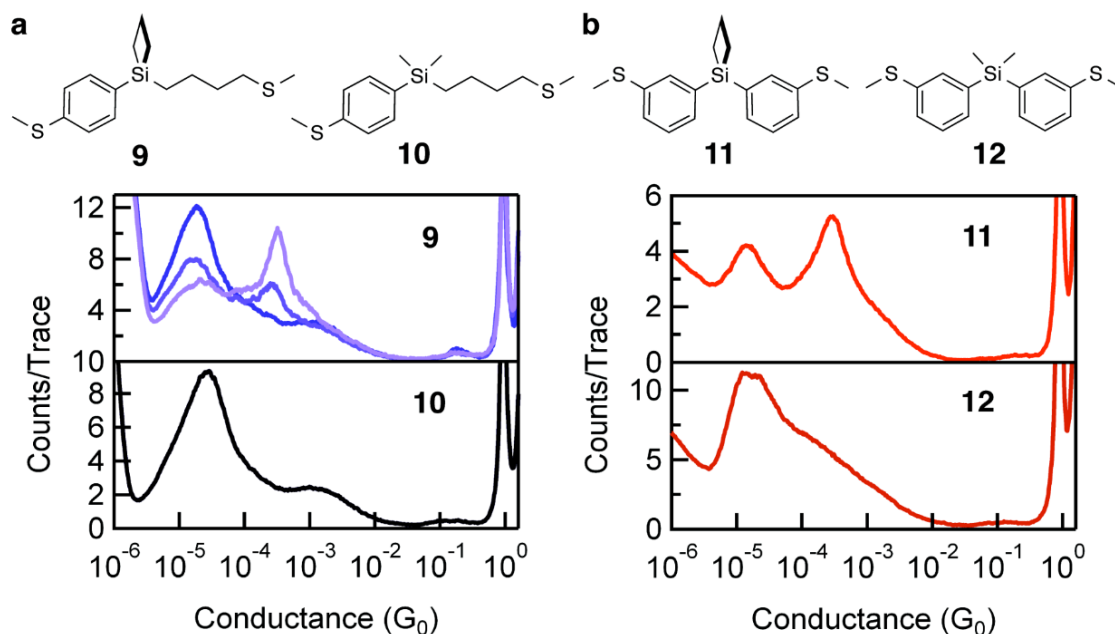


Figure 4.9: 1D histograms of (a) **9** and **10**; (b) **11** and **12**. (a) For **9**, the lightest line compiles the first 2000 traces while the darkest line compiles the last 2000 traces over 15 000 traces.

by whether the thioanisole linkers are para- or meta-substituted. Meta-linked **11** gives two sharp conductance peaks ( $2.7 \times 10^{-4} G_0$ ,  $1.4 \times 10^{-5} G_0$ ) similar to the high and low G states for **1** (Figures 4.9b). Dimethylsilane analog **12** furnishes a single peak ( $1.7 \times 10^{-5} G_0$ ) similar to the low G state in **11**. Conductance in **11** and **12** implies the  $\sigma$ -framework is the dominant conduit for diarylmonosilanes. The presence of the high G state in **11** further suggests the strained silane ‘shorts’ end-to-end conductance.

## Conclusion

The silacyclobutane family is useful in silicon-directed organic synthesis. The Lewis acidity at the silicon center activates an array of organic transformations that are otherwise difficult to achieve with unstrained silanes.<sup>285–287</sup> This Lewis acidity implies that the Si–C bond is strongly polarized toward the carbon. We speculate that it is these vicinal car-

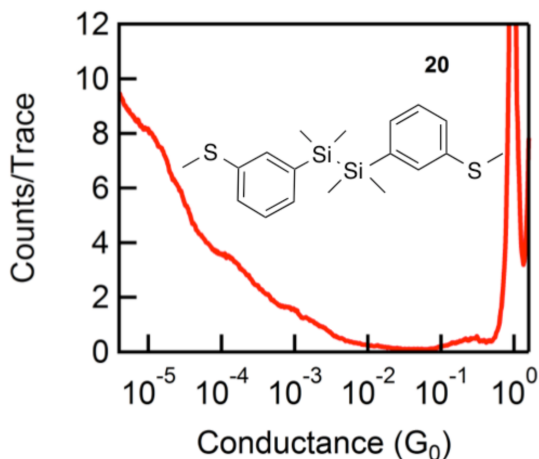


Figure 4.10: 1D histograms of bis(3-thioanisole)tetramethyldisilane **20**, which does not yield conductive junctions.

bons or polarized Si–C bonds that contact the gold electrode and propose that the Lewis acidic properties of silacyclobutanes in organic reaction chemistry manifest here as a new conductance state. Drawing such an analogy between reaction chemistry and molecular electronics opens the possibility that the vast store of synthetic methodology can be applied to create new types of molecular devices.

We demonstrate here for the first time that strained silanes couple directly to gold electrodes. This coupling enables strained silicon molecular wires with alkyl sulfide linkers to conduct through two distinct pathways: sulfur-to-sulfur and sulfur-to-silacycle. We find that the molecular wire ‘chooses’ its conductive pathway based on the surface environment of the Au electrodes. Furthermore, we can controllably switch from the high to low G state in a single junction by modulating the tip–substrate distance. Our studies here uncover the electronic effects of straining silicon at the molecular level and provide a foundation for the realization of strained silicon molecular components.

## Elongation and Compression Experiments Details

Here, we describe our modified STM-BJ studies regarding the junction elongation and compression experiments, as detailed in Figure 4.2b. We begin both experiments by reaching a gold-gold contact of  $5G_0$  to ensure a new Au point contact configuration each time. We then pull out the gold tip (20nm/s) to the desired tip-substrate displacement and hold the tip for 70 ms. In the elongation experiment, we pull the tip for another 0.2nm. In the compression experiment, we push back for another 0.2nm. We hold for another 70ms, then pull until junction breaks. The push/pull 0.2 nm distance was chosen based on the difference in extension displacement between the high and low G molecular plateaus, as seen in Figure 4.2a. The high G state was defined by a range between  $\log(G/G_0) = -2.9$  to  $-3.7$ ; the low G state was defined by a range between  $\log(G/G_0) = -3.7$  to  $-5.2$ . Traces starting in the high G state during the first hold period were selected for the elongation experiment; traces starting in the low G state during the first hold period were selected for the compression experiment. We used the same range to determine whether we were observing the high or low G state in the second hold period.

We used an algorithm to select traces based on this criteria from a set of 20,000 traces for both the elongation and compression experiments. We started our measurement at 1 mM, and every 5000 traces, we added solvent to the experimental setup to maintain a dilute concentration. 2-dimensional histograms are shown in Figure 4.11 for the selected traces from the elongation and compression experiments.

Elongation: Among 2200 traces selected with the criteria stipulated above, 254 traces (12%) show no switching after pulling the gold tip by 0.2 nm, 1435 traces (65%) switch from

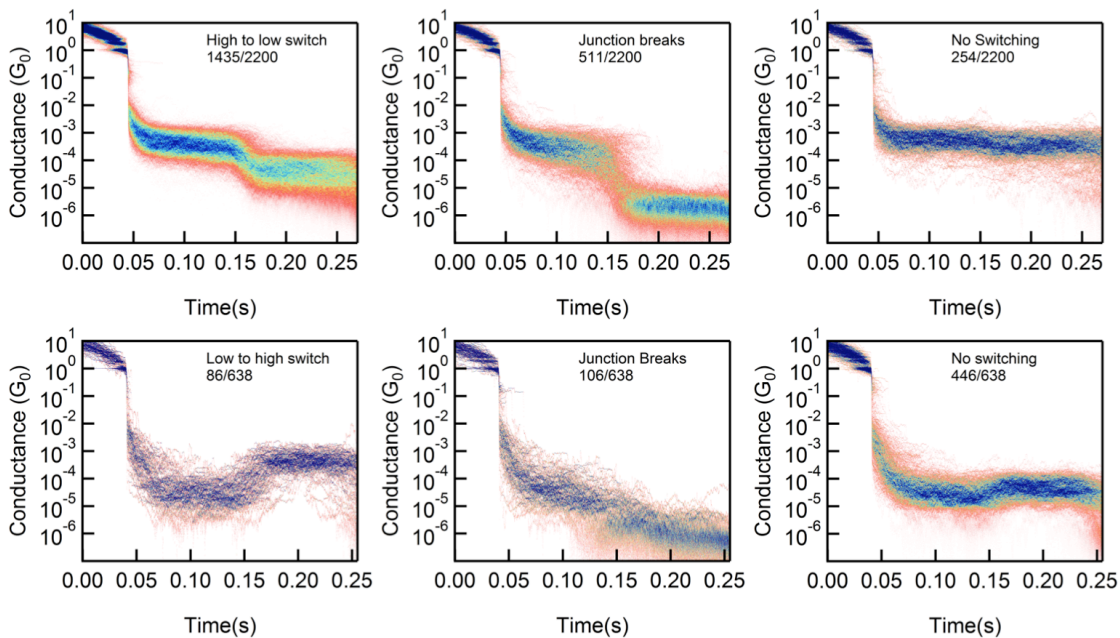


Figure 4.11: 2D histograms of (Top) Elongation and (Bottom) Compression conductance measurement of **1**. Conductance traces were categorized into (Left) “Junction Switching”, (Middle) “Junction Breaking” and (Right) “No Switching” three groups.

high to low  $G$  state, and the remaining 511 traces (23%) result in a junction break.

Compression: 638 traces demonstrated a molecule bridging the gap in the low  $G$  conformer during the first hold. 446 of these traces (70%) resulted in no switching after pushing the tip from 0.6 to 0.4 nm, 86 traces (13%) showed switching from low to high  $G$  state, while the remaining 106 traces (17%) resulted in a junction break.

## 4.2 Ring-Strained Disilanes Creates High Conductance Pathways by Way of Direct $\sigma$ Si-Si to Au Coordination

### Preface

This section is based on the manuscript entitled *High-Conductance Pathways in Ring-Strained Disilanes by Way of Direct  $\sigma$ -Si-Si to Au Coordination* by Nathaniel Kim, Haixing Li, Latha Venkataraman, and James Leighton published in JACS.<sup>16</sup> Nathaniel Kim of Prof. Leighton' group synthesized and characterized all compounds. I performed the conductance measurements and data analysis.

### Abstract

A novel and highly conducting electronic contact between a strained disilane and Au is demonstrated through scanning tunneling microscope-based single molecule measurements. Conformationally locked cis diastereomers of bis sulfide anchor-equipped 1,2-disilaacenaphthenes readily form high-conducting junctions in which both sulfide anchors bind in a bipodal fashion to one gold electrode, providing enough stability for a stable electrical contact between the Si-Si  $\sigma$  bond and the other electrode.

### Introduction

The advent of reliable methods to measure single molecule conductance through metal-molecule-metal junctions<sup>83,274,288,289</sup> has inspired efforts to probe molecular and electronic

structure-conductivity relationships as well as the nature of the interaction between the anchor or contact groups and the electrodes.<sup>254</sup> While typically the anchor groups (i.e. sulfides and amines) both mechanically and electronically couple to the electrodes, it has also been demonstrated that different structures within a molecule can serve as mechanical and electronic anchors.<sup>10,277</sup> For example, the work of Su et al. showed that sulfides can serve as a mechanical anchor while a silacyclobutane group formed the electrical anchor enabling a high conductance pathway through the molecular backbone.<sup>10</sup> Here, in an effort to further explore and elucidate strained silacycle-electrode interactions, we have examined the conductance properties of sulfide anchor-equipped 1,2-disilaacenaphthenes, and find that a novel bipodal molecule to gold substrate binding mode enables the strained high energy Si-Si  $\sigma$  bond to form a stable electrical contact without a mechanical anchor.

## Results and Discussion

Bisthioanisole substituted 1,2-disilaace-naphthenes **1** (trans) and **2** (cis) (Figure 4.12) were synthesized by adapting known procedures for the synthesis of 1,2-disilaacenaphthenes.<sup>290–292</sup> Though we have thus far been unable to obtain crystals of either **1** or **2**, we calculated their structures using the B3LYP functional and the 6-31G\*\* basis sets with Jaguar. In contrast to acenaphthene which manifests angle strain at the 1 and 8 positions of the naphthalene, the far longer Si-Si bond (2.35 and 2.29 Å for **1** and **2**, respectively) results in angle strain at silicon (C(Np)-Si-Si bond angles = 92° for both **1** and **2**), which raises the energy of the Si-Si  $\sigma$  bond.

The conductance properties of disilanes **1** and **2** were evaluated using the scanning tunneling microscope-based break junction (STM-BJ) technique.<sup>8</sup> While the trans

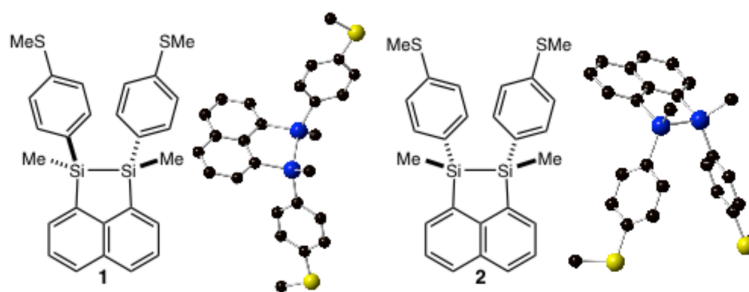


Figure 4.12: 1,2-Disilaacenaphthenes **1** and **2**, and the DFT-optimized structures (H atoms omitted for clarity).

diastereomer **1** showed only a single low conductance peak (low  $G$ ) at  $4.0 \times 10^{-5} G_0$  attributable to the sulfur to sulfur pathway (Figure 4.13a), the cis diastereomer **2** showed a prominent high conductance (high  $G$ ) peak at  $1.4 \times 10^{-3} G_0$  along with a less prominent low  $G$  peak at  $1.9 \times 10^{-5} G_0$  (Figure 4.13b).

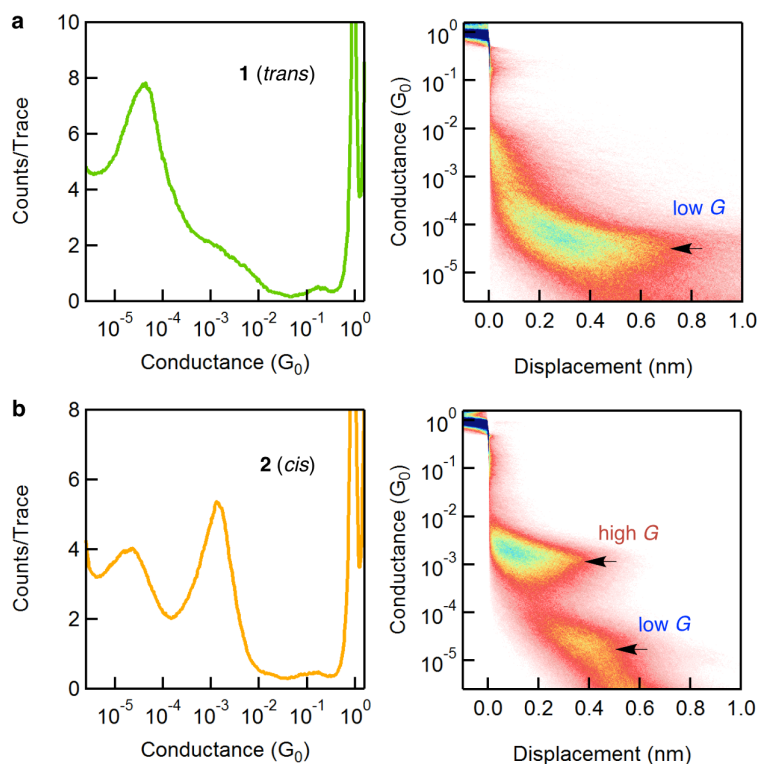


Figure 4.13: 1D and 2D conductance histograms generated from 13,500 and 20,000 conductance traces measured at an applied voltage of 250 mV without any data selection for (a) trans disilane **1** and (b) cis disilane **2**.

The low G band for **2** could be readily attributed to the sulfur to sulfur pathway (Figure 4.14a), but the origin of the prominent high G band was less immediately clear. The shorter displacement value ( $\sim 0.4$  nm) associated with the high G band is indicative of a conduction path from the silacycle to one of the SMe groups,<sup>10</sup> but a binding arrangement with the non-conducting thioanisole serving as a mechanical anchor on the silacycle-contacting electrode (in analogy to the silacyclobutane) was difficult to envision given the  $\sim 4^\circ$  dihedral angle of the thioanisole groups around the Si-Si bond. Conversely, this rigid co-planar arrangement of the thioanisole groups suggested the possibility that both sulfurs bind to one of the gold electrodes in a bipodal fashion, with the strained high energy Si-Si  $\sigma$  bond in contact with the other electrode (Figure 4.14b). Such a bipodal binding mode would be expected to greatly reduce the entropic cost associated with sustaining a stable contact between the weakly donating Si-Si  $\sigma$  bond and the gold electrode. It is possible as well that the naphthyl group and/or the methyl groups provide additional stability through van der Waals interactions with the gold electrode.<sup>83</sup>

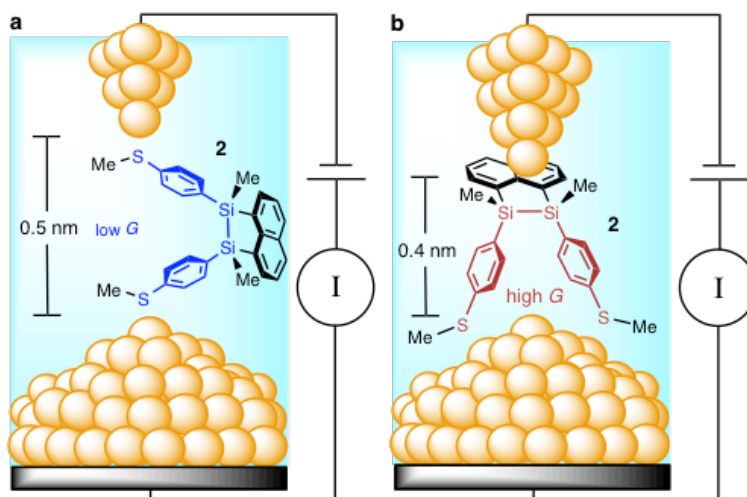


Figure 4.14: (a) The low G sulfur to sulfur junction for **2**. (b) Bipodal binding of both thioanisole groups to one gold electrode with the other making direct electrical contact to the Si-Si  $\sigma$  bond.

In an effort to further elucidate the nature of the silacycle-electrode contact, we prepared disilaacenaphthenes **3** (trans) and **4** (cis) in which one of the thioanisole groups has been replaced with a  $-C_6H_4CH_2SCH_3$  group. As shown in Figure 4.15a and d, the 1D and 2D histograms for **3** revealed two conductance bands at  $1.6 \times 10^{-5}$  and  $3.5 \times 10^{-4} G_0$ , while the 1D and 2D histograms for **4** showed two similar conductance features at  $1.8 \times 10^{-5} G_0$  and  $3.4 \times 10^{-4} G_0$  (Figure 4.15b and d). In the latter case, a concentration dependence was noted as the first 16,000 traces showed primarily the high  $G$  band, while the last 10,000 showed mainly the low  $G$  peak (Figure 4.15c, e and f).

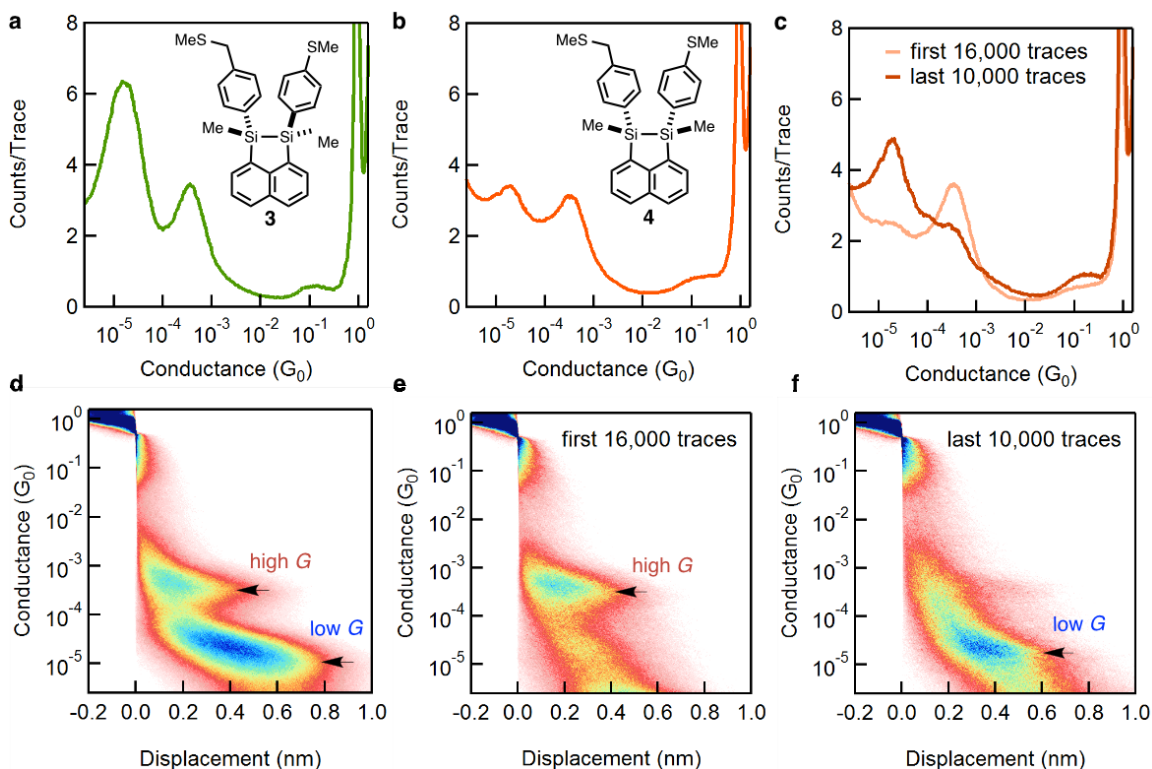


Figure 4.15: 1D conductance histograms for (a) trans disilane **3**, (b) combined traces for cis disilane **4**, and (c) traces split into two groups (first 16,000 and last 10,000) for cis disilane **4**. 2D conductance histograms for (d) trans disilane **3** and (e)(f) cis disilane **4**. (e) is made from first 16,000 traces; (f) is made from last 10,000 traces.

As with **1** and **2**, the displacement values associated with the low  $G$  peaks of **3** ( $\sim 0.8$

nm) and **4** ( $\sim 0.6$  nm) are consistent with the sulfur to sulfur pathways and each is, as expected due to the addition of a methylene group,  $\sim 0.1$  nm longer than the corresponding values for **1** ( $\sim 0.7$  nm) and **2** ( $\sim 0.5$  nm) respectively. The displacement values associated with the high G peaks are both  $0.4$  nm, once again indicative of silacycle to sulfide conduits. For **3**, this may be understood as shown in Figure 4.16a, with the alkyl sulfide serving as a mechanical anchor in analogy to the high G configuration of the silacyclobutane.<sup>10</sup> Conversely, we suggest that the cis isomer **4** binds in a bipodal fashion similarly to **2**, with conduction proceeding primarily or exclusively through the thioanisole group (Figure 4.16b). The significant drop in the high G to low G ratio relative to **2** is easily rationalized within this framework as the added methylene group is expected to increase the entropic cost of sustaining the weak Si-Si to Au electrical contact, while the observed concentration dependence may be understood as a consequence of the alkyl sulfide binding more strongly to the gold substrate: at high concentrations, the surface is saturated with alkyl sulfides leaving no available coordination sites for the less strongly binding aryl sulfides.

The conductance switching characteristics of **2-4** upon junction elongation support the proposed high G binding configurations. We used a modified ramp in which the high G junction was established and then elongated by  $0.2$  nm, and analyzed the impact of elongation on the junction conductance in large data sets of 3000-6000 traces (Figures 4.18-4.21). For both **2** and **4**, a switch from the high G to low G state was observed in 37% of the traces (Table 4.1), while in the majority of traces the high G junction was either maintained (11% and 23%) or broken (54% and 40%). In contrast, trans **3** showed the high G to low G switch in 65% of the traces, which is exactly the same number as for

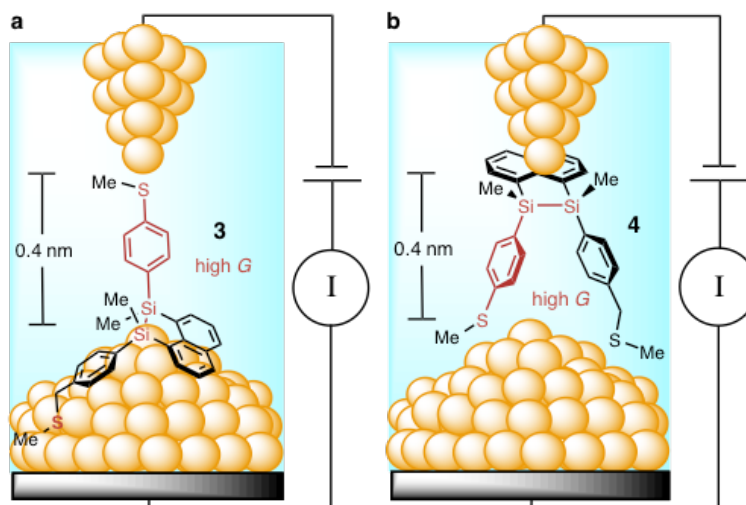


Figure 4.16: (a) Junction binding model for the high G state of **3**, with mechanical anchoring by the alkyl sulfide stabilizing the weak Si-Si to gold contact. (b) Junction binding model for the high G state of **4**, with bipodal sulfide binding to one electrode stabilizing the weak coupling of the Si-Si bond to the other gold electrode.

the silacyclobutane.<sup>10</sup> In these cases, the energetic cost of the high G to low G switch is expected to be minimal as the mechanically anchoring sulfide need only slide across the gold surface, consistent with the high frequency (65%) of the switch. Conversely, given the proposed bipodal binding configurations, the energetic cost of the high G to low G switch for **2** and **4** is expected to be significantly higher as it requires one of the thioanisole-Au contacts to break and a significant degree of molecular reorientation, consistent with the lower frequency of the high G to low G switch.

Molecule	Pull distance	High-to-Low	High-to-High	High-to-break
Cis <b>2</b>	(0.1nm)	29%	38%	33%
Cis <b>2</b>	(0.2 nm)	37%	11%	54%
Trans <b>3</b>	(0.2 nm)	65%	26%	9%
Cis <b>4</b>	(0.2 nm)	37%	23%	40%

Table 4.1: Switching percentages for Molecules **2-4** in the push-pull experiments.

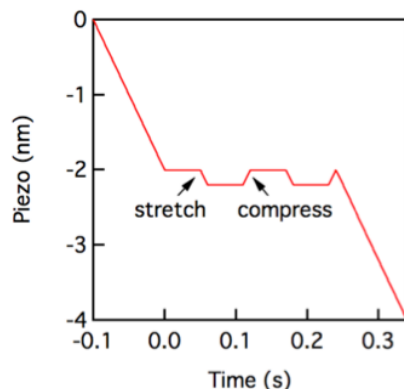


Figure 4.17: Piezo displacement plotted versus time for the push-pull experiment. We elongate the molecular junction, hold the junction in place for 0.05 s, first stretch the electrodes by 2 Å (or 1 Å), hold the junction at this new displacement for another 0.1 s, next compress the electrodes by 2 Å or 1 Å, then repeat this one more time and finally retract the electrodes until the junction breaks.

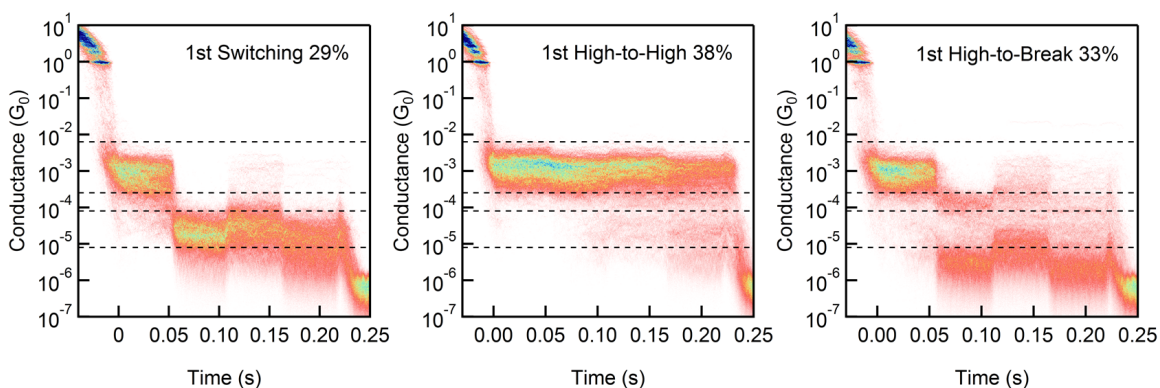


Figure 4.18: 2D histograms constructed from the measured traces on cis disilane **2** with 0.1nm stretch/compress distance. Vertical dashed lines indicate the high and low conductance peak range for cis disilane **2**. Left: 2D histogram demonstrates a high-to-low switching during the first pulling. Middle: 2D histogram demonstrates a sustaining junction in the first pulling. Right: 2D histogram demonstrates a breaking junction in the first pull.

The magnitudes of the high G conductance bands for **3** and **4** ( $3.5$  and  $3.4 \times 10^{-4} G_0$ ) are nearly identical though significantly smaller than that of the high G band for **2** ( $1.4 \times 10^{-3} G_0$ ). The proposed high G binding modes for **2-4** are consistent with these data as **3** and **4** conduct primarily or exclusively through a single Si-C<sub>6</sub>H<sub>4</sub>-SMe pathway (in close analogy to the high G pathway ( $4.2 \times 10^{-4} G_0$ ) for the previously described silacy-

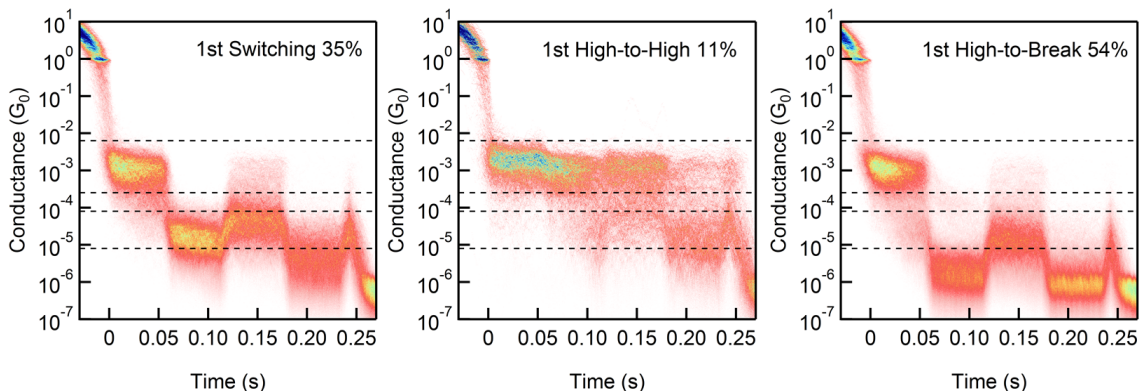


Figure 4.19: 2D histograms constructed from the measured traces on cis disilane **2** with 0.2nm stretch/compress distance. Vertical dashed lines indicate the high and low conductance peak range for cis disilane **2**. Left: 2D histogram demonstrates a high-to-low switching during the first pulling. Middle: 2D histogram demonstrates a sustaining junction in the first pulling. Right: 2D histogram demonstrates a breaking junction in the first pull.

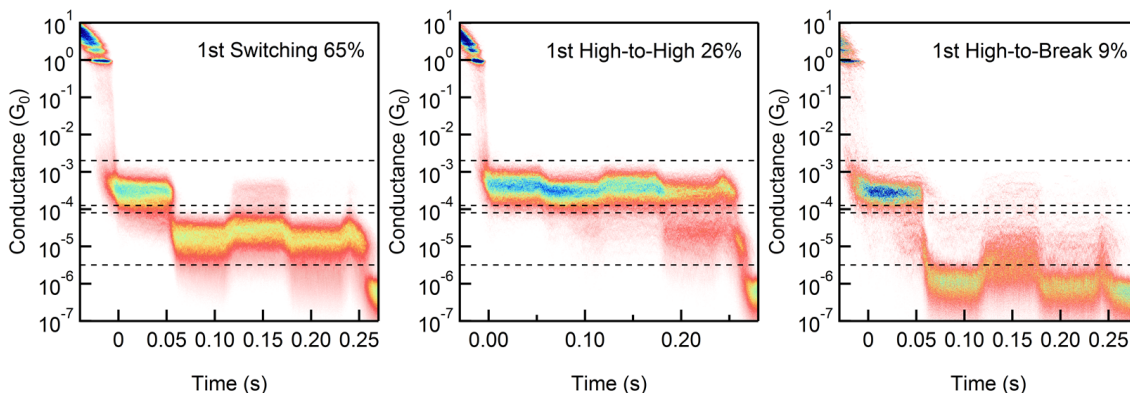


Figure 4.20: 2D histograms constructed from the measured traces on trans disilane **3** with 0.2nm stretch/compress distance. Vertical dashed lines indicate the high and low conductance peak range for trans disilane **3**. Left: 2D histogram demonstrates a high-to-low switching during the first pulling. Middle: 2D histogram demonstrates a sustaining junction in the first pulling. Right: 2D histogram demonstrates a breaking junction in the first pull.

clobutane<sup>10</sup>), while **2** conducts through two such pathways in parallel (we note here that Breslow, Venkataraman and Hybersten have demonstrated that the conductance through parallel components can be more than twice that of the corresponding single component circuit<sup>293</sup>).

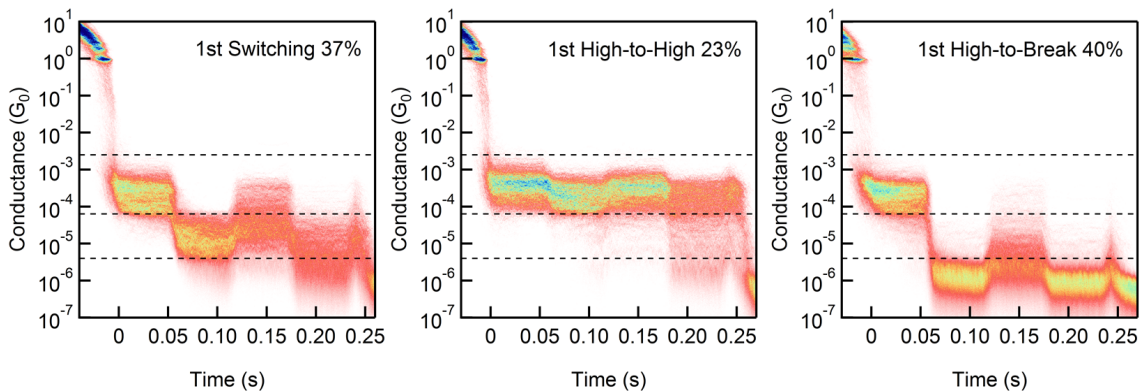


Figure 4.21: 2D histograms constructed from the measured traces on cis disilane **4** with 0.2nm stretch/compress distance. Vertical dashed lines indicate the high and low conductance peak range for cis disilane **4**. Left: 2D histogram demonstrates a high-to-low switching during the first pulling. Middle: 2D histogram demonstrates a sustaining junction in the first pulling. Right: 2D histogram demonstrates a breaking junction in the first pull.

Taken together, these data strongly support the conclusion that the primary electrical contact made in the high G binding modes is to the Si-Si  $\sigma$  bond. This makes sense in light of demonstrations of transition metal catalyzed additions of the strained Si-Si bond of 1,2-disilaacenaphthenes across reactive pi systems<sup>294–296</sup> (e.g. benzyne) which presumably proceed by way of oxidative addition of the Si-Si bond to the metal center and which may be preceded by  $\sigma$ -complex formation. Indeed, a copper to Si-Si  $\sigma$ -complex has been characterized,<sup>297</sup> and oxidative addition of a gold(I) species to a Si-Si bond has been demonstrated.<sup>298,299</sup> Other than the silacyclobutane<sup>10</sup> and the compounds reported here, the only previous report of a direct contact between silicon and a gold substrate is Fichou et al.'s demonstration that alkynyltrimethylsilanes can form self-assembled monolayers on gold surfaces,<sup>279,300</sup> but the detailed nature of the Si-Au interaction is still under investigation.<sup>280,301,302</sup> Our work clearly evidences a direct Si to Au contact in single molecule circuits and provides a well-precedented framework to understand that contact as being

a metal to Si-Si bond  $\sigma$ -complex.<sup>303</sup>

## Conclusion

Though conductance through multipodal (typically tripodal) anchor groups has been demonstrated,<sup>304–307</sup> our work also establishes a new strategy to leverage the reduction in entropic costs that derive from multipodal anchoring to stabilize otherwise too-weak-to-form electrical contacts between weak donors and metal electrodes. This strategy may prove generalizable beyond strained silacycles, and may provide a platform to explore reactions such as oxidative addition at the single molecule level.

---

## *Conclusion*

Over these four chapters, we have shown a rich new vein of research in single molecule conductance based on silicon molecular systems. Scanning Tunneling Microscope Break Junction has been the key experimental technique in these studies, allowing us to probe the fundamental transport physics of a metal-molecule-metal junction. We were driven by the following question: how will the charge transport properties of the silicon change as the active regions transition from microscale to molecular scale? By applying our understanding of the chemistry of the molecules, we hope to synthetically engineer function into devices built from silicon based molecules.

We first describe a single molecule approach to address the fragility of the low- $\kappa$  dielectrics. Instead of studying bulk dielectrics that contain a number of different interconnected chemical bonds, we synthesize molecular analogs of the low- $\kappa$  dielectrics containing one chemical bond and measure their breaking probabilities under an applied voltage. In the assessment of molecular backbones that consist of C—C, Si—Si, Ge—Ge, Si—C, and Si—O bonds, we found that Si—Si and Ge—Ge bonds both rupture under an applied voltage above 1V. In contrast, C—C and Si—C do not rupture. We additionally designed the disilaacenaphthene system of which the bond-ruptured species would still constitute an intact junction and could thus conduct through an alternate pathway. By

probing the tunneling current of the broken junctions of disilaacenaphthene, we show that the Si-Si bond ruptures under high bias and this bond cleavage yields a new conduction pathway through the naphthyl group. We further investigate the bond rupture mechanism using *ab initio* calculations and molecular dynamic simulations and show that the tunneling electrons excite the molecular vibrational modes leading to the bond rupture. Forming a stable molecular junction and then inducing the breaking of chemical bonds through the application of external stimuli elucidates the weak-link in the dielectrics and enables studies of fundamental reactions at the single molecule level.

We study the electrical properties of silicon at the molecular scale by carrying out conductance measurements on linear silanes and germanes. Silanes and germanes terminated with methyl sulfide linker groups show a slower decay in conductance with increasing length than the alkanes, demonstrating a more effective charge transport through Si—Si and Ge—Ge bonds than the analogous C—C bond. Surprisingly, these strongly coupled Si—Si and Ge—Ge  $\sigma$ -bonds display a unique mode of molecular conductance switching by a mechanical modulation of the junction distance. This molecular switching in oligosilanes and oligogermanes is caused by a stereoelectronic effect of the two terminal dihedral angles that couple the molecule to the gold electrodes. This finding showcases how the principles of mechanistic chemistry can be applied to create functionalities in single molecule electronic devices. Moreover, we explored different metals as the contact electrodes to form single molecule junctions with thiol-terminated silanes. We found that unlike many other molecular systems, Ag-molecule-Ag junctions show higher conductances than either Pt-molecule-Pt or Au-molecule-Au junctions.

Next, we expand our single-molecule conductance study from linear silanes to sili-

con rings. A di-substituted ring can have the two substituents on the same side of the ring or opposite side of the ring, a phenomenon referred to as isomerism. Additionally, each silicon ring isomer has numerous conformations. In order to determine how isomerism and each isomer's conformations affect electron transfer in molecular components, we choose five-membered silicon ring as a sample system to perform single molecule conductance measurement. We discover that the conductance of the isomers is facilitated or inhibited by their conformation, and the measured broad conductance peaks are a result of multiple conformations. This information is important as we continue to explore the electronic properties of other cyclic silanes.

We embed silicon rings - including four-membered and five-membered rings and 221 and 222 bicyclics - in a silicon molecular wire and measure their electron transport properties. We find that the four-membered ring has a similar conductance as its linear counterpart; the rest show much lower conductances than their linear versions. In particular, the conductance of one bicyclic silane is extremely low. Density functional theory calculation shows a clear anti-resonance close to the Fermi energy, indicating a destructive quantum interference feature in this system. This finding provides us with experimental evidence that the quantum interference effect also exists in  $\sigma$ -bonded molecular wires.

Lastly, we provide two examples of high-conducting pathway in silanes by incorporating strain into the molecule. The first is the strained silacyclobutane. With this strained silacycle, the molecular wire conducts not only from the terminal sulfur-to-sulfur, but also from sulfur-to-silacycle. Therefore we observe two conductance features, and we can switch between the two conductance states in a single molecule junction by modulating the tip-substrate electrode distance. The second is disilaacenaphthene terminated

with thioanisole groups. With a ring-strained disilane, a novel bipodal binding mode is realized wherein both thioanisole groups coordinate to the gold substrate. Such contact constitutes a clear example of a direct Si to Au contact in single molecule circuits and enables a more efficient pathway for charge transport.

The work presented in this thesis details a deeper understanding of the fundamental transport physics of silicon at the single molecule level. This knowledge is critical as silicon electronics is now entering the sub-nanometer scale. From a wider perspective, this research has proven that the understanding about reaction chemistry of the molecular components can be applied to design functional ultraminiaturized electronics.

---

## Bibliography

- (1) Feynman, R. P. *Engineering and science* **1960**, *23*, 22–36.
- (2) Shvets, A. *CPU World* **2014**.
- (3) Lonsdale, K. *Proceedings of the Royal Society of London* **1929**, 494–515.
- (4) Ha, T.; Enderle, T.; Ogletree, D.; Chemla, D. S.; Selvin, P. R.; Weiss, S. *Proceedings of the National Academy of Sciences* **1996**, *93*, 6264–6268.
- (5) Rust, M. J.; Bates, M.; Zhuang, X. *Nature methods* **2006**, *3*, 793–796.
- (6) Betzig, E.; Patterson, G. H.; Sougrat, R.; Lindwasser, O. W.; Olenych, S.; Bonifacino, J. S.; Davidson, M. W.; Lippincott-Schwartz, J.; Hess, H. F. *Science* **2006**, *313*, 1642–1645.
- (7) Hess, S. T.; Girirajan, T. P.; Mason, M. D. *Biophysical journal* **2006**, *91*, 4258–4272.
- (8) Xu, B.; Tao, N. J. *Science* **2003**, *301*, 1221–1223.
- (9) Venkataraman, L.; Klare, J. E.; Tam, I. W.; Nuckolls, C.; Hybertsen, M. S.; Steigerwald, M. L. *Nano Letters* **2006**, *6*, 458–462.
- (10) Su, T. A.; Widawsky, J. R.; Li, H.; Klausen, R. S.; Leighton, J. L.; Steigerwald, M. L.; Venkataraman, L.; Nuckolls, C. *Journal of the American Chemical Society* **2013**, *135*, 18331–18334.
- (11) Chen, W.; Li, H.; Widawsky, J. R.; Appayee, C.; Venkataraman, L.; Breslow, R. *Journal of the American Chemical Society* **2014**, *136*, 918–920.
- (12) Su, T. A.; Li, H.; Steigerwald, M. L.; Venkataraman, L.; Nuckolls, C. *Nat Chem* **2015**, *7*, 215–220.
- (13) Li, H.; Su, T. A. A.; Zhang, V.; Steigerwald, M. L. L.; Nuckolls, C.; Venkataraman, L. *J Am Chem Soc* **2015**, *137*, 5028–33.

- (14) Su, T. A.; Li, H.; Zhang, V.; Neupane, M.; Batra, A.; Klausen, R. S.; Kumar, B.; Steigerwald, M. L.; Venkataraman, L.; Nuckolls, C. *Journal of the American Chemical Society* **2015**, *137*, 12400–12405.
- (15) Li, H.; Kim, N. T.; Su, T. A.; Steigerwald, M. L.; Nuckolls, C.; Darancet, P.; Leighton, J. L.; Venkataraman, L. *Journal of the American Chemical Society* **2016**, *138*, 16159–16164.
- (16) Kim, N. T.; Li, H.; Venkataraman, L.; Leighton, J. L. *J Am Chem Soc* **2016**, *138*, 11505–11508.
- (17) Li, H.; Garner, M. H.; Shangguan, Z.; Zheng, Q.; Su, T. A.; Neupane, M.; Li, P.; Velian, A.; Steigerwald, M. L.; Xiao, S.; Nuckolls, C.; Solomon, G. C.; Venkataraman, L. *Chemical Science* **2016**, *7*, 5657–5662.
- (18) Su, T. A.; Li, H.; Klausen, R. S.; Widawsky, J. R.; Batra, A.; Steigerwald, M. L.; Venkataraman, L.; Nuckolls, C. *Journal of the American Chemical Society* **2016**, *138*, 7791–7795.
- (19) Ross, I. M. *Bell Labs Technical Journal* **1997**, *2*, 3–14.
- (20) Melliar-Smith, C. M.; Haggan, D. E.; Troutman, W. W. *Bell Labs Technical Journal* **1997**, *2*, 15–28.
- (21) Cui, Y.; Lieber, C. M. *Science* **2001**, *291*, 851–853.
- (22) Tian, B.; Zheng, X.; Kempa, T. J.; Fang, Y.; Yu, N.; Yu, G.; Huang, J.; Lieber, C. M. *Nature* **Oct. 2007**, *449*, 885–9.
- (23) Liu, C.-C.; Feng, W.; Yao, Y. *Phys. Rev. Lett.* **Aug. 2011**, *107*, 076802.
- (24) Liu, F.; Liu, C.-C.; Wu, K.; Yang, F.; Yao, Y. *Phys. Rev. Lett.* **Aug. 2013**, *111*, 066804.
- (25) Tao, L.; Cinquanta, E.; Chiappe, D.; Grazianetti, C.; Fanciulli, M.; Dubey, M.; Molle, A.; Akinwande, D. *Nat Nanotechnol* **Mar. 2015**, *10*, 227–31.
- (26) Liu, N.; Lu, Z.; Zhao, J.; McDowell, M. T.; Lee, H.-W.; Zhao, W.; Cui, Y. *Nat Nano* **2014**, *9*, 187–192.
- (27) Su, X.; Wu, Q.; Li, J.; Xiao, X.; Lott, A.; Lu, W.; Sheldon, B. W.; Wu, J. *Advanced Energy Materials* **2014**, *4*, 1300882, 1300882–n/a.
- (28) Reed, M.; Zhou, C.; Muller, C.; Burgin, T.; Tour, J. *Science* **1997**, *278*, 252–254.

- (29) Frei, M.; Aradhya, S. V.; Koentopp, M.; Hybertsen, M. S.; Venkataraman, L. *Nano letters* **2011**, *11*, 1518–1523.
- (30) Liang, W.; Shores, M. P.; Bockrath, M.; Long, J. R.; Park, H. *Nature* **June 2002**, *417*, 725–729.
- (31) Park, J.; Pasupathy, A. N.; Goldsmith, J. I.; Chang, C.; Yaish, Y.; Petta, J. R.; Rinkoski, M.; Sethna, J. P.; Abruna, H. D.; McEuen, P. L.; Ralph, D. C. *Nature* **June 2002**, *417*, 722–725.
- (32) Cui, X.; Primak, A.; Zarate, X.; Tomfohr, J.; Sankey, O.; Moore, A.; Moore, T.; Gust, D.; Harris, G.; Lindsay, S. *Science* **2001**, *294*, 571–574.
- (33) Guo, X. et al. *Science* **2006**, *311*, 356–359.
- (34) Guo, X.; Gorodetsky, A. A.; Hone, J.; Barton, J. K.; Nuckolls, C. *Nature nanotechnology* **2008**, *3*, 163–167.
- (35) Jia, C. et al. *Science* **2016**, *352*, 1443–1445.
- (36) Jia, C.; Ma, B.; Xin, N.; Guo, X. *Acc. Chem. Res* **2015**, *48*, 2565–2575.
- (37) Aradhya, S. V.; Nielsen, A.; Hybertsen, M. S.; Venkataraman, L. *ACS nano* **2014**, *8*, 7522–7530.
- (38) Van Wees, B. J.; van Houten, H.; Beenakker, C. W. J.; Williamson, J. G.; Kouwenhoven, L. P.; van der Marel, D.; Foxon, C. T. *Phys. Rev. Lett.* **Feb. 1988**, *60*, 848–850.
- (39) Wharam, D.; Thornton, T. J.; Newbury, R.; Pepper, M.; Ahmed, H.; Frost, J.; Hasko, D.; Peacock, D.; Ritchie, D.; Jones, G. *Journal of Physics C: solid state physics* **1988**, *21*, L209.
- (40) Nitzan, A.; Ratner, M. A. *Science* **2003**, *300*, 1384–1389.
- (41) Lindsay, S. M.; Ratner, M. A. *Advanced Materials* **2007**, *19*, 23–31.
- (42) Hybertsen, M. S.; Venkataraman, L.; Klare, J. E.; Whalley, A. C.; Steigerwald, M. L.; Nuckolls, C. *Journal of Physics: Condensed Matter* **2008**, *20*, 374115.
- (43) Solomon, G. C.; Andrews, D. Q.; Hansen, T.; Goldsmith, R. H.; Wasielewski, M. R.; Van Duyne, R. P.; Ratner, M. A. *The Journal of Chemical Physics* **2008**, *129*, 054701.
- (44) Xia, J.; Capozzi, B.; Wei, S.; Strange, M.; Batra, A.; Moreno, J. R.; Amir, R. J.; Amir, E.; Solomon, G. C.; Venkataraman, L., et al. *Nano letters* **2014**, *14*, 2941–2945.

- (45) Guédon, C. M.; Valkenier, H.; Markussen, T.; Thygesen, K. S.; Hummelen, J. C.; Van Der Molen, S. J. *Nature nanotechnology* **2012**, *7*, 305–309.
- (46) Sautet, P.; Joachim, C. *Chemical Physics Letters* **1988**, *153*, 511–516.
- (47) Solomon, G. C.; Andrews, D. Q.; Goldsmith, R. H.; Hansen, T.; Wasielewski, M. R.; Van Duyne, R. P.; Ratner, M. A. *Journal of the American Chemical Society* **2008**, *130*, PMID: 19053483, 17301–17308.
- (48) Bergfield, J. P.; Solomon, G. C.; Stafford, C. A.; Ratner, M. A. *Nano Letters* **2011**, *11*, PMID: 21661755, 2759–2764.
- (49) Markussen, T.; Stadler, R.; Thygesen, K. S. *Nano Letters* **2010**, *10*, PMID: 20879779, 4260–4265.
- (50) Markussen, T.; Stadler, R.; Thygesen, K. S. *Physical Chemistry Chemical Physics* **2011**, *13*, 14311–14317.
- (51) Borges, A.; Fung, E.-D.; Ng, F.; Venkataraman, L.; Solomon, G. C. *The Journal of Physical Chemistry Letters* **2016**, *7*, PMID: 27934052, 4825–4829.
- (52) Manrique, D. Z.; Huang, C.; Baghernejad, M.; Zhao, X.; Al-Owaedi, O. A.; Sadeghi, H.; Kaliginedi, V.; Hong, W.; Gulcur, M.; Wandlowski, T.; Bryce, M. R.; Lambert, C. J. *Nature Communications* **2015**, *6*, 6389.
- (53) Frisenda, R.; Janssen, V. A.E. C.; Grozema, F. C.; van der Zant, H. S. J.; Renaud, N. *Nat Chem* **Dec. 2016**, *8*, 1099–1104.
- (54) Solomon, G. C.; Herrmann, C.; Hansen, T.; Mujica, V.; Ratner, M. A. *Nat Chem* **Mar. 2010**, *2*, 223–8.
- (55) Chen, F.; Shinosky, M. *IEEE Transactions on Electron Devices* **2009**, *56*, 2–12.
- (56) Chen, F.; Bravo, O.; Harmon, D.; Shinosky, M.; Aitken, J. *Microelectronics Reliability* **2008**, *48*, 1375–1383.
- (57) Chen, F.; Shinosky, M. A. *Microelectronics Reliability* **2014**, *54*, 529–540.
- (58) Wu, E. Y.; Li, B.; Stathis, J. H. *Applied Physics Letters* **2013**, *103*, –.
- (59) Lombardo, S.; Stathis, J. H.; Linder, B. P.; Pey, K. L.; Palumbo, F.; Tung, C. H. *Journal of Applied Physics* **2005**, *98*, –.
- (60) Maex, K.; Baklanov, M.; Shamiryman, D.; Brongersma, S.; Yanovitskaya, Z. *Journal of Applied Physics* **2003**, *93*, 8793–8841.

- (61) Volksen, W.; Miller, R. D.; Dubois, G. *Chemical reviews* **2009**, *110*, 56–110.
- (62) Patitsas, S. N.; Lopinski, G. P.; Hul'ko, O.; Moffatt, D. J.; Wolkow, R. A. *Surface Science* **2000**, *457*, L425–L431.
- (63) Foley, E.; Kam, A.; Lyding, J.; Avouris, P. *Physical Review Letters* **1998**, DOI: 10 . 1103/PhysRevLett . 80 . 1336.
- (64) Shen, T. C.; Wang, C.; Abeln, G. C.; Tucker, J. R.; Lyding, J. W.; Avouris, P.; Walkup, R. E. *Science (New York, N.Y.)* **1995**, *268*, 1590–1592.
- (65) Reichert, J.; Ochs, R.; Beckmann, D.; Weber, H. B.; Mayor, M.; Löhneysen, H. v *Physical Review Letters* **2002**, *88*, 176804.
- (66) Darancet, P.; Widawsky, J. R.; Choi, H. J.; Venkataraman, L.; Neaton, J. B. *Nano Letters* **2012**, *12*, 6250–6254.
- (67) Park, Y. S.; Whalley, A. C.; Kamenetska, M.; Steigerwald, M. L.; Hybertsen, M. S.; Nuckolls, C.; Venkataraman, L. *Journal of the American Chemical Society* **2007**, *129*, 15768–15769.
- (68) Parameswaran, R.; Widawsky, J. R.; Vázquez, H.; Park, Y. S.; Boardman, B. M.; Nuckolls, C.; Steigerwald, M. L.; Hybertsen, M. S.; Venkataraman, L. *The Journal of Physical Chemistry Letters* **2010**, *1*, 2114–2119.
- (69) Bain, C. D.; Troughton, E. B.; Tao, Y. T.; Evall, J.; Whitesides, G. M.; Nuzzo, R. G. *Journal of the American Chemical Society* **1989**, *111*, 321–335.
- (70) Ulman, A. *Chemical Reviews* **1996**, *96*, 1533–1554.
- (71) Kim, Y.; Hellmuth, T. J.; Bürkle, M.; Pauly, F.; Scheer, E. *ACS nano* **2011**, *5*, 4104–4111.
- (72) Taylor, J.; Brandbyge, M.; Stokbro, K. *Physical Review Letters* **2002**, *89*, 138301.
- (73) Batra, A.; Darancet, P.; Chen, Q.; Meisner, J. S.; Widawsky, J. R.; Neaton, J. B.; Nuckolls, C.; Venkataraman, L. *Nano Lett* **2013**, *13*, 6233–7.
- (74) Frei, M.; Aradhya, S. V.; Hybertsen, M. S.; Venkataraman, L. *Journal of the American Chemical Society* **2012**, *134*, 4003–4006.
- (75) Huang, Z.; Chen, F.; Bennett, P. A.; Tao, N. *Journal of the American Chemical Society* **2007**, *129*, 13225–13231.
- (76) Sanderson, R. T. *Journal of the American Chemical Society* **1983**, *105*, 2259–2261.

- (77) Thierfelder, C.; Assadollahzadeh, B.; Schwerdtfeger, P.; Schäfer, S.; Schäfer, R. *Physical Review A* **2008**, *78*, 52506.
- (78) Klausen, R. S.; Widawsky, J. R.; Steigerwald, M. L.; Venkataraman, L.; Nuckolls, C. *J Am Chem Soc* **2012**, *134*, 4541–4.
- (79) Kobayashi, T.; Pannell, K. H. *Organometallics* **1990**, DOI: 10 . 1021 / om00158a012.
- (80) Kobayashi, T.; Pannell, K. H. *Organometallics* **1991**, DOI: 10 . 1021 / om00052a049.
- (81) Block, E.; Dikarev, E. V.; Glass, R. S.; Jin; Li, B.; Li, X.; Zhang, S.-Z. *Journal of the American Chemical Society* **2006**, *128*, 14949–14961.
- (82) Apfel, U. P.; Troegel, D.; Halpin, Y.; Tschierlei, S.; Uhlemann, U.; Gorls, H.; Schmitt, M.; Popp, J.; Dunne, P.; Venkatesan, M.; Coey, M.; Rudolph, M.; Vos, J. G.; Tacke, R.; Weigand, W. *Inorg Chem* **2010**, *49*, 10117–32.
- (83) Aradhya, S. V.; Frei, M.; Hybertsen, M. S.; Venkataraman, L. *Nature materials* **2012**, *11*, 872–876.
- (84) Colinge, J.-P.; Lee, C.-W.; Afzalian, A.; Akhavan, N. D.; Yan, R.; Ferain, I.; Razavi, P.; O'Neill, B.; Blake, A.; White, M.; Kelleher, A.-M.; McCarthy, B.; Murphy, R. *Nat Nano* **2010**, *5*, 225–229.
- (85) Shen, X.; Sun, B.; Liu, D.; Lee, S.-T. *J Am Chem Soc* **2011**, *133*, 19408–19415.
- (86) Yu, P. et al. *ACS Nano* **2013**, *7*, 10780–10787.
- (87) Shin, H.; Qiu, W.; Jarecki, R.; Cox, J. A.; Olsson, R. H.; Starbuck, A.; Wang, Z.; Rakich, P. T. *Nature Communications* **2013**, *4*, 1944.
- (88) Van Laer, R.; Kuyken, B.; Van Thourhout, D.; Baets, R. *Nat Photon* **2015**, *9*, 199–203.
- (89) Löfås, H.; Orthaber, A.; Jahn, B. O.; Rouf, A. M.; Grigoriev, A.; Ott, S.; Ahuja, R.; Ottosson, H. *The Journal of Physical Chemistry C* **2013**, *117*, 10909–10918.
- (90) Kiely, J. S.; Boudjouk, P. *Journal of Organometallic Chemistry* **1979**, *182*, 173–183.
- (91) Ando, W.; Wakahara, T.; Akasaka, T.; Nagase, S. *Organometallics* **1994**, *13*, 4683–4685.
- (92) Wakahara, T.; Kodama, R.; Akasaka, T.; Ando, W. *Bulletin of the Chemical Society of Japan* **1997**, *70*, 665–670.

- (93) Gryparis, C.; Stratakis, M. *Chem Commun (Camb)* **2012**, *48*, 10751–3.
- (94) Gryparis, C.; Kidonakis, M.; Stratakis, M. *Organic Letters* **2013**, *15*, 6038–6041.
- (95) Hochstrasser, R. M. *Accounts of Chemical Research* **1973**, *6*, 263–269.
- (96) Perdew, J. P.; Burke, K.; Ernzerhof, M. *Physical Review Letters* **1996**, *77*, 3865–3868.
- (97) Perdew, J. P.; Burke, K.; Ernzerhof, M. *Physical Review Letters* **1997**, *78*, 1396–1396.
- (98) Ordejón, P.; Artacho, E.; Soler, J. M. *Physical Review B* **1996**, *53*, R10441–R10444.
- (99) José, M. S.; Emilio, A.; Julian, D. G.; Alberto, G.; Javier, J.; Pablo, O.; Daniel, S.-P. *Journal of Physics: Condensed Matter* **2002**, *14*, 2745.
- (100) Choi, H. J.; Cohen, M. L.; Louie, S. G. *Physical Review B* **2007**, *76*, 155420.
- (101) Brandbyge, M.; Mozos, J.-L.; Ordejón, P.; Taylor, J.; Stokbro, K. *Physical Review B* **2002**, *65*, 165401.
- (102) Lou, L.; Nordlander, P. *Physical Review B* **1996**, *54*, 16659–16662.
- (103) Choi, Y. C.; Pak, C.; Kim, K. S. *The Journal of Chemical Physics* **2006**, *124*, 094308.
- (104) Vegiri, A.; Schevkunov, S. V. *The Journal of Chemical Physics* **2001**, *115*, 4175–4185.
- (105) Li, Y.; Doak, P.; Kronik, L.; Neaton, J. B.; Natelson, D. *Proceedings of the National Academy of Sciences* **2014**, *111*, 1282–1287.
- (106) Huang, Z.; Chen, F.; D’Agosta, R.; Bennett, P. A.; Di Ventra, M.; Tao, N. *Nat Nano* **2007**, *2*, 698–703.
- (107) Chen, Y.-C.; Zwolak, M.; Di Ventra, M. *Nano Letters* **2003**, *3*, 1691–1694.
- (108) Reed, M. A.; Tour, J. M. *Scientific American* **2000**, *282*, 86–93.
- (109) Song, H.; Reed, M. A.; Lee, T. *Advanced Materials* **2011**, *23*, 1583–1608.
- (110) Turro, N. J., *Modern molecular photochemistry*; University science books: 1991.
- (111) Butenhoff, T. J.; Moore, C. B. *Journal of the American Chemical Society;(USA)* **1988**, *110*.
- (112) Phelan, N. F.; Orchin, M. *J. Chem. Educ* **1968**, *45*, 633.

- (113) Van der Molen, S. J.; Liao, J.; Kudernac, T.; Agustsson, J. S.; Bernard, L.; Calame, M.; van Wees, B. J.; Feringa, B. L.; Schönenberger, C. *Nano letters* **2008**, *9*, 76–80.
- (114) Auwärter, W.; Seufert, K.; Bischoff, F.; Eciya, D.; Vijayaraghavan, S.; Joshi, S.; Klappenberger, F.; Samudrala, N.; Barth, J. V. *Nature nanotechnology* **2012**, *7*, 41–46.
- (115) Darwish, N.; Díez-Pérez, I.; Da Silva, P.; Tao, N.; Gooding, J. J.; Paddon-Row, M. N. *Angewandte Chemie International Edition* **2012**, *51*, 3203–3206.
- (116) Eliel, E. L.; Wilen, S. H.; Mandel, L. N. *Recueil des Travaux Chimiques des Pays Bas* **1995**, *114*, 378.
- (117) Choi, B.-Y.; Kahng, S.-J.; Kim, S.; Kim, H.; Kim, H. W.; Song, Y. J.; Ihm, J.; Kuk, Y. *Physical review letters* **2006**, *96*, 156106.
- (118) Donhauser, Z.; Mantooth, B.; Kelly, K.; Bumm, L.; Monnell, J.; Stapleton, J.; Price, D.; Rawlett, A.; Allara, D.; Tour, J., et al. *Science* **2001**, *292*, 2303–2307.
- (119) Moore, A. M.; Dameron, A. A.; Mantooth, B. A.; Smith, R. K.; Fuchs, D. J.; Ciszek, J. W.; Maya, F.; Yao, Y.; Tour, J. M.; Weiss, P. S. *Journal of the American Chemical Society* **2006**, *128*, 1959–1967.
- (120) Blum, A. S.; Kushmerick, J. G.; Long, D. P.; Patterson, C. H.; Yang, J. C.; Henderson, J. C.; Yao, Y.; Tour, J. M.; Shashidhar, R.; Ratna, B. R. *Nature Materials* **2005**, *4*, 167–172.
- (121) Rahimi, M.; Troisi, A. *Physical Review B* **2009**, *79*, 113413.
- (122) Moresco, F.; Meyer, G.; Rieder, K.-H.; Tang, H.; Gourdon, A.; Joachim, C. *Physical Review Letters* **2001**, *86*, 672.
- (123) Franco, I.; Solomon, G. C.; Schatz, G. C.; Ratner, M. A. *Journal of the American Chemical Society* **2011**, *133*, 15714–15720.
- (124) Shibano, Y.; Sasaki, M.; Tsuji, H.; Araki, Y.; Ito, O.; Tamao, K. *Journal of organometallic chemistry* **2007**, *692*, 356–367.
- (125) Ruehl, K. E.; Matyjaszewski, K. *Journal of organometallic chemistry* **1991**, *410*, 1–12.
- (126) Anklam, E. *Synthesis* **1987**.
- (127) Agrait, N; Rodrigo, J.; Vieira, S *Physical Review B* **1993**, *47*, 12345.

- (128) González, M. T.; Wu, S.; Huber, R.; van der Molen, S. J.; Schönenberger, C.; Calame, M. *Nano Letters* **2006**, *6*, 2238–2242.
- (129) Sandorfy, C. *Canadian Journal of Chemistry* **1955**, *33*, 1337–1351.
- (130) Schepers, T.; Michl, J. *Journal of Physical Organic Chemistry* **2002**, *15*, 490–498.
- (131) Salomon, A.; Cahen, D.; Lindsay, S.; Tomfohr, J.; Engelkes, V. B.; Frisbie, C. D. *Advanced Materials* **2003**, *15*, 1881–1890.
- (132) Temirov, R.; Lassise, A.; Anders, F.; Tautz, F. *Nanotechnology* **2008**, *19*, 065401.
- (133) Bruot, C.; Hihath, J.; Tao, N. *Nature nanotechnology* **2012**, *7*, 35–40.
- (134) Gonzalez, M. T.; Díaz, A.; Leary, E.; García, R.; Herranz, M. A.; Rubio-Bollinger, G.; Martín, N.; Agraït, N. *Journal of the American Chemical Society* **2013**, *135*, 5420–5426.
- (135) Trouwborst, M.; Huisman, E.; Bakker, F.; van der Molen, S.; van Wees, B. *Physical review letters* **2008**, *100*, 175502.
- (136) Chang, S.; He, J.; Zhang, P.; Gyarfás, B.; Lindsay, S. *Journal of the American Chemical Society* **2011**, *133*, 14267–14269.
- (137) Lin, J.; Beratan, D. N. *The Journal of Physical Chemistry A* **2004**, *108*, 5655–5661.
- (138) Lafferentz, L.; Ample, F.; Yu, H.; Hecht, S.; Joachim, C.; Grill, L. *Science* **2009**, *323*, 1193–1197.
- (139) Fan, F.-R. F.; Yang, J.; Cai, L.; Price, D. W.; Dirk, S. M.; Kosynkin, D. V.; Yao, Y.; Rawlett, A. M.; Tour, J. M.; Bard, A. J. *Journal of the American Chemical Society* **2002**, *124*, 5550–5560.
- (140) Piqueras, M. C.; Crespo, R.; Michl, J. *The Journal of Physical Chemistry A* **2003**, *107*, 4661–4668.
- (141) George, C. B.; Ratner, M. A.; Lambert, J. B. *The Journal of Physical Chemistry A* **2009**, *113*, 3876–3880.
- (142) Michl, J.; West, R. *Accounts of Chemical Research* **2000**, *33*, 821–823.
- (143) Goddard III, W. A.; Harding, L. B. *Annual Review of Physical Chemistry* **1978**, *29*, 363–396.
- (144) McConnell, H. M. *The Journal of Chemical Physics* **1961**, *35*, 508.

- (145) Woitellier, S; Launay, J.; Joachim, C *Chemical Physics* **1989**, *131*, 481–488.
- (146) Venkataraman, L.; Klare, J. E.; Nuckolls, C.; Hybertsen, M. S.; Steigerwald, M. L. *Nature* **2006**, *442*, 904–907.
- (147) Markoff, J. *New York Times* **July 2015**.
- (148) Ni, Z.; Liu, Q.; Tang, K.; Zheng, J.; Zhou, J.; Qin, R.; Gao, Z.; Yu, D.; Lu, J. *Nano letters* **2011**, *12*, 113–118.
- (149) Bianco, E.; Butler, S.; Jiang, S.; Restrepo, O. D.; Windl, W.; Goldberger, J. E. *ACS Nano* **2013**, *7*, 4414–4421.
- (150) Heath, J. R.; Shiang, J.; Alivisatos, A. *The Journal of chemical physics* **1994**, *101*, 1607–1615.
- (151) Heath, J. R.; LeGoues, F. K. *Chemical Physics Letters* **1993**, *208*, 263–268.
- (152) Gu, G; Burghard, M; Kim, G.-T.; Düsberg, G.; Chiu, P.; Krstic, V; Roth, S; Han, W. *Journal of Applied Physics* **2001**, *90*, 5747–5751.
- (153) Mahenderkar, N. K.; Liu, Y.-C.; Koza, J. A.; Switzer, J. A. *ACS nano* **2014**, *8*, 9524–9530.
- (154) Barth, S.; Kolešnik, M. M.; Donegan, K.; Krstic, V.; Holmes, J. D. *Chemistry of Materials* **2011**, *23*, 3335–3340.
- (155) Hanrath, T.; Korgel, B. A. *The Journal of Physical Chemistry B* **2005**, *109*, 5518–5524.
- (156) Morgan, G. T.; Drew, H. D. K. *Journal of the Chemical Society, Transactions* **1925**, *127*, 1760–1768.
- (157) Amadoruge, M. L.; Weinert, C. S. *Chemical reviews* **2008**, *108*, 4253–4294.
- (158) Weinert, C. S. *Dalton Transactions* **2009**, 1691–1699.
- (159) Roewe, K. D.; Rheingold, A. L.; Weinert, C. S. *Chemical Communications* **2013**, *49*, 8380–8382.
- (160) Mochida, K.; Hata, R.; Chiba, H.; Seki, S.; Yoshida, Y.; Tagawa, S. *Chemistry letters* **1998**, *27*, 263–264.
- (161) Kumada, M.; Sakamoto, S.; Ishikawa, M. *Journal of Organometallic Chemistry* **1969**, *17*, 235–240.

- (162) Peterson, D. J. *The Journal of Organic Chemistry* **1967**, *32*, 1717–1720.
- (163) Kamenetska, M.; Koentopp, M.; Whalley, A. C.; Park, Y. S.; Steigerwald, M. L.; Nuckolls, C.; Hybertsen, M. S.; Venkataraman, L. *Physical Review Letters* **2009**, *102*, 126803.
- (164) Matsuura, Y. *Journal of Applied Physics* **2014**, *115*, 043701.
- (165) West, R. *Journal of organometallic chemistry* **1986**, *300*, 327–346.
- (166) Tsuji, H.; Terada, M.; Toshimitsu, A.; Tamao, K. *Journal of the American Chemical Society* **2003**, *125*, 7486–7487.
- (167) Tamao, K.; Tsuji, H.; Terada, M.; Asahara, M.; Yamaguchi, S.; Toshimitsu, A. *Angewandte Chemie* **2000**, *112*, 3425–3428.
- (168) Imhof, R.; Antic, D.; David, D. E.; Michl, J. *The Journal of Physical Chemistry A* **1997**, *101*, 4579–4586.
- (169) Tsuji, H.; Michl, J.; Tamao, K. *Journal of organometallic chemistry* **2003**, *685*, 9–14.
- (170) Drenth, W.; Noltes, J.; Bulten, E.; Creemers, H. *Journal of Organometallic Chemistry* **1969**, *17*, 173–174.
- (171) Boberski, W.; Allred, A. *Journal of Organometallic Chemistry* **1975**, *88*, 65–72.
- (172) Okano, M.; Mochida, K. *Chemistry Letters* **1990**, *19*, 701–704.
- (173) Wierschke, S. G.; Chandrasekhar, J.; Jorgensen, W. L. *Journal of the American Chemical Society* **1985**, *107*, 1496–1500.
- (174) Lambert, J. B.; Zhao, Y.; Emblidge, R. W.; Salvador, L. A.; Liu, X.; So, J.-H.; Chelius, E. C. *Accounts of chemical research* **1999**, *32*, 183–190.
- (175) Nguyen, K. A.; Gordon, M. S.; Wang, G.-t.; Lambert, J. B. *Organometallics* **1991**, *10*.
- (176) Lambert, J. B.; Wang, G. T.; Teramura, D. H. *The Journal of Organic Chemistry* **1988**, *53*, 5422–5428.
- (177) Eaborn, C.; Pande, K. *Journal of the Chemical Society (Resumed)* **1960**, 1566–1571.
- (178) Klausen, R. S.; Widawsky, J. R.; Su, T. A.; Li, H.; Chen, Q.; Steigerwald, M. L.; Venkataraman, L.; Nuckolls, C. *Chemical Science* **2014**, *5*, 1561–1564.

- (179) Meisner, J. S.; Ahn, S.; Aradhya, S. V.; Krikorian, M.; Parameswaran, R.; Steigerwald, M.; Venkataraman, L.; Nuckolls, C. *Journal of the American Chemical Society* **2012**, *134*, PMID: 23167533, 20440–20445.
- (180) Engelkes, V. B.; Beebe, J. M.; Frisbie, C. D. *Journal of the American Chemical Society* **2004**, *126*, 14287–14296.
- (181) Venkataraman, L.; Park, Y. S.; Whalley, A. C.; Nuckolls, C.; Hybertsen, M. S.; Steigerwald, M. L. *Nano letters* **2007**, *7*, 502–506.
- (182) Glass, R. S.; Block, E.; Gruhn, N. E.; Jin; Lorance, E.; Zakai, U. I.; Zhang, S.-Z. *The Journal of Organic Chemistry* **2007**, *72*, PMID: 17915922, 8290–8297.
- (183) Bard, A. J.; Faulkner, L. R., et al. *Electrochemical Methods* **2001**, *2*.
- (184) Song, L.; Lin, Y.; Wu, W.; Zhang, Q.; Mo, Y. *The Journal of Physical Chemistry A* **2005**, *109*, 2310–2316.
- (185) Fogarty, H. A.; Imhof, R.; Michl, J. *Proceedings of the National Academy of Sciences of the United States of America* **2004**, *101*, 10517–10522.
- (186) Fukazawa, A.; Tsuji, H.; Tamao, K. *Journal of the American Chemical Society* **2006**, *128*, 6800–6801.
- (187) Sabater, C; Untiedt, C.; Palacios, J.; Caturla, M. *Physical review letters* **2012**, *108*, 205502.
- (188) Madelung, O Semiconductors: Data Handbook. 2004.
- (189) Krebs, R. E., *The history and use of our earth's chemical elements: a reference guide*; Greenwood Publishing Group: 2006.
- (190) Van Schrojenstein Lantman, E. M.; Deckert-Gaudig, T.; Mank, A. J. G.; Deckert, V.; Weckhuysen, B. M. *Nat Nano* **2012**, *7*, 583–586.
- (191) Zhang, J.; Vukmirovic, M. B.; Xu, Y.; Mavrikakis, M.; Adzic, R. R. *Angewandte Chemie International Edition* **2005**, *44*, 2132–2135.
- (192) Lima, F. H. B.; Zhang, J.; Shao, M. H.; Sasaki, K.; Vukmirovic, M. B.; Ticianelli, E. A.; Adzic, R. R. *The Journal of Physical Chemistry C* **2007**, *111*, 404–410.
- (193) Wu, D.-Y.; Liu, X.-M.; Duan, S.; Xu, X.; Ren, B.; Lin, S.-H.; Tian, Z.-Q. *The Journal of Physical Chemistry C* **2008**, *112*, 4195–4204.

- (194) Kötz, E. R.; Neff, H.; Müller, K. *Journal of Electroanalytical Chemistry and Interfacial Electrochemistry* **1986**, *215*, 331–344.
- (195) Christensen, N. E. *Journal of Physics F: Metal Physics* **1978**, *8*, L51.
- (196) Jiang, N.; Foley, E. T.; Klingsporn, J. M.; Sonntag, M. D.; Valley, N. A.; Dieringer, J. A.; Seideman, T.; Schatz, G. C.; Hersam, M. C.; Van Duyne, R. P. *Nano Letters* **2012**, *12*, 5061–5067.
- (197) Kaneko, S.; Nakazumi, T.; Kiguchi, M. *The Journal of Physical Chemistry Letters* **2010**, *1*, 3520–3523.
- (198) Kim, T.; Vázquez, H.; Hybertsen, M. S.; Venkataraman, L. *Nano Letters* **2013**, *13*, 3358–3364.
- (199) Peng, Z.-L.; Chen, Z.-B.; Zhou, X.-Y.; Sun, Y.-Y.; Liang, J.-H.; Niu, Z.-J.; Zhou, X.-S.; Mao, B.-W. *The Journal of Physical Chemistry C* **2012**, *116*, 21699–21705.
- (200) Wang, Y.-H.; Li, D.-F.; Hong, Z.-W.; Liang, J.-H.; Han, D.; Zheng, J.-F.; Niu, Z.-J.; Mao, B.-W.; Zhou, X.-S. *Electrochemistry Communications* **2014**, *45*, 83–86.
- (201) Ko, C.-H.; Huang, M.-J.; Fu, M.-D.; Chen, C.-h. *Journal of the American Chemical Society* **2010**, *132*, 756–764.
- (202) Kiguchi, M.; Tal, O.; Wohlthat, S.; Pauly, F.; Krieger, M.; Djukic, D.; Cuevas, J. C.; van Ruitenbeek, J. M. *Physical Review Letters* **2008**, *101*, 046801.
- (203) Yelin, T.; Korytar, R.; Sukenik, N.; Vardimon, R.; Kumar, B.; Nuckolls, C.; Evers, F.; Tal, O. *Nat Mater* **Apr. 2016**, *15*, 444–449.
- (204) Wang, Y.-H.; Zhou, X.-Y.; Sun, Y.-Y.; Han, D.; Zheng, J.-F.; Niu, Z.-J.; Zhou, X.-S. *Electrochimica Acta* **2014**, *123*, 205–210.
- (205) Wang, Y.-H.; Hong, Z.-W.; Sun, Y.-Y.; Li, D.-F.; Han, D.; Zheng, J.-F.; Niu, Z.-J.; Zhou, X.-S. *The Journal of Physical Chemistry C* **2014**, *118*, 18756–18761.
- (206) Geng, W. T.; Nara, J.; Ohno, T. *Thin Solid Films* **2004**, *464–465*, 379–383.
- (207) Lawson, J. W.; Bauschlicher, C. W. *Physical Review B* **2006**, *74*, 125401.
- (208) Xie, Z.; Bâldea, I.; Smith, C. E.; Wu, Y.; Frisbie, C. D. *ACS Nano* **2015**, *9*, 8022–8036.
- (209) Kim, B.; Choi, S. H.; Zhu, X. Y.; Frisbie, C. D. *Journal of the American Chemical Society* **2011**, *133*, 19864–19877.

- (210) Aradhya, S. V.; Frei, M.; Halbritter, A.; Venkataraman, L. *ACS Nano* **2013**, *7*, 3706–3712.
- (211) Cui, L.; Jeong, W.; Hur, S.; Matt, M.; Klöckner, J. C.; Pauly, F.; Nielaba, P.; Cuevas, J. C.; Meyhofer, E.; Reddy, P. *Science* **2017**, DOI: 10 . 1126 / science . aam6622.
- (212) Hölzl, J; Schulte, F. In *Solid Surface Physics*; Springer: 1979, pp 1–150.
- (213) Schulz, M. *Nature* **1999**, *399*, 729–730.
- (214) Lu, J.; Nagase, S. *Physical Review Letters* **2003**, *90*, 115506.
- (215) Guisinger, N. P.; Greene, M. E.; Basu, R.; Baluch, A. S.; Hersam, M. C. *Nano Letters* **2004**, *4*, 55–59.
- (216) Lenfant, S.; Krzeminski, C.; Delerue, C.; Allan, G.; Vuillaume, D. *Nano Letters* **2003**, *3*, 741–746.
- (217) Hersam, M. C.; Guisinger, N. P.; Lyding, J. W. *Nanotechnology* **2000**, *11*, 70.
- (218) Rakshit, T.; Liang, G.-C.; Ghosh, A. W.; Datta, S. *Nano Letters* **2004**, *4*, 1803–1807.
- (219) Sergani, S.; Furmansky, Y.; Visoly-Fisher, I. *Nanotechnology* **2013**, *24*, 455204.
- (220) Nakamura, M.; Yoshida, S.; Katayama, T.; Taninaka, A.; Mera, Y.; Okada, S.; Takeuchi, O.; Shigekawa, H. *Nat Commun* **2015**, *6*, DOI: 10 . 1038 / ncomms9465.
- (221) Hong, W.; Li, H.; Liu, S. X.; Fu, Y.; Li, J.; Kaliginedi, V.; Decurtins, S.; Wandlowski, T. *J Am Chem Soc* **2012**, *134*, 19425–31.
- (222) Emanuelsson, R.; Löfås, H.; Wallner, A.; Nauroozi, D.; Baumgartner, J.; Marschner, C.; Ahuja, R.; Ott, S.; Grigoriev, A.; Ottosson, H. *Chemistry – A European Journal* **2014**, *20*, 9304–9311.
- (223) Löfås, H.; Emanuelsson, R.; Ahuja, R.; Grigoriev, A.; Ottosson, H. *The Journal of Physical Chemistry C* **2013**, *117*, 21692–21699.
- (224) Whittaker, S. M.; Brun, M.; Cervantes-Lee, F.; Pannell, K. H. *Journal of Organometallic Chemistry* **1995**, *499*, 247–252.
- (225) Fischer, R.; Frank, D.; Gaderbauer, W.; Kayser, C.; Mechtler, C.; Baumgartner, J.; Marschner, C. *Organometallics* **2003**, *22*, 3723–3731.

- (226) Marschner, C. *European Journal of Inorganic Chemistry* **1998**, 1998, 221–226.
- (227) Wallner, A.; Hlina, J.; Konopa, T.; Wagner, H.; Baumgartner, J.; Marschner, C.; Flörke, U. *Organometallics* **2010**, 29, 2660–2675.
- (228) Mastryukov, V. S.; Hofmann, M.; Schaefer, H. F. *The Journal of Physical Chemistry A* **1999**, 103, 5581–5584.
- (229) Naruse, Y.; Ma, J.; Takeuchi, K.; Nohara, T.; Inagaki, S. *Tetrahedron* **2006**, 62, 4491–4497.
- (230) Bande, A.; Michl, J. *Chemistry – A European Journal* **2009**, 15, 8504–8517.
- (231) Fogarty, H. A.; Ottosson, C.-H.; Michl, J. *Journal of Molecular Structure* **2000**, 556, 105–121.
- (232) Chen, J. Z.; Thygesen, K. S.; Jacobsen, K. W. *Physical Review B* **2012**, 85, 155140.
- (233) Quek, S. Y.; Venkataraman, L.; Choi, H. J.; Louie, S. G.; Hybertsen, M. S.; Neaton, J. B. *Nano Letters* **2007**, 7, 3477–3482.
- (234) Koentopp, M.; Burke, K.; Evers, F. *Physical Review B* **2006**, 73, 121403.
- (235) Bahn, S. R.; Jacobsen, K. W. *Computing in Science Engineering* **2002**, 4, 56–66.
- (236) Mortensen, J. J.; Hansen, L. B.; Jacobsen, K. W. *Physical Review B* **2005**, 71, 035109.
- (237) Larsen, A. H.; Vanin, M.; Mortensen, J. J.; Thygesen, K. S.; Jacobsen, K. W. *Physical Review B* **2009**, 80, 195112.
- (238) Yanson, A. I.; Bollinger, G. R.; van den Brom, H. E.; Agrait, N.; van Ruitenbeek, J. M. *Nature* **1998**, 395, 783–785.
- (239) González, M. T.; Leary, E.; García, R.; Verma, P.; Herranz, M. Á.; Rubio-Bollinger, G.; Martín, N.; Agrait, N. *The Journal of Physical Chemistry C* **2011**, 115, 17973–17978.
- (240) Christian, A. M.; Dapeng, D.; Herre, S. J.v.d. Z.; Jan, M. v. R. *New Journal of Physics* **2008**, 10, 065008.
- (241) Inkpen, M. S.; Lemmer, M.; Fitzpatrick, N.; Milan, D. C.; Nichols, R. J.; Long, N. J.; Albrecht, T. *Journal of the American Chemical Society* **2015**, 137, 9971–9981.
- (242) Vacek, J.; Chocholousova, J. V.; Stara, I. G.; Stary, I.; Dubi, Y. *Nanoscale* **2015**, 7, 8793–8802.

- (243) Guo, Y.-D.; Yan, X.-H.; Xiao, Y.; Liu, C.-S. *Scientific Reports* **2015**, *5*, 16731.
- (244) Tsuji, Y.; Hoffmann, R. *Chemistry – A European Journal* **2016**, *22*, 4878–4888.
- (245) Hoffmann, R. *Accounts of Chemical Research* **Jan. 1971**, *4*, 1–9.
- (246) Jeong, M.; Doris, B.; Kedzierski, J.; Rim, K.; Yang, M. *Science* **2004**, *306*, 2057–2060.
- (247) Wallner, A.; Emanuelsson, R.; Baumgartner, J.; Marschner, C.; Ottosson, H. *Organometallics* **2013**, *32*, 396–405.
- (248) Press, E. M.; Marro, E. A.; Surampudi, S. K.; Siegler, M. A.; Tang, J. A.; Klausen, R. S. *Angewandte Chemie* **2017**, *129*, 583–587.
- (249) Tsuji, H.; Fogarty, H. A.; Ehara, M.; Fukuda, R.; Casher, D. L.; Tamao, K.; Nakatsuji, H.; Michl, J. *Chemistry – A European Journal* **2014**, *20*, 9431–9441.
- (250) Wagner, H.; Baumgartner, J.; Marschner, C.; Poelt, P. *Organometallics* **2011**, *30*, 3939–3954.
- (251) Tsurusaki, A.; Koyama, Y.; Kyushin, S. *Journal of the American Chemical Society* **2017**.
- (252) Tour, J. M. *Accounts of Chemical Research* **2000**, *33*, 791–804.
- (253) Hybertsen, M. S.; Venkataraman, L. *Accounts of Chemical Research* **2016**, *49*, 452–460.
- (254) Su, T. A.; Neupane, M.; Steigerwald, M. L.; Venkataraman, L.; Nuckolls, C. *Nature Reviews Materials* **2016**, *1*, 16002.
- (255) Li, C.; Pobelov, I.; Wandlowski, T.; Bagrets, A.; Arnold, A.; Evers, F. *Journal of the American Chemical Society* **2008**, *130*, 318–326.
- (256) Van der Laan, G. P.; de Haas, M. P.; Hummel, A.; Frey, H.; Möller, M. *The Journal of Physical Chemistry* **1996**, *100*, 5470–5480.
- (257) Grozema, F. C.; Siebbeles, L. D.; Warman, J. M.; Seki, S.; Tagawa, S.; Scherf, U. *Advanced Materials* **2002**, *14*, 228–231.
- (258) Kitao, T.; Bracco, S.; Comotti, A.; Sozzani, P.; Naito, M.; Seki, S.; Uemura, T.; Kitagawa, S. *Journal of the American Chemical Society* **2015**, *137*, 5231–5238.
- (259) Marschner, C. *Organometallics* **2006**, *25*, 2110–2125.

- (260) Fischer, R.; Baumgartner, J.; Kickelbick, G.; Marschner, C. *Journal of the American Chemical Society* **2003**, *125*, 3414–3415.
- (261) Ogura, K.; Fujita, M.; Takahashi, K.; Iida, H. *Chemistry Letters* **1982**, *11*, 1697–1698.
- (262) Iwamoto, T.; Tsushima, D.; Kwon, E.; Ishida, S.; Isobe, H. *Angewandte Chemie* **2012**, *124*, 2390–2394.
- (263) Pramanik, A.; Sarkar, P. *The Journal of Chemical Physics* **2015**, *143*, 114314.
- (264) Tamblyn, I.; Darancet, P.; Quek, S. Y.; Bonev, S. A.; Neaton, J. B. *Physical Review B* **2011**, *84*, DOI: ARTN20140210 . 1103/PhysRevB . 84 . 201402.
- (265) Pedersen, K. G.; Strange, M.; Leijnse, M.; Hedegård, P.; Solomon, G. C.; Paaske, J. *Physical Review B* **2014**, *90*, 125413.
- (266) Frederiksen, T.; Munuera, C.; Ocal, C.; Brandbyge, M.; Paulsson, M.; Sanchez-Portal, D.; Arnau, A. *ACS Nano* **2009**, *3*, 2073–2080.
- (267) Thuo, M. M.; Reus, W. F.; Nijhuis, C. A.; Barber, J. R.; Kim, C.; Schulz, M. D.; Whitesides, G. M. *Journal of the American Chemical Society* **2011**, *133*, 2962–2975.
- (268) Jiang, L.; Sangeeth, C. S. S.; Nijhuis, C. A. *Journal of the American Chemical Society* **2015**, *137*, 10659–10667.
- (269) Yuan, L.; Thompson, D.; Cao, L.; Nerngchangnong, N.; Nijhuis, C. A. *The Journal of Physical Chemistry C* **2015**, *119*, 17910–17919.
- (270) Strange, M.; Thygesen, K. S. *Beilstein Journal of Nanotechnology* **2011**, *2*, 746–754.
- (271) Aviram, A. *Journal of the American chemical society* **1988**, *110*, 5687–5692.
- (272) Joachim, C.; Gimzewski, J.; Aviram, A. *Nature* **2000**, *408*, 541–548.
- (273) Heath, J. R.; Ratner, M. A. *Physics Today* **2003**, *56*, 43–49.
- (274) Tao, N. *Nature nanotechnology* **2006**, *1*, 173–181.
- (275) Kamenetska, M.; Quek, S. Y.; Whalley, A. C.; Steigerwald, M. L.; Choi, H. J.; Louie, S. G.; Nuckolls, C.; Hybertsen, M. S.; Neaton, J. B.; Venkataraman, L. *J Am Chem Soc* **2010**, *132*, 6817–21.
- (276) Quek, S. Y.; Kamenetska, M.; Steigerwald, M. L.; Choi, H. J.; Louie, S. G.; Hybertsen, M. S.; Neaton, J. B.; Venkataraman, L. *Nat Nanotechnol* **2009**, *4*, 230–4.

- (277) Meisner, J. S.; Kamenetska, M.; Krikorian, M.; Steigerwald, M. L.; Venkataraman, L.; Nuckolls, C. *Nano letters* **2011**, *11*, 1575–1579.
- (278) Fatemi, V.; Kamenetska, M.; Neaton, J.; Venkataraman, L. *Nano letters* **2011**, *11*, 1988–1992.
- (279) Marchenko, A.; Katsonis, N.; Fichou, D.; Aubert, C.; Malacria, M. *Journal of the American Chemical Society* **2002**, *124*, 9998–9999.
- (280) Marqués-González, S.; Yufit, D. S.; Howard, J. A.; Martín, S.; Osorio, H. M.; García-Suárez, V. M.; Nichols, R. J.; Higgins, S. J.; Cea, P.; Low, P. J. *Dalton Transactions* **2013**, *42*, 338–341.
- (281) Vonlanthen, D.; Rotzler, J.; Neuburger, M.; Mayor, M. *European journal of organic chemistry* **2010**, *2010*, 120–133.
- (282) Ke, S.-H.; Yang, W.; Baranger, H. U. *Nano letters* **2008**, *8*, 3257–3261.
- (283) Aradhya, S. V.; Meisner, J. S.; Krikorian, M.; Ahn, S.; Parameswaran, R.; Steigerwald, M. L.; Nuckolls, C.; Venkataraman, L. *Nano letters* **2012**, *12*, 1643–1647.
- (284) Roy, X.; Schenck, C. L.; Ahn, S.; Lalancette, R. A.; Venkataraman, L.; Nuckolls, C.; Steigerwald, M. L. *Angewandte Chemie International Edition* **2012**, *51*, 12473–12476.
- (285) Myers, A. G.; Kephart, S. E.; Chen, H. *Journal of the American Chemical Society* **1992**, *114*, 7922–7923.
- (286) Denmark, S. E.; Griedel, B. D.; Coe, D. M. *Journal of organic chemistry* **1993**, *58*, 988–990.
- (287) Matsumoto, K.; Oshima, K.; Utimoto, K. *The Journal of Organic Chemistry* **1994**, *59*, 7152–7155.
- (288) Moth-Poulsen, K.; Bjørnholm, T. *Nature nanotechnology* **2009**, *4*, 551–556.
- (289) Nichols, R. J.; Haiss, W.; Higgins, S. J.; Leary, E.; Martin, S.; Bethell, D. *Phys Chem Chem Phys* **2010**, *12*, 2801–15.
- (290) Kiely, J. S.; Boudjouk, P. *Journal of Organometallic Chemistry* **1979**, *182*, 173–183.
- (291) Ando, W.; Wakahara, T.; Akasaka, T.; Nagase, S. *Organometallics* **1994**, *13*, 4683–4685.
- (292) Wakahara, T.; Kodama, R.; Akasaka, T.; Ando, W. *Bulletin of the Chemical Society of Japan* **1997**, *70*, 665–670.

- (293) Vazquez, H; Skouta, R; Schneebeli, S; Kamenetska, M; Breslow, R; Venkataraman, L; Hybertsen, M. *Nature Nanotechnology* **2012**, *7*, 663–667.
- (294) Yoshida, H.; Ikadai, J.; Shudo, M.; Ohshita, J.; Kunai, A. *Journal of the American Chemical Society* **2003**, *125*, 6638–6639.
- (295) Yoshida, H.; Ikadai, J.; Shudo, M.; Ohshita, J.; Kunai, A. *Organometallics* **2005**, *24*, 156–162.
- (296) Yoshida, H.; Nakano, S.; Mukae, M.; Ohshita, J. *Organic letters* **2008**, *10*, 4319–4322.
- (297) Gualco, P.; Amgoune, A.; Miqueu, K.; Ladeira, S.; Bourissou, D. *Journal of the American Chemical Society* **2011**, *133*, 4257–4259.
- (298) Gualco, P.; Ladeira, S.; Miqueu, K.; Amgoune, A.; Bourissou, D. *Angewandte Chemie International Edition* **2011**, *50*, 8320–8324.
- (299) Joost, M.; Gualco, P.; Coppel, Y.; Miqueu, K.; Kefalidis, C. E.; Maron, L.; Amgoune, A.; Bourissou, D. *Angewandte Chemie International Edition* **2014**, *53*, 747–751.
- (300) Katsonis, N.; Marchenko, A.; Taillemite, S.; Fichou, D.; Chouraqui, G.; Aubert, C.; Malacria, M. *Chemistry—A European Journal* **2003**, *9*, 2574–2581.
- (301) Katsonis, N.; Marchenko, A.; Fichou, D.; Barrett, N. *Surface Science* **2008**, *602*, 9–16.
- (302) Watcharinyanon, S.; Nilsson, D.; Moons, E.; Shaporenko, A.; Zharnikov, M.; Albinsson, B.; Mårtensson, J.; Johansson, L. S. *Physical Chemistry Chemical Physics* **2008**, *10*, 5264–5275.
- (303) Crabtree, R. H. *Angewandte Chemie International Edition in English* **1993**, *32*, 789–805.
- (304) Ie, Y.; Hirose, T.; Nakamura, H.; Kiguchi, M.; Takagi, N.; Kawai, M.; Aso, Y. *Journal of the American Chemical Society* **2011**, *133*, 3014–3022.
- (305) Ie, Y.; Tanaka, K.; Tashiro, A.; Lee, S. K.; Testai, H. R.; Yamada, R.; Tada, H.; Aso, Y. *The journal of physical chemistry letters* **2015**, *6*, 3754–3759.
- (306) Karimi, M. A.; Bahoosh, S. G.; Valášek, M.; Bürkle, M.; Mayor, M.; Pauly, F.; Scheer, E. *Nanoscale* **2016**, *8*, 10582–10590.
- (307) Kiguchi, M.; Takahashi, Y.; Fujii, S.; Takase, M.; Narita, T.; Iyoda, M.; Horikawa, M.; Naitoh, Y.; Nakamura, H. *The Journal of Physical Chemistry C* **2014**, *118*, 5275–5283.